UNIVERSITY OF SOUTHAMPTON

FACULTY OF ENGINEERING AND APPLIED SCIENCE

SCHOOL OF ENGINEERING SCIENCES

Thesis submitted for the Degree of Doctor of Philosophy

REAL-TIME ELECTROSTATIC CHARGE MONITORING OF THE WEAR SURFACES AND DEBRIS GENERATED BY SLIDING BEARING STEEL CONTACTS

by Sebastian Morris

June 2003

UNIVERSITY OF SOUTHAMPTON

ABSTRACT

FACULTY OF ENGINEERING AND APPLIED SCIENCE
SCHOOL OF ENGINEERING SCIENCES
Doctor of Philosophy

REAL-TIME ELECTROSTATIC CHARGE MONITORING OF THE WEAR SURFACES AND DEBRIS GENERATED BY SLIDING BEARING STEEL CONTACTS

by Sebastian Morris

An electrostatic sensor was originally developed for condition monitoring of the gas path of jet engines and turbines. It was used to detect changes in the level of debris present in the gas path, which can be related to component deterioration such as blade rubbing, combustion chamber erosion and poor combustion performance. Preliminary studies have been carried out in the University of Southampton to apply this technology to monitor oil-lubricated contacts. Precursor charge events have been successfully detected prior to the onset of significant wear and the charging mechanisms involved are thought to be tribocharging, triboemissions, surface charge variation and debris generation. This thesis presents research conducted to establish the contributions of surface charging and debris generation to the overall charge detected during wear.

During the monitoring of lubricated sliding wear of bearing steel, the occurrence and location of precursor signals prior to catastrophic failure were detected using improved signal processing that utilises a three-dimensional colour map which relates the exact magnitude, duration and position of charge features on the wear surface. The polarity of the signals was predominantly positive for tests with a mineral base oil and both positive and negative for a fully synthetic oil. The sources of the precursor signals have been confirmed to be surface charging due to the formation of white layers and the generation and entrainment of wear debris. Electrostatic sensing was also found to be sensitive to very small changes in wear rate, not detectable by the measurement of volume loss. Further tests were carried out to study the effects of surface charge and debris generation and entrainment separately. The electrostatic monitoring system was found to be sensitive to small changes in the surface charge due to contact potential difference (CPD) effects arising from subtle differences in surface work functions. It is also sensitive to the transition between mild and severe oxidational wear under unlubricated steel sliding conditions by detecting the dynamic behaviour of CPD change related to the dynamics of wear. Charge features related exclusively to the presence of wear debris have been identified during tests carried out on a modified pin-on-disc rig with base oil lubrication. Wear debris from normal adhesive wear produced positively charged debris while wear debris from wear induced by debris seeding produced negatively charge debris. This difference is thought to be related to differences in the wear mechanism. Electrostatic sensing was also sensitive to the change in the wear rate and volume of debris generated. Further tests confirmed that one of the main debris charging mechanisms was tribocharging, which is affected directly by the test materials and lubricant conductivity. Some work has been carried out to optimise the electrostatic sensor for use in debris detection in the oil line of lubricated systems. The concept of a micro-macro sensor with the potential to detect debris size has been proposed. In order to achieve the design, preliminary work has been carried out to improve the resolution of the current sensor design. Further proposals are made as to how this work can be further developed, in terms of better understanding of debris and surface charging mechanisms and the implementation of computer modeling to aid the design and optimisation of sensors as well as to further understand electric field behaviour within a tribocontact.

TABLE OF CONTENTS

ACKNOWLEDGEMENTS

I am grateful to the Office of Naval Research (ONR)/US Navy for their financial support (Grant No. N00014-97-0100) of this project and also to Smiths Aerospace Electronics Systems Southampton, particularly their representative Dr. Honor Powrie, for their technical support and advice.

I would like to thank especially Dr. Robert Wood and Dr. Terry Harvey for their supervision of this work and also to my other colleagues, particularly Dr. Ling Wang and Mr. K.S. Tan for their support and general advice.

I am particularly grateful to the Surface Engineering and Tribology Group technicians for their general help in the laboratory and also to SKF Limited, University of Swansea Dynamics and Condition Monitoring Group, National Physical Laboratory (NPL) and Osprey Metals Limited for supplying test materials free of charge.

NOMENCLATURE

Term	Meaning	Unit
Chapter 2		
a	Debris width	m
b	Debris length	m
Chapter 3		
A	Area	m^2
b	Ion mobility	$m^{-2}\ V^{-1} s^{-1}$
C	Capacitance	F
C_F	Capacitance of the Faraday cup	F
C_o	Effective contact capacitance	pF
C_r	Sensing ring capacitance	F
D	Flux density	$C\ m^{-2}$
D_m	Molecular diffusion coefficient	$m^2\ s^{-1}$
d	Distance of a point charge from an isolated conducting plate	m
E	Electrical field strength	$V\ m^{-1}$
e	Charge on an electron	1.602×10^{-19} C
ε	Relative permittivity medium	$F\ m^{-1}$
ε_o	Permittivity of free space	$F\ m^{-1}$
F	Force	N
F_c	Faraday constant	$96485\ C\ mol^{-1}$
κ	Conductivity	$\Omega^{-1}\ m^{-1}$
λ	Debye length	m
η	Dynamic viscosity	$Kg\ m^{-1}\ s^{-1}$
ϕ	Work function	eV
$Q_{enclosed}$	Total charge contained within the enclosed volume	C
q	Charge	C
q_c	Charge induced on sensor	C
$q_{induced}$	Charge induced on the Faraday cup	C
$q_{particle}$	Charge on particle	C
q_{ring}	Charge on sensing ring	C
R_q	rms Surface roughness	μm
R	Gas Constant	$8.3144\ J\ mol^{-1}\ K^{-1}$
r_{ionic}	Hydrodynamic radius	m
S	Area of enclosing surface	m^2
T	Temperature	K
V	Voltage	V
V_{CPD}	Contact potential difference	eV
v	Velocity	$m\ s^{-1}$
z	Charge on ion	-
Chapter 4		
α_t	Coefficient of thermal expansion	$\mu m\ ^oC^{-1}$
α	Pressure viscosity index	Pa
ΔT	Temperature change.	^oC
E^*	Contact modulus	Pa
h	Pin vertical displacement	m

h_{min}	Minimum film thickness	m
L	Original length	m
η_0	Base viscosity at atmospheric pressure	kg m^{-1} s^{-1}
R	Radius of curvature sphere	m
r	Radius of curvature of pin	m
U	Entraining horizontal velocity	m s^{-1}
V_{loss}	Total volume loss	m^3
W	Normal load	N
Chapter 5		
F	Applied normal force	N
m_{pin}	Mass loss of pin	kg
ρ	Bearing steel density	kg m^{-3}
S	Sliding distance	m
V_{total}	Total volume loss	m^3
W	Specific wear rate	m^3 N^{-1} m^{-1}
Chapter 7		
A	Debris surface area	m^2
a	Particle radius	m
α_{abs}	Fraction of emitted species that are not absorbed by lubricant	-
C_{eff}	Debris effective capacitance	pF
$D_{\pm}$	Ionic diffusivities	m^2 s^{-1}
$\Delta\phi$	Work function difference	eV
E_{bond}	Energy of bonds broken during exoemission	J
E_{debris}	Energy of bonds broken during debris formation	J
$E_{critical}$	Threshold voltage	V m^{-1}
E_a	The applied electric field	V m^{-1}
E_p	Electric field on the tip of pin	V m^{-1}
ε	Dielectric constant of lubricant	3 C^2 N^{-1} m^{-2}
ε_o	Permitivitty of free space	8.85×10^{-12} C^2 N^{-1} m^{-2}
$K_{\pm}$	Adsorption rates	mol s^{-1}
$K'_{\pm}$	Desorption rates	mol s^{-1}
κ	Conductivity	pS m^{-1}
$n_{\pm}$	Localised ionic concentrations	mol dm^{-3}
N_{ads}	Number of adsorbate molecules per unit area	m^{-2}
N_{bond}	Number of bonds broken during exoemission	-
N_{debris}	Number of bonds broken during debris formation	-
μ	Induced dipole moment	C m^{-1}
ρ	Recombination rate	Dimensionless
Q_o	Initial charge	C
Q	Charge remaining after time t	C
$Q_{prefabs}$	Surface charge due to preferred absorption	C
q_M	Maximum charge on particle	C

r_{tip}	Radius of tip	m
t	Time	s
τ	Relaxation constant	s^{-1}
τ_{debris}	Debris relaxation constant of charge	s^{-1}
V	The potential difference	V
$V_{critical}$	Critical voltage	V
v	Entrained oil velocity	ms^{-1}
Chapter 8		
g	Gravity	m
h_a	Distance of the release point to point c	m
m_{fov}	Total field of view	s
$t_{droplet}$	Time taken for a 2 mm oil droplet to move past a sensor of width w_{sensor}	s
t_{peak}	Duration from a to b	m
w_{sensor}	Sensor width	m

ABBREVIATIONS

Abbreviations	Meaning
A/D	Analogue to digital
ACS	Absolute charge system
BBPS	Baseband power spectrum
BEM	Boundary element method
CPD	Contact potential difference
DAT	Digital audio tape
ED-XRF	Energy dispersive X-ray fluorescence
EDMS	Engine distress monitoring system
EDX	Energy Dispersive X-ray
EHL	Elasto-Hydrodynamic lubrication
FEM	Finite element method
FDM	Finite difference method
FZG	Forschungsstelle für Zahnräder und Getriebebau (Research centre for gears and gear construction) University of Munich, Germany
IDMS	Ingested debris monitoring system
LVDT	Linear vertical displacement transducer
OLS	Oil line sensor
PC	Personal computer
rms	Root mean square
SEM	Scanning electron microscope
SOA	Spectrometric oil analysis
UHF	Ultra high frequency
WSS	Wear site sensor

TABLE OF FIGURES

1 INTRODUCTION

2 CONDITION MONITORING

3 FUNDAMENTALS OF ELECTROSTATICS

4 ELECTROSTATIC CHARGE MONITORING OF LUBRICATED SLIDING WEAR

5 SURFACE CHARGE EXPERIMENTS

6 REAL-TIME MONITORING OF CHARGED DEBRIS

7 SIMULATED DEBRIS CHARGING AND OIL LINE SENSOR CALIBRATION

8 OIL LINE SENSOR OPTIMISATION

9 CONCLUSIONS AND FURTHER WORK

APPENDICES

TABLE OF TABLES

1

INTRODUCTION

1.1 CONDITION MONITORING

Rapid advances in the design and working condition of mechanical systems in industrial, aerospace and military equipment over the years have resulted in the ever-increasing complexity of problems encountered in the management of their maintenance. In the last four decades, maintenance philosophies have progressed from breakdown maintenance in the 1950's to productive maintenance that is practiced today. During this period, a huge range of analytical instruments and methods have been developed to produce information on operational parameters and equipment condition in order to improve maintenance management. The ability to monitor the performance of machinery components in terms of wear and durability is extremely invaluable. In industry, large sums of money are spent replacing worn or failed components. According to a survey conducted in 1997, the average cost of wear was about 0.25% of company turnover but plants with higher figures require further attention to reduce costs. Often unnecessary component change takes place simply because the machine operator has no information on the remaining life span of the components. In many cases, component failures are detected only when the machines actually cease to operate. Thus, it is essential to monitor wear occurrences and severity so prediction of any forthcoming failure can be made and hence accurate maintenance schedules can be planned.

1.2 ELECTROSTATICS

The first recorded awareness of the existence of static electricity dates back to the time of the ancient Greeks. For many scientists and engineers today the words 'static electricity' tend to bring ancient Wimhurst machines, Van de Graff generators and 'hair raising' experiments in the local science museum to mind. Yet static electricity, or more accurately, electrostatic phenomena, is much more common than this view might suggest. Phenomenon such as lightning, the crackling sound heard when undressing on cold dry winter days, electric shocks from doorknobs, filing cabinets and cars etc. are manifestations of electrostatic charging. It was many centuries before the potential uses of electrostatics were realized. In the modern world, electrostatic technology is widely used in various industrial activities such as particle separation, coating of various materials, fabrication of semiconductors, printing, mining etc. Scientifically, electrostatics in general is still not well understood and is subjected to countless active research in various aspects of the subject.

Recently, the technique of electrostatic sensing technology has been applied to condition monitoring technologies. It is a novel technology originally developed for the detection of debris in the gas path (intake and exhaust) of jet engines and turbines. The technique monitors discrepancies between the amount of debris ingested and the amount of debris present in the exhaust gas. These can be related to gas path component deterioration such as blade rubbing, combustion chamber erosion, poor combustion performance and the wear of abradable seals and coatings. The advantage of the electrostatic system is that it uses a direct measurement of debris produced by engine faults, rather than secondary effects such as abnormal levels of vibration and/or temperature. Another advantage of this technique is that it is sensitive to a wide range of debris sizes and most material types; ferrous, metallic (non-ferrous) and non-metallic debris.

1.3 WORK TO DATE

Fundamental research of electrostatic monitoring has been extensively carried out at the University of Southampton for the past 6 years. It is part of the NICOP project (see Section 1.4) entitled 'Dynamic and Quasi-static Charge Measurement Probes for Machinery Component Diagnostics' undertaken in collaboration with Georgia Institute of Technology (GeorgiaTech). It has been established that the electrostatic sensing system is sensitive to various aspects such as oil charging and chemistry, surface changes and charged particles of various materials. The test materials studied are typically those used in lubricated high contact stress applications such as gears and bearings. Other less common materials, such as ceramics, will also be studied in future test programmes. Preliminary development work has also shown the viability of the electrostatic monitoring technique to detect the onset of adhesive wear in oil-lubricated contacts (scuffing) [1-3]. Precursor charge events were detected prior to the onset of scuffing and were thought to relate to one or more of the following: tribocharging phenomena, triboemissions, surface charge variations and debris generation.

1.4 STATEMENT OF INTENT

This PhD research project aims to focus on understanding the contribution of surface charge and wear debris to the overall charge detected from the electrostatic sensors. More specifically, this project is intended to establish the charge levels and mechanisms associated with surface charge generation and wear debris production, entrainment and transportation in oil-lubricated sliding bearing steel contacts. These will be investigated for various mineral base oil and fully formulated synthetic oil. The overall objective is to look into the feasibility of mapping the charge densities associated with surface charging and wear debris generated by different wear mechanisms. This information would allow responses from the sensors to be associated with exact types of wear mechanisms which then can be used to assess the severity of wear.

1.5 PROJECT STRUCTURE

Figure 1.1 shows a flow chart outlining the overall structure of the PhD project.

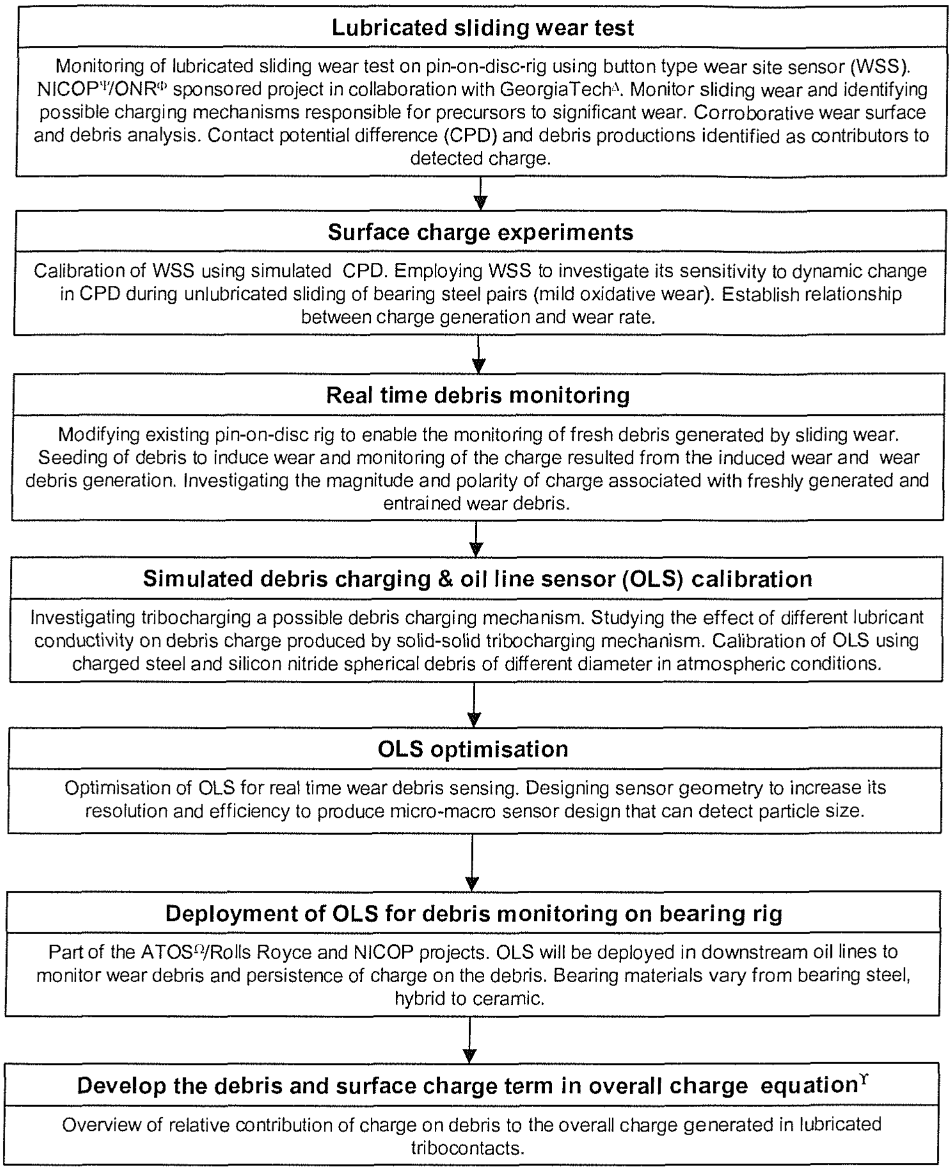

Lubricated sliding wear test

Monitoring of lubricated sliding wear test on pin-on-disc-rig using button type wear site sensor (WSS). NICOP$^{\Psi}$/ONR$^{\Phi}$ sponsored project in collaboration with GeorgiaTech$^{\Delta}$. Monitor sliding wear and identifying possible charging mechanisms responsible for precursors to significant wear. Corroborative wear surface and debris analysis. Contact potential difference (CPD) and debris productions identified as contributors to detected charge.

Surface charge experiments

Calibration of WSS using simulated CPD. Employing WSS to investigate its sensitivity to dynamic change in CPD during unlubricated sliding of bearing steel pairs (mild oxidative wear). Establish relationship between charge generation and wear rate.

Real time debris monitoring

Modifying existing pin-on-disc rig to enable the monitoring of fresh debris generated by sliding wear. Seeding of debris to induce wear and monitoring of the charge resulted from the induced wear and wear debris generation. Investigating the magnitude and polarity of charge associated with freshly generated and entrained wear debris.

Simulated debris charging & oil line sensor (OLS) calibration

Investigating tribocharging a possible debris charging mechanism. Studying the effect of different lubricant conductivity on debris charge produced by solid-solid tribocharging mechanism. Calibration of OLS using charged steel and silicon nitride spherical debris of different diameter in atmospheric conditions.

OLS optimisation

Optimisation of OLS for real time wear debris sensing. Designing sensor geometry to increase its resolution and efficiency to produce micro-macro sensor design that can detect particle size.

Deployment of OLS for debris monitoring on bearing rig

Part of the ATOS$^{\Omega}$/Rolls Royce and NICOP projects. OLS will be deployed in downstream oil lines to monitor wear debris and persistence of charge on the debris. Bearing materials vary from bearing steel, hybrid to ceramic.

Develop the debris and surface charge term in overall charge equation$^{\Upsilon}$

Overview of relative contribution of charge on debris to the overall charge generated in lubricated tribocontacts.

Figure 1.1 Overall structure of PhD project.

Ψ NICOP stands for Naval International Cooperative Opportunities In Science and Technology Program and is a funding mechanism to encourage international collaboration in science & technology for the mutual benefit of the US Navy and international participants. NICOP is managed by the Office of Naval Research International Field Offices (ONRIFO) by actively seeking non-US complimentary strengths in science and technology with the intent of setting up collaborative programs. NICOP is a means of initiating international science & technology collaboration, establishing working relationships, and leveraging the benefits of international programs. Through capitalization, mutual respect and staff interaction will lead to further collaboration and long-term relationships, to the mutual benefit of all participants and their national interests. A NICOP research project entitled 'Dynamic and Quasi-static Charge Measurement Probes for Machinery Component Diagnostics' is currently undertaken by the University of Southampton in collaboration with GeorgiaTech. Its aim is to improve the definition of charging mechanisms under experimental conditions and apply the technology in 'realistic' environment in order to develop a prototype sensor system including fault detection algorithms. This PhD research forms part of the University of Southampton The knowledge in science and technology acquired from this project is intended to be applied to Naval (marine) gearboxes and naval aircraft components maintenance.

Φ ONR stands for Office of Naval Research a division of the United States Navy. ONR coordinates, executes, and promotes the science and technology programs of the United States Navy and Marine Corps through universities, government laboratories, and non-profit and for-profit organizations. It provides technical advice to the Chief of Naval Operations and the Secretary of the Navy, works with industry to improve technology and manufacturing processes while reducing fleet costs, and fosters continuing academic interest in naval relevant science from the high school through post-doctoral levels.

Δ GaTech stands for Georgia Institute of Technology a collaborator with University of Southampton for the NICOP/ONR program.

Ω ATOS stands for Advanced Transmission and Oil System Concepts and is a three-year European research project with Rolls Royce as the main sponsor. There are 13 partners from 4 European countries (UK, Germany, Belgium and Italy) involved in the project. The project is composed of seven work packages with specific objectives. The University of Southampton is within Work Package 1 (hybrid bearing validations). The task of the University of Southampton within the work package is to investigate the wear mechanism of silicon nitride pairing with various bearing steel materials under oil lubricated conditions using electrostatic method to develop a new monitoring system for aircraft engine bearings.

ϒ For the overall charge equation, please refer to Chapter 7

1.6 THESIS STRUCTURE

This thesis is divided into several chapters. The first chapter contains the introduction to the general subject area covered by this thesis.

Chapter 2 to Chapter 3 contains the literature review and background studies. Chapter 2 provide the background for condition monitoring, reviewing commonly used techniques with an emphasis on wear debris analysis and monitoring and also novel condition monitoring techniques using electrostatic sensing technology. Chapter 3 reviews related electrostatic fundamentals covering basic sensor designs and related mechanisms of charge generation.

Chapter 4 to Chapter 8 discusses the test programmes (experimental work) designed and carried out to achieve the research objective. The test programmes have been designed to further develop the understanding of electrostatic charge generation during lubricated sliding wear concentrating on the degree of contribution from surface charging and wear debris

Chapter 4 discusses the test programme that has been developed to investigate charge generation leading to the scuffing of bearing steel. Button type wear site sensors (WSS) were employed and mineral base and fully formulated synthetic oil were used as lubricants. The main objective of the tests was to pinpoint precursor signals prior to scuffing (severe adhesive wear) for sliding ball on disc test configuration and to establish the possible causes of the precursor signals through corroborative analysis which includes wear debris and wear surface analysis. CPD effect and debris formation was identified as the main source of charge detected.

Chapter 5 contains discussion of the work conducted to develop a better understanding of CPD effects. It details the simulated surface charging test as well as the unlubricated sliding test, designed to calibrate the WSS. Surface charging was simulated by inserting different metals and an insulator into a bearing steel disc and the sensitivity of the WSS to the associated surface charge is investigated. The unlubricated sliding wear experiments were designed to study the sensitivity of the WSS to dynamic surface charging (dynamic CPD effects) due to the dynamic nature of mild oxidational wear. The lack of lubrication eliminates charging events associated with the presence of lubricants.

Chapter 6 discusses the test programme designed to investigate the charge contribution of debris formation, entrainment and transportation. Two categories of test were carried out with mineral base oil lubrication; normal and induced wear debris.

Chapter 7 details the work carried out to investigate the possible debris charging mechanism in oil and the calibration of OLS for oil line debris monitoring. The effect of oil conductivities on debris charging is also discussed. An overview of a debris charging model will also be discussed here.

Chapter 8 presents preliminary work carried out to optimise OLS to obtain a compromise between high resolution and adequate efficiency for oil line debris monitoring. This is a first step in designing OLS that is sensitive to debris size.

Chapter 9 details the overall conclusion of the work presented and planned future work. Figure 1.2 below summarises the structure of this thesis, demonstrating the step-by-step approach toward achieving the overall objectives.

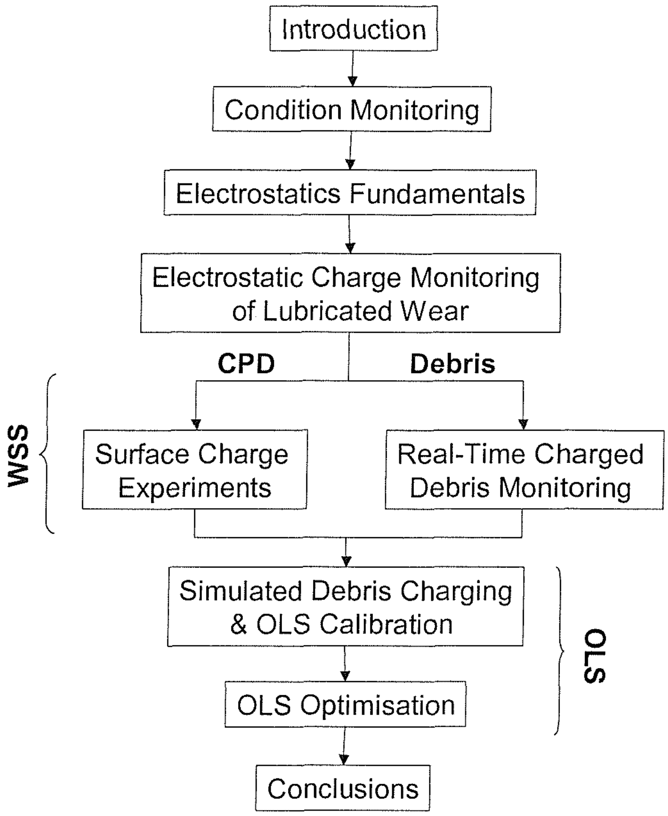

Figure 1.2 Summary of thesis structure.

2

CONDITION MONITORING

2.1 INTRODUCTION

Condition monitoring is defined as the assessment on a continuous or periodic basis of mechanical and electrical condition of machinery, equipment and systems from the observations and/or recordings of selected measurement parameters [4].

The key components of any successful monitoring activity comprise of [5]:

- Dependable detection
- Effective diagnosis
- Reliable decision

Detection is an essential element of any condition based monitoring. The failure of the sensing device or analysis technique will render the condition monitoring process redundant. Successful detection will enable the operator to monitor and track the fault trend and the associated decline in component performance. Effective diagnosis will enable the operator to separate the 'cause' from 'effect'. The third component is the most significant and critical component. Reports from the operator will lead to the recommendation whether to cease operation in order to conduct inspections or repairs. The transition from what might be termed as 'benign' to active wear that must be monitored closely especially when it then deteriorates further to a 'failure' condition. Figure 2.1 shows schematically the transition from 'benign' to 'active' wear and subsequent failure, as a function of operating time. From the wear rate, in the early period of the machinery life it may appear as if severe wear in taking place. This is the running-in period. For a machine that is operating within its designed envelope, the level of wear rate will soon decrease to a lower value and stay there for most of the remainder of its operating lifetime. As a transition from benign to active wear occurs the combination of detection and diagnosis will enable the severity and nature of the problem to be determined. At this point the decision on how long operation should be continued before interruption has to be made.

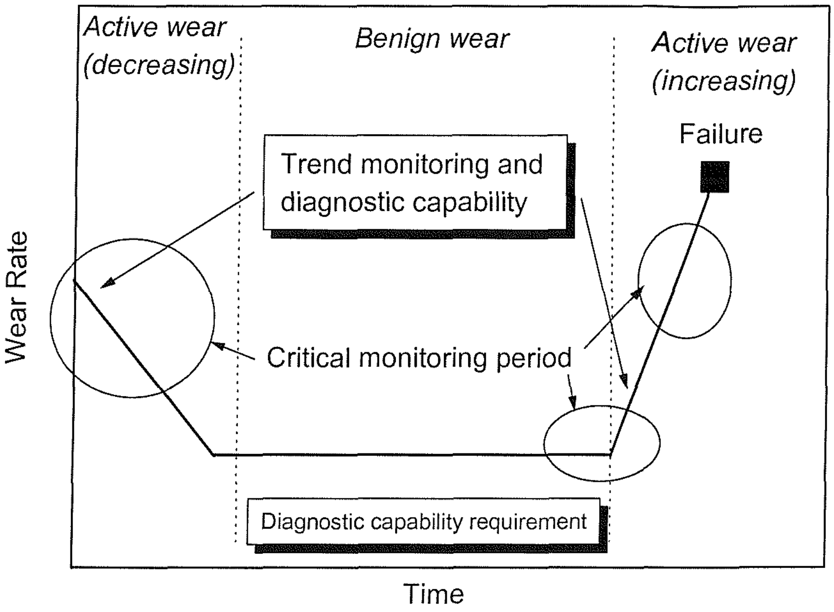

Figure 2.1 *Monitoring requirements for detecting and analysing transitions from benign to active wear [5].*

Growth of condition monitoring has been fuelled by industrial demand to minimise the consequence of machine failures and to utilise existing maintenance resources more effectively [6]. The reliance of most industries on complex machinery means that any breakdowns can have a substantial impact on profitability. Profitability is affected by factors such as loss of availability, cost of spares, cost of breakdown labour, cost of secondary damage and risk of injury to people and the environment. These pressures are reflected by recent legislation setting standards in areas such as product liability, health and safety, and pollution control. Machinery breakdowns have been made more complicated due to the fact that equipment and products are manufactured to tighter specifications, using minimal material to reduce manufacturing costs. This requires higher manufacturing tolerances to ensure the production of reliable and high quality products.

These pressures have created a demand for maintenance systems that are able to minimise equipment failure risks. This has accelerated the development of maintenance systems based on the condition of equipment, rather than waiting until failure occurs or replacing parts on a regular basis. The fulfilment of these demands have been made possible due to the growth in cost-effective condition monitoring tools as a direct result of technological advancements. Reduced costs of instrumentation and the improved data storage, using low-cost computer systems are one of the examples. The increased capabilities of instrumentation, such as data presentation and also faster and more effective analysis using specialist software have also contributed immensely.

Condition monitoring can provide several advantages compared to other strategies of maintenance:

- Improved availability of equipment
- Reduced breakdown costs
- Improved reliability and safety
- Improved planning

2.2 CONDITION MONITORING TECHNIQUES

A concise review of basic condition monitoring techniques has been conducted by Barron [6] and Neale [7]. The following next sections discuss several basic measurement techniques commonly used for the condition monitoring of machinery. It will also include a novel use of electrostatic sensor and sensing technology as a condition monitoring technique.

2.2.1 Manual Inspection

In manual inspection the maintenance staff use their senses of sight, touch and hearing to make an assessment of the condition of the equipment [6]. Generally, two main categories of manual inspection techniques are used;

1. Internal inspections

   This is carried out by dismantling the equipment, using inspection hatches or by inserting an optical probe.

2. External inspections

   This technique tends to be more general. It is used to pick up obvious faults such as rubber components perishing or loosening of bolts. The type of components monitored is limited by access and any problems need to be deduced from the observations made.

2.2.2 Vibration

This technique can be defined as the measurement of cyclic movement or vibration generated by the dynamic action of the internal components of the machine. Vibration will occur on any part of a machine which is subjected to a rotation that is not about its centre of gravity. Vibration measurement levels can therefore give an indication of possible problems due to uneven component movement. For example, gear teeth and rolling bearings with pitted surfaces due to fatigue wear, which have suffered damage or build up of deposits, will tend to show unbalanced vibration. Vibration signals can be analysed in terms of amplitude or mean velocity. The frequency of vibration signals is another important characteristic as its content can give a direct indication of the source and also relate to the movement of the machine components, as shown in Figure 2.2.

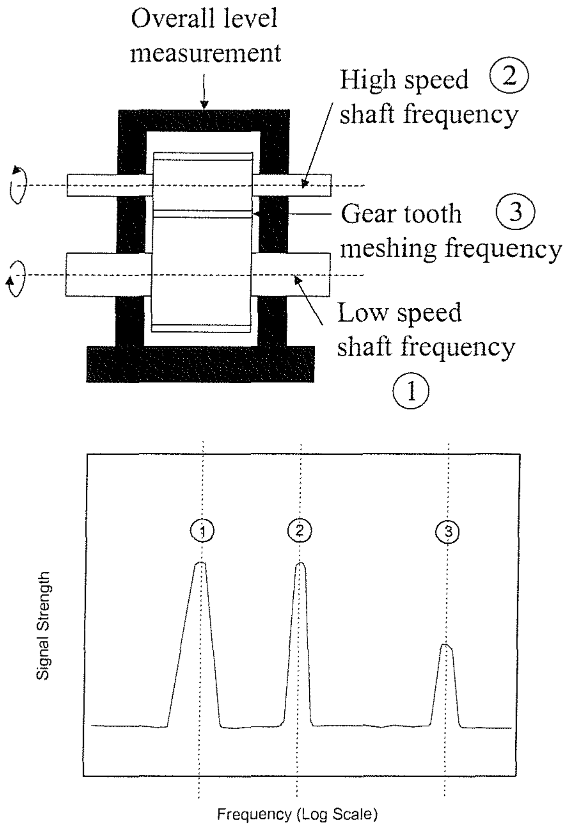

Figure 2.2 *The generation of vibration at signal frequencies related to various machine components [7].*

2.2.3 Temperature

The condition of a machine can be monitored by monitoring the temperature of critical points near the moving surfaces of machines components. Temperature pattern on a machine assembly can also be used to monitor the condition of a machine. Machine components subjected to relative motion operating satisfactorily within their designed characteristic will have relatively low friction and therefore their operating temperature will be generally low. Any major increase in the temperature can be a direct indication of some form of fault. Bearings are frequently fitted with temperature monitoring systems, usually located near the highest loaded area in order to detect any defect. As well as localised temperature measurements, area measurement by infrared thermography can also be used to monitor the temperature distribution around a machine casing. This can be useful to detect bearing thermal instability as well as showing partial blockages in pipes or ducts carrying warm fluids. Electrical faults can also be detected using infrared thermography, identifying localised areas of overheating.

2.2.4 Performance

Condition monitoring of a machine can be carried out by studying the relationships between the operating characteristics or the consistency of its internal components behaviour. This may involve continuous comparison of two or more factors, such as the flow and temperature changes across a heat exchanger, or the delivery pressure and running speed of a pump, shown in Figure 2.3. In some machines, directly monitoring their output can be a useful way of monitoring their internal condition. This is especially true for machines that produce a continuously moving material output, such as textile weaving machines. In this case, internal component deterioration frequently shows as variations in the pattern of the output material.

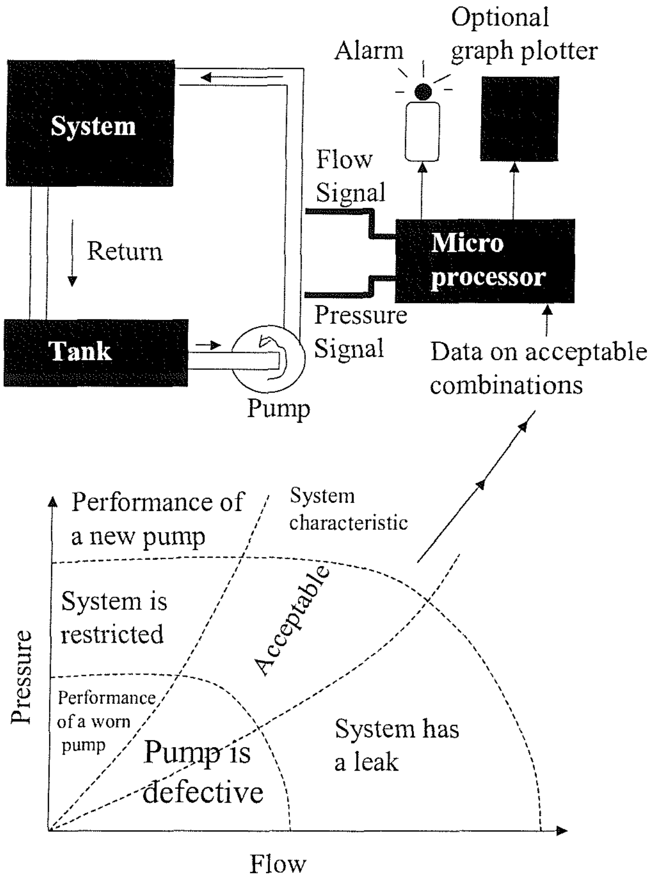

Figure 2.3 The comparison of two or more performance variables to indicate the condition of a machine [7].

2.2.5 Expected Safe Life

Condition monitoring is not possible for machines that do not show progressive signs of deterioration. A good example of this is a high-speed gas turbine rotor, which has a long life, but is limited by thermal creep and fatigue. The most effective technique to monitor components of this kind is to monitor their operating time under various conditions to determine when their expected safe life is being reached, and then withdraw them from service.

2.2.6 Oil and Wear Debris Analysis

Degradation of lubricating oil can be attributed to numerous factors such as thermal oxidation, contamination due to the ingress of coolants, fuels and other lubricants and build-up of particles in the system caused by component wear or the generation of soot are the typical examples. The properties of oils can be accessed in several ways, namely acidity for oxidation, viscosity for lubrication, flashpoint for contamination and chemical composition for chemical degradation. By and large they indicate whether the oil needs changing, failure of components such as seals and heat exchangers as well as components overheating. One of the more established oil analysis techniques is spectrometric oil analysis. It analyses the concentration of particular elements in the oil and compares this to a new oil sample. Any changes in the concentration or presence of a particular element can be attributed to wear.

The surface of the components of machinery subjected to relative motion is designed to be separated by a lubricant film. If however, the components are overloaded, inadequately lubricated or contaminated by hard particles, the surface can be damaged and will generate wear debris. The rate of wear debris production and their size can give a good diagnosis of the severity of the problem. Various wear debris analysis techniques are available for the examination of oil samples and to extract wear particles in order to analyse their concentration, size and shape, shown in Figure 2.4. Alternatively, it maybe preferable to sample through direct collection of particles within the lubricant system, by means such as magnetic plugs or filters.

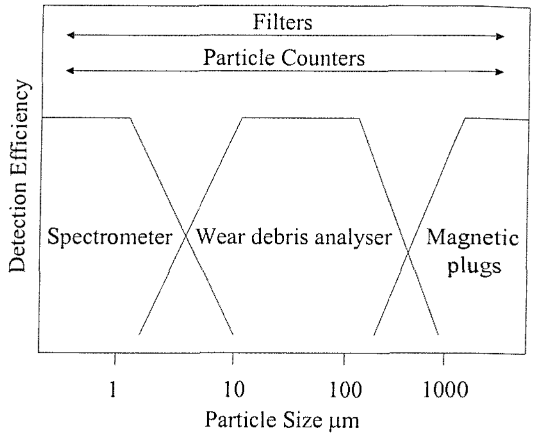

Figure 2.4 *The particle size range of various wear debris collection and analysis processes [7]*

Wear debris analysis condition monitoring techniques will be given a special interest due to the scope of this thesis and will be discussed in detail in the next section, Section 2.3.

2.2.7 Electrostatics

Electrostatic sensing technology is a novel technology originally developed for the detection of debris in the gas path of jet engines and turbines. Two electrostatic sensing systems have been successfully employed in the condition monitoring of gas path faults and these include EDMS (Engine Distress Monitoring System) and IDMS (Ingested Debris Monitoring System). EDMS detects the electrostatic charge associated with debris by placing a sensor in the jet pipe of a jet engine [8,9]. Changes in the amount of debris present in the exhaust gas may be related to gas path component deterioration such as blade rubbing, combustion chamber erosion, poor combustion performance and wear of abradable seals and coatings. Installing electrostatic sensors in the intake of a jet engine will enable foreign objects entering the engine to be detected and discriminated. This is known as the IDMS as detailed in [10].

The advantage of the electrostatic system is that it uses a direct measurement of debris produced by engine faults, rather than secondary effects such as excessive vibration and/or temperature exceedances. The technique is sensitive to a wide range of debris sizes and most material types; ferrous, metallic (non-ferrous) and non-metallic debris

Research work in the application of electrostatic sensing technology under oil-lubricated systems is being conducted at University of Southampton. Tests involve using rigs such as the pin-on-disc, reciprocating contact wear and FZG gear tester. Section 2.4 will discuss electrostatic condition monitoring in greater detail.

2.3 WEAR DEBRIS ANALYSIS AND DETECTION

2.3.1 Introduction

Wear debris is the direct result of wear of solids. Different wear mechanisms will generally produce different types of wear debris. Wear debris analysis is a very useful but relatively costly technique used in condition monitoring. The primary objectives of wear debris analysis are as follows: to detect the incidences of wear and the wear debris concentration as a function of time; to diagnose the type and, by inference, to deduce the cause [11].

Existing wear debris analysis techniques and detection will be reviewed in this section. This section will also highlight different techniques of assessment of wear debris in order to associate them with specific wear mechanism and severity. Graphical examples of common types of wear debris will also be presented.

2.3.2 Trend Analysis

The essential criteria to relate wear debris characteristic to their wear condition is shown in Figure 2.5. Wear debris analysis involves the analysis of debris found in, or coming from, a system or component [12]. In wear debris analysis, the severity of wear in a particular system or component can be determined by the quantity of particles generated. [11]. Therefore, a quick estimation of the severity of wear can be made by gravimetric analysis [13].

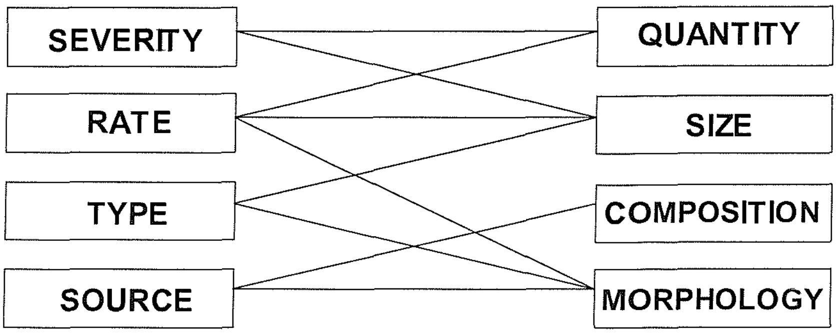

Figure 2.5 The relationship between wear and wear particle characteristic [12].

Trend analysis is the process by which a change in machine condition is determined from an examination of changes of specific sensors or outputs [13]. A typical trend for debris formation is shown in Figure 2.6. A system using bearings and gears exhibits a high but decreasing level of wear rate when first operated, i.e. debris generated by the running-in process. Then the level of wear stays at a low and acceptable level, a characteristic of a well lubricated system, although a slight increase or fluctuation may occur. Finally the level of wear starts to rise very steeply showing the occurrence of fatigue or fracture with the accompanying of ever-increasing amount of debris generated curve as shown in Figure 2.6.

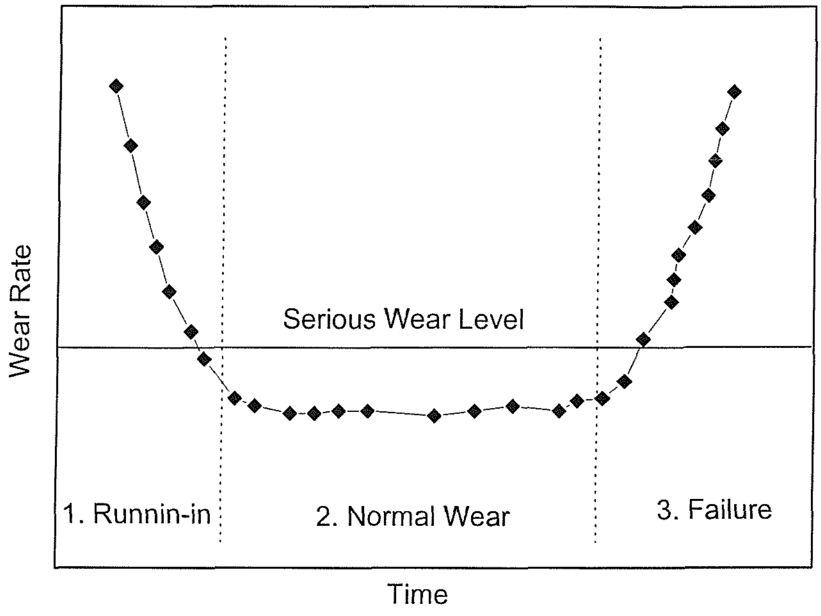

Figure 2.6 *The three classical stages can be represented in the 'bath-tub' wear rate graph (time not to scale) [12].*

2.3.3 Debris Morphology

During wear, the mode or mechanism can be related to the morphological properties of the debris produced, such as shape, size, surface topography and colour. Each of the attributes can be used to identify the different aspects of wear processes in a system.

Shape

The shape analysis of debris can be performed using optical microscopy (>100 μm), Scanning Electron Microscope (SEM) or metallurgical microscopy (<1 μm). Shape analysis can give an indication of the type and origin of wear. Table 2.1 shows typical debris shape and their possible origins [13].

Debris Shape	Typical Names	Possible Origins
	Spheres	Metal fatigue, welding sparks, glass peening beads
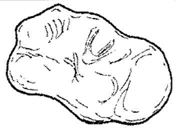	Pebbles and smooth ovoids	Quarry dust, atmospheric dust.
	Chunks and slabs	Metal fatigue, bearing pitting, rock debris
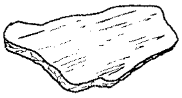	Platelets and Flakes	Running-in metal wear, paint or rust, copper in grease.
	Curls, spirals, slivers	Machining debris produced at high temperature
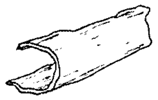	Rolls	Probably similar to platelets but in a rolled form
	Strands and fibres	Polymers, cotton and wood fibres. Occasionally metal

Table 2.1 Typical debris shape and their possible origins [13].

The overall 'outline' and inspections of the edge detail can be used to define wear debris shape [11] shown by Figure 2.7. The aspect ratio and the roundness factor provide general indications of the effect the wear process has on particle formation. They are defined as;

$$aspect\ ratio = \frac{b}{a} \qquad 2.1$$

$$roundness\ factor = \frac{(perimeter)^2}{(4\pi \times area)} \qquad 2.2$$

These two parameters tend to be dependent on each other due to the relationship between area and perimeter, any detectable changes in edge detail will be reflected in the significant increase of the roundness factor relative to aspect ratio.

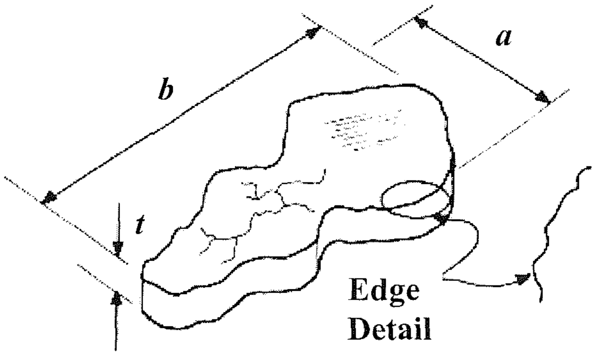

Figure 2.7 *Shape analysis of wear debris [11].*

Thickness, *t*, analysis can be carried out using SEM analysis [14] or even a conventional optical microscope, with the help of a special software to counteract limited depth of field problems [15]. Analysis with SEM can have an added benefit of direct verification of material composition.

Although wear rate manifests itself in the amount of wear debris formed, the change of the amount of a particular type of wear debris and hence wear mechanism may be more crucial. In this case a scatter plot of the aspect ratio value of debris may lead to a better representation of the trend as shown in Figure 2.8.

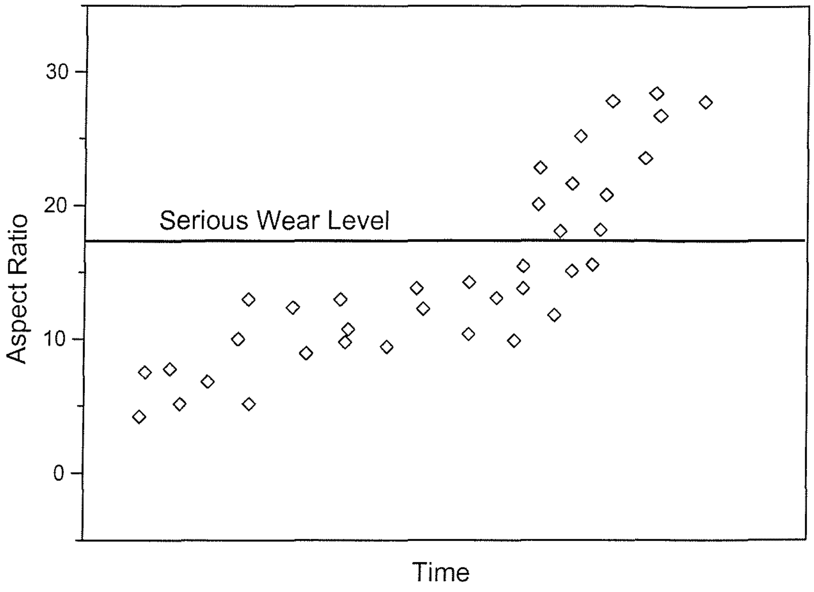

Figure 2.8 *Trending of particle morphology [12].*

Size

The size and size ratio of wear debris can indicate the origin and the mechanism of wear that is responsible for the generation. Several examples (for oil sampling technique) are shown below:

- High ratio of large to small debris = severe sliding (high stress contact)
- Debris size < 5 μm = benign (normal) wear
- Debris size > 15 μm = abnormal wear, component requires attention

Surface topography and colour

Surface topography provides information about the possible wear mechanism and the parent material. Direct visual inspection can give immediate distinction between wear debris due to severe sliding wear, pitting and plastic deformation. The colour [16] and shape of wear debris can also help to distinguish debris materials; for example, between metal oxides or polymer material.

2.3.4 Advanced debris morphology analysis

Over the recent years, numerous research has been carried out to develop advanced debris morphology analysis techniques. This has been greatly encouraged by the advancement of computing power and cost-efficient equipment [16]. Due to the scope of this thesis these will only be treated with a general overview.

Advanced analysis of debris size has been carried out by the implementation of Weibull distribution and moments analysis [17,18]. They have each been found to be a powerful method for identifying and distinguishing different wear modes. Fractals have been applied to the analysis of surface, size, shape and dimension of wear debris [19-23]. Fourier transforms have also been used to classify different debris shape and surface texture [24,25]. Computer software which analyses shape, colour, size and surface condition of wear debris has been developed to be used as a semi-automatic debris classification system [26].

2.3.5 Wear and wear debris

Difficulties arise when trying to relate a particular debris to the wear mechanism responsible for its formation. Close examination and cross referencing the appearance of the debris with existing 'standard' descriptions for a particular debris type and the wear mechanism responsible for its creation is essential. The exact categorising of the wear mechanism must be fully understood to avoid any confusion in identifying the debris.

Table 2.2 shows basic wear mechanisms, a description of these mechanisms and morphologic description of the debris. Table 2.3 shows the definition of the morphological descriptor according to the ferrography concept with graphical examples of the corresponding debris [13]. Figure 2.9 shows the relationships between the particle description and wear behaviour in highly stressed contacts in transmission applications [27].

Mechanism	Description	Debris description
Adhesive	Occurs in sliding. Plastic deformation – junction growth. Failure occurs at junction. Metal transfer during 'running-in' (initial operation) and when contact temperature leads to local welding of asperities.	Large irregular particles >10 μm, unoxidised
Abrasion	*Two Body* – Hard asperities abrade softer contact surface. *Three Body* – Foreign bodies or hardened particles abrade both contacting surface when trapped or passing through the contact region.	Contains mainly the debris from the softer materials in a form of fine swarf unoxidised materials. May contain lumps.
Fretting	Damage due to oscillatory slip under normal load. Initially adhesive asperity contacts are formed then junction fracture. Loose particles will become oxidised and may cause third body abrasion	Fine fully oxidised. Some spherical particles.
Corrosion	Chemical or electrochemical process predominates. Normally involves the corrosion of worn surface and wear of corroded surfaces. Affected by temperature. Rate doubles with every increase of 10 °C	Always highly reacted i.e. no free metal present. Fine and amorphous.
Delamination	*Asperity to asperity contact* – Fracture due to repeating loading and unloading *Softer surface* – becomes smoother and cracks nucleate in sub-surface resulting in the formation of thin sheet delamination. Harder surface – cyclic loading inducing plastic shear deformation	Thin and wide with hole in the surface. Uneven edge.
Pitting fatigue	Occurs under rolling action. Repeated cycle of loading and unloading. Cracks develop at maximum shear stress area, surface flaws and metal impurities. *Sub-surface fatigue* – spalling (large chunks) *Surface initiated fatigue* – pitting or micropitting.	Chunky and thick

Table 2.2 Description of wear mechanism with the description of the corresponding wear debris produced [13].

Particle type	Description	Example
Rubbing	20 µm or smaller chord dimension and approx. 1 µm thick. Results from flaking of pieces from mixed shear layer. Mostly benign.	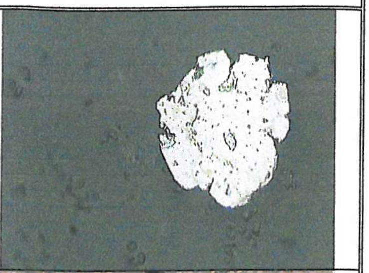
Cutting	Swarf like chips of fine wire coils. Resulting from abrasive cutting tool action	
Laminar	Thin, bright, free metal particle. Usually 1 µm thick, 20-50 µm chord dimension. Uneven edge profile with holes in the surface. Originate from gear or other rolling element bearing wear	
Fatigue	Chunky, 20-50 µm chord width, several micron thick	
Spheres	Usually ferrous, 1 to >10 µm diameter. Generated by rolling contact fatigue condition when microcracks occur.	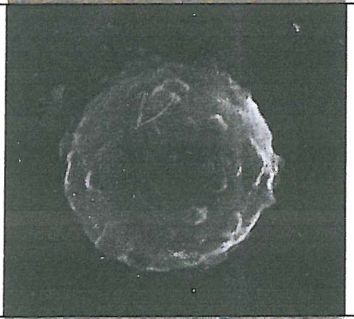
Severe sliding	Large >50 µm and several microns thick. Scratch mark of long straight edges on surface. Typically from gear wear	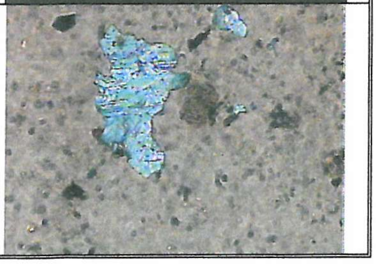

Table 2.3 Wear particle type, description and picture [13].

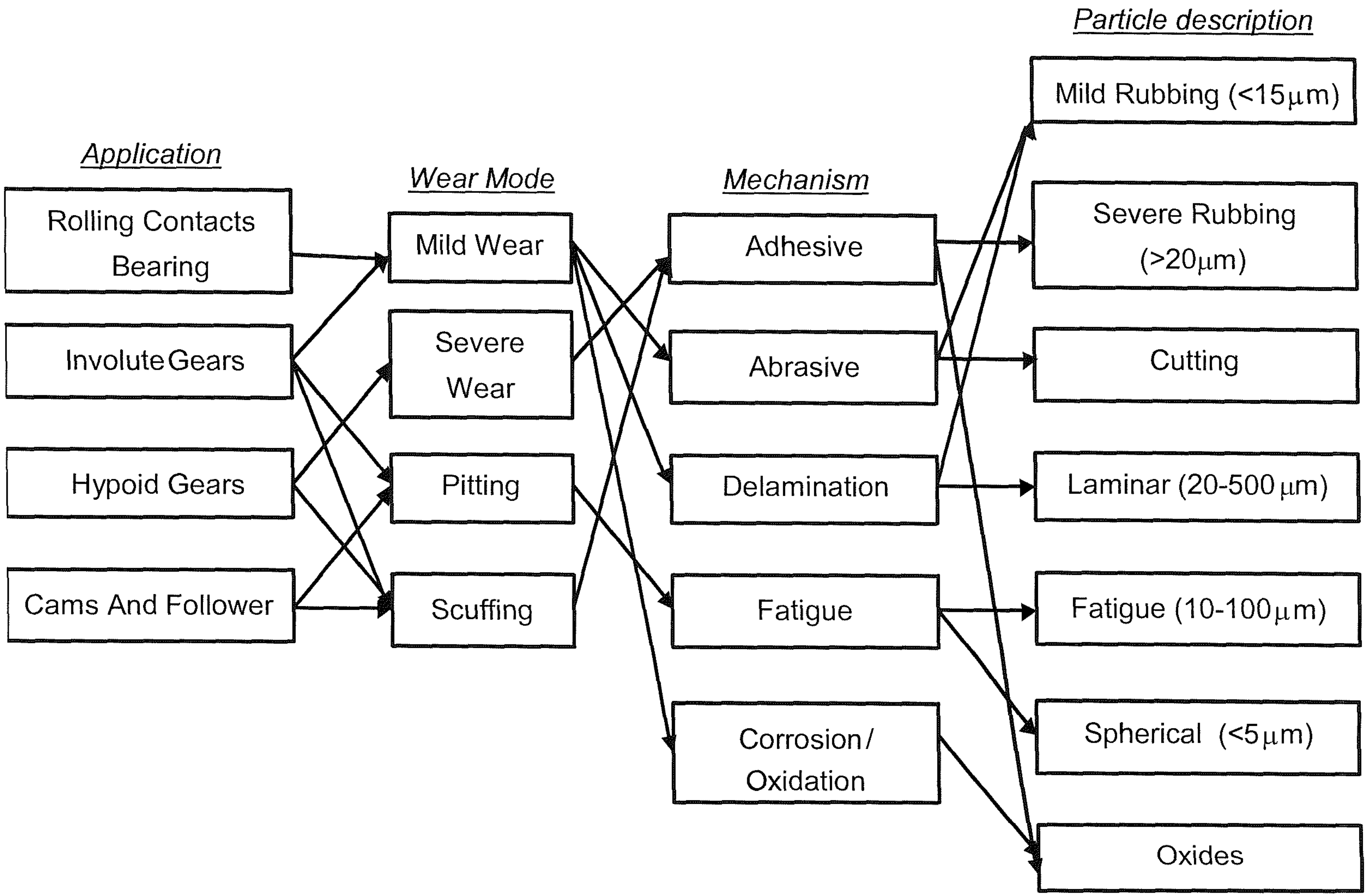

Figure 2.9 The relationships between particle description and wear behaviour in highly stressed contacts in transmission applications [24]

2.3.6 Practical Wear Debris Detection and Analysis

Monitoring systems can be divided into three categories namely in-line, on-line and off-line [28]. These are summarised by Figure 2.10. In-line connections examine all the system oil that passes through the machine circuit at that point. On-line connections draw off proportions of the flow as a sample and return it back to the system. Off-line analysis involves the removal of a sample volume (usually at periodic intervals) and this is analysed remotely from the machine (generally a laboratory).

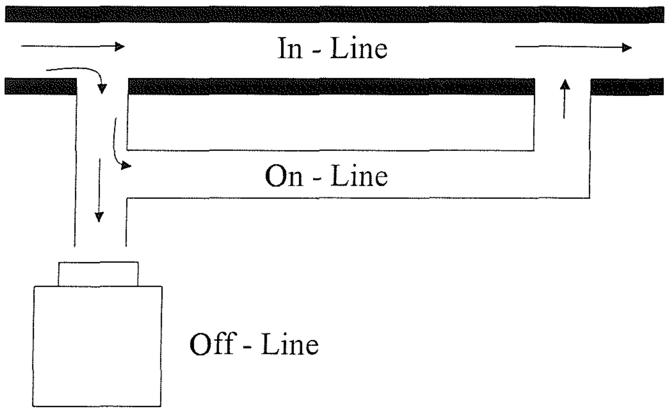

Figure 2.10 Types of connection to a system [12].

In-line

In-line analysis seems to have an overall benefit as compared to the other two techniques as total examination is being conducted and no external influences are involved. In practice however, it can cause problems to the machine systems by restricting flow in the circuit. Not all on-line systems have been tested with all fluids and flow characteristics and the motion path of the debris can also influence reading. As everything needs to be analysed in real-time, a lot of computer processing power is needed.

On-line

On-line analysis is a compromise between flow disturbance and the time needed to analyse. Instruments for on-line analysis can be fitted after the system is running at any desirable position. For realistic representation of the system, a fair amount of fluid needs to be sampled otherwise genuine evidence can be missed.

In-line and on-line particle detectors / analysis

Many current in-line and on-line analysers can only determine the particle count against particle size and hence a distribution of debris size [13,29]. Although this does not give as much information as the off-line techniques, the speed of analysis outweighs this. It is mainly used to monitor the increase in the rate of wear by measuring the concentration of particulate debris. Table 2.4 shows the types of analysis that can be implemented to obtain particle 'count' or distribution for wear debris analysis.

Analyser	**On/In -line**	**Size Range (µm)**						**Description**	**Comments**
		0.01	0.1	1	10	100	100		
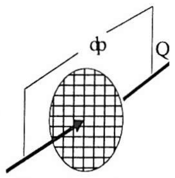 Filter blockage	On			▨	▨	▨		Flow passes through a fine mesh of known pore size. The change in flow characteristics indicates how many pores are blocked and hence how many particles greater than the pore size per fluid quantity. Several pore sizes can be used	Very rugged technique and able to deal with all fluids and mixed fluids. All solid debris is sensed, metallic or non-metallic. Primarily detects the bulk of the particle, i.e. its ability to block holes and clearances.
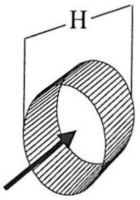 Inductance	Both					▨	▨	A coil placed around the pipe through which flows passes detects metal particles by an inductance change – ferrous and non-ferrous differently	Sensitivity is limited and hence a small bore pipe is preferable if particles below 100 µm are to be detected. Air bubbles can be isolated.
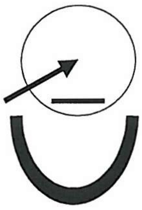 Magnetic Attraction	Both			▨	▨	▨	▨	There are several techniques but essentially a magnet which attract particles. The particle maybe trapped and/or sensed by flux change as they pass the magnet	Only detects ferromagnetic particles. Total view of 'large' and 'small' particles rather than count.
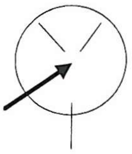 Light Optical - Fraunhofer	On	▨	▨	▨	▨	▨	▨	An array of detectors ahead of a light beam, passed through the fluid, detect the proportion of small through to large particle diffraction. (Small particle diffracted more highly)	Particle distribution only. Can detect sub-microns particles. Dense liquid and air entrainment may confuse results.

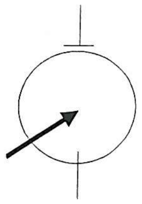 Optical - obscuration	On		▨	▨	▨	▨	▨	Each particle casts a shadow as the fluid passes through a light beam. A photo diode then measures the drop in the intensity of the light on the diode.	Very accurate count for low particle numbers. (Large numbers of small particles can be seen as small numbers of large particles) Dense liquid and air entrainment can confuse results.
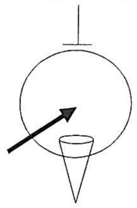 Optical – transition time	On			▨	▨	▨	▨	As a rotating focused light beam passes over particles, the transition time is measured and is proportional to the particle size. A photo diode measures the intensity.	Can be fitted in a probe placed within the fluid or shone from the side. Effective for wide range of particle size up to concentration as high as 70% debris
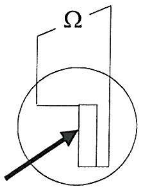 Thin film wear	Both				▨	▨	▨	When the fluid is projected at a surface coated with a thin conducting layer, the resistance across the thin film is increased as the particles wear the surface away.	Needs to be set for particular types of debris and viscosities. Although it works primarily in the on-line condition, in-line is feasible. Detects the quantity of debris rather than size.
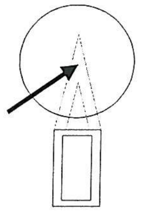 Ultrasonic	Both		▨	▨	▨	▨	▨	An ultrasonic beam is focused into the bulk of the fluid and reflected back when particles are hit. This 'echo' depends on the size of this discontinuity.	Used primarily in water but also effective in other fluids. May be confused with other discontinuities such as air bubbles or oil droplets or mixed fluids.

Table 2.4 *Types of detection techniques used in-line or on-line for wear debris analysis [13,29].*

Off-line

This technique is cheap to set up but time consuming and requires a lot of man hours to analyse samples taken. The time-dependant nature of this technique means that existing faults can further degrade while analysis is taking place. The advantage is that particles trapped can later be fully analysed with advanced analysis techniques.

Off-line debris analysis

Off-line debris analysis is an alternative technique that has a relatively low start – up cost [28]. Off-line analysis will generate the results needed if great care is taken during sampling. The main drawback of this technique is that it is time consuming and an expert is needed to analyse the results. The advantages of off-line debris analysis is the availability of wear debris available for examination gives greater credibility in the final decision [13] and in some cases evidence is needed to confirm earlier findings. There are several off-line analysis techniques available and are as follows:

Patch analysis

This is the oldest and the most effective technique. A known quantity of fluid is passed through a filter membrane and the debris trapped is then analysed. Depending on the level of detail required, several methods of examination could be carried out.

- Gravimetric Analysis

The filter patch is weighed before the debris deposited and then weighed it again after deposition. The patch needs to be cleansed of the oil and then dried. To take away the mass of plasticisers in the oil, a second patch may be placed in the oil as a control.

- Shade analysis

The change in colour and grey scale of the deposited membrane is compared to new membrane. Darkening is as a result of deposited debris. This is a rough analysis as the change in colour can also be due to the effect of the oil and results categorised only into 4 grades.

- Standard comparison

This involves the use of membranes made to a recognised standard level of debris concentration, commonly associated with ISO standard cleanliness levels.

- Particle counts

This method is only used when the concentration of particles is not high and when the interest only lies in larger particles. Provided the distribution of particles are even on the membrane, only particles on one area of the grid printed on the membrane need to be counted. The total quantity can be obtained by multiplying according to the proportion actually counted.

- Visual observation

This technique is often combined with techniques mentioned above. This is a detail observation by eye examining debris features such as colour and shape to determine the origin.

- Scanning Electron Microscope

This technique will provide detailed information of the debris shape and also composition when the Electron Dispersive X-ray (EDX) Analysis is present.

Ferrography

Ferrography is a technique where ferrous wear debris is separated into size bands by passing oil containing ferrous debris over a glass substrate in the presence of high gradient magnetic field. Larger particles will be deposited near the entry point of the oil whilst smaller particles or weakly magnetic particles will be deposited near the oil outlet, as shown by Figure 2.11. The capture of non-ferrous particle using this technique tends to be random due to the fact that they are not attracted to magnetic field.

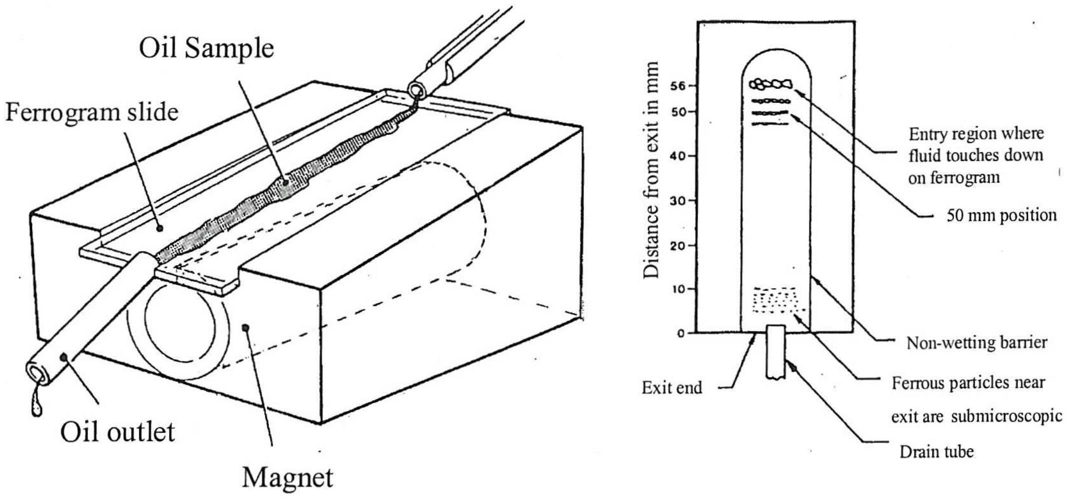

Figure 2.11 The ferrographic concept [13].

The wear debris captured on the glass substrate can then be heated up to a certain temperature and the change of the colour of the wear debris is observed. At different temperatures, debris of different metal will show different colours. Table 2.5 shows the colour generated by different metal when heated. It includes both ferrous and non-ferrous materials.

Temperature (°C)	Colours	Metal
20	Red / Yellow	Copper, oil
330	Speckled Blue / Orange	Probably oxidised Lead / Tin
	Blue	Carbon, Low alloy steels
	Tan	Cadmium
	Straw / Bronze	Medium alloy steels
400	Light Grey	Carbon, low alloy steels
	Light Tan	Titanium
	Tan/Straw + some deep purple	Molybdenum
	Deep Bronze + some speckled blue	Medium alloy steels
	Some yellowing	Stainless steel
480	Bronze with Blue	High Nickel alloy
	Tan	Titanium, Zinc
	Straw / Bronze with some blue	Stainless steel
540	Blue or Blue Grey	High Nickel alloy
	Deep Tan	Titanium
	Tan/Blue	Zinc

Table 2.5 Metal generated colour when slide heated [13].

Particle concentration

Wear debris concentration can be measured using, respectively, optical, inductive and magnetic coil methods. Sampling has to be carried out at regular intervals and the changes in the concentration can be monitored to determine the trend of wear.

Advanced Techniques

Recent advances in wear debris analysis, includes Spectrometric Oil Analysis (SOA). It is a highly automated technique capable of analysing the composition of debris smaller than 5 μm [30]. Energy Dispersive X-ray Fluorescence (ED-XRF) is used to determine the composition of much larger debris size (>10 μm).

2.4 ELECTROSTATIC CONDITION MONITORING

Electrostatic monitoring is an emerging condition monitoring technique and has been applied successfully to detect the presence of foreign debris in the gas path of turbine engines [10]. This technology is now being developed for the application of wear monitoring in oil lubricated contacts. This section will review the research into applying electrostatic monitoring techniques in oil-lubricated systems.

2.4.1 Sliding Wear Monitoring

Tasbaz *et al* [1,2] investigated the generation of charge during wear of a metal-to-metal contacts using pin-on-disc and the Plint TE/77 reciprocating contact wear rigs. Electrostatic sensors were placed adjacent to the sliding metal-to-metal contacts. Figure 2.12 and Figure 2.13 show schematic diagrams of each test rig together with the location of the electrostatics sensors and the load cells.

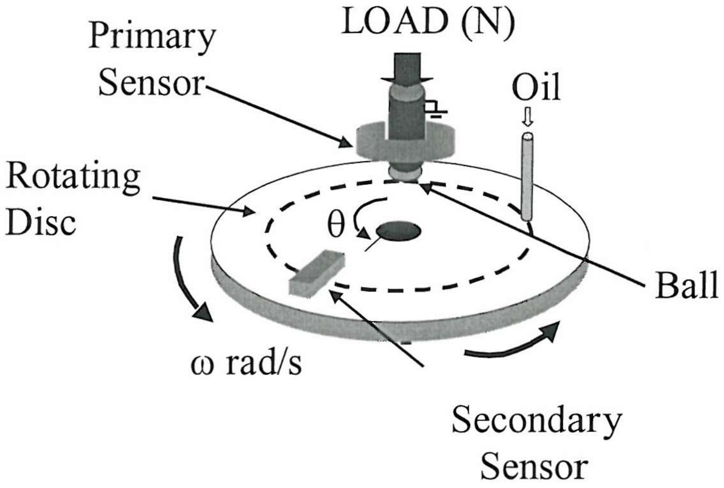

Figure 2.12 Schematic diagram of the pin-on-disc test rig [2].

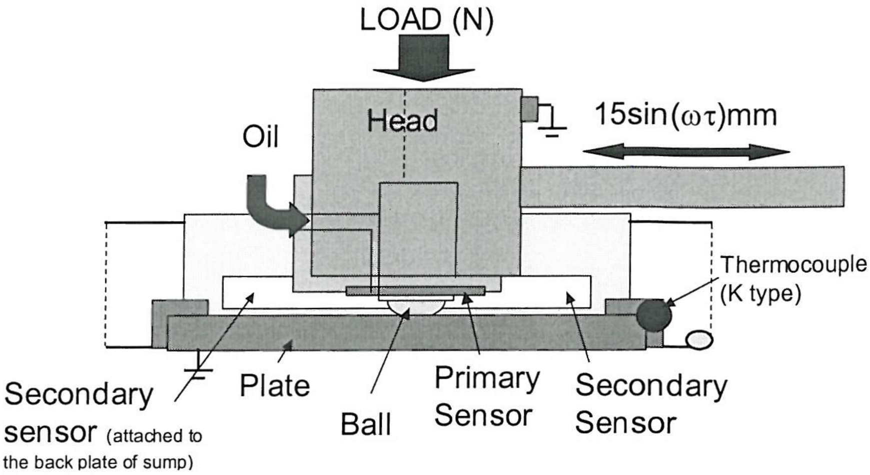

Figure 2.13 The schematic diagram of the Plint TE/77 reciprocating contact wear rig [2].

Both of these rigs were fitted with a primary and secondary sensor. The primary sensor was designed to detect any charge generation at or near the point of contact. The secondary sensors were placed remote from the contact area to investigate the possibility of charge transportation. The pin and plate were manufactured using bearing steel (En32a and En31, respectively) and Shell Vitrea ISO 32 base oil was used to lubricate the contact.

Figure 2.14 shows the response of the pin-on-disc primary and the secondary sensors just prior to severe scuffing failure at the contact. It can be seen that a once per revolution precursor signal was detected on both sensors corresponding to the increase in the coefficient of friction in a discrete area i.e. contact surface failure. The magnitude as well as the duration of the signals increased towards complete scuffing failure and similar behaviour for the coefficient of friction was observed.

Figure 2.15 shows the sensor responses eight minutes prior to complete scuffing failure for the same test. Precursor signals were observed without corresponding change in the coefficient of friction value. The ball and the plate surface were analysed during this stage of the test and the presence of white layers were detected. White layers are known to be a manifestation of a first transition scuffing [1,2] (see Section 4.1.1).

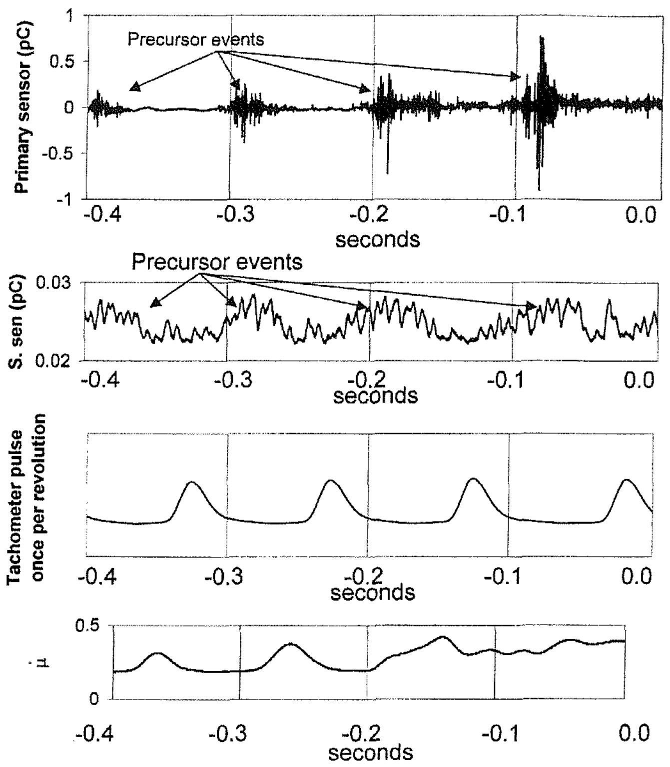

Figure 2.14 Pin-on-disc primary sensor, secondary sensor (500 Hz low pass filter), tachometer (once per revolution) and coefficient of friction, showing single precursor event per revolution at a sliding speed of 2.2 m/s, disc speed of 620 rpm, track radius 34 mm, contact stress 3.82 GPa, 50 N load for 0.4 to 0.0 seconds prior to severe scuffing failure [2].

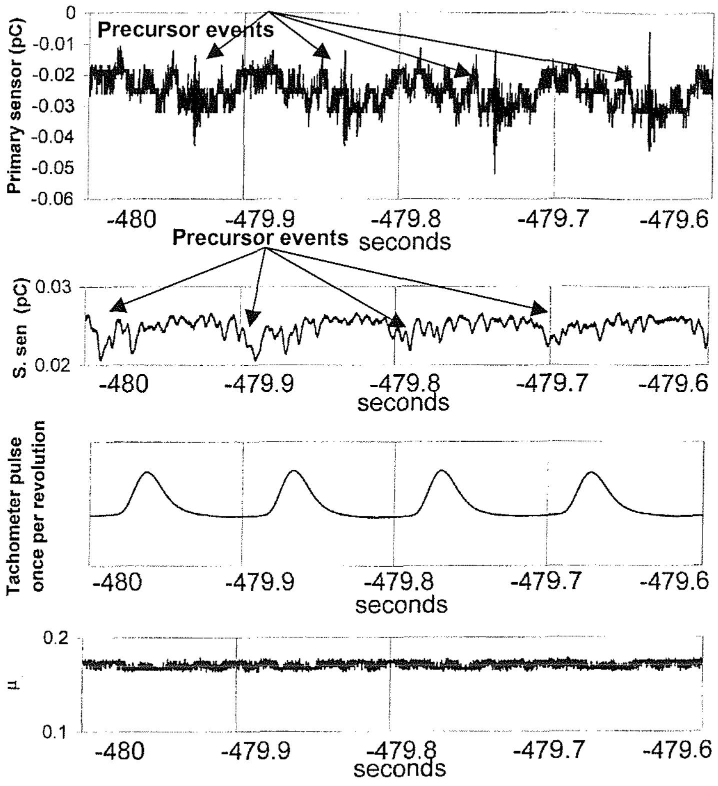

Figure 2.15 Pin-on-disc primary sensor, secondary sensor (500 Hz low pass filter), tachometer (once per revolution) and coefficient of friction, showing single precursor event per revolution at a sliding speed of 2.2 ms^{-1}, disc speed of 620 rpm, track radius 34 mm, contact stress 3.82 GPa, 50 N load for 480 seconds prior to severe scuffing failure [2].

For the tests with the Plint TE/77 rig, the contact was 'run-in' using a low load of 30 N for 5 minutes, to avoid an immediate scuffing failure. After that period the load was increased to 250 N with loading rate of 1 Ns^{-1}. Figure 2.16 shows the primary sensor response as well as the sliding force measured. Bipolar signals can be seen approximately every 30 seconds during the running-in period. This was thought to be the result of the tribocharging of the oil meniscus surrounding the contact area as it builds up and decays. The sensor response indicates the presence of several strong precursor events during and after loading the contact. Surface examination revealed the presence of white layers, indicating the occurrence of first transition scuffing. Complete contact failure indicated by the sudden increase in the coefficient of friction, occurred about 20 minutes into the test as indicated by a sharp increase in sliding force.

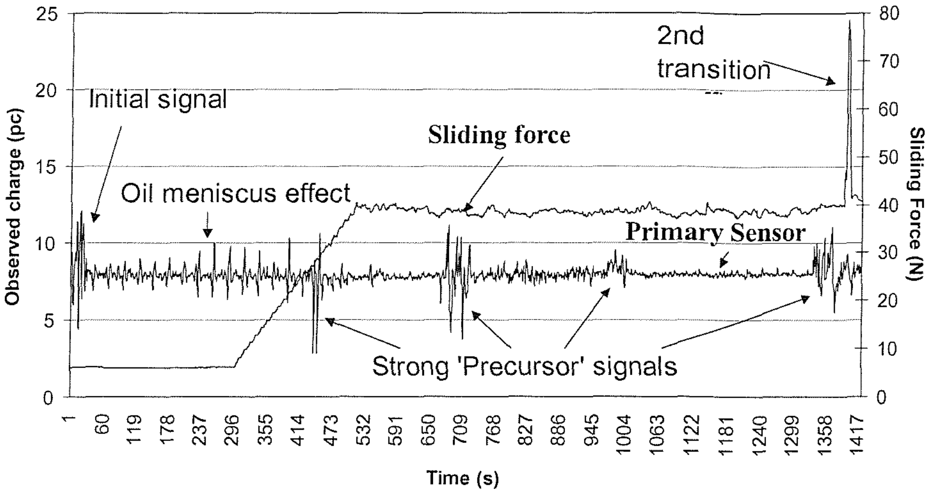

Figure 2.16 Plint rig primary sensor (rms signal) and friction load cell outputs prior to 2^{nd} transition scuffing. Sample frequency 10 kHz, r.m.s average of 10000 data point taken producing one data per second, contact reciprocating frequency 15 Hz, stroke length 15.11 mm, sliding speed peak 0.71 ms^{-1}, run-in load 30 N for 300 s, load ramped at $1Ns^{-1}$, final load 250 N [2].

2.4.2 FZG Spur Gear Test

Testing of the electrostatic monitoring technology in a realistic environment and test conditions have been made by Powrie *et al* [3]. Electrostatic sensors were placed near the mesh zone in a FZG gear test rig as shown in Figure 2.17. Two additional sensors were placed on the oil flow path, to investigate the possibility of the transportation of charge. Tests were carried out in several load stages, each load stage lasted approximately 15 minutes (equivalent of 21700 revolutions of the pinion gear). After the end of each loading stage, the gears were inspected visually to look for any sign of scuffing damage to the teeth. A magnetic filter in the oil recirculation system was used to collect the debris generated. At the end of each load stage the filter was removed and debris collected for counting (using an optical microscope). The tests were carried out until signs of failure were detected at the end of the 15 minutes stage. It was found that scuffing occurred on load stage 6. Figure 2.18 shows the sketch of the tooth damage, which had occurred by the end of each load stage. At load stage 6, teeth 2 to 7 (and hence teeth 10 to 15 by symmetry) on the pinion gear were found to be damaged.

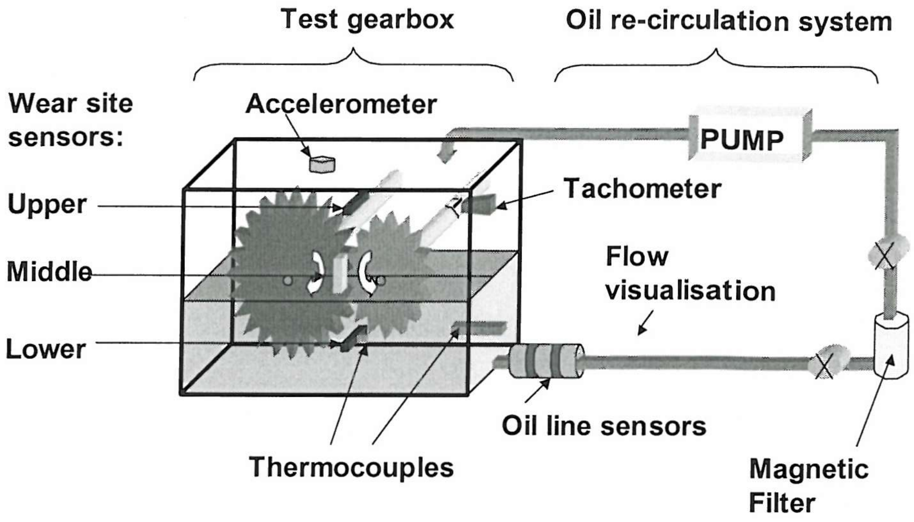

Figure 2.17 *The schematic diagram of the FZG gear test rig [3].*

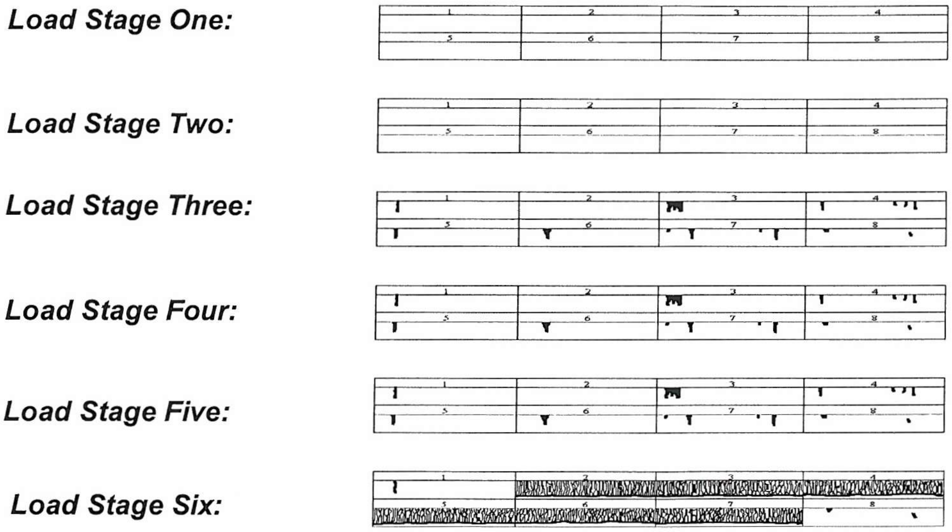

Figure 2.18 *Detailed sketch of pinion gear at the end of each load stage[3].*

Electrostatic signals from the wear site sensors were recorded and analysed using gear vibration analysis technique such as the Baseband Power Spectrum (BBPS) and signal averaging. Figure 2.19 shows the results of the BBPS for the start and end of the load stage 6 for the lower sensor. From the analysis, it is clear that a significant peak occurred twice per revolution, corresponding to the damaged regions. The same trend was found from analysis of the signal from the middle and upper sensors. This shows that the charge generated by the scuffing of the teeth resides on the wear surface. The frequency of the 'mesh tone' corresponds to the number of teeth on the gear.

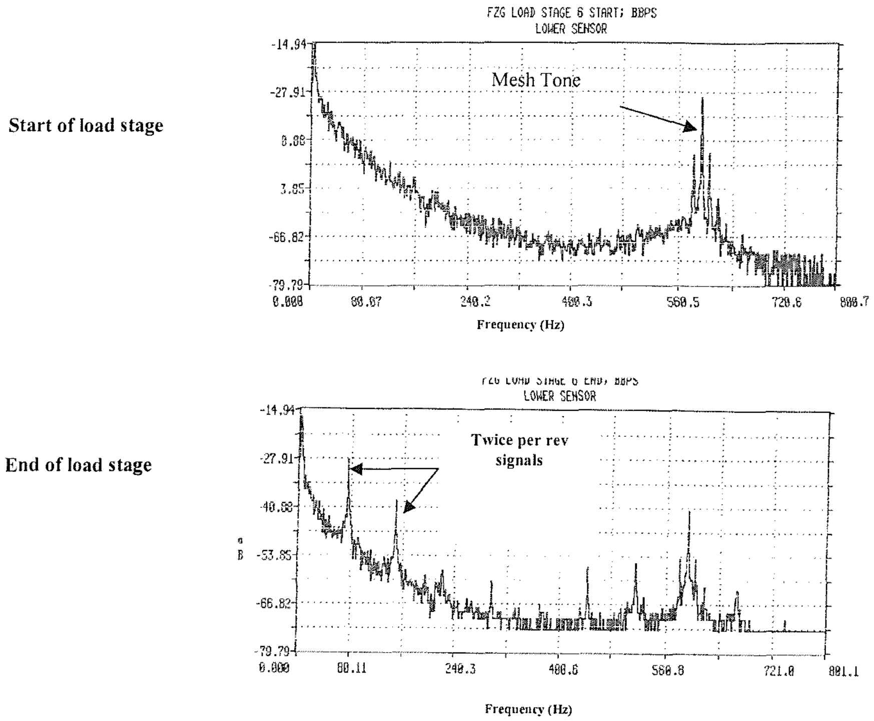

Figure 2.19 Baseband power spectrum of lower wear site sensor at start and end of load stage 6 [3].

Signal average analysis (both raw and filtered to remove meshing noise), from the three wear site sensors is illustrated in Figure 2.20. It shows the presence of the two damaged regions of teeth are clearly evident, even in the unfiltered data. The phase shift of the signals is also clear between the three sensors. The phase shift is due to the different position of the sensors and there will be a difference in the time they sense the damaged teeth.

The oil line sensors monitored the presence of debris in the flow by recording any velocity that is lower than the velocity of the oil flow. Figure 2.21 shows the on-line sensor analysis results. It is obvious that there is a direct correlation with wear debris particles captured in the magnetic filter [3].

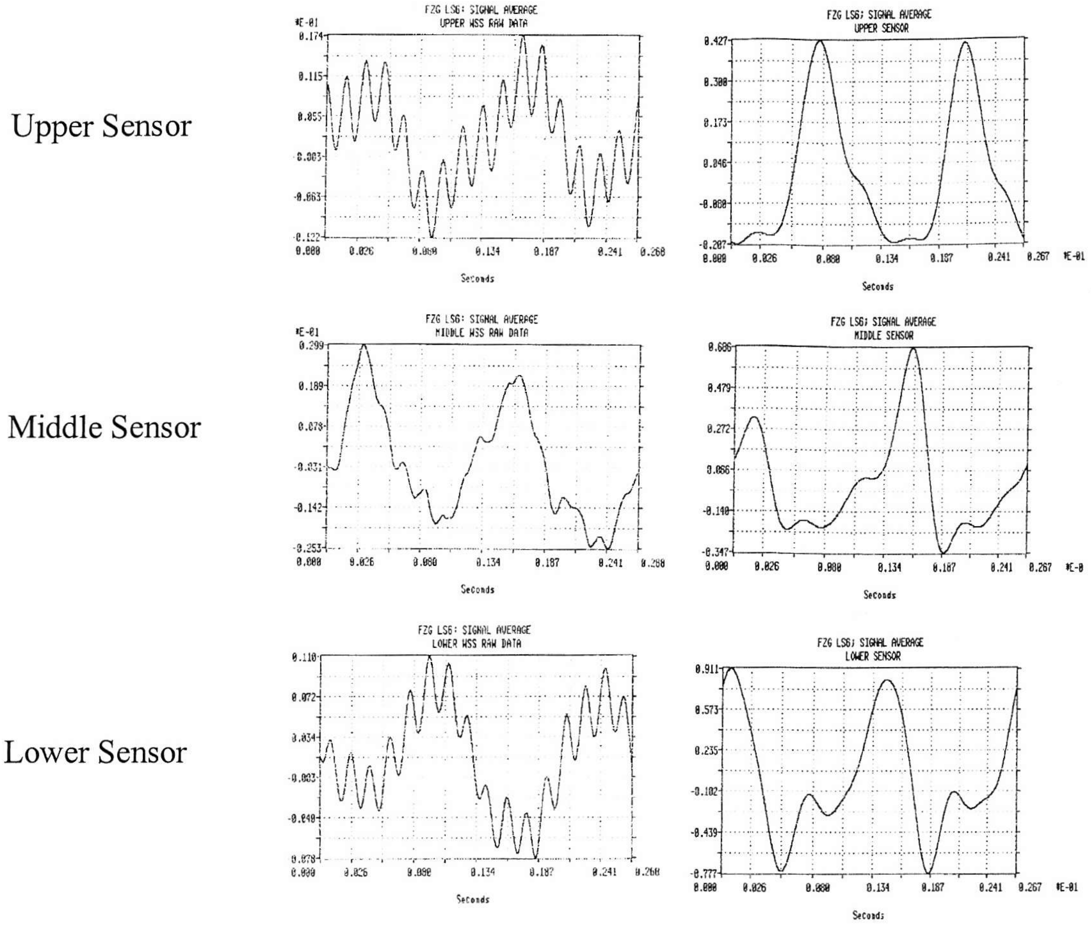

(a) (b)

Figure 2.20 Wear site sensor signal averages (a) raw signal (b) filtered for load stage 6 [3].

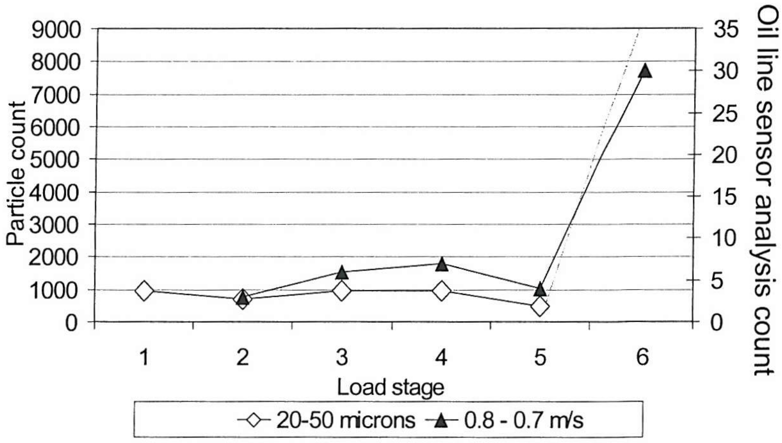

Figure 2.21 Oil sensor analysis and particle count per load stage [3].

3 FUNDAMENTALS OF ELECTROSTATICS AND SENSOR TECHNOLOGY

3.1 INTRODUCTION

Basic electrostatic theory will be discussed in this section covering the electrostatic charge characteristic for a point charge as well as volume charge. The effective charge measurement technique for charged particles will also be reviewed. Basic designs of electrostatic sensors and mechanisms of charge generation will also be discussed.

3.2 ELECTRIC FIELD

An electric field is the region where electrical (or coulombic) forces act. The electrical field strength, E, is defined as the force, F, imparted on a charge, q, within the field, as expressed by Equation 3.1.

$$F = qE \qquad 3.1$$

3.2.1 Electric Field of a Point Charge

For a point charge the electric field strength is given by:

$$E(r) = \frac{q}{4\pi\varepsilon_o \varepsilon r^2} \qquad 3.2$$

Where r is the radius of an imaginary sphere, ε_o is the permitivitty of free space and ε is the relative permitivitty of the medium.

The electric field strength will have the same magnitude on the surface of a drawn imaginary sphere of radius, r, which is concentric with the point charge. The field line will be directed radially away from the charge as indicated in Figure 3.1.

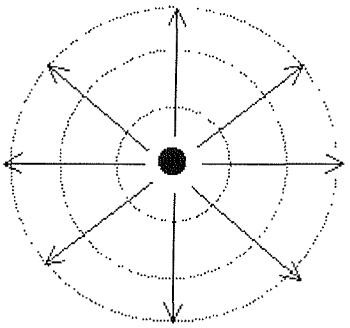

Figure 3.1 Radial emanation of field line on from point charge in space.

3.2.2 Electric Field of a Volume Charge

A lumped parameter formulation can often be made when considering macroscopic bodies subjected to electrostatic forces. This approach assumes that the charge on an object can be described by a capacitance relation. For a single body, this takes the form:

$$q = CV \qquad 3.3$$

Where C is the capacitance and V is the voltage.

When dealing with liquids or powder clouds, electrical charges will be distributed through a volume of space usually bounded by the container. To determine the value of the total electric field, Gauss' theorem can be applied, which can be written as:

$$\oint_S D_\perp dS = Q_{enclosed} \qquad 3.4$$

Where $D_\perp$ is the normal component of the flux density passing through the element of area dS, and $Q_{enclosed}$ is the total charge contained within the enclosed volume. The integral is taken over the whole of enclosing surface S, see Figure 3.2. If the relative permitivitty is constant throughout the volume, Equation 3.4 can be rewritten as:

$$\varepsilon\varepsilon_o \oint_S E_\perp dS = Q_{enclosed} \qquad 3.5$$

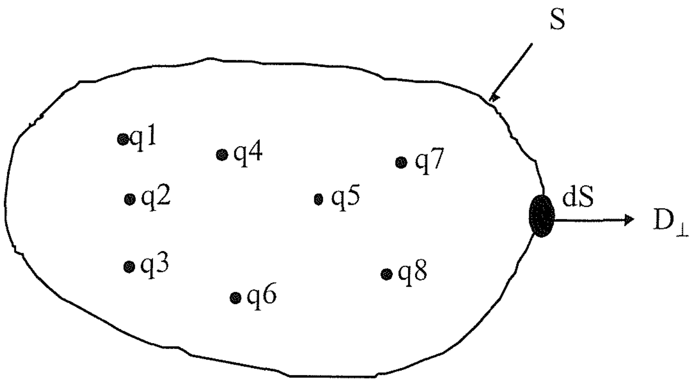

Figure 3.2 *General application of Gauss' theorem [31].*

3.3 FLUX DENSITY (FIELD DISPLACEMENT)

By definition, if the magnitude of charge q Coulombs emanates from the source then q number of lines can be assumed to emanate from the charge [31]. By symmetry rules uniform flux line must emanate from a point charge. For a point charge of q Coulombs, the flux density, $D(r)$, of flux lines passing through an imaginary concentric sphere of radius r surrounding the charge is given by:

$$D(r) = \frac{q}{4\pi r^2} = \varepsilon\varepsilon_0 E(r) \qquad 3.6$$

It is evident from Equation 3.6 that the flux density is directly proportional to the strength of the electric field at that point. It is also evident from Equation 3.6 that if r is the separation, the flux density is very high when near and decreases in an inverse square relationship with distance. The flux density for charge on a surface increase with increase of curvature as shown in Figure 3.3.

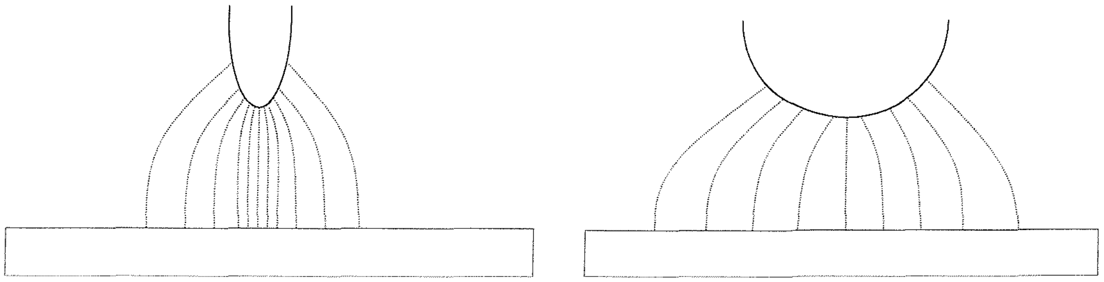

Figure 3.3 *Flux density characteristic with varying curvature.*

3.4 MEASUREMENT OF CHARGE

There are several ways of measuring the absolute charge on particles; a Faraday cup is the classic example. Figure 3.4 shows a cross-section of a typical Faraday cup. It consists of a conducting chamber with a small opening through which particles or liquids can enter. The cup is isolated from the surroundings by an earth 'cage' to prevent unwanted charge from the surroundings being measured. The cage also acts as a shield to radio frequency emissions from nearby electrical equipment.

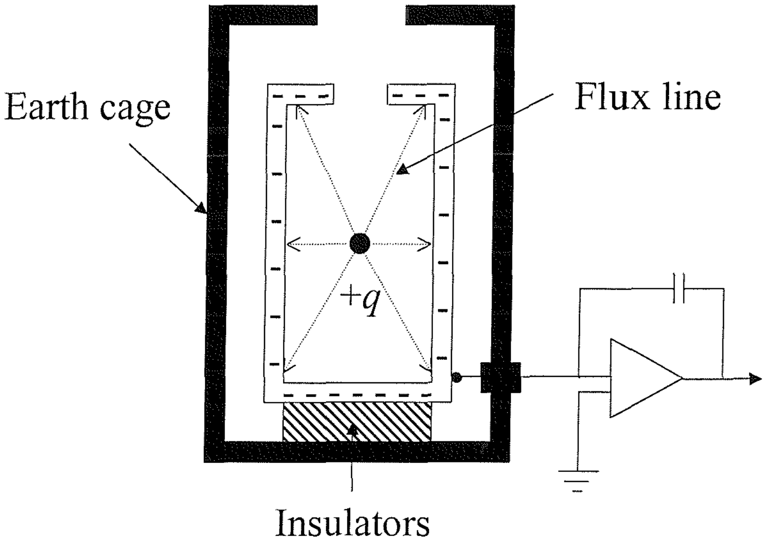

Figure 3.4 Cross-section through a cylindrical Faraday cup.

When a charged particle enters the Faraday cup, an equal and opposite charge is induced on the surface of the cup. If the cup is isolated, this occurs via charge movement within the cup leading to charge separation. However, if an external measuring circuit is connected to the Faraday cup, electrons can move (to and from) to match the charge on the particle. This movement of electrons (charge) can be measured using an electrometer or if a high-input impedance voltmeter is connected, the potential would be:

$$V_F = \frac{q}{C_F} \qquad 3.7$$

If the capacitance of the cup is taken as C_F.

When measuring charge with a Faraday cup, it is not necessary for the particle to be in contact with the surface of the chamber for the charge on it to be detected (as indicated by Gaussian Theorem). Since this measurement technique works using the principle of induction charging, it is essential that all field lines from the charged particle terminate only on the inner walls of the isolated chamber to ensure high accuracy. The magnitude of the charge induced on the cup is proportional to the amount of flux lines terminating on the wall, for 100% accuracy.

3.5 ELECTROSTATIC SENSORS

The most basic form of electrostatic sensors work on the basis of induction charging. This section will discuss the general properties and experiments conducted using inductive sensors.

3.5.1 Image Charge in Conducting Surfaces

Figure 3.5 shows the sequence of events that leads to the formation of an induced charge in a conductor [31]. Figure 3.5(a) shows an isolated conducting plate at a distance d from a point charge $+q$. The plate will initially cut across a number of equipotential surfaces which surround the point charge so that a potential difference and hence an electric field exists between them. The free charges in the conductor will redistribute themselves developing an opposing field, a process known as polarisation. This process can proceed in a few picoseconds to a point where the electric field in the conductor becomes zero. If a positive charge is near a conducting plate, polarisation is achieved by drawing an excess of electrons to the front surface leaving the back surface positively charged.

Potential difference will be induced within the plate in Figure 3.5(a) due to the proximity to the positive charge. If the plate is earthed as shown in Figure 3.5(b), the potential difference will be reduced to zero, as a result of drawing electrons from earth to neutralise the effects of positive charge on the back surface leaving only electrons on the plate. This will result in the plate being negatively charged. Thus a positively charged particle will induce a negative charge at the surface of a conductor and *vice versa*.

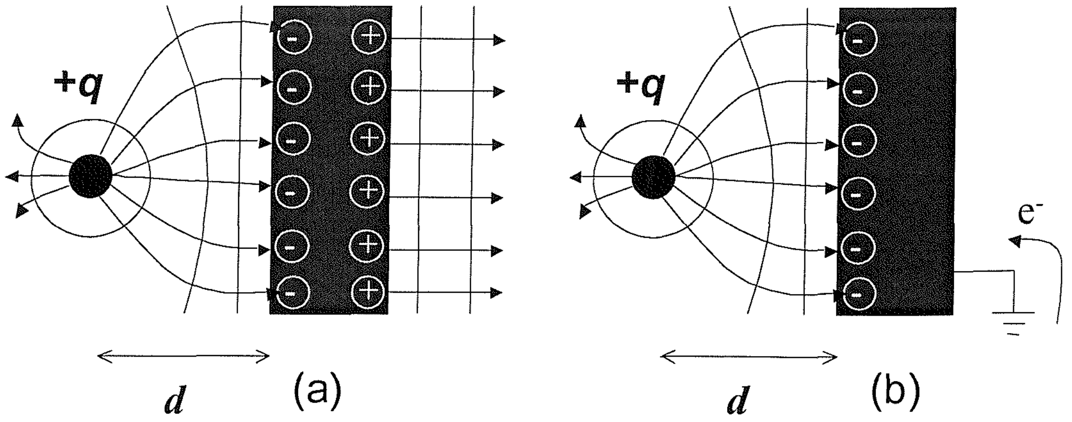

Figure 3.5 *Charge induction in conductor surfaces. (a) Polarisation of an isolated plate in the field of a point charge +q. (b) When the plate is connected to earth positive charges are conducted away reducing the plate potential to zero.*

3.5.2 Basic Inductive Sensors

Inductive sensors are the most basic form of electrostatic sensor. It works on the basis of the induction charging. Consider a flat type inductive sensor as shown in Figure 3.6 and a point charge of $+q$ moving past it. Electric (E-) field lines due to charge $+q$ terminate on the sensor face. The electrons in the sensor redistribute to balance the additional charge in the vicinity of the sensor resulting in a current flow, which is measured by the conditioner. The signal conditioning thus converts the detected charge into a proportional voltage signal.

Due to the sensor's finite area, not all of the E-field lines will terminate on the sensor face and hence not all the charge q will be detected. The dependency of the amount of charge detected by the sensor, q_A, may be approximated as follows:

$$q_A \approx \frac{qA}{x^2} \qquad 3.8$$

Where A is the sensor area and x is the distance between the charged particle and the sensor face [32].

From latest experience gained from work presented in this thesis, inductive sensors are affected by the proximity of any earth surfaces. This is due to the competition of the field displacements on the sensor face and other earthed surfaces.

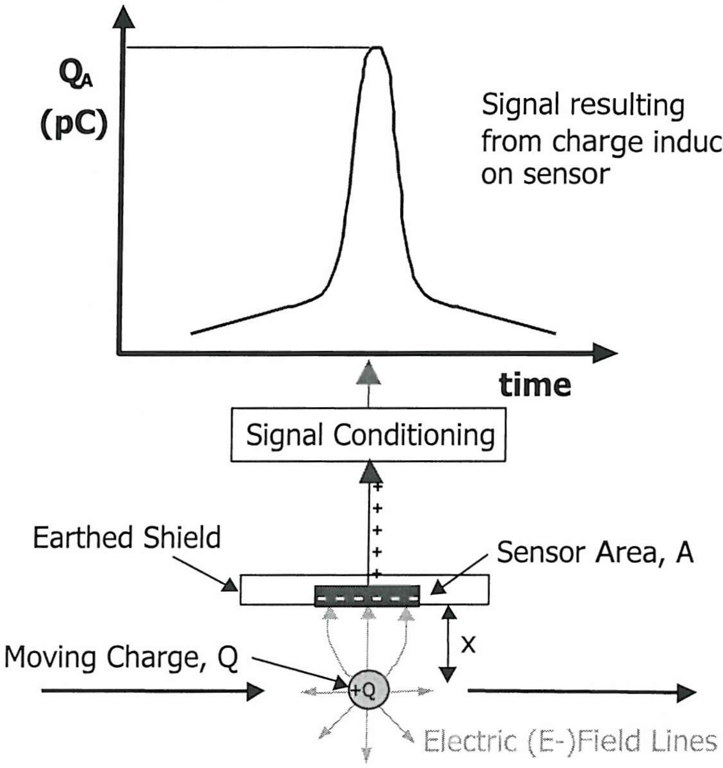

Figure 3.6 Simplified representation of sensor principle

Inductive sensors can take several forms, for example button [33] or ring [34-37]. Button type sensors are especially good for monitoring charge on surfaces, e.g. wear sites. Ring sensors are employed in pipe flow to detect charge on particles driven by fluid motion to act as a flow meter or to detect the presence of wear debris in a lubrication oil line [3]. The advantage of the ring sensors is that the presence of any charged particle in the flow will be detected.

Ring sensors have been developed by Gajewski [34-37]. The schematic of the ring sensor and the measuring circuit is shown in Figure 3.7.

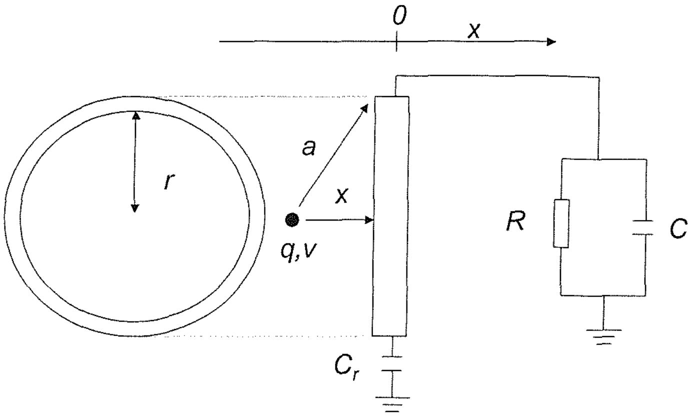

Figure 3.7 *Gajewski's ring probe. The measuring circuit is represented by the RC circuit on the diagram.*

If we consider a particle with charge $q_{particle}$, moving along the axis of the ring with radius *r*, with velocity *v* and C_r as the capacitance of the ring. If we also consider that the ring may initially have a charge q_{ring}, two cases can be envisaged:

Case 1. $q_{particle} \neq 0$ and $q_{ring} = 0$.

Case 2. $q_{particle} = 0$ and $q_{ring} \neq 0$

In case 1 the potential on the ring surface, V_1, generated by the point charge at the centre of the sensor is given by:

$$V_1 = \frac{q_{particle}}{4\pi\varepsilon_o a} = \frac{q_{particle}}{4\pi\varepsilon_o \sqrt{x^2 + r^2}} \qquad 3.9$$

Where *x* is the shortest distance of the particle to the ring wall.

In case 2, the potential is given by:

$$V_2 = \frac{q_{ring}}{C_r} \qquad 3.10$$

By combining Equation 3.9 and 3.10, the total potential *V*, of the ring is given by:

$$V = V_1 + V_2 = \frac{q_{particle}}{4\pi\varepsilon_o\sqrt{x^2 + r^2}} + \frac{q_{ring}}{C_r} \qquad 3.11$$

Next the RC parallel circuit connected to the ring probe was considered. After some mathematical manipulation the peak voltage is represented by the following equation:

$$V_{\max} = \pm\frac{2}{9}\sqrt{3}\,\frac{C_r C}{C_r + C}\,\frac{q_{particle}R}{4\pi\varepsilon_o}\,\frac{v}{r^2} \qquad 3.12$$

This equation can be simplified to:

$$V_{\max} = \pm c.q_{particle}.v \qquad 3.13$$

The constant *c* was found by calibration of the electrode with a standard charge.

Off-centre effects

The effect of particles moving off-centre, i.e. closer to the sensor wall, through the Gajewski type ring sensor has been investigated experimentally by Vercoulen using a ring of 40 mm in radius [38]. Charged water droplets were used and the off centre distance was altered in eight steps. Two sets of experiments were conducted, one moving from the centre towards the wall of the ring and moving from the wall of the ring towards the centre. Graphs of peak voltages versus off centre distances were plotted for both sets of tests and are shown in Figure 3.8.

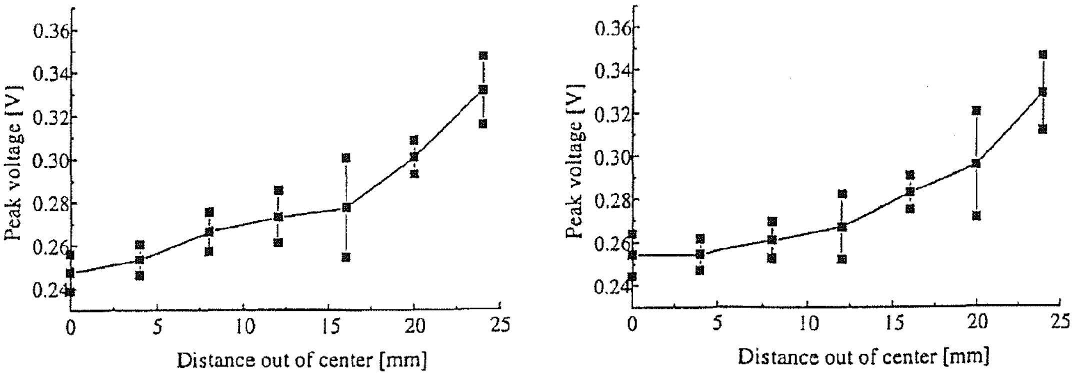

Figure 3.8 *Vercoulen's off centre test results [38]*

The effect is not significant for small off centre deviations but gets more profound near to the ring wall. Harvey *et al* [39] also studied the effect of deviations from the central axis position using a ring sensor and charged oil droplets. Harvey *et al* recorded the value of the percentage of sensor response, given by:

$$\text{Percentage Sensor Response} = \frac{\text{Charge Sensed}}{\text{Absolute Charge}} \times 100 \qquad 3.14$$

A ring sensor of 50 mm in diameter was used. In this case the charge sensed (recorded) by the sensor is analogous to the peak voltage recorded in Vercoulen's work. Figure 3.9 shows the result of the investigation.

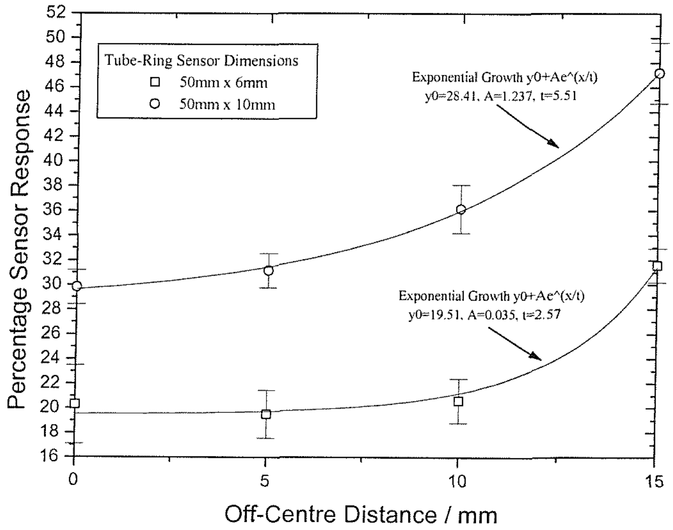

Figure 3.9 *The effect of off-centre for 50 mm x 6 mm and 50 mm x 10 mm sensor [39].*

Although the number of off centre distances in the test was less than that in Vercoulen's, the results are very similar.

Diameter effects

Harvey *et al* also studied the effect of the ring sensor diameter using charged oil droplets. These results are shown in Figure 3.10. The percentage of sensor response was found to increase with the decrease in sensor diameter.

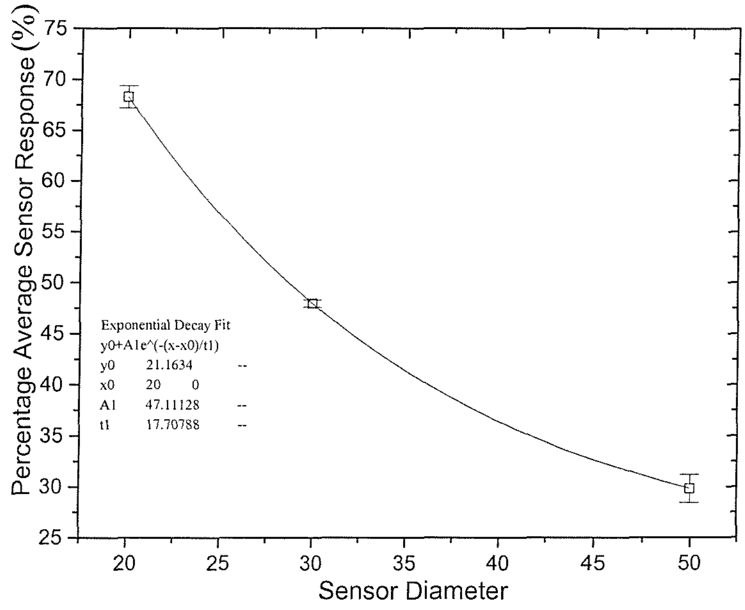

Figure 3.10 The effect of variation in the sensor diameter (length was kept constant at 10 mm) [39].

3.6 MECHANISMS OF CHARGE GENERATION

3.6.1 Introduction

A schematic diagram of the possible mechanisms that could lead to charge generation as a consequence of frictional work and/or wear is shown in Figure 3.11.

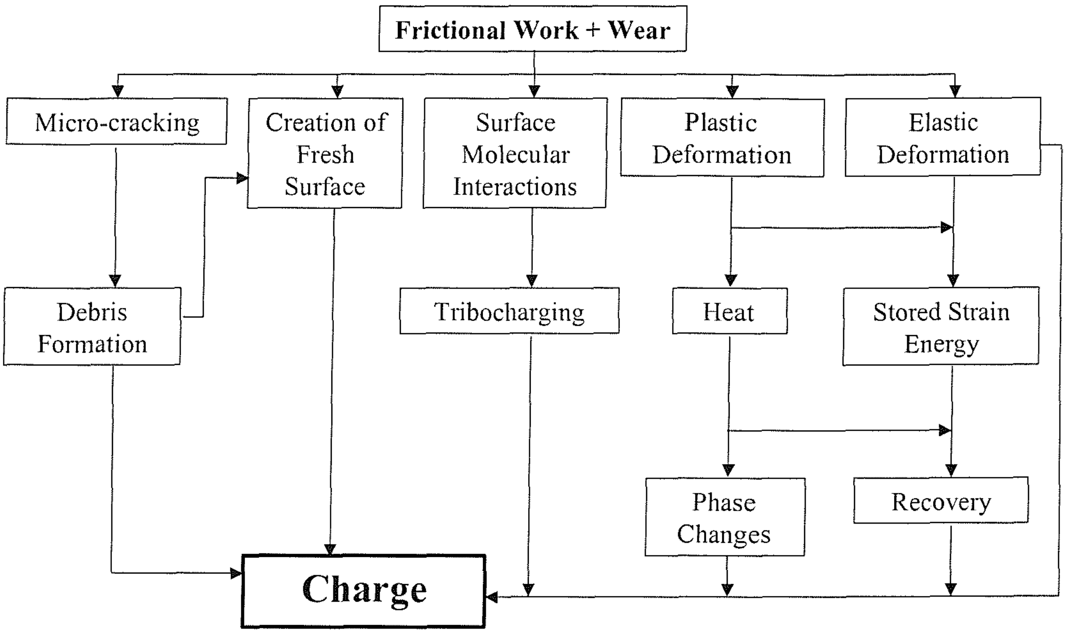

Figure 3.11 Schematic Diagram of Charge Generation.

3.6.2 Tribocharging

Tribocharging in general can be divided into two categories; tribocharging due to solid-solid interactions and solid-fluid interactions.

Solid - liquid interactions

When a metal body is immersed in oil, it will have a double layer of diffused charge species. This phenomenon has been extensively studied by Helmholtz [40], Gouy [41], Chapman [42], Stern [43] and Grahame [44]. The charge species in oil are thought to be the product of oxidation and reduction processes, and also the presence of polynuclear aromatic [45-47], organo-sulfur [47] impurities or water [48]. When a metal is immersed in oil, depending on its work function, one type/polarity of ion will be preferred for absorption onto its surface, say negative. If the oil is neutral at the beginning, there must be an excess of positive ions in the bulk of the liquid of equal magnitude. This will create a potential difference between the metal and the bulk of the oil. With negative ions preferentially absorbed on to the metal surface, it will become more negative relative to the bulk of the oil. The double layer thickness is related to the balance of ion diffusion, migration and convection. It is also affected by other factors such as temperature, permitivitty of the liquid and solid, and the concentration of charged species in the liquid [49]. In a stagnant equilibrium condition the thickness of the double layer can be characterised using the Debye length, λ. The Debye length is given by;

$$\lambda = \sqrt{\frac{\varepsilon D_m}{\kappa}} \qquad 3.15$$

Where D_m is the molecular diffusion coefficient, ε is permitivitty and κ is the conductivity.

This expression shows that charged species will diffuse over a distance λ during a time $\tau = \varepsilon/\kappa$, the relaxation time. The diffusion coefficient can be found using;

$$D = \frac{bRT}{zF_c} \qquad 3.16$$

Where b = mobility, z = charge of ion, R = gas constant, T = temperature F_c = Faraday constant.

The mobility can be found using;

$$b = \frac{ze}{6\pi\eta r_{ionic}} \qquad 3.17$$

Where e = charge of an electron, η = dynamic viscosity of the medium and r_{ionic} = hydrodynamic radius of the ion. The Debye length is in the order of nanometres in concentrated electrolytes but it can reach tenths of micrometer in a highly insulating hydrocarbon.

Tribocharging is thought to occur due to the stripping action on double layers created by the relative motion at the metal-oil interface. This stripping force entrains part of the double layer charge as shown in Figure 3.12, which contains positive charge. This results in the liquid carrying part of the double layer charge and thus generates free electrostatic charges.

Under mild wear conditions, tribocharging will only produce a constant background charge level, however, as the tribocontact decays and frictional heating ensues, thus affecting oil chemistry, this situation may change.

The wear debris formed will also have their own double layer. As the debris moves between the contacting surfaces, their double layer could also be sheared and hence could alter the charge initially carried by the wear debris from their formation. There is also the possibility that particles can become charged as they pass through the double layers of the contacting surface.

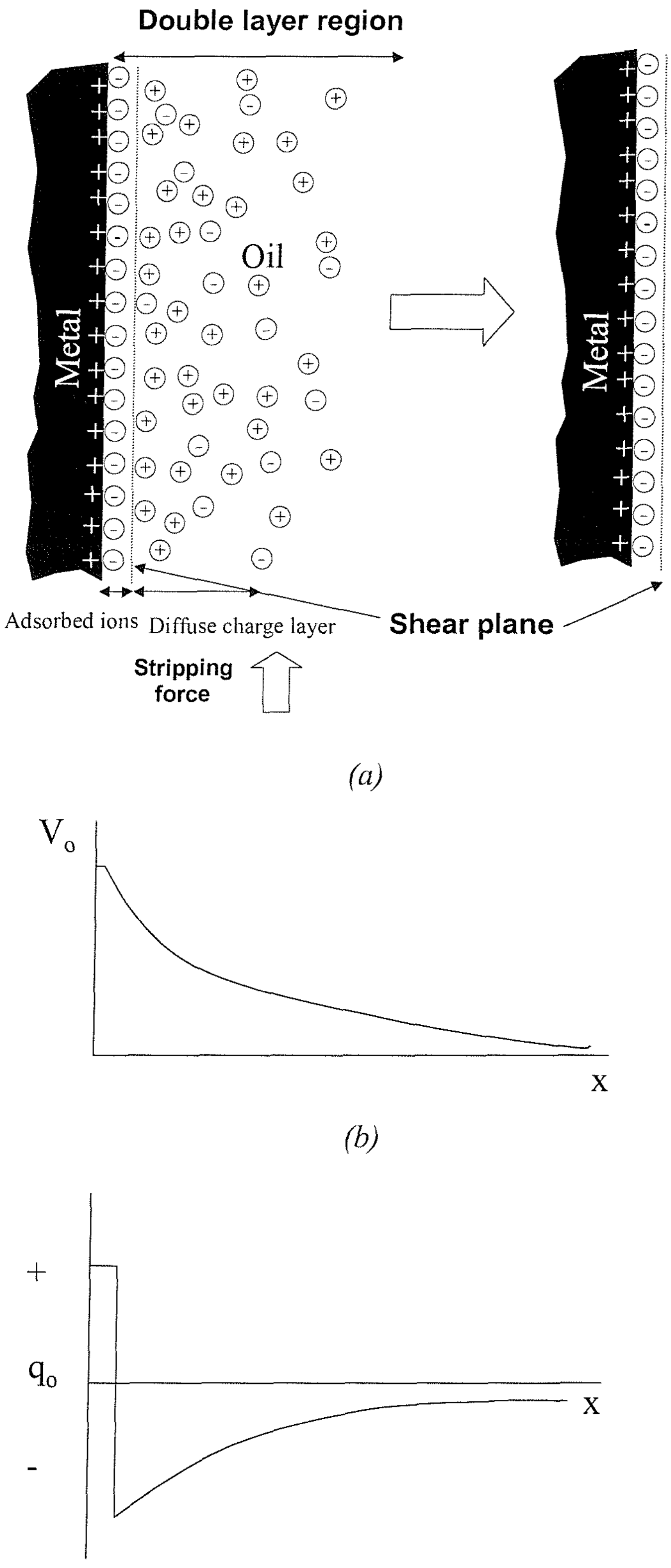

(a)

(b)

(c)

Figure 3.12 (a) Schematic diagram of an electrical double layer. The dotted lines show the shear line. The potential (b) and charge distribution across the interface (c) [31].

3.6.3 Fundamental studies

To understand the mechanisms of charge generation on debris in oil, the behaviour of the oil medium needs to be fully understood. This, coupled with the understanding of the charge generation mechanism by the actual wear and formation of the debris itself, would be extremely valuable information to interpret any charge detected by the sensors. The charging ability of oil has been investigated by Harvey *et al* [39] using a standard spinning disc rig arrangement, as shown in Figure 3.13. Investigations were carried out on the effects of the oil viscosity, temperature, disk roughness and oil aging.

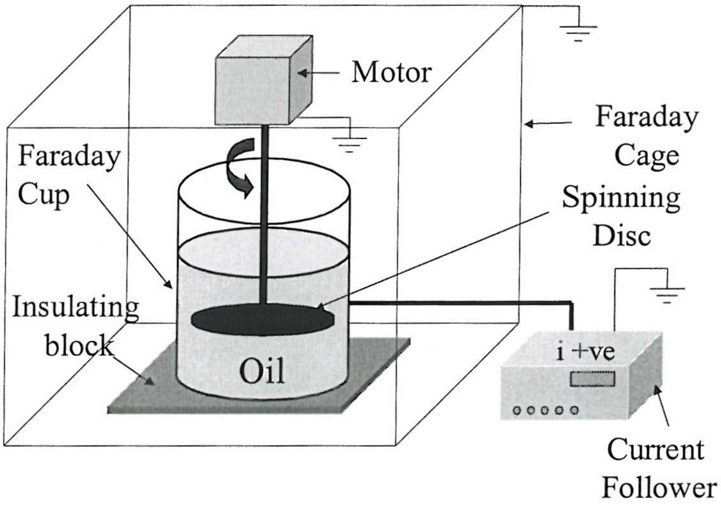

Figure 3.13 Spinning disc test rig used by Harvey et al [39].

It was discovered that the charging ability of the oils increases with increases in viscosity and temperature. The charging ability as a function of temperature is shown in Figure 3.14. Experiments on aged oils were conducted and they were aged by mechanical action and exposure to air and sunlight. Aging by exposure to air had no effect on the charging ability. Charging ability increased due to aging by mechanical action and exposure to sunlight. Surface roughness effects were also studied. An increase in the surface roughness of the disc increased the level of charge ability generated.

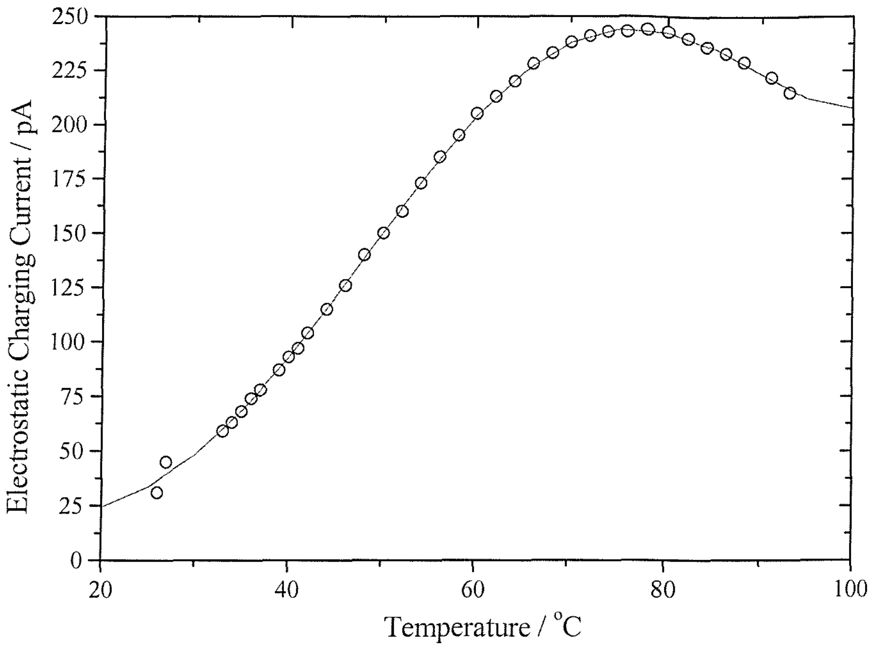

Figure 3.14 *The effects of temperature on the electrostatic charging current [39].*

Solid - solid interactions.

The occurrence of charging when two solids are brought into contact is called contact charging. This phenomenon has been discovered and studied for several centuries but still little is understood about this area. A good review of this subject has been made by Taylor *et al* [31]. At the most basic level, contact charging is a simple phenomenon. When two different solids (*A* and *B*), initially electrically neutral, as shown Figure 3.15(a), are brought into contact, charges must transfer from one surface to the other in order to achieve thermodynamic equilibrium, Figure 3.15(b). If the contacting solids are isolated from earth and separation occurs fairly quick, then the excess charge will be retained by both solids, Figure 3.15(c).

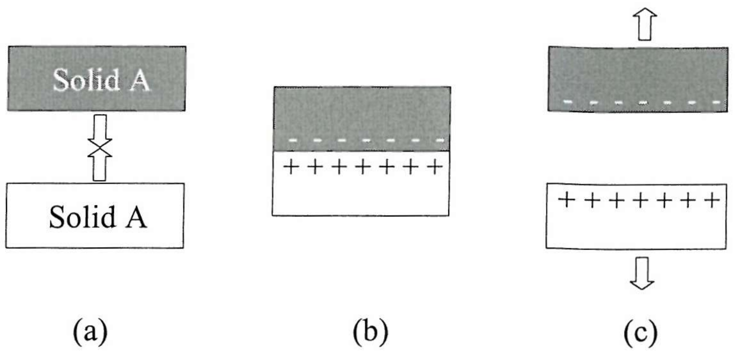

Figure 3.15 Three stages of contact charging. (a) Two dissimilar solid brought together. (b) Charges transfer between them. (c) Charges were retained after separation [31].

Contact charging occurs between all solids regardless whether they are conductors or insulators. If both solids are conductors, the charge retained after separation is often small as charges flow very rapidly to the very last point of contact and recombine, as illustrated in Figure 3.16(a). If they are both good insulators charges are not able to flow back to the last point of contact, as they are trapped on, or just inside, the insulators' surface, as illustrated in Figure 3.16(b). Hence they will retain a far larger charge compared to conductor-conductor contact.

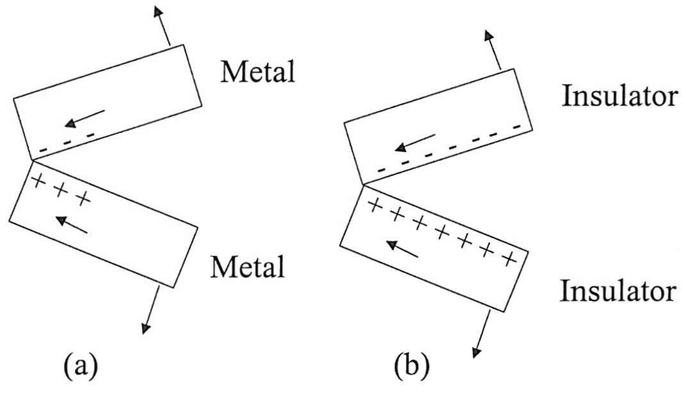

Figure 3.16 (a) Charge moves towards and recombining at the last point of contact. (b) Charges remained trapped on or just under the surface of insulators [31].

Due to the complicated manner of the charging mechanisms of metal-insulator and insulator-insulator, and given the scope of this thesis, no attempt will be made in this section to discuss them in detail. In the case of metal-metal interactions, it is directly related to the contact potential difference theory. This will be discussed in detail in Section

3.6.4. Separated charge on metals was found to be proportional to the contact potential difference from work conducted by Harper [50]. The charge retained after separation can be found using the expression;

$$q = C_o V_c \qquad 3.18$$

Where V_c is the contact potential difference and C_o is an effective capacitance. This expression was verified as quantitatively valid by Lowell [51], therefore the equalisation of Fermi levels on contact is entirely responsible for charge q. It was also proven that for a metal-metal contact, the magnitude of the separated charge is independent of separation velocity and the effect of mutual sliding of the contacting pair.

Triboelectric series

The triboelectric series shown in Table 3.1 has been compiled by Unger [52]. Using this series it is possible, within limits, to predict the polarity of charge produced on each member of a pair of solids that have been rubbed together. For a given pair, the solid that is on a higher position in the series will become positively charged and the solid on a lower position will become negatively charged. Generally, for insulators it was found that by increasing the speed of rubbing, the transfer of charge could be increased [53]. Theoretically, the further the two materials are separated on the series, the higher the rate of charge transfer i.e. charge magnitude. Triboelectric series should be considered only as a general guide as they are notoriously hard to reproduce especially for a pair of materials that are close to each other on the series. Theoretically, the series suggests that a pair of identical material would not produce any charge transfers if they were rubbed on each other. This was found to be untrue from experiments. Therefore localised variation on the contact surface must exist, such as local temperature difference and material transfer. In the case of metal-metal contact, the Triboelectric series is loosely analogous to their position arranged based on their work function values.

+ Positive
Air
Asbestos
Glass
Mica
Nylon
Wool
Lead
Aluminium
Paper
Cotton
Steel
Wood
Polystyrene
Polyethylene
Hard Rubber
Nickel, Copper
Brass, Silver
Gold, Platinum
Sulphur
Polyester
Polyethylene
Polypropylene
PVC
Silicon
Teflon
- Negative

Table 3.1 Triboelectric Series [52].

3.6.4 Contact Potential Difference

Work function is defined as the minimum work required, in a vacuum, to extract an electron from the Fermi level of a conducting phase through a surface. Different materials have different Fermi levels and hence different work functions. When two metals, M_a and M_b, are brought into contact their Fermi energies (ϕ_{Ma} and ϕ_{Mb}) equalize. This equalisation is achieved by electron transfer and results in the generation of an electrical charge on the respective surfaces, as shown in Figure 3.17. This charge separation results in a contact potential difference, V_{CPD}, between the two surfaces that is related to the difference in work function as shown in Equation 3.19:

$$eV_{CPD} = \phi_{Ma} - \phi_{Mb} \qquad 3.19$$

The variation in surface contact potential difference can be used as a condition monitoring technique as shown by Yang et al [54,55] and Zanoria *et al* [56]. In a lubricated sliding contact, changes in the work function can be attributed to first transition scuffing events, such as the formation of white layers. This will be discussed further in Section 4.1.1. For unlubricated wear, the reactive fresh surfaces created by the delamination of oxide films will typically have a lower work function compared to the oxidised or unworn surface of the parent metal [57].

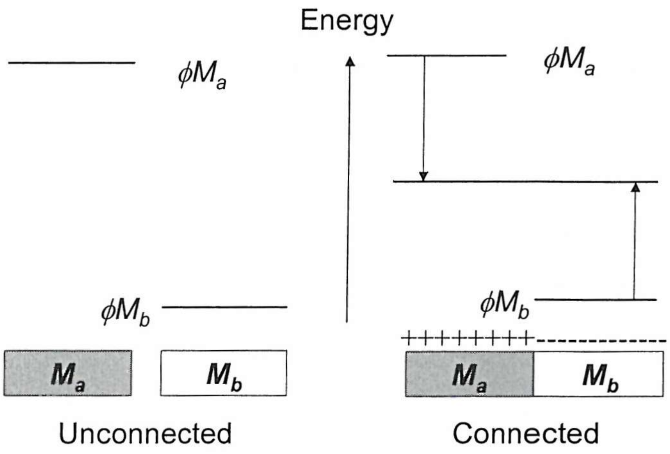

Figure 3.17 Schematic diagram of contact potential difference theory [58].

3.6.5 Charged Particle Emissions

A review of charged particle emissions phenomenon from solids has been conducted by Kajdas *et al* [59]. Several terms have been used by researchers to describe this phenomenon: including triboemission and fractoemission. Triboemission is defined as the emission of low energy electrons, ion, photons and neutral particles **during** tribological surface damage. Fractoemission is defined as the emission of particles and photons **during and after** fracture.

Triboemissions

Triboemission has been studied by Nakayama *et al* [60-68], who studied this phenomenon on various solids under various atmospheres and conditions. The work involved the scratching of various metals, semiconductors and insulators, on a modified pin-on-disc machine, using a diamond stylus with various tip diameters. The general trend obtained from these results indicate the intensity of emitted negative charge increases in the order of conductor < semiconductor < insulator as shown in Figure 3.18. However the reverse order was found for the intensity of photon emission (i.e. insulators < semiconductor < conductor). The intensity of positive charged particles emitted from an insulator differs little compared to the intensity of negatively charged particles as shown in Figure 3.19. This was not the case with conductors and semiconductors as the intensity of positively charged particle emissions is a lot smaller than the intensity for negatively charged particles. This was thought to be due to a greater supply of bulk (interior) electrons from the more conducting solids.

Triboemission increases with the decrease of the stylus tip radius and increasing sliding speed, applied load and decreasing hardness, showing that triboemission intensity is directly related to the severity of surface damage.

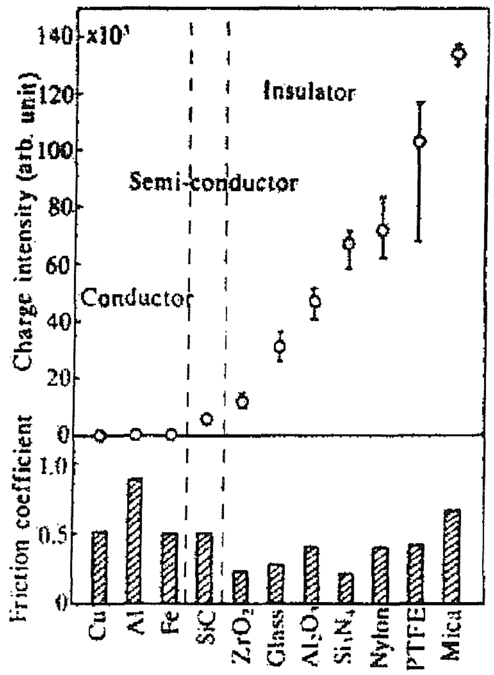

Figure 3.18 Charge intensity of negatively charged particles and corresponding friction coefficient in various solids in air: vertical angle 85° with sharp edge, applied load 0.5N, sliding speed 7 cm/s [62].

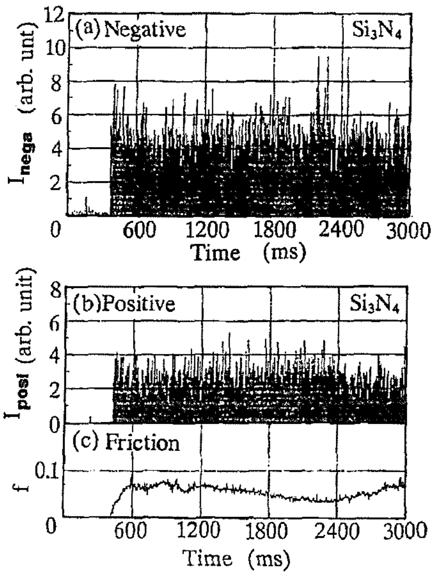

Figure 3.19 Dependence of emission intensities of negatively and positively charged particles: (a) negative, (b) positive and (d) friction coefficient f during scratching Sl_3N_4 in propane gas on scratching time [61].

It was also found that humidity, atmosphere type and surrounding gas pressure affected the intensity of triboemission. In hydrocarbon atmospheres the intensity of emissions decreases as the hydrocarbon chain length increases. In a branched hydrocarbon atmosphere, the intensity is slightly less than that of a straight chain of the corresponding number of carbon atoms. For example, the intensity of triboemission in iso-butane is slightly less that that in n-butane.

Tests conducted in atmospheres of helium, argon and oxygen at varying pressure show that for each gas there is a maximum level for the emission intensity of positively and negatively charged particles and photons. The maxima pressure for maximum emissions in increasing order is He<Ar<O_2 as shown in Figure 3.20. Pressure change however does not influence the ratio of negatively charged particles to positively charged particles.

Under simulated boundary conditions using n-hexane, n-undecane and n-hexadecane (saturated hydrocarbon liquids), the emission intensities were slightly lower than in dry sliding. The friction coefficient was unaffected by the pressure of hydrocarbons and thus presumed not to affect wear rates (surface damage). The lower intensity of emission was thought to relate to the rate of production and disappearance of the low energy electrons and ions in the contact region. In conductors e.g. metals, any low energy electrons produced that contact the body of the metal will rapidly reabsorb/recombine and hence reduce the intensity detected. For insulators, electrons that are emitted will be released into the surrounding gas or liquid although some might recombine with the positive ions to form neutral particles. With increasing lubricant chain length the intensity of emission decreases. This is probably due to the fact that the adsorption is affected by the stability of molecular structure, i.e. the ability to form stable ions.

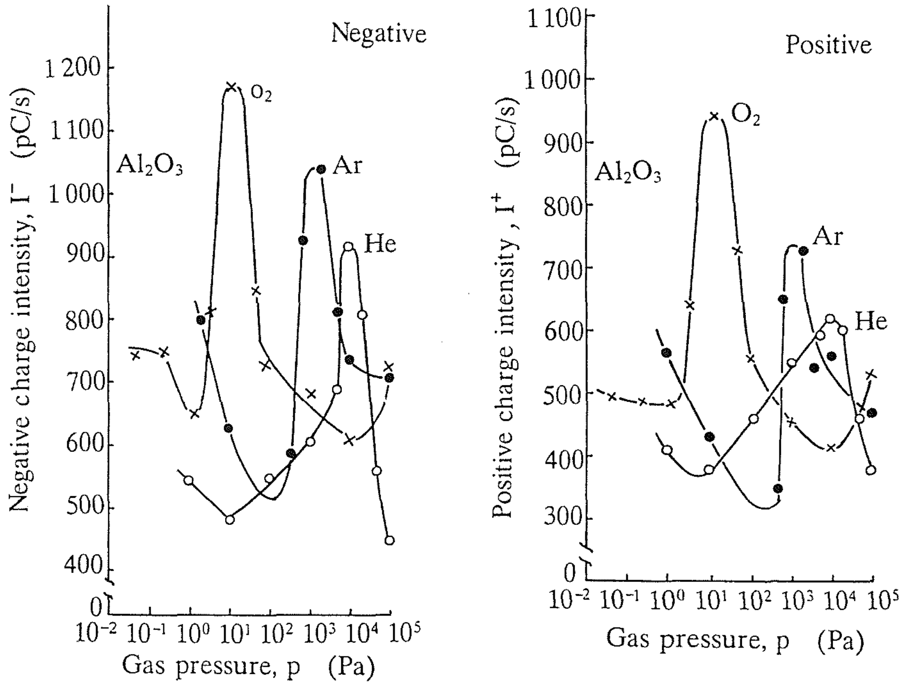

Figure 3.20 *Plot of negative and positive charge intensity against gas pressure for O_2, Ar, and He [65].*

Mechanisms

Conductors (e.g. metals)

If the value of exothermic heat of formation exceeds the work function of the fresh metal surfaces, electrons will be emitted. The emission of charged particles increases exponentially with the increase of formation of oxides and nitrides depending on the metal species. This suggests that when oxides are forming, there is enough energy to generate triboemission. The 'electrified fissure model' for the emissions of charged particles suggests that the emission of electrons from the oxide film during plastic deformation of metal together with charge separation across opposing cracks, results in a strong local field within the cracks with sufficient intensity to cause field emission of electrons from the crack walls [69].

Insulator (e.g. ceramics)

In an insulator, gas ionisation mechanisms are thought to be responsible for the emission of charged particles and electrons [63]. Discharge of surrounding gas molecules occurs at and near the damage surface. The discharge is due to a microplasma state formed by the intense electric field generated by charge separation at and near the damaged area. This will cause the surrounding gas molecules to be ionised.

Fractoemissions

Fractoemission is defined as the emission of particles and photons during and after fracture of materials. The emitted particles usually consist of electrons, negative ions, positive ions and neutral species [59]. Fractoemission detection can sometimes act as a probe to detect crack propagation. It has been found that the rate of electron emission during tensile failure is directly related to the rate of acoustic emission, as shown in Figure 3.21 [70]. Plastic deformation results in roughening due to intersection of slip lines with the surface and this will usually cause any oxide layer to break up exposing nascent micro-asperities. Consequently, due to the lower work function of the nascent surface it will react with the surrounding medium and cause emission of low-energy electrons.

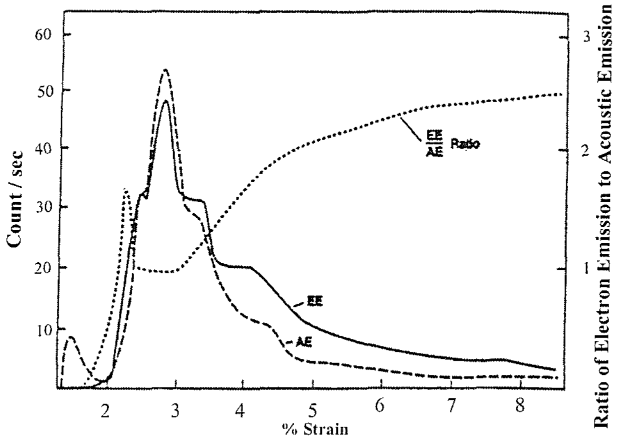

Figure 3.21 Electron emission (EE) and acoustic emission (AE) rates and their ratio (EE/AE) as a function of strain for a sample of anodised aluminium [70].

3.6.6 Charge Generation Associated With Different Lubrication Regimes

The value of the ratio of minimum film thickness to surface roughness (λ) provides the measure of the likelihood and severity of asperity interactions and can be obtained from Equation 3.20.

$$\lambda = \left(\frac{h_{\min}}{\sigma_c}\right) = \left(\frac{h_{\min}}{\sqrt{R_{q1}^{2} + R_{q2}^{2}}}\right) \qquad 3.20$$

Where, h_{min} is the minimum EHL film thickness, σ_c is the composite rms surface roughness, R_q is the rms surface roughness of the surfaces 1 and 2 in the sliding contact. Figure 3.22 shows the schematic representation of different lubrication and adhesive wear regimes in oil lubricated sliding contacts [33]. The schematic representation has been divided into regions of full-film EHL, partial EHL and boundary lubrication.

In the full-film EHL region, where $\lambda > 3$, the sliding surfaces are fully separated by an EHL film. In this region, asperity contact and wear are negligible and the coefficient of friction remains low. Electrostatic sensing employed in this region would pick up low levels of electrostatic charge. These charges originate from tribocharging due to the shearing (induced by relative motion) of the double layer present at metal/lubricant interfaces as discussed earlier.

The partial EHL region, where $1<\lambda<3$, the EHL film is sufficiently thin for some large asperities to come into contact. As λ approaches unity the coefficient of friction and contact pressure will increase. This will be followed by an increase in the contact temperature. These events will lead to the occurrence of first transition scuffing and hence the formation of white layers which have a different work function from the parent metal. Electrostatic sensing employed in this lubrication region would pick up electrostatic charge due to the combination of tribocharging, variation in the contact potential difference as well as some plastic deformation of the asperity, degradation of oxide layers and low levels of debris formation. Wear in this lubrication region is smooth sliding wear. When the value of λ is smaller than unity (partial EHL), boundary lubrication exists. In this region, second transition scuffing can occur. This is accompanied by a sharp increase in the coefficient of friction and rise in adhesive wear rate. Electrostatic sensing employed in these conditions would pick up relatively high levels of electrostatic charge produced by triboemission from plastic deformation and cracking of the contacting surface. The formation of larger quantity and larger size of debris will also contribute to the formation of charge.

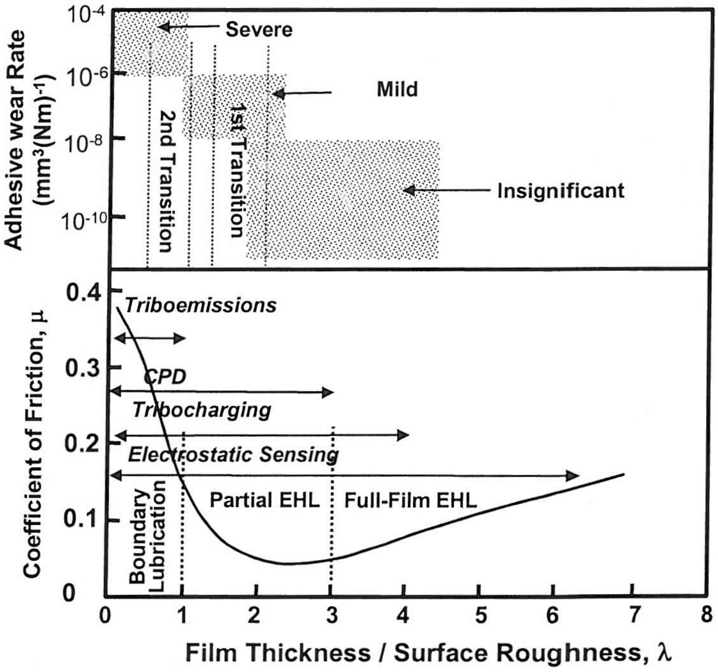

Figure 3.22 *The schematic representation of different lubrication and adhesive wear regimes [33].*

4

ELECTROSTATIC CHARGE MONITORING OF LUBRICATED SLIDING WEAR

4.1 INTRODUCTION

This chapter details the investigation of charge generation during scuffing of B.S. 534A99 (En31) bearing steel lubricated by mineral base and fully formulated synthetic oil. A pin-on-disc test rig was used and the test conditions were designed to induce second transition scuffing in a controlled manner. Precursor charge events prior to second transition scuffing were identified and post-test analysis on the disc relates the charge features to the condition and property of the worn surfaces and the generation and entrainment of wear debris.

Before discussing the tests the relevant basics of adhesive wear will be reviewed in the following section.

4.1.1 Background

Adhesive wear

Adhesive wear can occur when two smooth surfaces rub against each other [71]. Smooth surfaces in fact are never perfectly smooth. High spots or asperities will exist and they can experience high contact stress and will weld (adhere) onto each other. The relative motion between the surfaces can break the adhesion. At the weld interface, material will be plucked away from the weaker surface resulting in material transfer onto the stronger material. Adhesive wear in the presence of a lubricant is termed as scuffing (or scoring in the U.S). Figure 4.1 shows a typical adhesive wear scar.

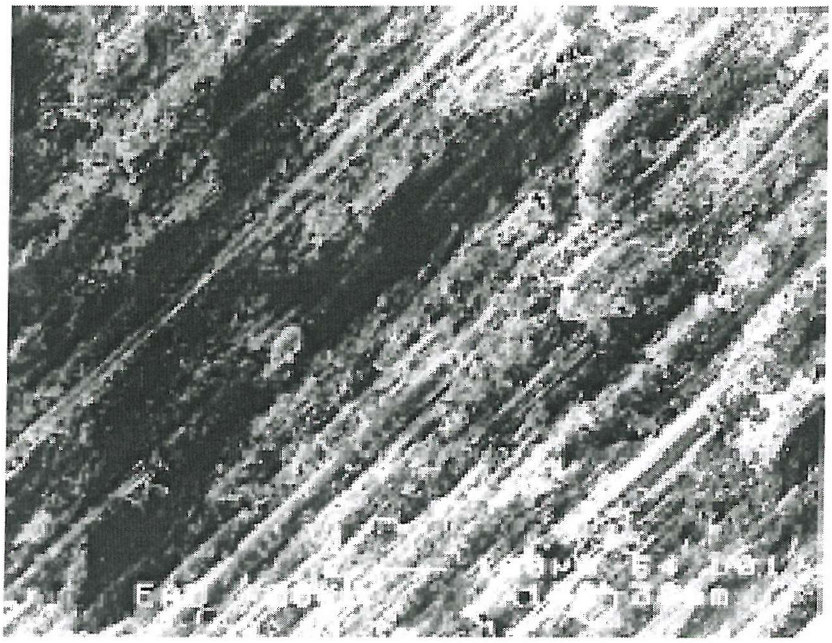

Figure 4.1 Typical adhesive wear scar [72]

Scuffing

The development of elastohydrodynamic (EHL) lubrication has enabled very highly stressed contacts such as gears and rolling element bearings to operate more efficiently with a low rate of wear. Equation 4.1 describes the minimum EHL film thickness in a sliding sphere on plane contact [73].

$$\frac{h_{\min}}{R} = 1.79\left(2\alpha E^{*}\right)^{0.49}\left(\frac{U\eta_0}{2E^{*}R}\right)^{0.68}\left(\frac{W}{2E^{*}R^{2}}\right)^{-0.073} \qquad 4.1$$

Where, h_{min} is the minimum EHL film thickness, R is the radius of curvature, α is the pressure viscosity index, E^* is the contact modulus, η_0 is the base viscosity at atmospheric pressure, U is the horizontal entraining velocity and W is the normal load on the surface.

If the EHL film is sufficiently thin (i.e. the ratio of minimum film thickness to surface roughness, $\lambda < 3$, see Equation 3.20), asperity-to-asperity contact can occur. This would lead to an increase in contact temperature and hence decrease in the oil viscosity, as viscosity decreases exponentially with increasing in temperature. This would in turn reduce the film thickness even further. Although the viscosity in the contact decreases, oil replenishment remains unaffected. This is because the replenishment is determined in the entry region, where the oil is in temperature equilibrium with the bulk contacting body [74]. Prolonged asperity-to-asperity contact and decrease in the film thickness would result in scuffing.

There are two stages of scuffing:

- *First transition* is a result of initial asperity-to-asperity contact. Friction or cold pressure welding can occur and the resulting high, localized contact temperature can change the phase of the contacting steel surface producing what are called *'white layers'* (see the following section). Thus, the occurrence of first transition scuffing can be verified by identifying the presence of white layers and is a likely pre-condition of surface failure. There is no increase in the wear rate at the first transition scuffing stage.

- *Second transition scuffing* occurs when there is a total collapse of the EHL film. It will result in severe adhesive wear with large transfer of material between the contacting surfaces, which can lead to catastrophic failure. A good indication of a second transition scuffing is a sharp increase in friction.

White layers

Some of the earliest observations on the occurrence of white layers on steel surfaces were reported by Stead [75] and Trent [76]. White layers are interpreted as the formation of martensite as a result of frictional heating followed by quenching by the colder sublayer. White layer formation in steel and cast iron can occur during various sliding conditions from low pressure dry contact to high pressure lubricated contacts and also rapid heat treatment processes [76-78]. In order for the white layer to be visualized, the contact surface has to be etched. White layers have a silvery appearance and are resistant to etchants [79,80]. White layers also have higher micro-hardness compared to the parent material [79,81]. Due to this property they are thought to have a higher wear resistance, although the presence of micro cracks in the layer or sublayer could result in the delamination of the white layers [82]. White layers are thought to form by several mechanisms namely martensitic transformation, localized plastic deformation and transformation due to thermomechanical processes [79,81,83].

4.2 EXPERIMENTAL PROCEDURE

The experiments were carried out using a modified pin-on-disc test rig fitted with an electrostatic sensor as illustrated schematically in Figures 4.2 and 4.3. The tests employed a 6 mm diameter B.S. 534A99 (En31) ball loaded against a B.S. 534A99 disc. The ball was fixed in an earthed brass housing to achieve pure sliding wear. Tests were carried out using two types of lubricating oil: Shell Vitrea ISO 32 (mineral base oil) and Exxon Turbo 2380 (fully formulated synthetic oil, currently known as BP Turbo 2380). The oil was fed using a pneumatic spray system and care was taken to avoid the formation of large droplets.

Tests were carried out until severe adhesive wear (second transition scuffing) occurred, which was indicated by a sudden increase in friction and the vibration on the test rig. For the base oil test, running-in was achieved by gradually increasing the linear sliding speed from 1 ms^{-1} to 4 ms^{-1} at regular intervals of 5 minutes. Scuffing was achieved by just increasing the sliding speed. For the synthetic oil, running-in was achieved by gradually increasing the linear sliding speed from 1 ms^{-1} to 4 ms^{-1} at regular intervals of 1 minute. Scuffing in this test was achieved by the combination of the increment of sliding speed and load. The running-in process for the synthetic oil was carried out in a less ‘gentle’ way as compared to the base oil test based on test experience using Exxon Turbo oil.

Table 4.1 summarises the test conditions for both tests. Typical initial values of λ for Shell Vitrea and Exxon Turbo are calculated as 1.4 and 1.0 using Equation 4.1, taking a sliding speed of 1 ms^{-1}, $E^* = 100 \times 10^9$ Pa, W = 50 N, $\alpha_{shell} = 2.52 \times 10^{-8}$ Pa and $\alpha_{exxon} = 2.52 \times 10^{-8}$ Pa. The rms surface roughness (R_a) of the disc and the ball was measured as 0.17 and 0.03 µm, respectively.

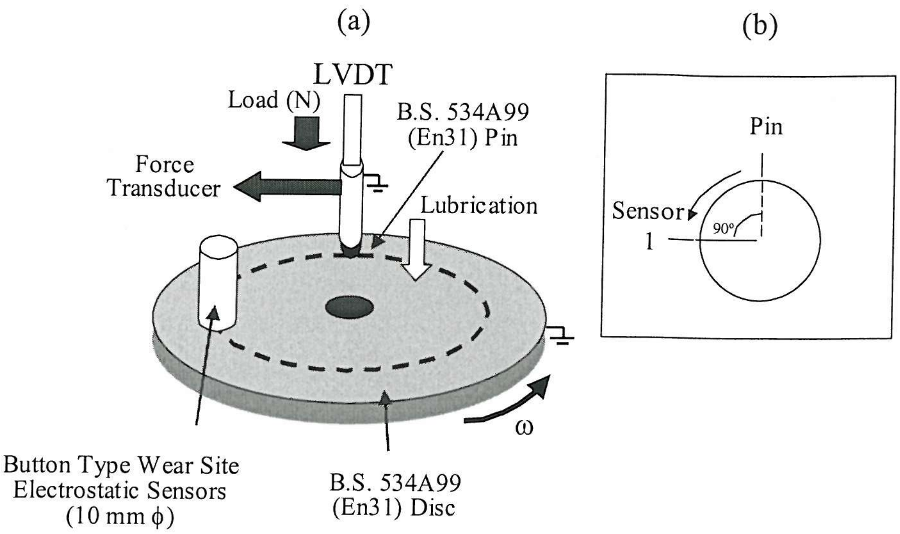

Figure 4.2 *(a) & (b) Schematic diagram of the scuffing test set-up and relative position of sensors.*

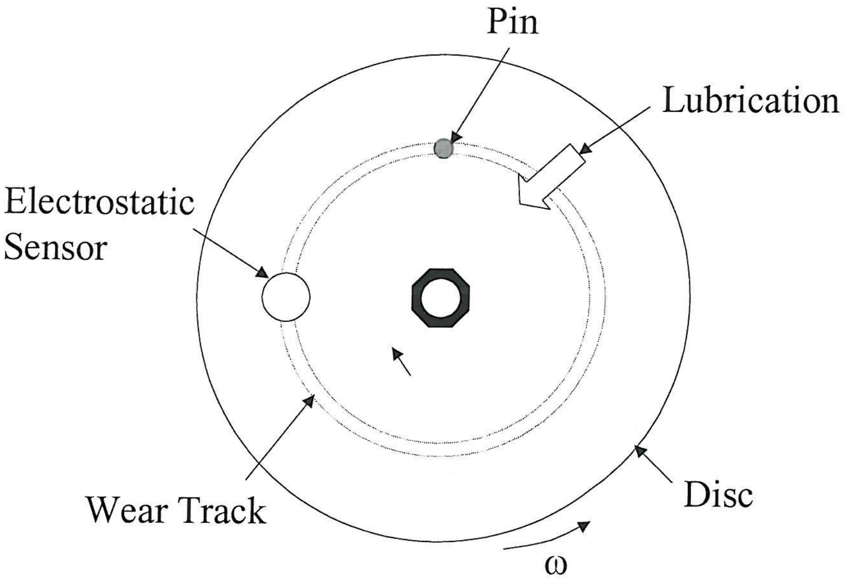

Figure 4.3 *Plan View of scuff test rig setup.*

	Test 1	Test 2
Pin Material	Bearing steel B.S. 534A99	
Disc Material	Bearing steel B.S. 534A99	
Contact radius (mm)	3	
Load (N)	50	100
Max. Sliding speed (ms^{-1})	6	7
Hertzian contact pressure (MPa)	2.4	3.0
Min. film thickness (μm)	0.27	0.2
Pin hardness (HV)	640	
Disc Hardness (HV)	220	
Pin roughness, R$_a$ (μm)	0.03	
Pin Yield Strength (MPa)	400	
Disc Yield Strength (MPa)	345	
Disc roughness, R$_a$ (μm)	0.17	
Oil	**Shell Vitrea ISO 32**	**Exxon Turbo 2380**
Oil feed	Mist Spray	
Oil temperature	Ambient (not heated)	
Oil dynamic viscosity @ 26 °C (cP)	48	37
Initial λ value	1.4	1.0

Table 4.1 Summary of test conditions for lubricated test.

4.2.1 Instrumentation

The block diagram of the instrumentation used is shown in Figure 4.4. The rig was fitted with a tachometer in order to monitor the disc rotational speed. The electrostatic sensor employed has a sensing area of 7.85 x 10^{-5} m^2 (10 mm diameter sensing face) and was positioned approximately 0.5 mm above the disc surface. The sensor was connected to a signal conditioner, which was operated at a gain of 500 mVpC^{-1} and a nominal frequency response range from 10 Hz to 10 kHz. It is also designed to minimize drift in the output signal whilst retaining the original characteristic of the detected charge. The signal conditioner converts the signals from the sensor to a voltage output. The amplifier high pass filter (10 Hz) eliminates background level drift. A calibrated force transducer employing a strain gauge system was used to record the change in the friction while a linear vertical displacement transducer (LVDT) was used to monitor the combined pin and disc vertical wear. During the test, signal outputs were displayed in real-time on an oscilloscope and all instrumentation data was recorded by a DAT recorder, as well as recorded by a PC acquisition system.

The signal conditioning unit is specially designed to monitor dynamic charge events and is insensitive to static unvarying charges, for example, the charge levels associated with the bulk of the disc. A constant charge level will output a zero output from the signal conditioner. Output from the signal conditioner has the same sign as the charge polarity that it is monitoring. When the high pass filter is activated, and if the charge is moving slower than 10 Hz (1 Hz if the high pass filter is deactivated), the signal conditioner will also output zero.

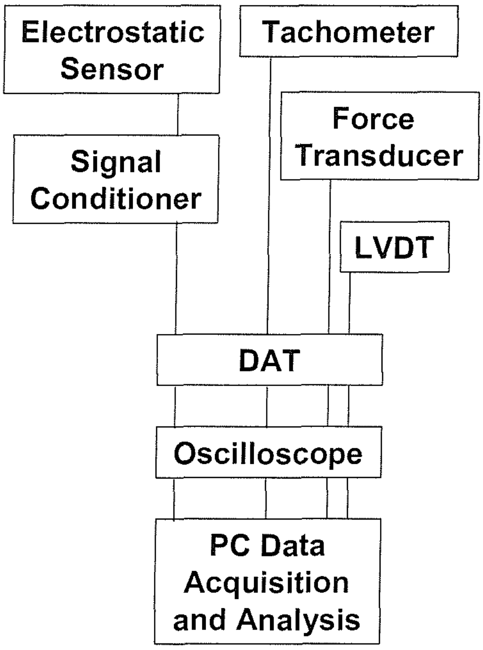

Figure 4.4 Block diagram of the instrumentation used for the lubricated wear tests.

4.2.2 Data Analysis

Electrostatic sensor and tachometer signals were analysed in real-time using a PC-based data acquisition system with software analysis developed by Smiths Aerospace Electronics Southampton. The signals were fed to the PC through an interface unit and then digitised via an A/D card. The electrostatic signals were analysed using a signal averaging technique, which uses the once per revolution tachometer signal for synchronisation with the disc rotation (see Figure 4.5). This software collects the synchronised data at 4000 Hz acquisition rate and, after a period of 10 seconds, the data is averaged to produce a single signal average. This method enhances synchronous signals and suppresses random, non-related effects. This information can determine any areas of the disc surface which cause consistently anomalous signals which can be related to surface damage.

Development of new features within the signal average as time progresses may be monitored by generating signal averages continuously. Multiple signal averages may then be represented in a three-dimensional graphical format such as a colour map. A colour map is a planar representation of successive signal averages, which uses colour (or grey-scale) to indicate the relative amplitudes of each signal average.

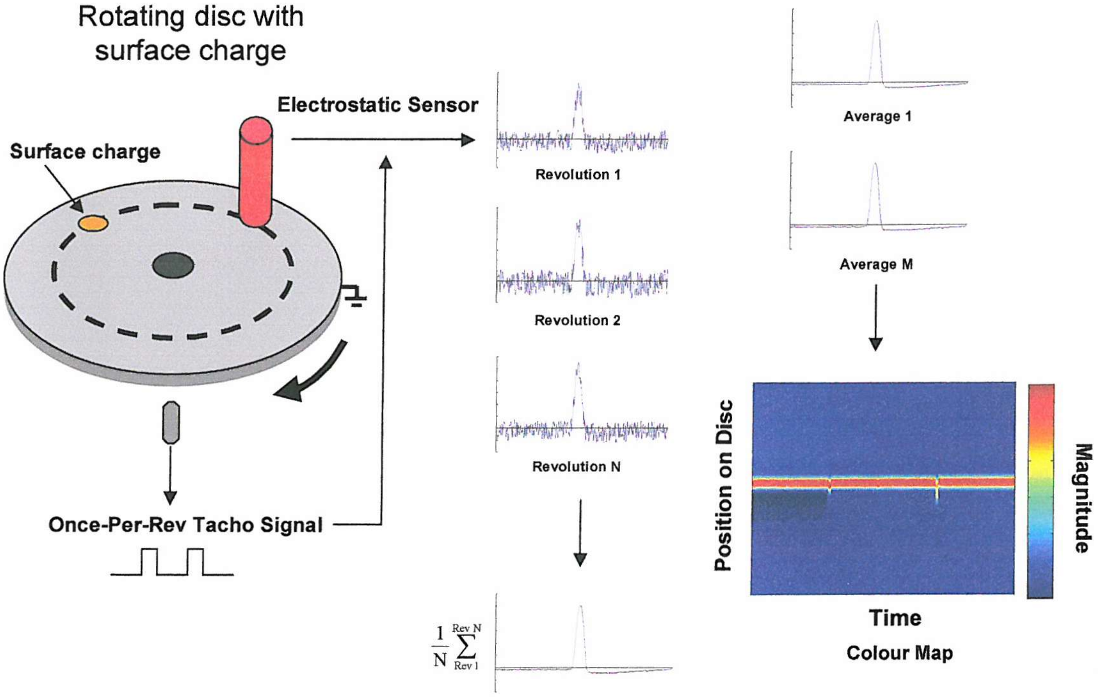

Figure 4.5 *Signal averaging concept.*

Data from the LVDT and force transducer was acquired with the rate of 4000 Hz. The signal was then averaged by the signal acquisition software to produce two points per second. Signal from the electrostatic sensor was also processed to produce two rms charge values of charge per second. Unless stated otherwise, all charging history line plots presented in this thesis are rms charge values. The processed data from the LVDT, force transducer and electrostatic sensor were stored as text files for further analysis.

The cumulative volume loss of the pin, V_{loss}, can be calculated from the vertical displacement of the pin, h, recorded by the LVDT using Equation 4.2

$$V_{loss} = \frac{\pi}{3} h^2 (3r - h) \qquad 4.2$$

Where r = radius of curvature of pin and h = vertical displacement.

Since the LVDT measures the height reduction due to wear of both pin and disc, the calculated volume loss will contain a large error margin. Bearing this in mind it should be appreciated that in the tests presented here, it is the trend of volume loss that is of interest and not the absolute value.

4.2.3 Corroborative Analysis

The mineral base and fully formulated synthetic oil tests were repeated but were stopped during development of significant charge features. Photographs of the disc surfaces were taken to record any centrifuged debris trail. Surface profilometry and metallurgical analysis (etching) of the wear track were then conducted to establish any relation of surface properties with the charge features seen. Surface profilometry was achieved using a Taylor Hobson form talysurf 120L stylus profiler.

The discs were cut into small sections and cleaned in an ultrasonic bath for inspection using Scanning Electron Microscope (SEM). After inspection by the SEM, the samples were cleaned again before etching for approximately 30 seconds in a 2% Nital solution. Etched samples were then inspected under an optical microscope to look for the presence of white layers. Debris was collected from the oil sump during testing as well by washing the pin and disc surfaces with solvent after testing. The debris-solvent mixture was then pipetted onto a glass slide and left to dry. The dried debris samples were then placed on a carbon adhesive disc attached to a SEM sample stub before being viewed using a SEM, to establish the predominant wear mechanism.

4.3 RESULTS AND DISCUSSION

4.3.1 Mineral Base Oil

This test lasted for 72 minutes with scuffing occurring at the sliding speed of 6 ms^{-1}. The colour map plot for electrostatic signal averages is shown in Figure 4.6. After the sliding speed reached 5 ms^{-1} it can be seen that positive features started to appear between positions of 60^o and 180^o on the disc wear surface. This positive feature disappeared after the duration of approximately 7 minutes but reappeared on the 37th minute of the test and gradually increases in magnitude. Immediately after the speed adjustment after the 64th minute (increased to 6 ms^{-1}) the positive feature increases in magnitude abruptly followed by a slow decrease.

Figure 4.7 shows a close-up of Figure 4.6 to reveal the area marked by the dotted red square in more detail. It was also observed that there were instances where the features seem to disappear for several minutes before reappearing again on the same position on the disc. This indicates that the source of the surface charge had been stripped away before reforming again on the same position/area of the disc. The positive features are thought to result from active wear sites, which could be associated with contact potential differences.

It is believed that the electrostatic sensor does not detect triboemissions as it was located downstream of the contacting surfaces and triboemission only occurs during the moment of actual physical damage. At high λ, solid-liquid tribocharging may be present but it would be constant (or little variation) and thus not detectable with the signal conditioning method used.

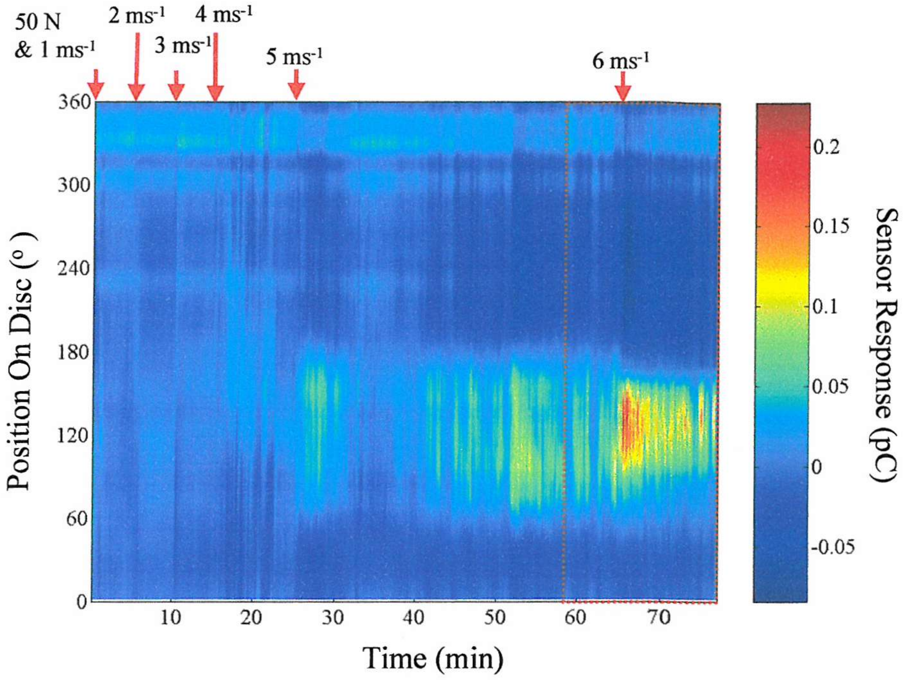

Figure 4.6 *Colour map plot of electrostatic signal averages from a B.S. 534A99 disc scuffing test lubricated with Shell Vitrea ISO 32, 50 N load.*

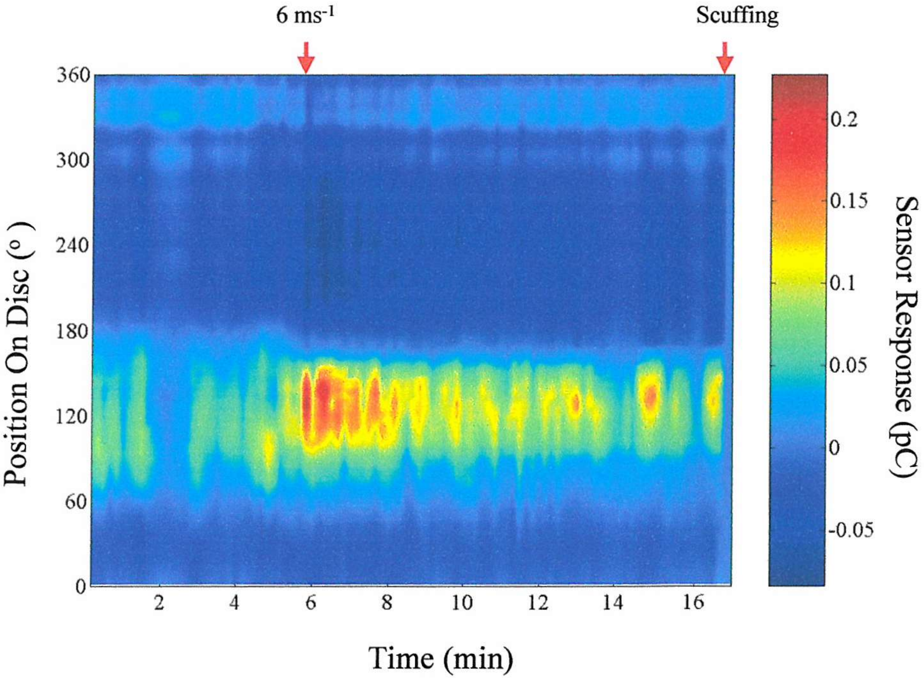

Figure 4.7 *Close-up of Figure 4.6 revealing the region marked by the dotted red square in greater detail. Shell Vitrea ISO 32, 50 N load.*

Figure 4.8 shows the plot of two signal averages taken at the 8th and 65th minute. The plot at the 8th minute is taken as a baseline plot. Figure 4.9 shows the difference between the two signal averages and referencing changes to the background signal, the additional features are identified as a wide peak and trough at 120° and 270° respectively. These features remained constant until the end of the test, acting as the precursor charge signal to secondary transition scuffing, which occurred after 72 minutes

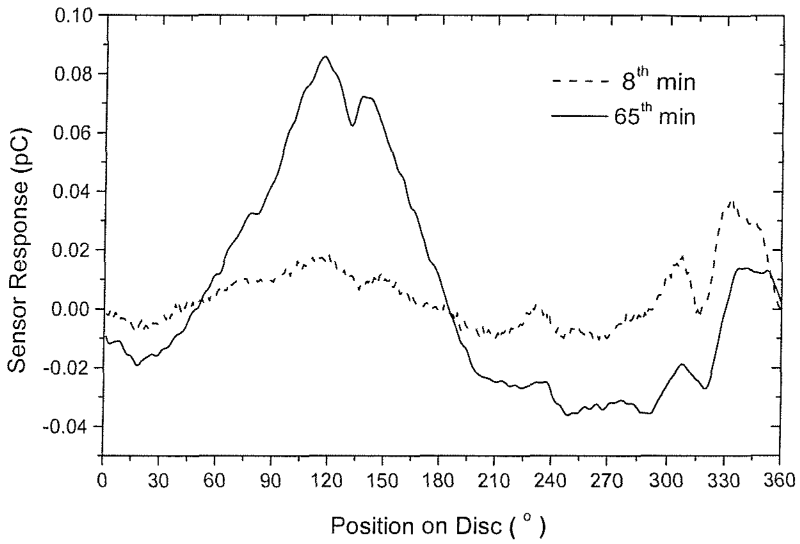

Figure 4.8 *Signal averages at the 8th and 65th minute for mineral base oil scuff test. Shell Vitrea ISO 32, 50 N load.*

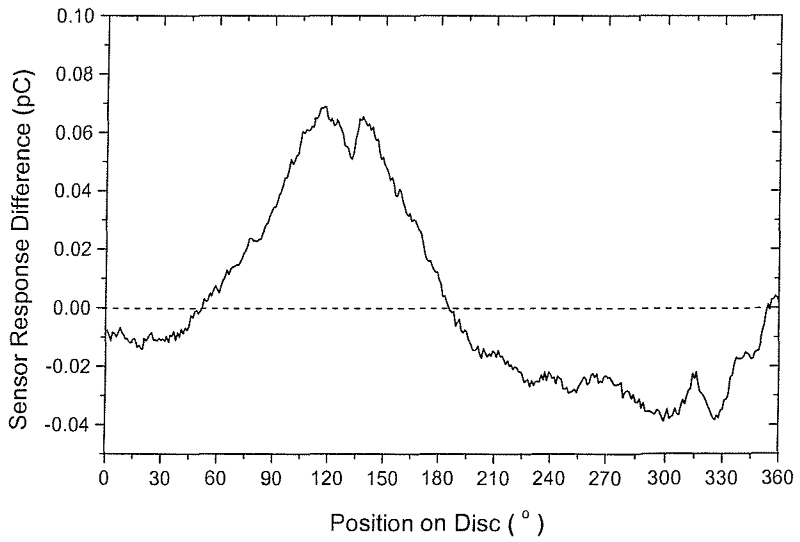

Figure 4.9 *The difference between signal averages at the 65th and 8th minute for mineral base oil scuff test highlighting a wide peak and trough at 120° and 270° respectively. Shell Vitrea ISO 32, 50 N load.*

Figure 4.10 shows the plot of friction, volume loss and charge against time for the whole duration of the test. Generally there is a step increase in the coefficient of friction when sliding speed was increased. At approximately the 60th minute (marked by a dotted line) there was a transient increase in the coefficient of friction which was also accompanied by a transient increase in the charge.

During the running-in period it can be seen that the volume loss started to increase rapidly after the sliding speed reached 3 ms^{-1}. Soon after the sliding speed reached 5 ms^{-1} the volume loss remained at a constant level until the end of the test before increasing abruptly during scuffing.

The general trend for the charge plot is that the level continued to increase throughout the duration of the test. The increase in sliding speed caused an increase in the charge level before decaying to the baseline level. After the sliding speed was increased to 5 ms^{-1} the baseline level increases steadily to the end of the test. Charge increased transiently with increase in friction and the severity of the contact condition and is more sensitive to these changes compared to the volume loss. The fluctuation of the coefficient of friction at the 60th minute (circled on the plot in Figure 4.10) can be seen to be accompanied by a transient increase of charge. All these occurrences are thought to relate to slight changes in the wear severity (not detected by volume loss measurements) and the eventual recovery of the wear surface.

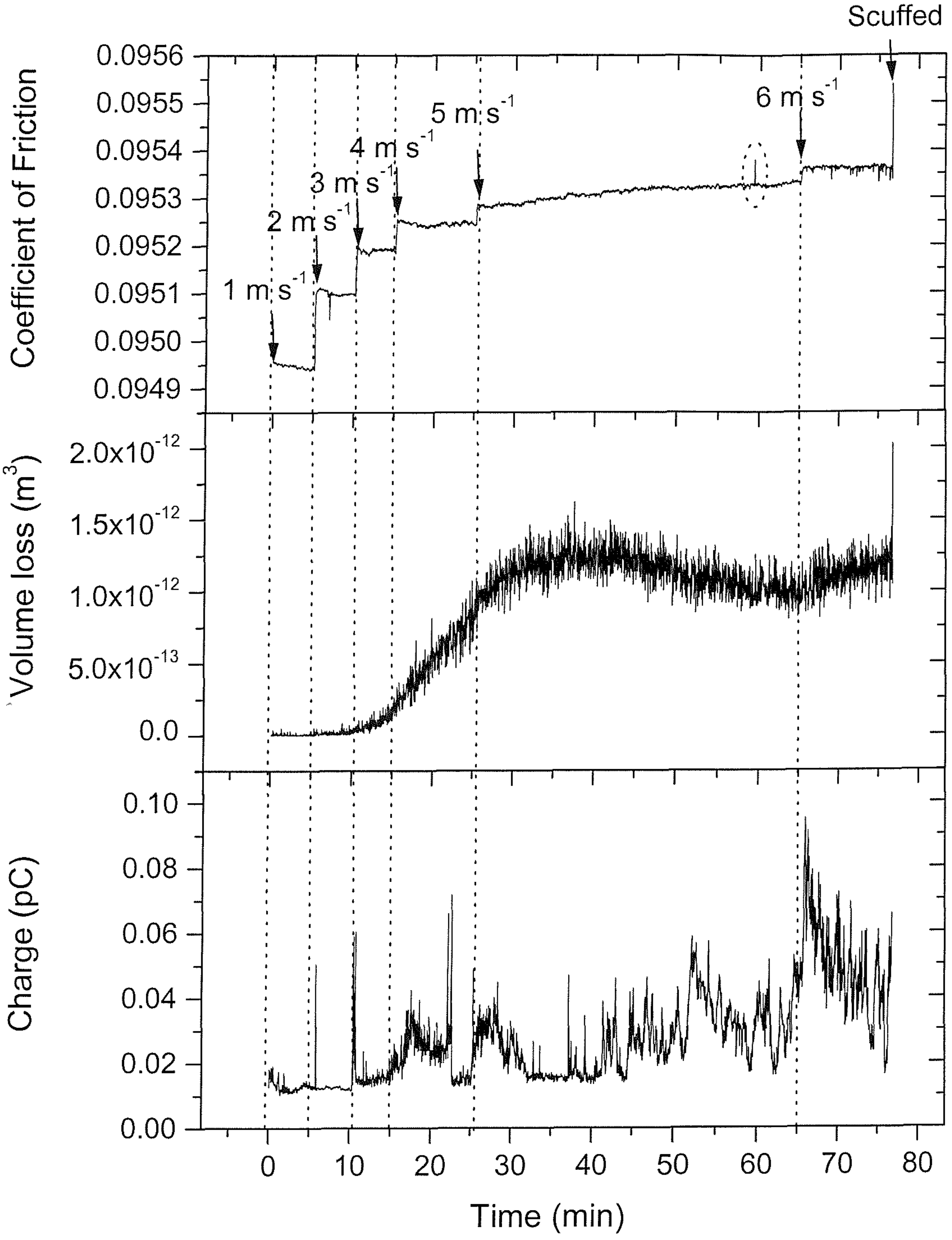

Figure 4.10 *Plots of friction, volume loss and charge against time for the mineral base oil scuffing test. Shell Vitrea ISO 32, 50 N load.*

4.3.2 Fully Formulated Synthetic Oil

Figure 4.11 shows the colour map plot for the 40-minute synthetic oil test, including the test parameters. During the running-in period some background features are seen, the magnitude of these features generally decreased to a constant level as the test progresses. During the running-in period, charging activity is high but soon recovers and a baseline charge level is established. There was no significant change in the charge features until approximately the 34th minute. Figure 4.12, an expansion of Figure 4.11, clearly shows the appearance of positive and negative charge features, some of which are persistent until scuffing. These charge features are precursor signals to second transition scuffing. From Figure 4.12 it can be observed that there were occasions when the features disappeared for several seconds before reappearing again on approximately the same position on the disc surface. The same explanation used to explain similar charging behaviour observed in the mineral base oil test applies here. The reason for the presence of both positive and negative charge precursor signals is still not clear at this point, although difference in oil chemistry could be responsible, for example, the interaction of additives with the nascent metal surfaces on active wear sites as the EHL film breaks down. The presence of significant amounts of debris will also contribute to the charge features.

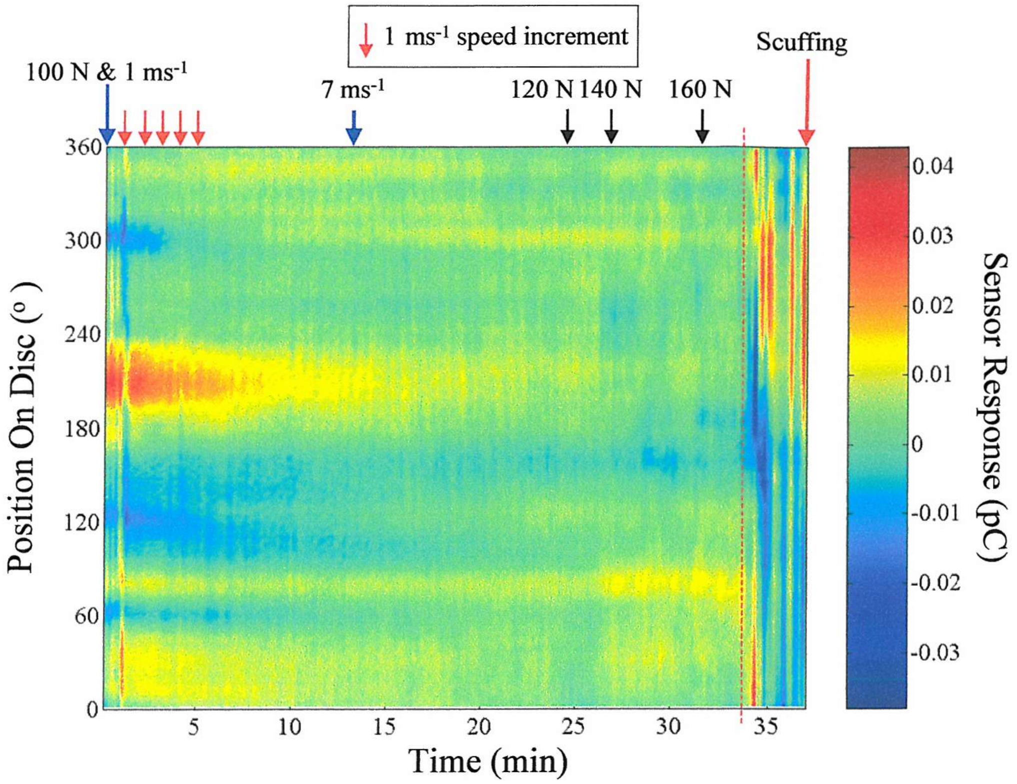

Figure 4.11 *Colour map of electrostatic signal averages from a B.S. 534A99 disc scuffing test lubricated with fully formulated synthetic oil.*

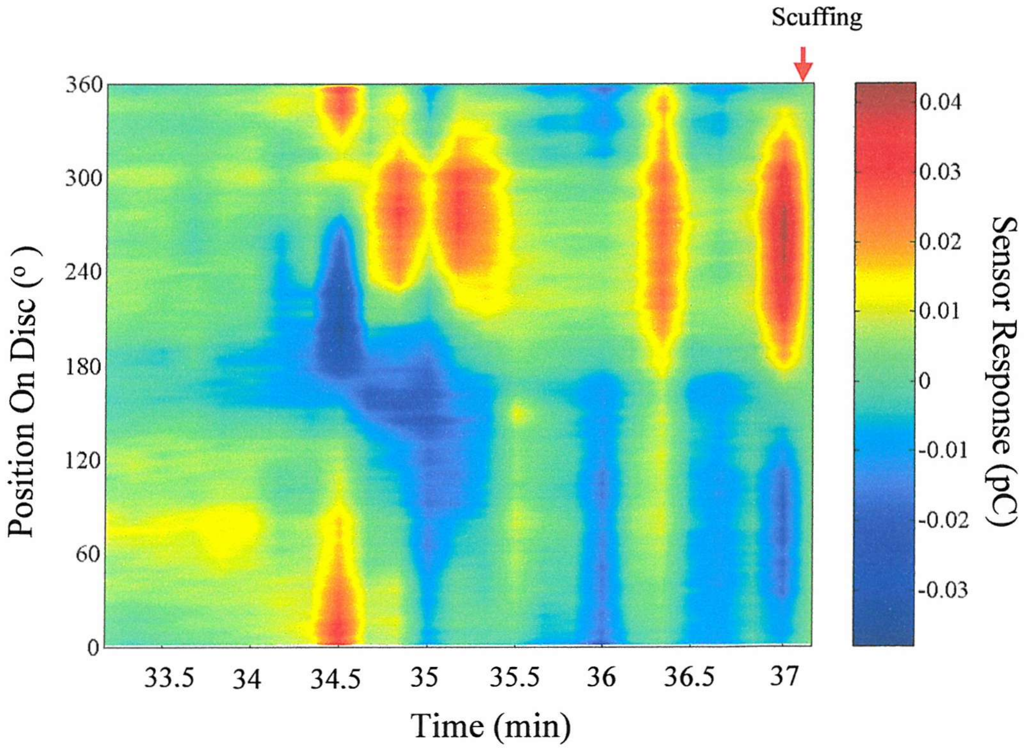

Figure 4.12 *Close-up of the region from the dotted onwards in Figure 4.11*

Figure 4.13 shows the plot of two signal averages at the 20th minute (background) and at the 38th minute (before scuffing). Figure 4.14 shows the difference between these two averages. Features are identified as a wide peak and trough at 80° and 260°, respectively. As in the case of the mineral base oil test, they are believed to be the result of localised surface charge generation.

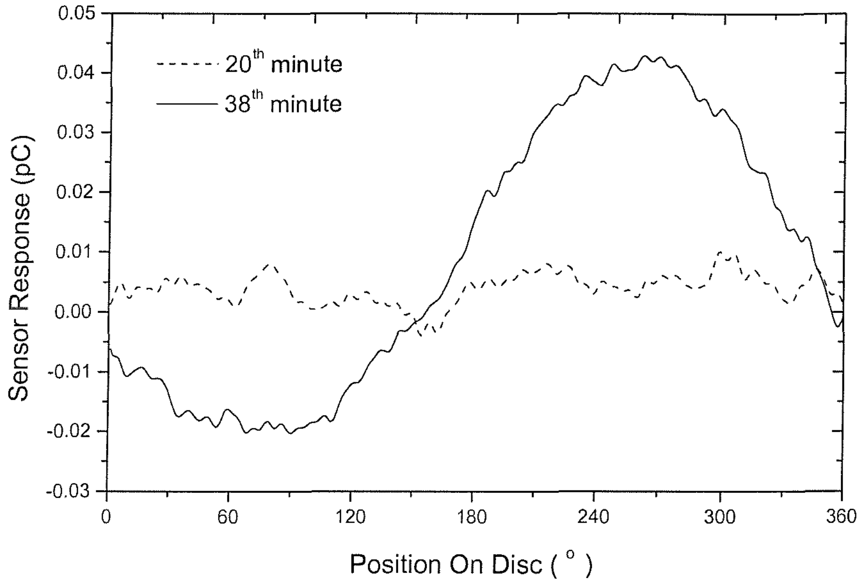

Figure 4.13 Signal averages at 20th and 38th minute for the fully formulated synthetic oil scuff test. Average at 20th minute is taken as a baseline average.

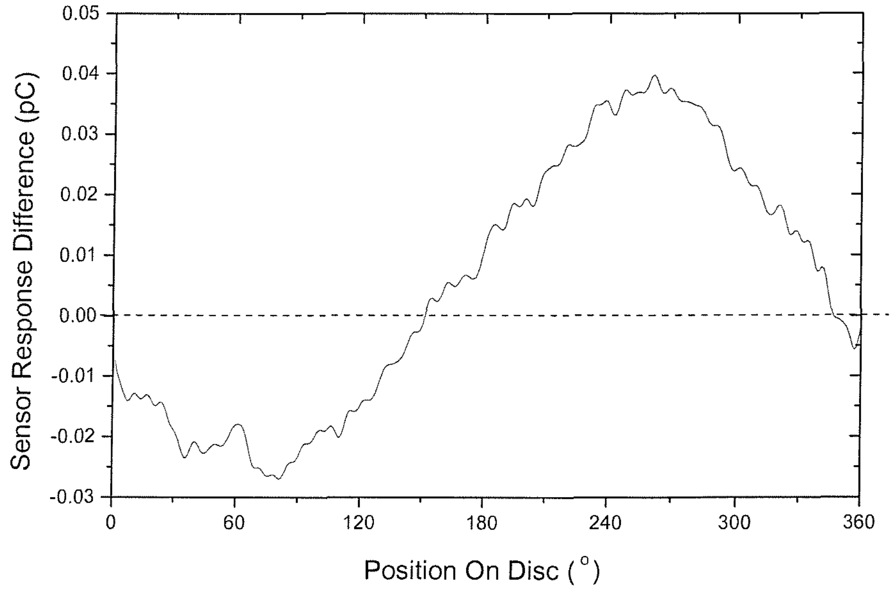

Figure 4.14 The difference between signal averages at 38th and 20th minute for the fully formulated synthetic oil scuff test.

Figure 4.15 shows the plot of coefficient of friction, volume loss and charge against time. During the running-in period, it can be seen that the coefficient of friction decreases from a value of 0.12 to 0.05. This value remained almost constant, with additions of load resulting in a sudden increase followed by a slow drift to the baseline level. During the running-in period, rough asperities are present, producing higher friction. These asperities are then worn to produce a smooth surface and consequently a reduction in the coefficient of friction. Just after the addition of load at the 34th minute, the friction increases steadily until scuffing. The physical changes to the wear surface prior to second transition scuffing caused changes to the roughness on the wear surface causing friction to increase producing increases in the charging activities. These physical changes are thought to produce more nascent surfaces on the disc and hence the increase in CPD effects which consequently causes increase in charging activities.

During the running-in period the volume loss can be seen to increase abruptly before decreasing to almost zero. This is followed by a steady increase in volume loss until a constant level is reached which persisted until the end of the test. The higher rate of volume loss during running-in is to be expected as a result of the rapid removal of rough asperities. The drop in the volume loss can be explained by considering frictional heating of the pin and the disc. The increase in contact temperature during the running-in period causes the pin and disc to expand causing errors in the LVDT measurements and as a result, the volume loss calculation. After the temperature stabilises, the normal level of the volume loss is established. From repeated tests, the bulk temperature increase measured using an infrared temperature probe, around the contact area during the running-in period, was found to be approximately 20 °C. Thus, for a 6 mm bearing steel ball diameter encased in a 18 mm brass holder the thermal expansion can be estimated using;

$$\text{Total Expansion} = L\alpha_t \Delta T \qquad 4.3$$

Where L = original length (6 mm for steel, 18 mm for brass holder), α_t = coefficient of thermal expansion (20 μm $^{\circ}C^{-1}$ for brass and 14 μm $^{\circ}C^{-1}$ for steel) and ΔT = temperature change.

Calculations indicate that a 20 °C temperature rise will produce a thermal expansion of 8.8 μm. This is equivalent to volume 'gain' of 0.7×10^{-12} m^3, comparable to the volume 'gain' of 1×10^{-12} m^3 deduced from Figure 4.15.

There were significant charging activities during the running-in period, which then decreased to a baseline level. Then at the 34th minute, there was a sudden increase in the charging activities. This coincides with the sudden increase in the coefficient of friction. The high level of charge activities persists until scuffing occurs.

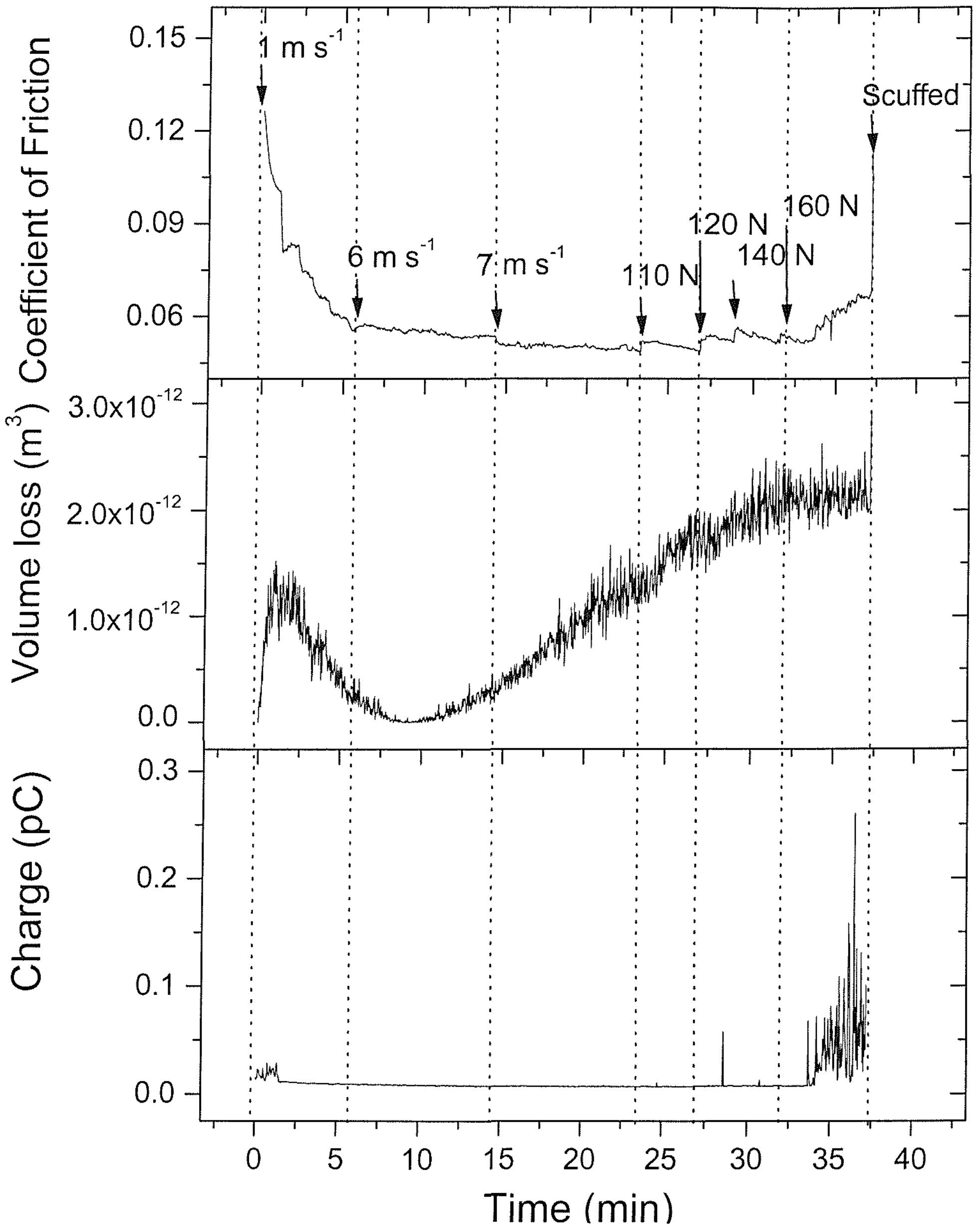

Figure 4.15 Plots of friction, volume loss and charge against time for the fully formulated synthetic oil scuffing test.

4.3.3 Corroborative Analysis

Figure 4.16 shows the colour map of the repeated mineral base oil test, which was stopped at the 63rd minute. At this point several charge features can be seen to be developing which can be related to the onset of scuffing.

Figure 4.17 shows a similar plot for the synthetic oil, which was stopped at the 37th minute. At this point, positive features can be seen to increase in magnitude between position 30° and 150°. Furthermore, a negative charge feature started to develop on position 250° at about 11 minute into the test. The close-up (Figure 4.18) of the region marked by the dotted lines in Figure 4.17 clearly shows that the negative feature is dynamic (increasing angular position) in nature and can be seen to move on the disc with the progression of time, before staying permanently on position 360°/0°. The dynamic charge behaviour is further demonstrated by the signal average line plots in Figure 4.19, taken at intervals of 20 seconds. The negative feature is thought to be caused by a single (or a cluster of) negatively charged debris which was moving on the wear track due to repeated entrainment into the contact, before being centrifuged out of the wear track.

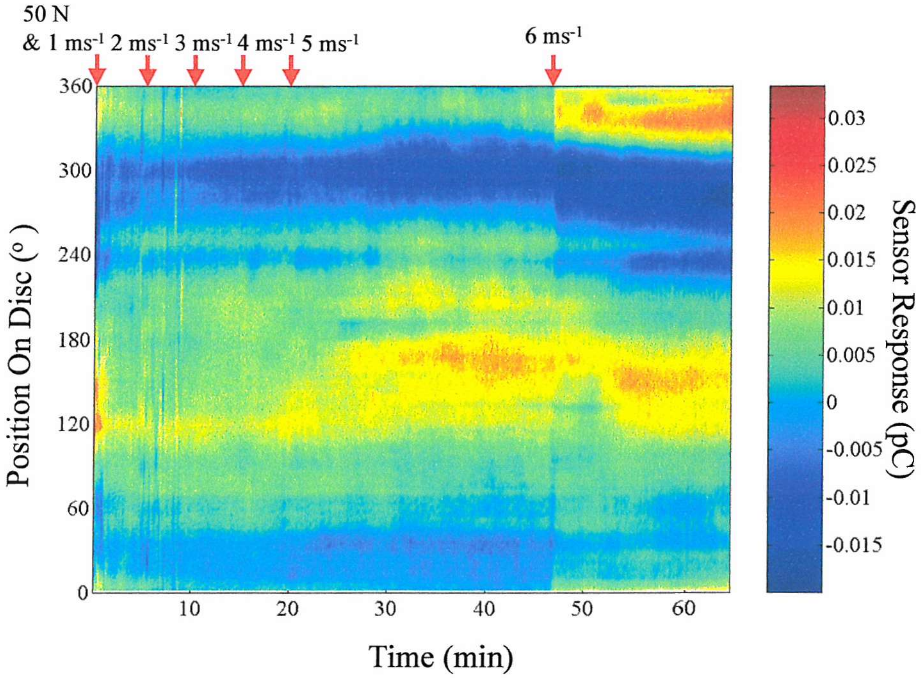

Figure 4.16 Colour map of electrostatic signal from a repeated B.S. 534A99 disc scuffing test lubricated with mineral base oil. Load = 50 N.

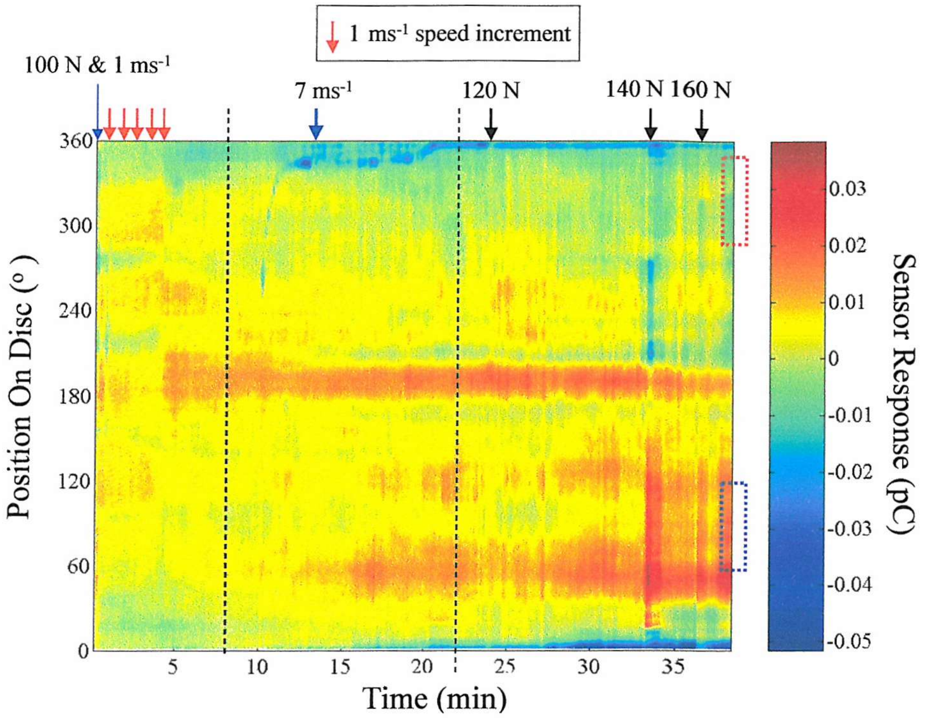

Figure 4.17 *Colour map of electrostatic signal from a repeat B.S. 534A99 disc scuffing test lubricated with fully formulated synthetic oil.*

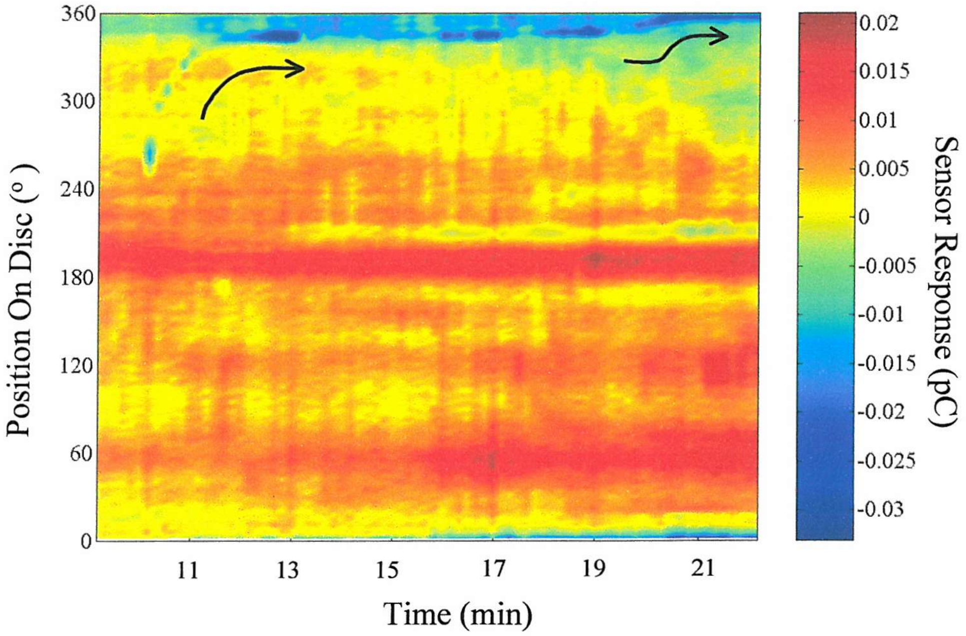

Figure 4.18 *Close-up of the region marked by dotted line on the colour map in showing a dynamic negative charge feature.*

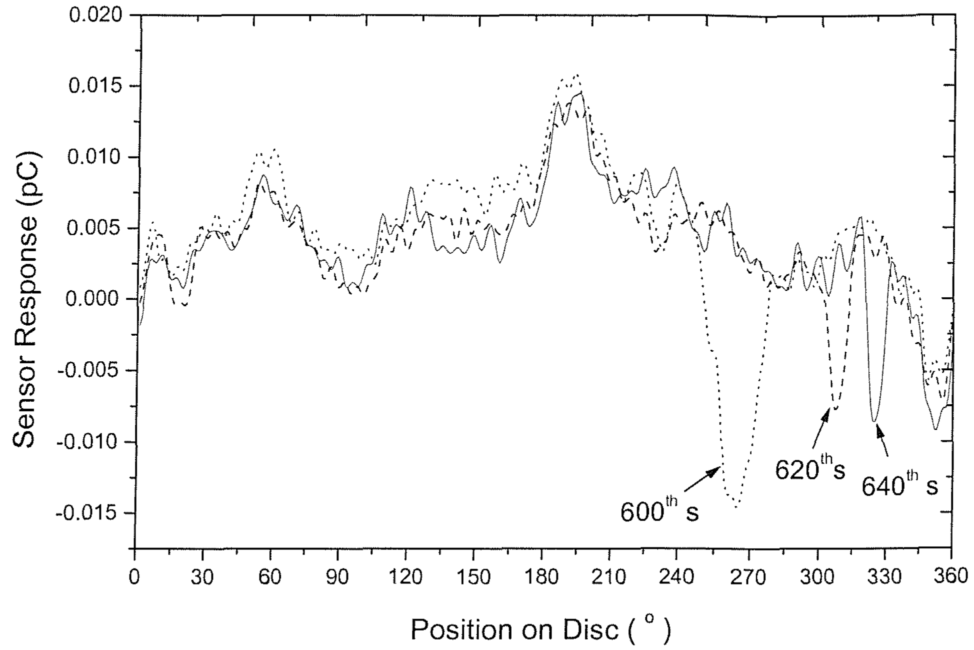

Figure 4.19 *Signal averages at the 600^{th}, 620^{th} and 640^{th} second of the repeated fully formulated synthetic oil test showing a dynamic negative feature.*

Scanning Electron Micrographs (SEM) of worn surfaces

SEM micrographs in Figure 4.20 show classical features associated with lubricated sliding wear, i.e., parallel shallow grooves and striations, as well as signs of delamination on the worn disc surface. There are also signs of two-body abrasion, possibly caused by debris entrainment or ploughing effect from hardened asperities on the pin wear surface. Figure 4.21 shows optical microscopy images of an etched disc surface from the fully formulated synthetic oil test. The images were taken from the region marked by the blue rectangle in Figure 4.17, the region that exhibited the presence of positive charge features (60^0 – 120^0). The images show the presence of white silvery areas on the surface. These surfaces are more resistant to etching compared to the rest of the bulk material. This is a confirmation of the presence of white layer on the disc wear surface, formed by first transition scuffing. This consequently results in contact potential difference (CPD) effects of discrete surface charge on the wear surface.

Inspection of the etched disc wear surface from the mineral base oil under optical microscope did not reveal the presence of a white layer. Figure 4.22 shows the optical microscopy images of an etched wear surface taken from the region of low charge marked by the red rectangle (300^0 – 350^0) in Figure 4.17. The white spots that can be seen on the surface are carbides within the steel. The signal average plot shown in Figure 4.23 indicates that no new charge features have formed relative to the background level (30th min). The difference between the two plots could be due to the increase in sliding speed.

Several tests were carried out to investigate the repeatability of the charge features observed for both lubricants and it was found to be poor. Each test will have its own unique charging behaviour but the majority of the repeat tests show the presence of precursor signals. These precursor signals manifest themselves in different magnitudes, positions and also the durations before catastrophic failure.

The reason for the momentary disappearance of the high magnitude charge features prior to failure, observed in Figures 4.7 and 4.12, can be explained by the delamination of the white layers. The brittle nature of white layers and evidence of delamination (see Table 2.2) found during inspections of worn surfaces using SEM verified this. After new white layers form over the delaminated region, the signal reappears and this was seen to lead to catastrophic contact failure.

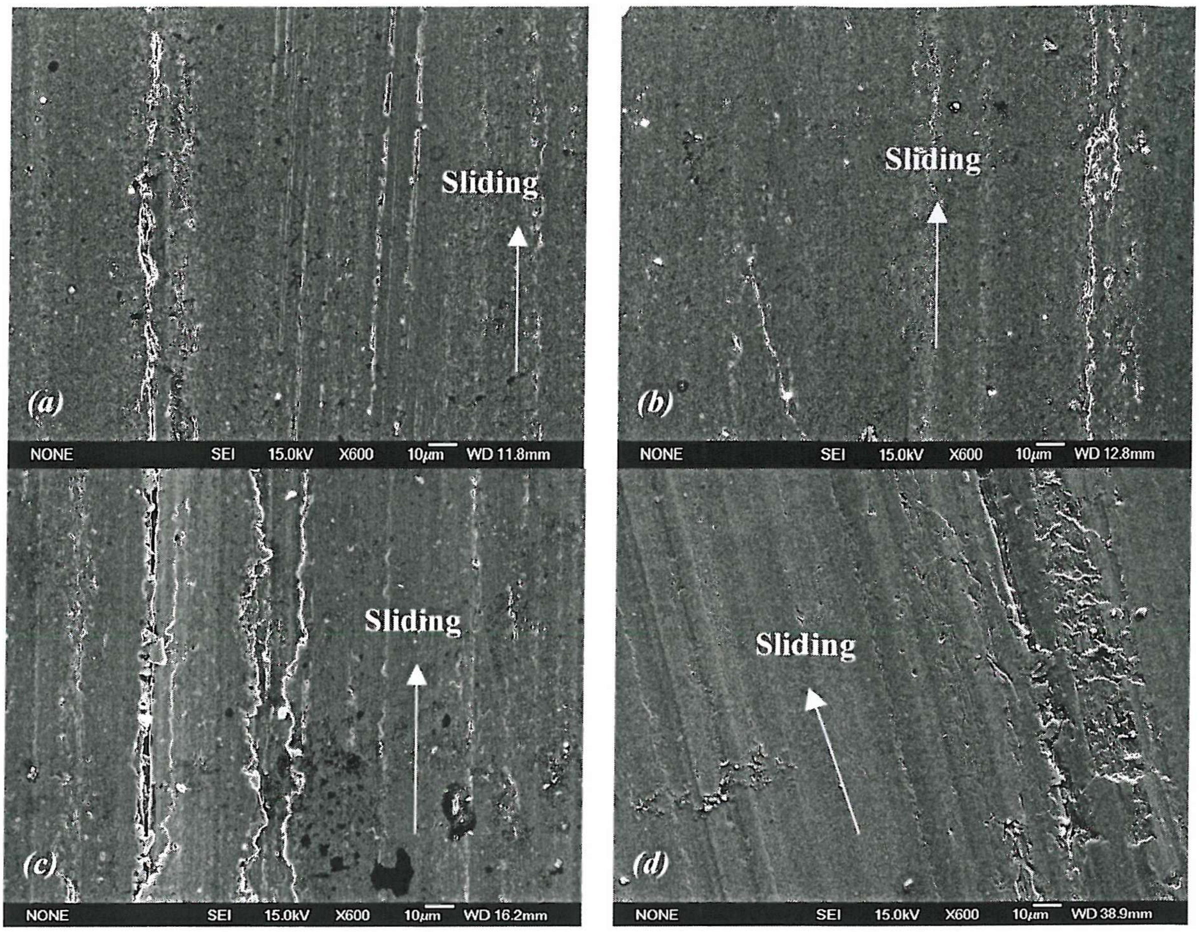

Figure 4.20 Micrographs of disc wear surface from the mineral base oil (a)-(b) and fully formulated synthetic oil test (c)-(d) showing relatively smooth surface with striations, typical of sliding wear. Two-body abrasion scars can also be seen.

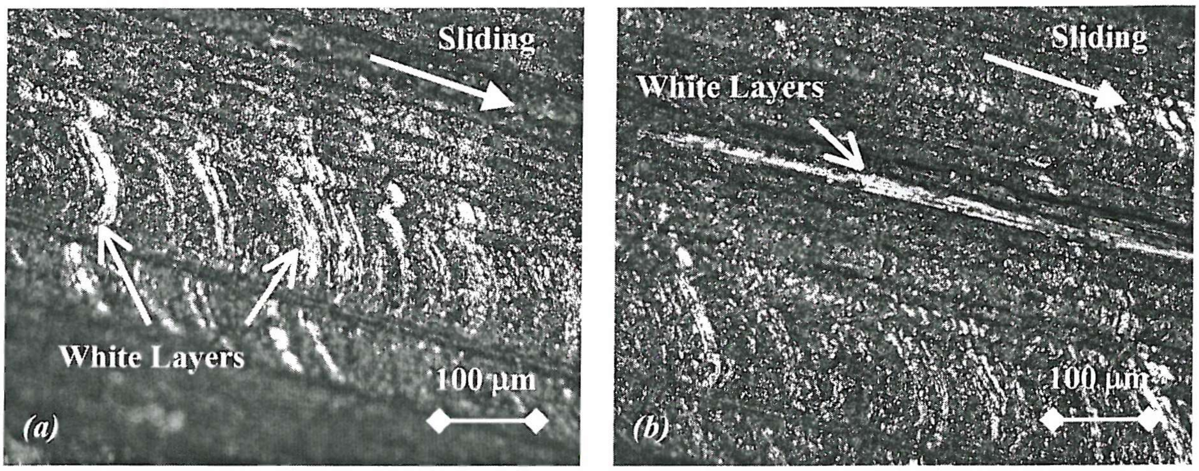

Figure 4.21 (a) – (b) Optical images of etched wear surface of the disc from the fully formulated synthetic oil test in the region marked by the blue square (60^o – 120^o) on Figure 4.17 showing white layers.

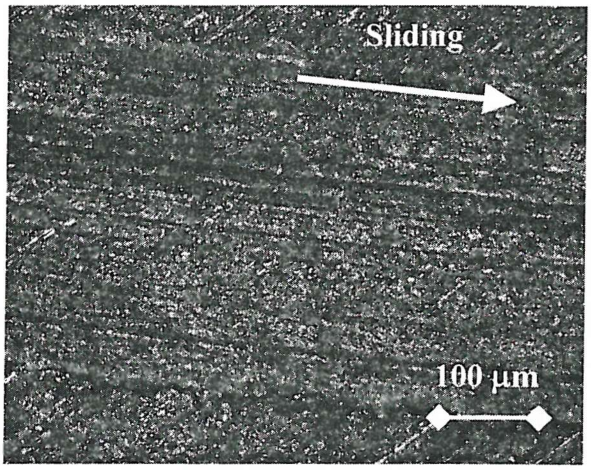

Figure 4.22 Optical image of the etched wear surface of the disc from the fully formulated synthetic oil test in the region marked by the red square (300° – 350°) on Figure 4.17. No white layers.

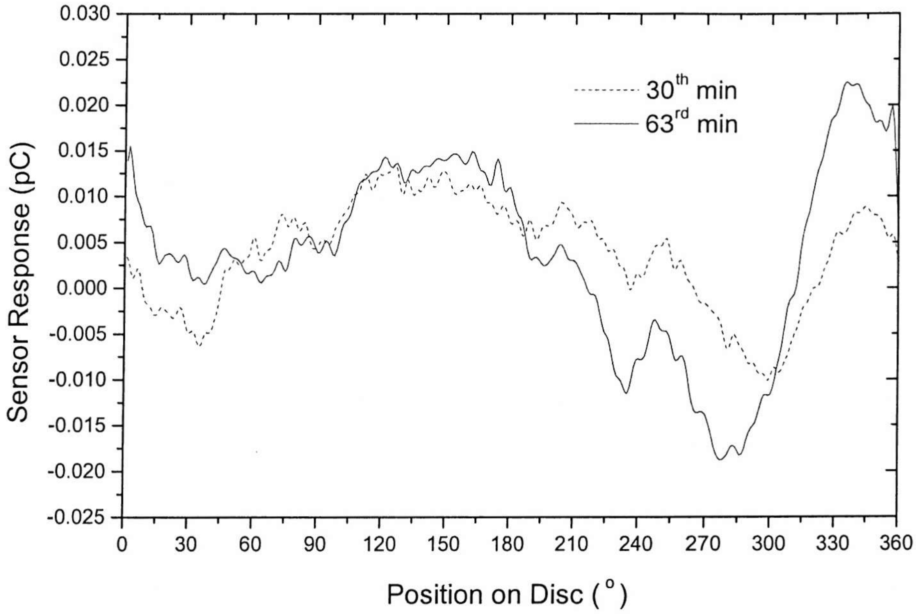

Figure 4.23 Signal average plots of the baseline charge level (30th minute) and charge level just before the test was stopped (63rd minute) for the base oil test.

Surface profilometry[Ψ]

Figure 4.24 shows the surface profilometry of the pin and disc of the mineral base oil test, indicating a wear track depth of approximately 5 µm. Surface profilometry was performed

---

[Ψ] All surface profilometries presented in this thesis were plotted from raw data using Matlab scripts courtesy of Mr. K.S. Tan.

in the location of charge features but they were found to be very similar to other parts of the wear surface. Figure 4.25 shows the pin and disc wear surfaces profilometry for the fully formulated synthetic oil indicating that the maximum depth of the disc wear scar was approximately 12 μm.

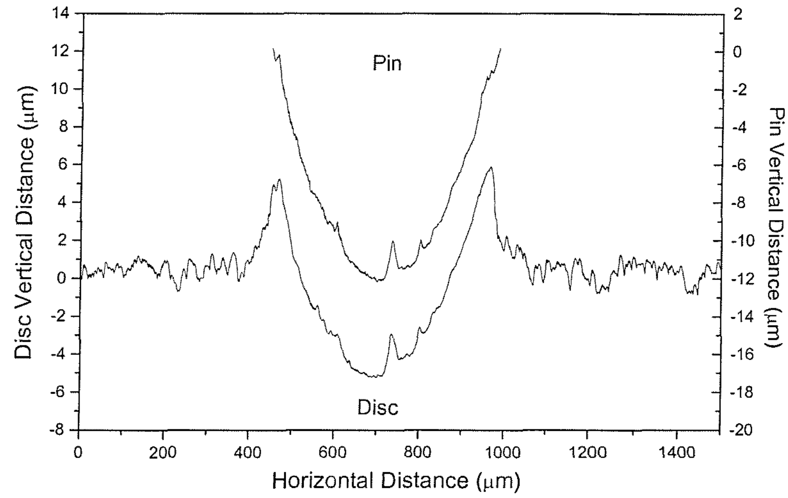

Figure 4.24 *Surface profilometry of the pin and disc wear surface of the mineral base oil scuffing test.*

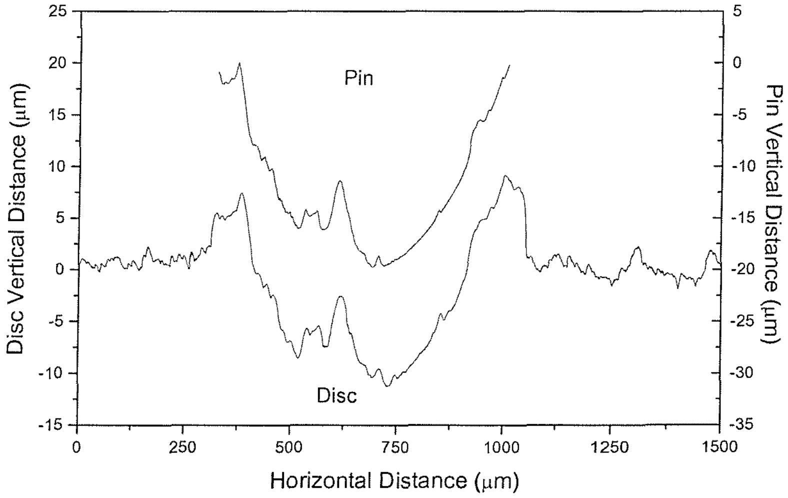

Figure 4.25 *Surface profilometry of the pin and disc wear surface of the fully formulated synthetic oil scuffing test.*

Wear debris analysis

The dynamic negative charge features seen in Figures 4.17 and 4.18 were due to the presence of wear debris. Figures 4.26 and 4.27 show optical images of the disc from the mineral base and fully formulated synthetic oil tests, respectively. Debris is radially dispersed outward from the centre of the disc forming 'spokes' on the discs due to centrifugal force. The debris paths are not perpendicular to the tangent of the disk circumference but forms a slight spiral motion as illustrated by Figure 4.28. It was also observed that fully formulated synthetic oil produced significantly larger amounts of debris compared to mineral base oil test.

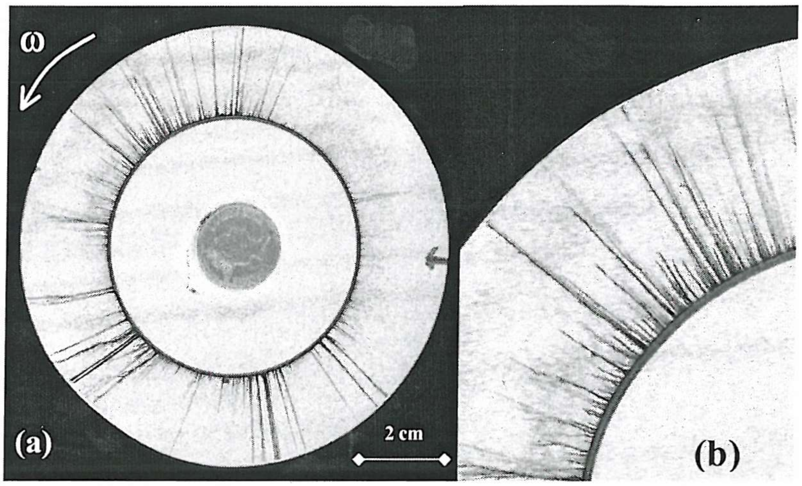

Figure 4.26 (a) Outward radial dispersion of wear debris (dark regions) on the disc from the mineral base oil scuffing test. (b) Close-up of the debris spokes.

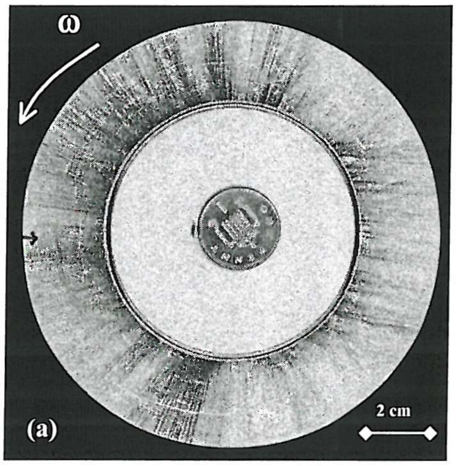

Figure 4.27 Outward radial dispersion of wear debris (dark regions) on the disc from the fully formulated synthetic oil test.

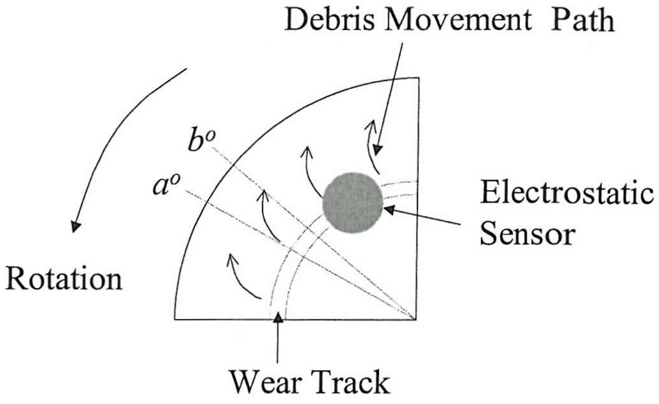

Figure 4.28 *Schematic showing wear debris being centrifuged out in a slight spiral motion path.*

Figures 4.29 and 4.30 show SEM micrographs of wear debris taken during the mineral base and synthetic oil tests, respectively. The debris is generally around 50 μm in length, 20 μm in width, or larger, and has a flake-like appearance. There are obvious striation marks on the surface of the debris indicating that they were produced by sliding wear. Comparisons with the literature (Table 2.3, Section 2.3.5) indicated that the wear debris collected was produced by severe sliding wear, which is consistent with the test conditions employed.

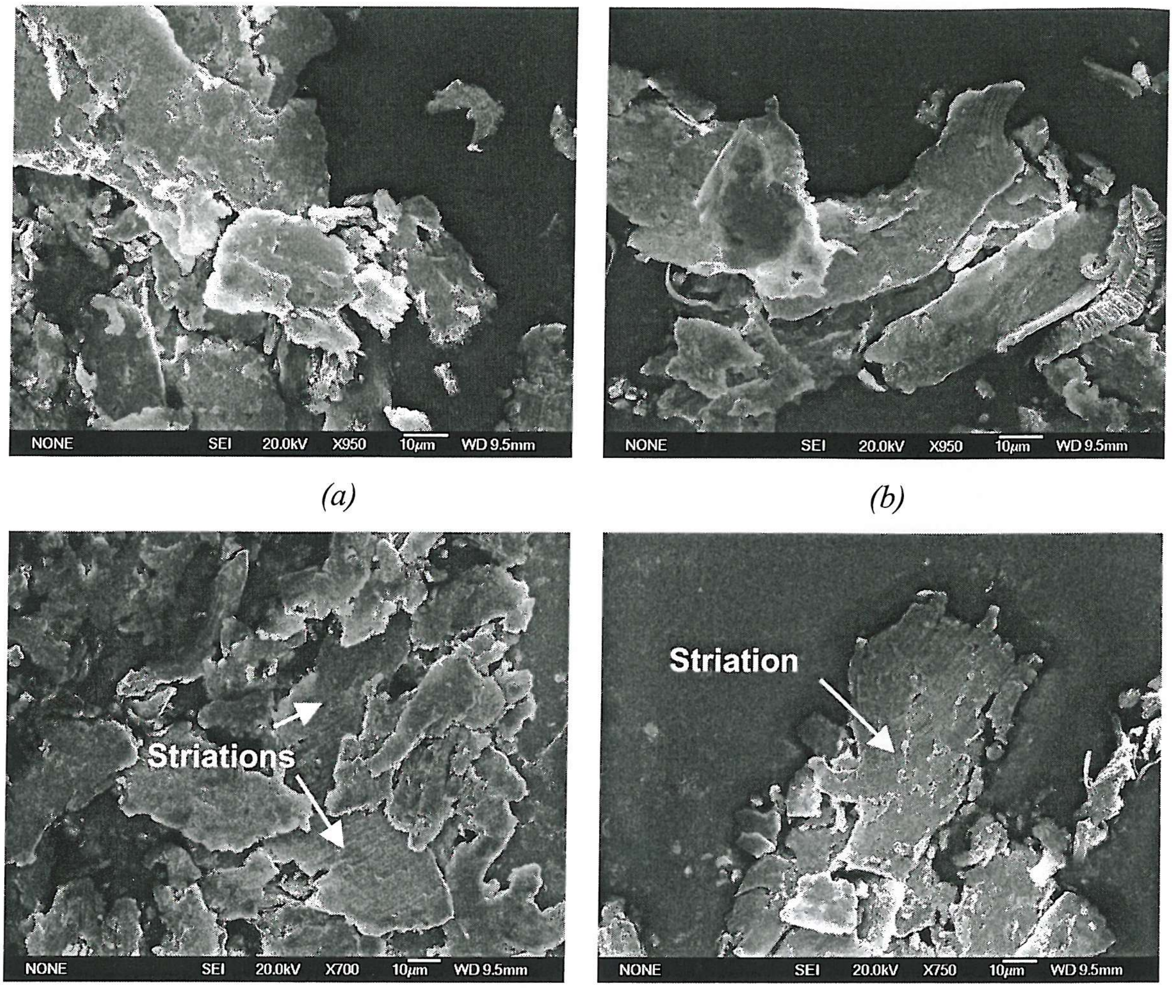

(a) *(b)*

(c) *(d)*

Figure 4.29 *Micrograph of debris taken after the repeated mineral base oil test.*

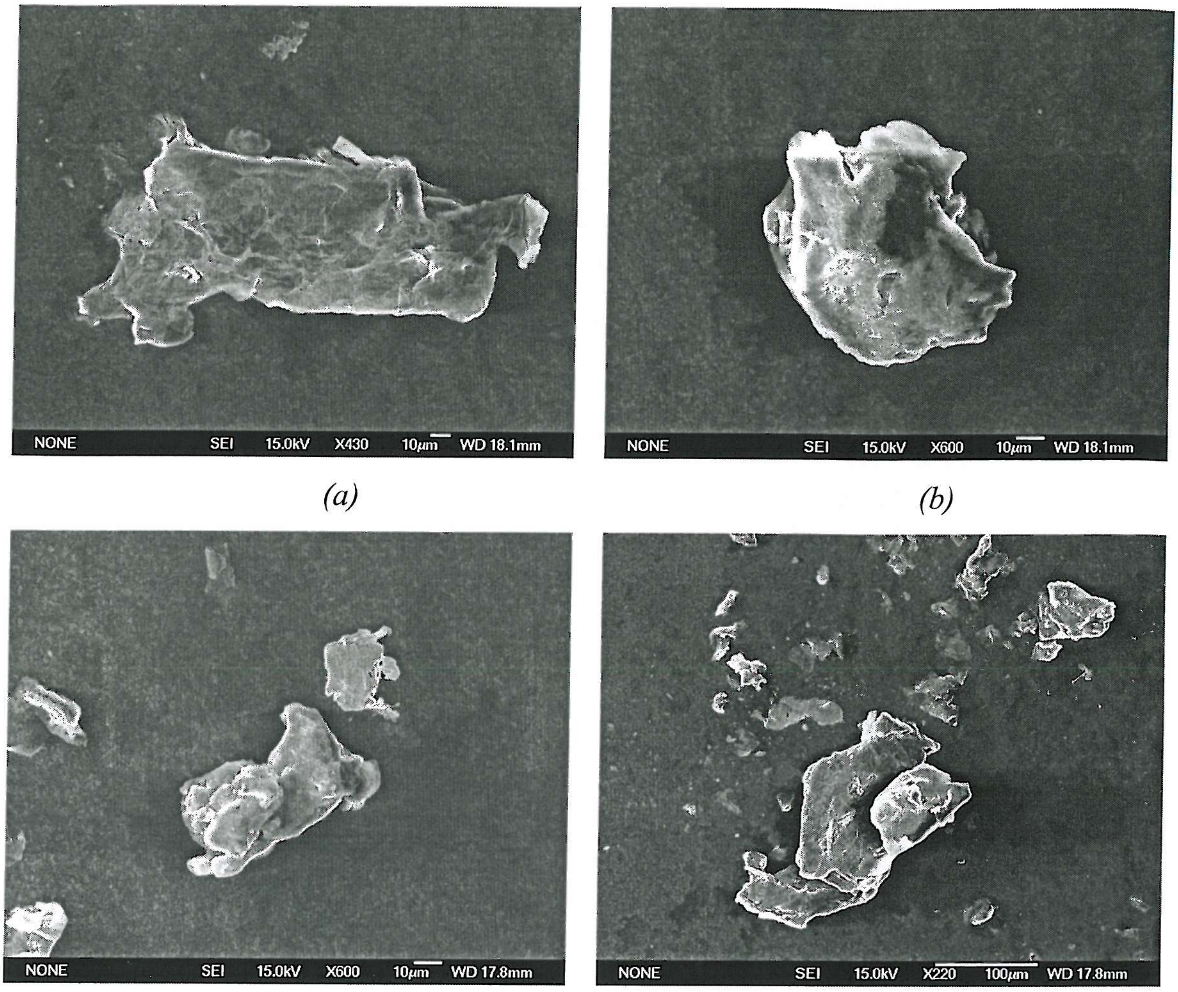

(a) *(b)*

(c) *(d)*

Figure 4.30 Micrograph of debris taken after the repeated fully formulated synthetic oil test.

Figure 4.31 shows a schematic summarising the possible sources of charge detected by the electrostatic sensor:

1. CPD effect – The formation of phase transformed regions (white layers) on the worn surface produces a discrete surface charge due to CPD effects. This is related directly to the deterioration of the contacting surfaces that eventually leads to catastrophic adhesive failure.
2. Centrifuged wear debris – Charge related to this type of source is dynamic in nature. On the colour map the charge features will move on the disc with the progression of time.
3. Entrained wear debris – This type of charge source is similar to the centrifuged wear debris on the colour plot. The total amount of angular displacement however is a lot larger than the one caused by the centrifuged debris.

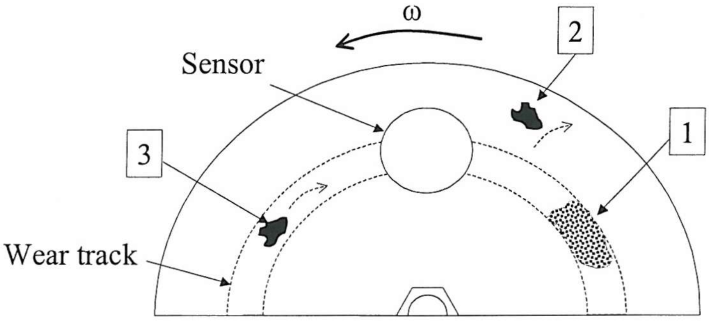

1
Discrete areas on the wear track that have different work function compared to the parent surface material. This is related to the formation of phase transformed region, i.e. white layers.

2
Wear debris being centrifuged out of the wear track. Its radial position on the disc surface changes over time due to the slight spiral path.

3
Wear debris on the wear track that moves position due to repeated entrainment into the Contact. The amount of movement is larger than that of centrifuged debris.

Figure 4.31 Schematic of possible sources of electrostatic charge detected by the electrostatic sensor.

4.4 CONCLUSIONS

Precursor charge signals were detected in both mineral base and fully formulated synthetic oil tests prior to catastrophic contact failure using an electrostatic sensing system. Dynamic charge features are related to the presence of debris and white layers (phase transformed regions). The formation of phase transformed regions results in a CPD effect and is related to precursor signals to scuffing. Charge features related to wear debris are dynamic in nature while charge features related to surface charge are static.

The predominant polarity of these precursor charge features was different for each lubricant, positive for the mineral oil test and both negative and positive for the fully formulated synthetic oil. This may reflect an influence of the oil chemistry and requires further investigation. The electrostatic sensing system was also found to be sensitive to small changes in wear rate detected by small fluctuations in friction, but not detected by measurements of volume loss (LVDT).

Surface profilometry of the disc worn surfaces found no relation between the surface profile and surface charge features.

5

SURFACE CHARGE EXPERIMENTS

5.1 INTRODUCTION

Chapter 4 has demonstrated that one of the sources of precursor charge signal is a CPD effect due to the presence of white layers. This chapter discusses the work carried out to calibrate the sensitivity of the wear site sensors (WSS) to CPD effects. Surface charge was simulated by placing inserts of different metals and an insulator into bearing steel discs rotated under the WSS in non-contact conditions. Further tests monitoring unlubricated sliding wear of bearing steel show the sensitivity of WSS to dynamic CPD effects.

5.2 CPD EFFECTS

5.2.1 Experimental Procedure

The experiments were carried out using a modified pin-on-disc test rig fitted with an electrostatic sensor, tachometer and an accurate speed controller, as shown in Figures 5.1 and 5.2 (during the non-contact testing, the pin was not deployed).

A CPD was created by drilling a 13 mm diameter hole in a B.S. 534A99 bearing steel disc to accommodate various inserts, as shown in Figure 5.1 (b). The inserts used were copper, aluminium, B.S. 534A99 bearing steel, B.S. 080A40 carbon steel and Delrin^{TM}. The discs were ground to ensure flatness. They were then cleaned with solvents to remove any oil film and surface contaminants before testing. A B.S. 534A99 blank disc was also tested as a control.

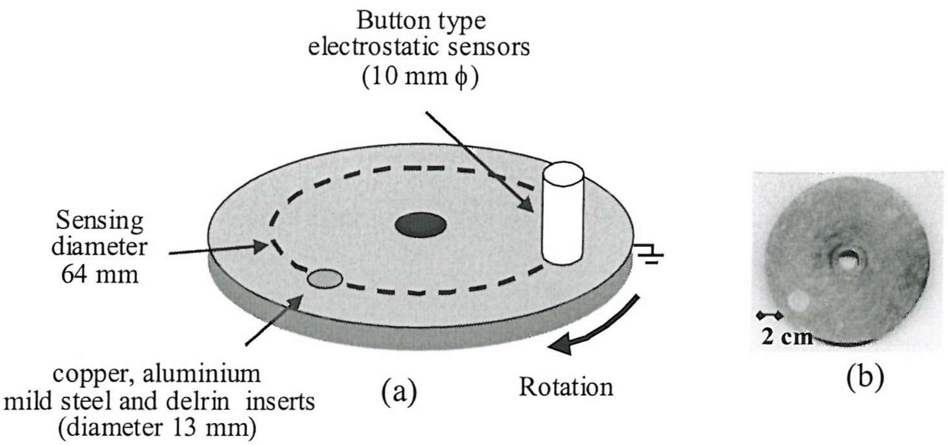

Figure 5.1 *Schematic diagram of the non-contact test set-up, (a) relative position of sensor (b) plan view of disc with an insert.*

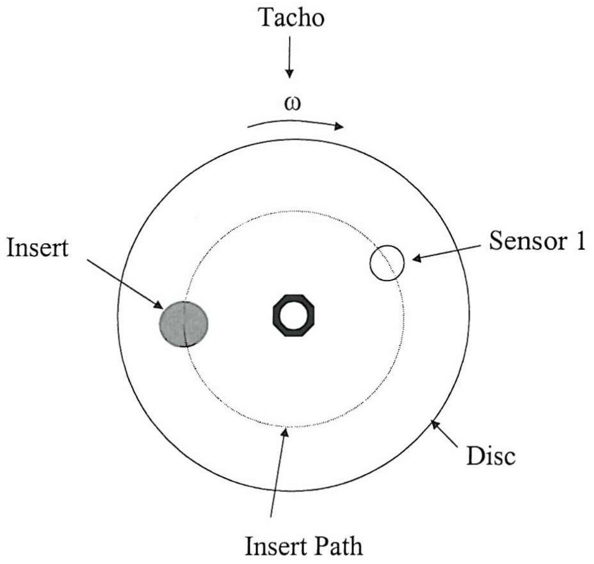

Figure 5.2 *Schematic plan view of non-contact test rig setup.*

Instrumentation

Figure 5.3 shows a schematic diagram of the pin-on-disc rig instrumentation. A WSS was positioned at 150° to the tachometer marker. The WSS had a sensing area of 7.85×10^{-5} m^2 (10 mm diameter) and was positioned approximately 0.5 mm above the disc surface. The sensor was connected to a signal conditioner unit, which was operated at 500 mV pC^{-1} gain with a nominal frequency response from 10 Hz to 10 kHz. The rest of the instrumentation setup is similar to the setup described in Section 4.2.1.

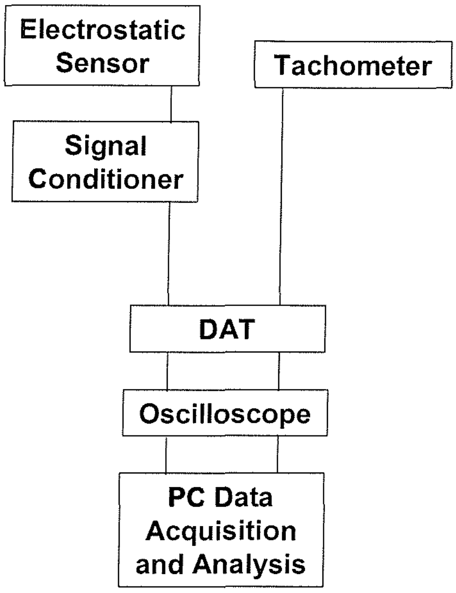

Figure 5.3 *Block diagram of the instrumentation for surface charge experiments.*

Data analysis

The electrostatic sensor and tachometer signals from the tests were analysed in the same way described in Section 4.2.2. For simplicity, results for the tests will be only presented using line plots.

5.2.2 Results and Discussion

Blank disc

Figure 5.4 shows the signal average from a blank B.S. 534A99 disc - no insert present. There is some amplitude variation in the electrostatic signal level during one revolution of the disc, which is loosely sinusoidal in shape. This characteristic is typical of a blank disc and is caused by the mounting arrangement of the disc which causes it to wobble. This creates a high (positive) and low (negative) spots on the disc surface, illustrated by Figure 5.5.

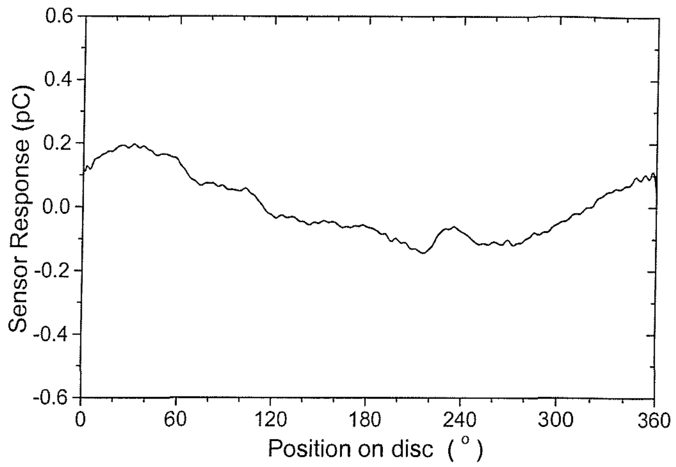

Figure 5.4 *A signal average from sensor 1 for a blank B.S. 534A99 disc.*

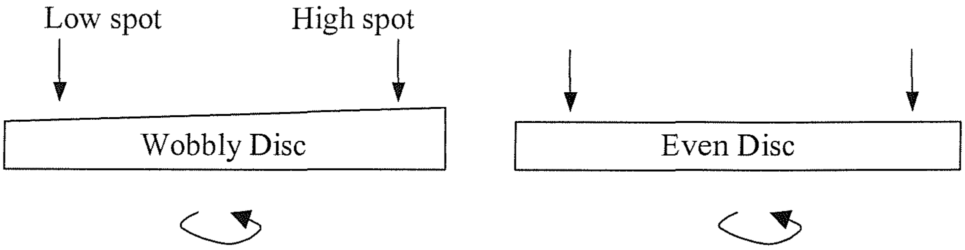

Figure 5.5 *Schematics explanation of disc wobble.*

Metal inserts

The result from a B.S. 534A99 insert in Figure 5.6 is indicating that the signal looks very similar to those seen in Figure 5.4 (for the blank disc), ignoring the difference in phase. This shows that the electrostatic sensor has no significant sensitivity to a uniform (metallic) material type. It also demonstrates that the method of fixing the insert does not influence the sensor signal, which is important when assessing the other results.

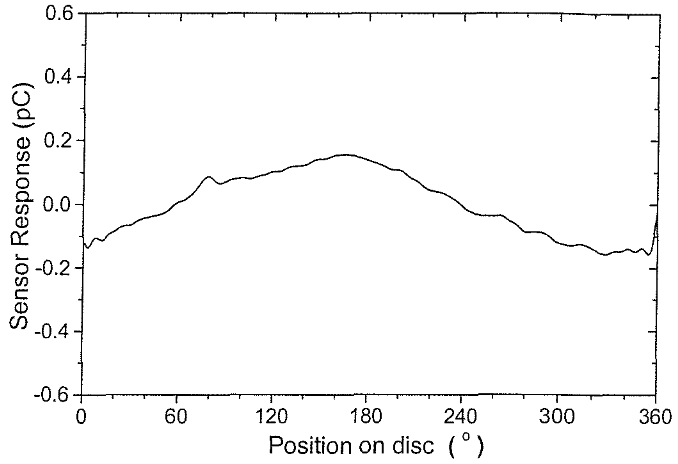

Figure 5.6 *A signal average for B.S. 534A99 disc with B.S. 534A99 steel insert.*

Figure 5.7 shows data from the sensor whilst monitoring a copper disc insert. The effect of the copper insert is to produce a negative signal relative to the rest of the disc material.

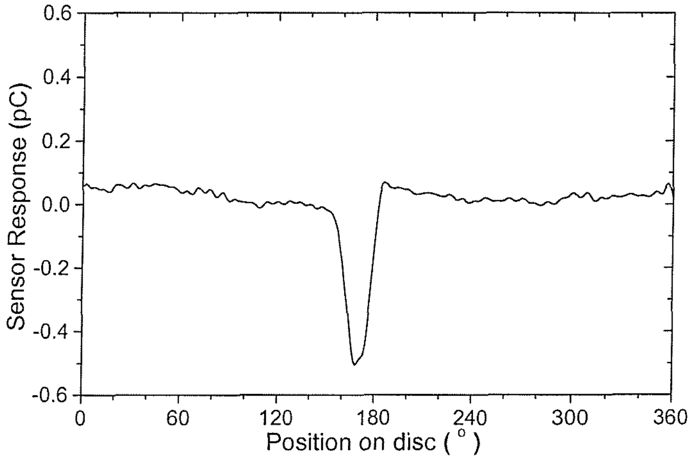

Figure 5.7 *Signal averages for B.S. 534A99 disc with copper insert.*

Figure 5.8 shows the output from the sensor during the Aluminium insert test indicating that the insert produces a positive signal relative to the rest of the disc material.

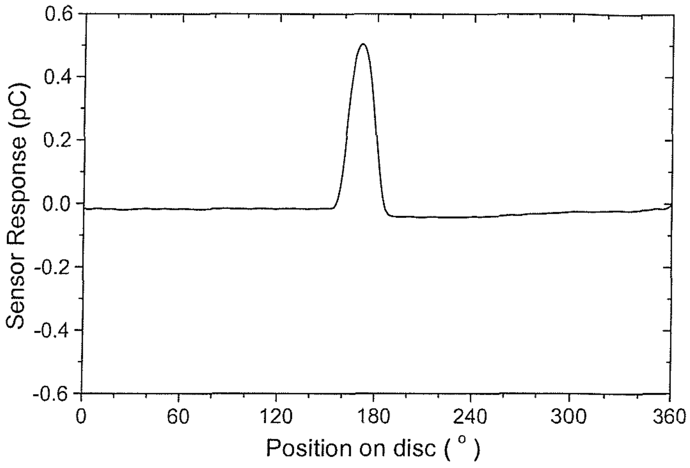

Figure 5.8 *A signal average for B.S. 534A99 disc with aluminium insert.*

The next test used a carbon steel (B.S. 080A40) disc insert, which was chosen to represent subtle changes to surface micro compositional (see Table 5.1) and micro structural features and hence the contact potential differences. It can be seen from Figure 5.9 that there is a negative signal produced relative to the rest of the disc material.

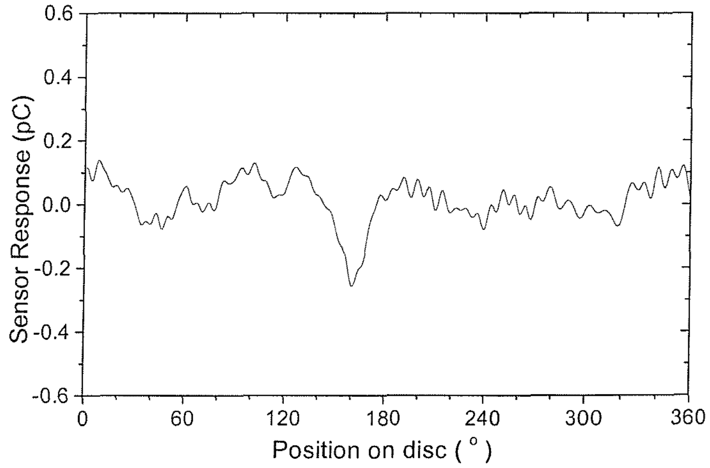

Figure 5.9 *A signal average for B.S. 534A99 disc with a carbon steel insert.*

The negative and positive responses shown by copper and aluminium respectively may be explained by inserting the appropriate values from Table 5.2 into Equation 3.19 (see Section 3.6.4). It is assumed that the work function of B.S. 534A99 steel may be approximated to that of iron. For copper and aluminium inserts the predicted polarity was negative and positive, respectively, consistent with the test results.

Metal	Composition (% wt)
B.S. 534A99	0.98-1.1 C, 0.23 Si, 0.35 Mn, 1.45 Cr, Remainder Fe
B.S. 080A40	0.37-0.44 C, 0 Si, 0.6-0.9 Mn, 0 Cr, Remainder Fe

Table 5.1 Composition of B.S. 534A99 and B.S. 080A40

Metal	ϕ_M (eV) (Photoelectric)
Zinc	3.63
Silver	4.26
Aluminium	4.28
Tin	4.28
Chromium	4.44
Tungsten	4.55
Iron	4.40
Copper	4.65
Gold	5.10
Nickel	5.15

Table 5.2 Work function values of various metals [84].

The carbon steel insert also produces a negative pulse. This means that there is a measurable difference between the work functions of carbon steel and B.S. 534A99 to set up a surface charge differential. The detection of the carbon steel inserts demonstrates the sensitivity of electrostatic sensing system to subtle changes in composition. This result would help to explain the observation of electrostatic charge 'precursor' signals in Chapter 4, where charge was generated and resided on a wear surface prior to significant failure, a phenomenon related directly to the formation of white layers.

Insulating (non-metallic) inserts

Two tests were conducted with a Delrin^{TM} insert. One test gave a negative signal with respect to the disc material (see Figure 5.10) whilst in the second test gave a positive signal with respect to the disc material (see Figure 5.11). This shows that Delrin^{TM} has a variable charge, thought to arise due to its insulative properties. It was found that the response by the Delrin^{TM} insert was greatly dependent on the pre-test preparation and handling (e.g. wiping it with solvent). Even if care was taken during handling, charge will still transfer onto it and since it is an insulator, it will remain there until it eventually decays. During the test it was observed that the amplitude of the sensor response decreased over time, indicating that charge leakage was taking place. This was not observed when tests with metal inserts were carried out, as they hold charge indefinitely. As anticipated, the mechanism of charge generation and retention associated with an insulator is different from that of metals.

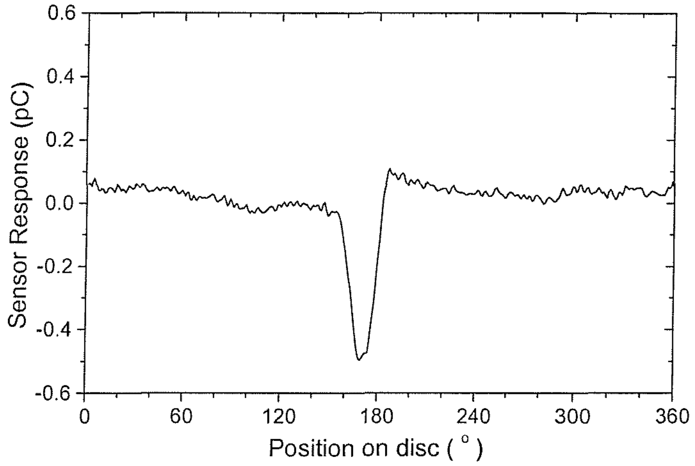

Figure 5.10 *A signal average for B.S. 534A99 disc with Delrin^{TM} insert (Test 1).*

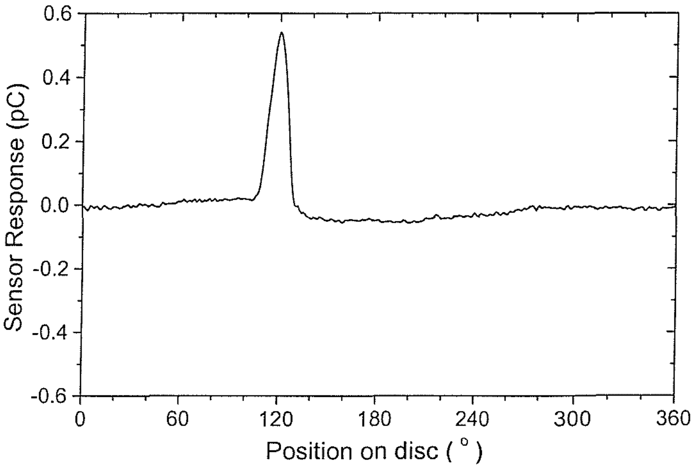

Figure 5.11 *A signal average for B.S. 534A99 disc with Delrin^{TM} insert (Test 2).*

5.3 SURFACE CHARGE DUE TO WEAR DYNAMICS

5.3.1 Introduction

Contact conditions for these tests were designed to produce mild oxidational wear based on the Lim and Ashby steel dry sliding wear map [85]. Before discussing the results of the tests, the proceeding sections will review some basics of oxidational wear and the steel dry sliding wear map.

5.3.2 Background

Oxidational wear

Some of the earliest studies on oxidational wear were conducted by Bowden and Tabor [86]. They found that the coefficient of friction of a sliding iron pair was less when both of the sliding surfaces have oxide layers compared to clean surfaces. Experiments with sliding clean surfaces were performed in a vacuum. It was also found that in tests conducted in atmospheric conditions, the electrical resistance between the contacting surfaces increased in the low friction events, confirming the presence of insulating oxide layers on the sliding surfaces. The influence of these oxide layers on sliding wear and friction was further studied by Wilson *et al* [87,88], who postulated that, at the start of the wear process, the initial oxide films are progressively destroyed and a period of severe wear ensues. The oxide film and wear debris accumulates to form thick layers on the contacting surfaces which enables mild wear to be attained. It has been established that, for an oxide film formed by unlubricated sliding surfaces and above a critical sliding velocity and film thickness, wear is mainly due to the delamination of this film [89]. Oxidation-delamination-reoxidation processes are also possible whereby the growth of oxides on an asperity tip, immediately after it has been delaminated by contact with the counter face, may be followed by removal of that oxide in the next contact. The fine particles of oxides removed in this way might agglomerate into larger transfer particles before finally being released as debris. At a sliding speed of around 1 ms^{-1} and low loads, the oxide film was found to be thin, patchy and brittle. However, at higher sliding speed (>10 ms^{-1}) and higher loads the films became thicker and continuous covering the whole sliding surface [90-92].

Steel dry sliding wear map

A dry sliding wear map for carbon steel pairings has been compiled by Lim and Ashby, see Figure 5.12 [85]. This was constructed from sliding wear data (volume loss) at each contact pressure and sliding velocity. Wear tests were calculated for different wear mechanisms. Areas on the map were identified such that within each, a different wear mechanism was dominant; i.e., wear mechanism that produced the major part of the wear. The field boundaries are lines along which two mechanisms give the same wear rate. The contours show the total wear rate and it is the sum of the contributions from all the mechanisms. The results used to construct the wear map were obtained from dry sliding test of a pin-on-disc test rig.

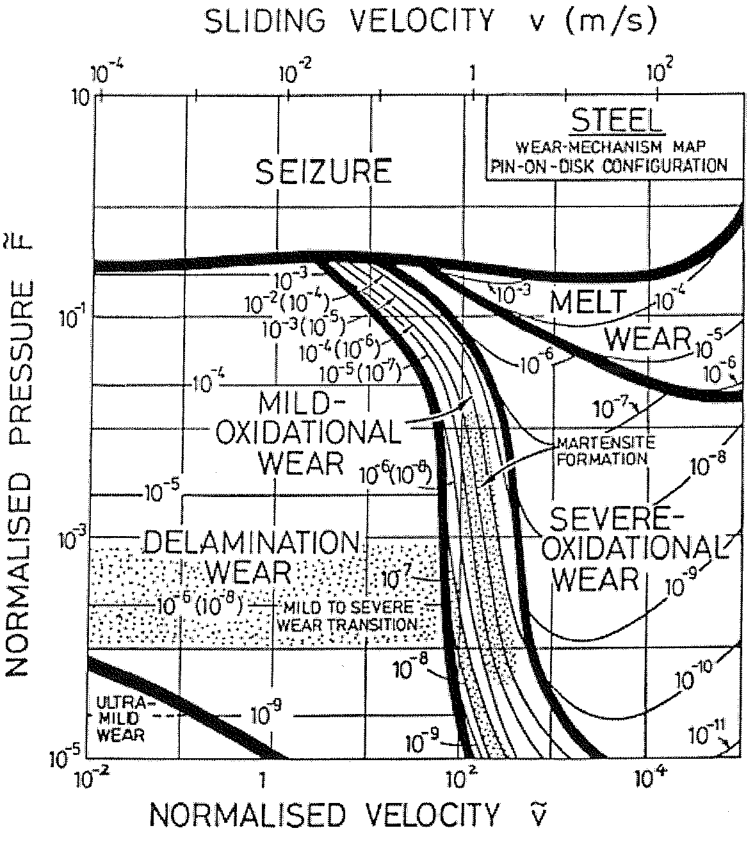

Figure 5.12 Wear mechanism map for low carbon steel sliding pairs based on physical modelling calibrated to experiments. The shaded region indicates transitions. Pin and disc materials are carbon steel. NB: Severe oxidational wear means high oxidational activity and not high (severe) wear rates.

5.3.3 Experimental Procedure

The unlubricated sliding wear experiments were carried out on the pin-on-disc test rig. Figure 5.13 shows the schematic diagram of the pin-on-disc setup. The pin has a 5 mm radius spherical end and was made of B.S.045M10 mild steel loaded against a B.S. 534A99 bearing steel ring mounted using adhesive on a bearing steel disc, as shown in Figure 5.14. The pin-on-disc rig is also fitted with a force transducer to monitor the friction and a linear vertical displacement transducer (LVDT) to monitor the vertical displacement of the pin, *h*.

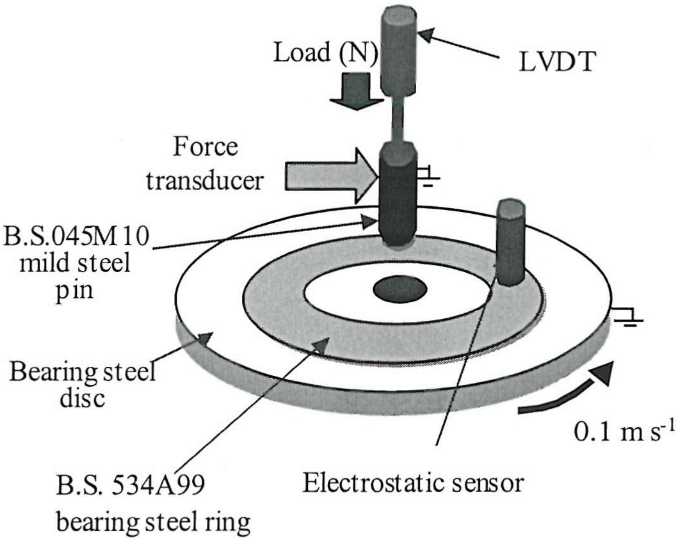

Figure 5.13 Schematic diagram of the test set-up and relative position of sensors.

Figure 5.14 Picture of ring mounted on a steel disc.

Table 5.3 summarises the test conditions used in the unlubricated sliding experiments. The contact load and sliding speed were constant throughout the test. At the end of the test, wear debris was collected and the test ring was then detached from the disc and cleaned for examination using optical and scanning electron microscopy. The mass loss of the pin and the ring were also measured. The test was repeated three times to ensure repeatability. The level of relative humidity was measured but not controlled and all tests were carried out at room temperature.

Pin	
Material	B.S.045M10 mild steel
Hardness (Vickers $_{100g\ load}$)	310
Effective Tip Radius (mm)	5
Surface finish	Ground
Roughness R_a (μm)	0.37
Ring	
Material	B.S. 534A99 bearing steel
Hardness (Vickers $_{100g\ load}$)	626
Surface finish	Ground
Roughness, R_a (μm)	0.2
Sliding Conditions	
Load (N)	10 N
Maximum Hertzian Contact (MPa)	1015
Sliding Speed (ms^{-1})	0.1
Sliding Distance (m)	1000
Test Duration (min)	167

Table 5.3 Summary of test conditions.

Instrumentation

Figure 5.15 shows a schematic representation of the instrumentation. It was similar to that described in Section 4.2.1 but instead of employing 10 mm diameter sensors, a 5 mm diameter sensor with sensing area of 1.96×10^{-5} m^2 was employed. The signal conditioner unit was operated at 1000 mV pC^{-1} gain.

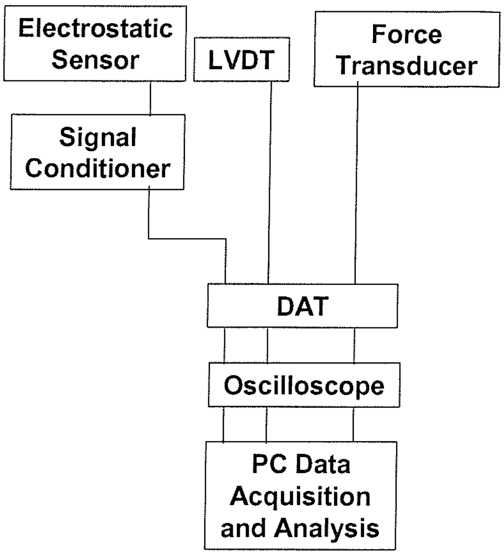

Figure 5.15 *Block diagram of instrumentation for unlubricated sliding wear test.*

Data analysis

The colour map plot was not used to analyse the results form these tests as the rotational speed of the disc was lower than the minimum rotational speed required for the signal averaging software to work.

The signals from the load cell and LVDT were sampled at 2000Hz and averages were produced every 4 seconds which were then stored as text files. The electrostatic charge signal was analysed post test by viewing raw data played back by the DAT recorder sampled at 360Hz. The volume loss of the pin, V_{loss}, was calculated using Equation 4.2 in Section 4.2.2. The specific wear rate was calculated using the equation below:

$$W = \frac{V_{loss}}{FS} \qquad 5.1$$

Where W = Specific wear rate ($m^3\,N^{-1}\,m^{-1}$), F = applied normal force (N) and S = Sliding distance (m).

To verify the accuracy of the volume loss calculated using the LVDT data, the total volume loss was also calculated from the pin mass loss, using the equation;

$$V_{total} = \frac{m_{pin}}{\rho_{steel}} \qquad 5.2$$

Where m_{pin} = mass loss of pin and ρ = bearing steel density.

5.3.4 Results and Discussions

Cumulative volume loss and coefficient of friction variation

The value of the pin total volume loss using the methods described in the previous section yielded different results. The value calculated using the LVDT readings for Test 2 was lower by almost an order of magnitude (5.84×10^{-10} m^3) than that calculated from the mass loss (1.9×10^{-9} m^3). This discrepancy can be explained by the thermal expansion of the pin and the ring. During the test, frictional heat is generated in the contact area and transferred to the pin (and the ring). Consequently, the pin expands causing a slight but significant increase in its height causing an error (reduction of vertical distance) in the LVDT method. The LVDT also records the reduction in the height of the pin due to wear, as well as the increasing depth of the ring wear track, inevitably introducing further error. Material transfer between the ring and the pin and the presence of oxide could also cause inaccuracies in the total volume loss value. However, the main objective of the experiment was to investigate the relationship between wear from a known mechanism and the corresponding electrostatic charging events hence, it is the wear trend and not the absolute value which is of primary importance.

Figures 5.16 to 5.18 compare the cumulative volume loss and coefficient of friction results from three identical tests. Several common trends can be identified. The volume loss plots (from the LVDT output) generally show that the rate of volume loss is relatively high in the early stage of the test but then gradually decreases. The coefficient of friction values oscillate between low and high states but the general trend is increasing in magnitude. The volume loss shows a good correlation with friction, i.e. any sudden increase or decrease in the coefficient of friction will be accompanied by a corresponding sudden increase or decrease in the volume loss.

Tests 1 and 2 exhibited similar behaviour and show two distinct regions. The initial region (running-in) has a high wear rate and high activity of friction fluctuations (high frequency). The second region is generally of lower wear rate with periods of high loss rates lasting for approximately 155 seconds per period.

In Test 3, significant fluctuations in friction and volume loss started to occur only in the last 1800 seconds of the test. The magnitude of the friction fluctuations and volume loss increment was also significantly lower than that of Tests 1 and 2. Nonetheless, the duration of high loss rate is similar to Tests 1 and 2. At the start of Test 3, the coefficient of friction was low but increases at a relatively high rate, then stayed almost constant until the onset of the friction rise and recovery events. Since results from all tests show common trends, for brevity, only results from the Test 2 will be presented from this point onward.

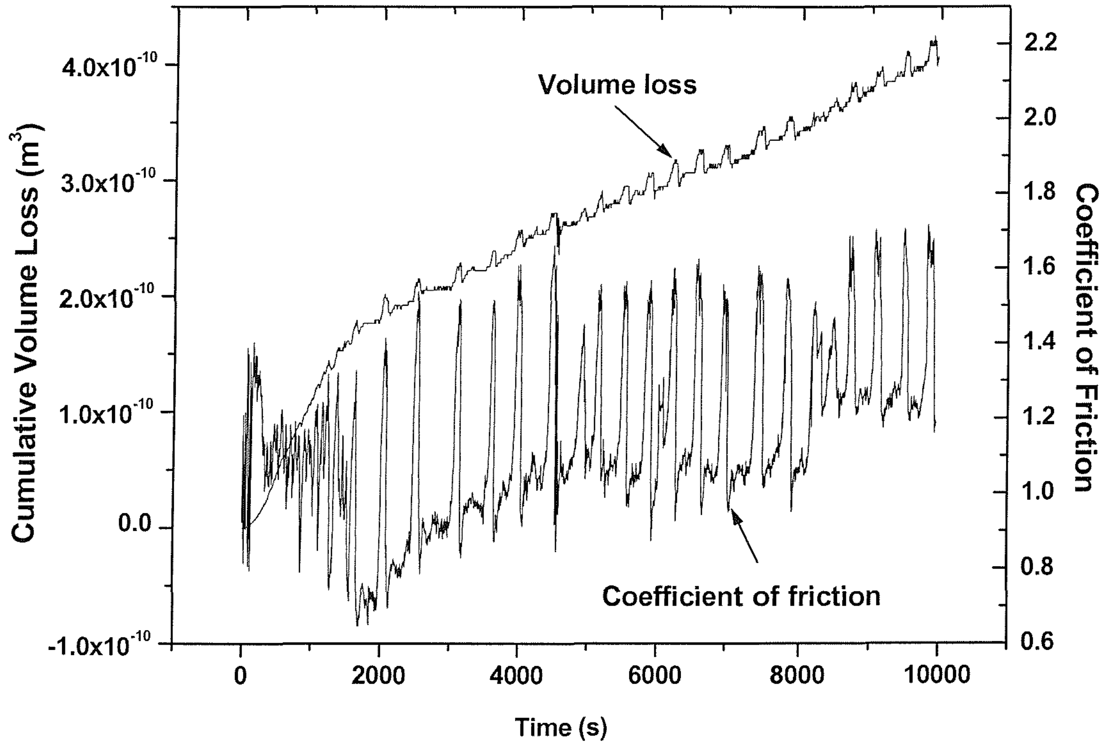

Figure 5.16 *Plot of volume loss and friction against time for Test 1, 0.1 ms^{-1} sliding speed, RH = 26%, load = 10 N (~1 GPa).*

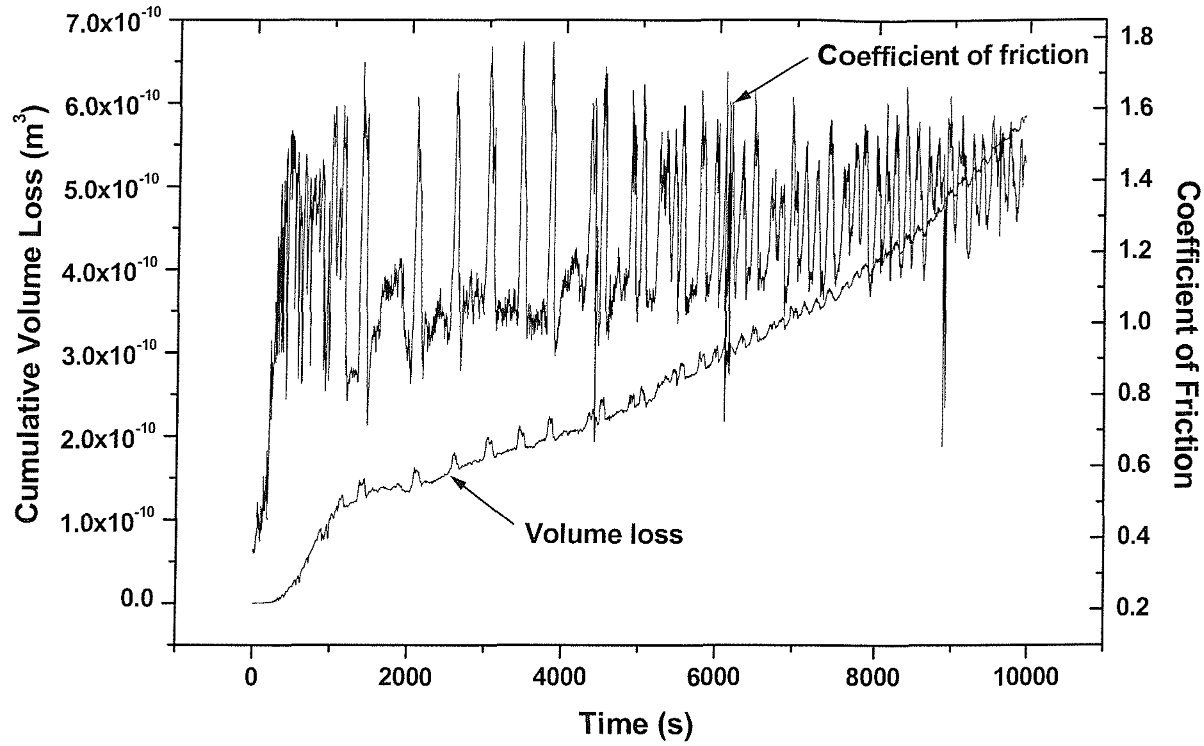

Figure 5.17 *Plot of volume loss and friction against time for Test 2, 0.1 ms^{-1} sliding speed, RH = 22.3%, load = 10 N (~1 GPa).*

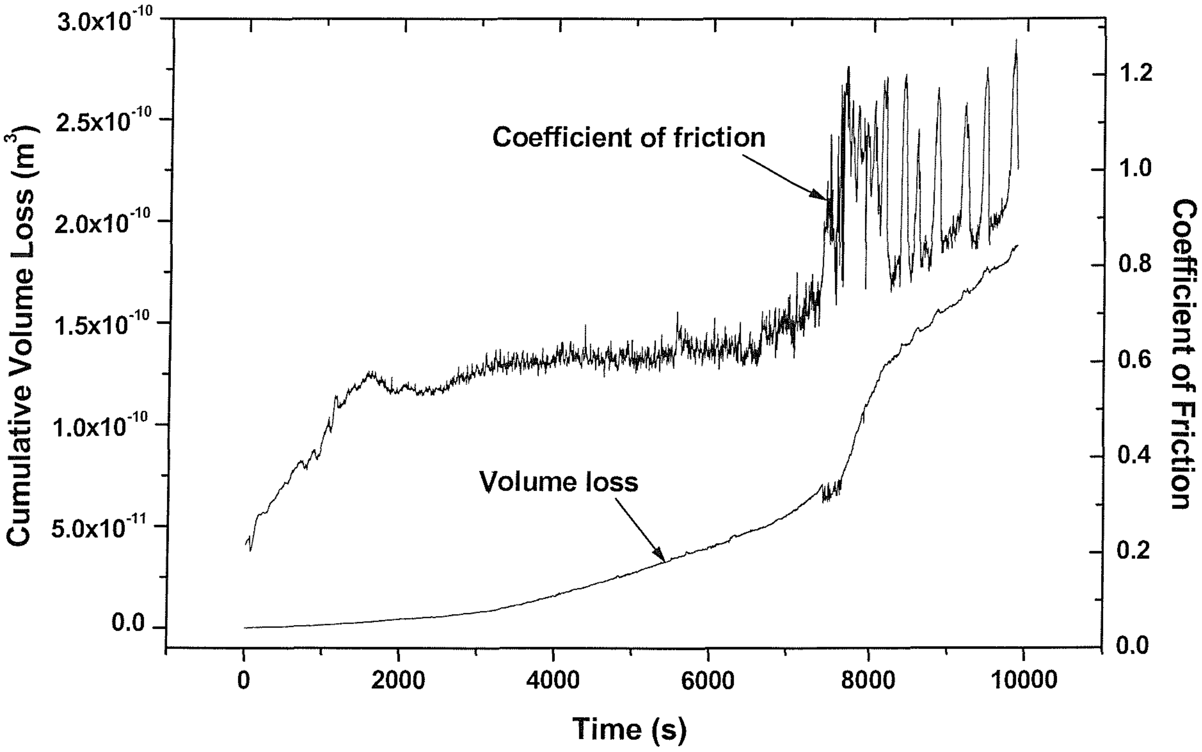

Figure 5.18 *Plot of volume loss and friction against time for Test 3, 0.1 ms^{-1} sliding speed, RH = 22.9%, load = 10 N (~1 GPa).*

Electrostatic charge detected and specific wear rate against time

Figure 5.19 shows the electrostatic charge detected and the specific wear rate against time. The plot can be divided into 4 regions: In Region 1, the electrostatic charge plot shows high levels of charging activity of a bipolar nature just after the test was started. These events lasted for approximately 240 seconds (240 revolutions). The specific wear rate in this region is low. In Region 2, the charge level decreased to a slightly lower level, approximately ± 0.2 pC and the specific wear rate was extremely high ($1\times10^{-13}m^3\ N^{-1}\ m^{-1}$). These events lasted for about 1200 seconds. Region 3 shows that the level of charge was lower and the specific wear rate was also decreasing. Figure 5.20 shows the close-up of this region. The electrostatic charge level in Region 3 was maintained as a background level throughout the remainder of the test. In this region however, there were also sudden events of increased bipolar charge. Each event lasted for about 155 seconds. In Region 4, the frequency of these events increased whilst the specific wear rate is almost constant. It was noted that these charge events correspond to the rise and recovery events in the specific wear rate plot.

From Figure 5.19 it can be seen that the specific wear rate increases rapidly in the first 1200 seconds until it reaches a peak. Then, the specific wear rate starts to decrease until it reaches a specific wear rate of about $5 \times 10^{-14}\ m^3\ N^{-1}\ m^{-1}$, approximately 4800 seconds into the test. Superimposing the initial test conditions of the present study onto the dry sliding wear map, compiled by Lim and Ashby [85], mild oxidative wear is predicted with wear rates of about $10^{-14}\ m^3\ N^{-1}\ m^{-1}$. This agrees well with Tests 1 to 3. After this point the specific wear rate stayed almost constant until the end of the test. As with the electrostatic charge plot, there were also sudden fluctuations which lasted about 155 seconds (see Figure 5.20), corresponding to the trends observed in the volume loss and the friction plots.

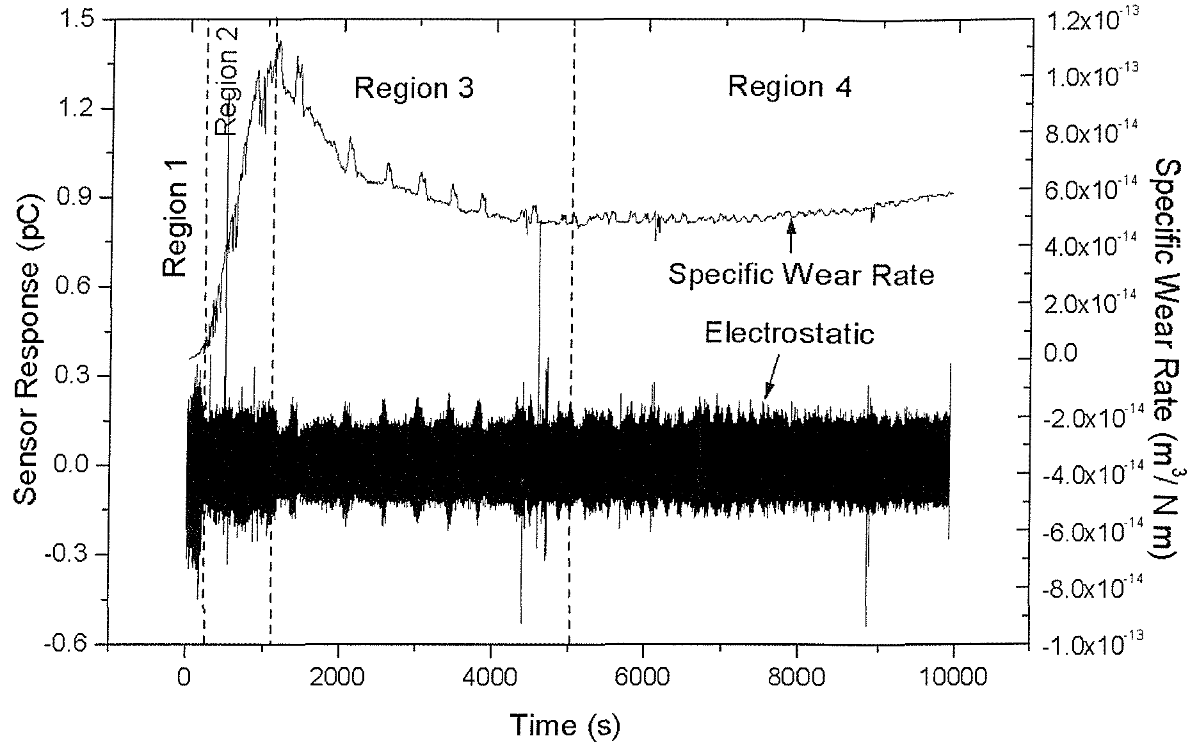

Figure 5.19 *The plot of electrostatic charge detected & specific wear rate against time for Test 2, 0.1 ms^{-1} sliding speed, RH = 22.3%, load = 10 N (~1 GPa), showing 4 distinct regions of events.*

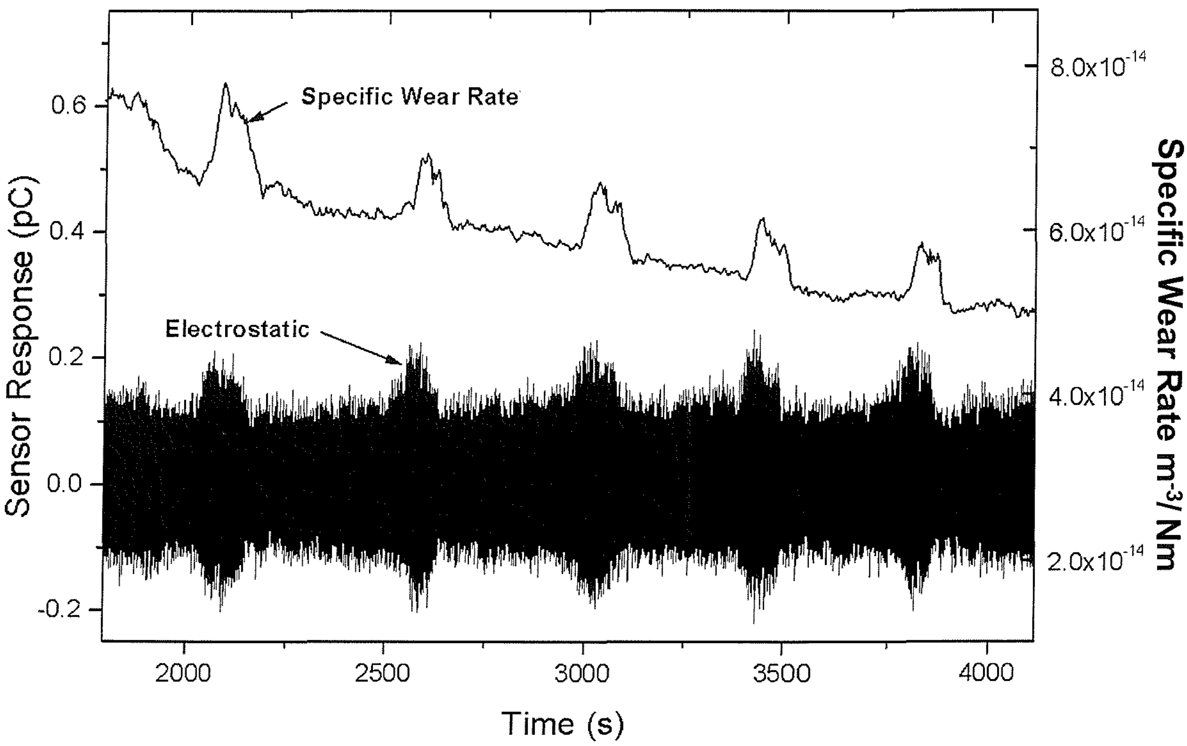

Figure 5.20 *Close-up of Region 3. 0.1 ms^{-1} sliding speed, RH = 22.3%, load = 10 N (~1 GPa).*

Electrostatic charge detected and rate of change of coefficient of friction

The plot of electrostatic charge and the coefficient of friction in Figure 5.21 shows a similar trend to that of Figure 5.19. The electrostatic charge plot correlates well with the friction plot. All the rise and recovery events on the friction plot correspond with the fluctuations in bipolar charge level. Figure 5.22 shows the close-up of Region 3.

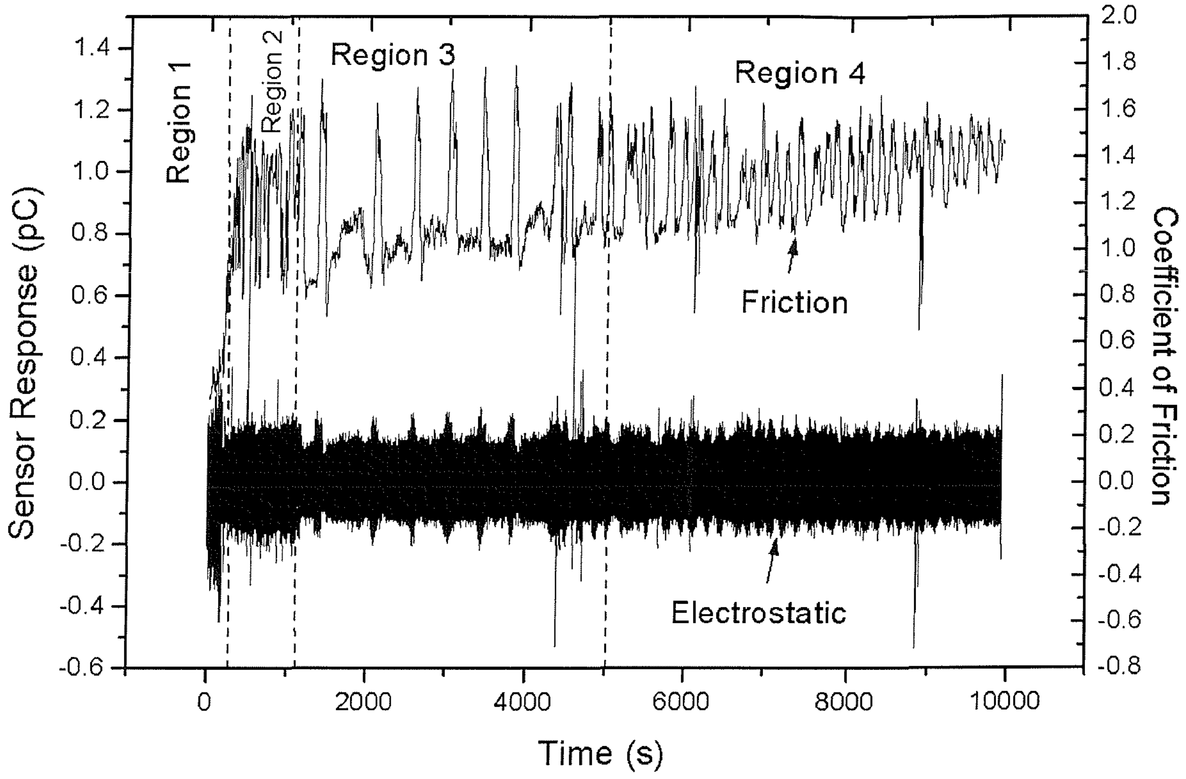

Figure 5.21 The plot of electrostatic charge and rate of change of coefficient of friction against time for Test 2 showing similar trend to that in Figure 5.19, 0.1 ms^{-1} sliding speed, RH = 22.3%, load = 10 N (~1 GPa).

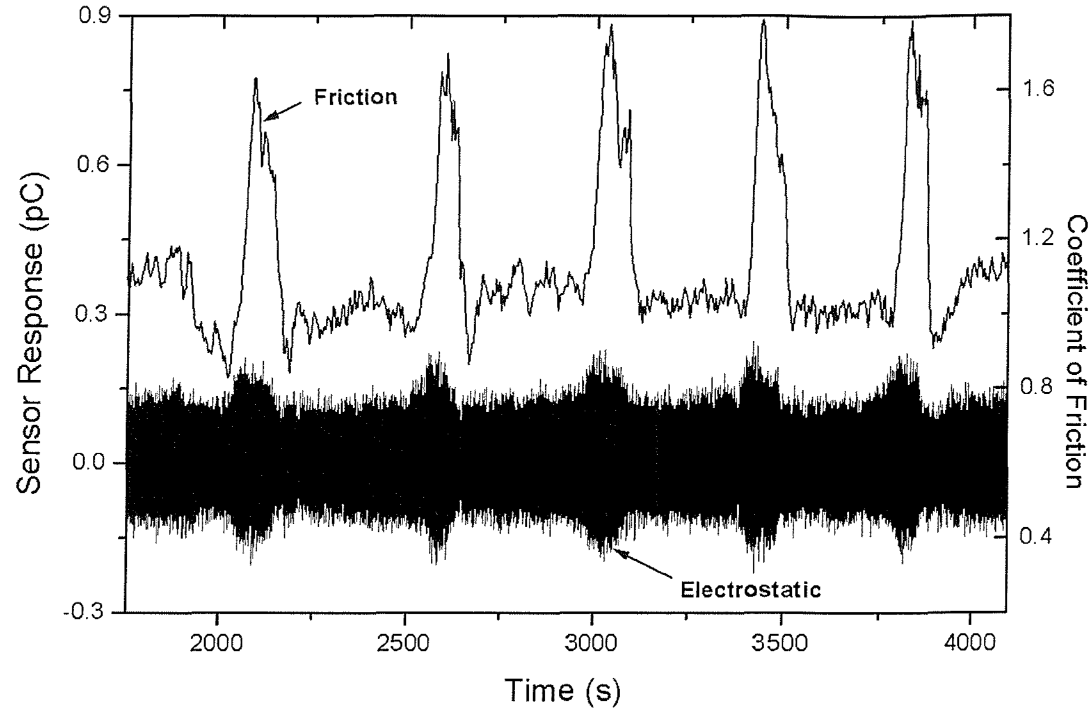

Figure 5.22 *Close-up of Region 3. 0.1 ms^{-1} sliding speed, RH = 22.3%, load = 10 N (~1 GPa).*

In summary, the wear process of unlubricated mild steel sliding on bearing steel can be divided into four regions. In Region 1, a 'running-in' process dominates, in which the oxide film and asperities of the unworn surface of the test ring are being removed, producing smooth surfaces.

In Region 2 the running-in process still dominates resulting in the increase in electrostatic signal, wear rate and friction. From the electrostatic charge point of view, these observations can be explained using contact potential difference theory: During the 'running-in' process, asperities and the original film on the unworn surface are being removed at a very high rate, i.e. yielding a high wear rate. This produces discrete areas of nascent metal surfaces. These nascent metal surfaces will have a lower work function than oxidised or unworn surfaces around them and hence charge differences occur.

Generally, Regions 1 and 2 are each affected by the initial surface finish of the pin and ring. Rougher surface finishes will result in higher initial wear rate and consequently higher electrostatic charging activities.

In Region 3, the level of average charge and wear rate decreased. The 'rise and recovery' events can be explained by considering 'oxidation-delamination-reoxidation' processes similar to that proposed by Kasai *et al* [57]. The baseline value of the plots signifies the moments when the contacting surfaces consist of oxide layers. Oxide layers on the asperities are continuously formed until it reaches a critical thickness, typically around 3 μm (from LVDT measurement), after which it is delaminated from the contact to form wear debris, exposing clean metal surfaces. When this happens, the sliding contact consists of oxide surface-clean surface or clean surface-clean surface pairing. This will result in increases in the contact temperature, coefficient of friction and the wear rate. The increase in contact flash temperature in a steel sliding pair at 0.1 ms^{-1} sliding speed can reach as high as 700 °C [93]. This will promote the growth of oxides on the contact surface. The higher values of coefficient of friction and the wear rate remain unchanged until enough oxide is formed in the contact to result in recovery. In this region, mild oxidational wear dominates. Since changes in the coefficient of friction is synonymous with the oxidation-delamination-reoxidation events, i.e. coefficient of friction varies in a descending order of metal-metal > metal-oxide > oxide-oxide, the same explanation applies. Figure 5.23 shows the schematics of the oxidation-delamination-reoxidation process.

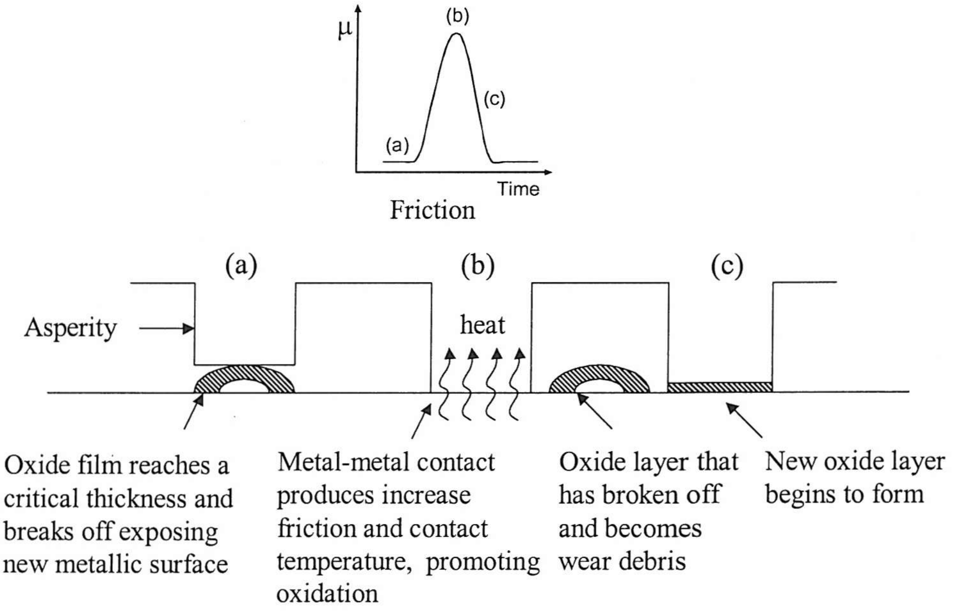

Figure 5.23 Schematics of the oxidation-delamination-reoxidation process. (a) Oxide film reaches a critical thickness. Friction is at baseline level. (b) Oxide layer breaks off and becoming wear debris exposing nascent metal surface. Friction increases. (c) New layer of oxide film starts to build up. Friction relaxes to baseline level.

In Region 4, the frequency of 'rise-and-recovery' events increased whilst the sliding wear rate is almost constant. The magnitude of charge, wear rate and friction during 'rise' events are slightly lower than in Region 3 and can be attributed to the decreasing contact pressure due to the increasing contact area of the pin on the disc. Hence, the contact condition is less severe, producing a lower wear rate, charge level and friction.

Figures 5.20 and 5.22 show that bipolar charge is detected slightly ahead of the rise friction and specific wear rate, which suggests the existence of precursor charge signals. However, the electrostatic data was plotted from raw data while the specific wear rate while the coefficient of friction was from four second averaged data, hence there is a mismatch between the resolutions of the plots. In Figure 5.24 below, the raw electrostatic data has been processed to produce an average every 4 seconds of data, identical to the processing of the specific wear rate and the coefficient of friction data. The dashed lines denote an increase in friction, which is accompanied by an increase in electrostatic charge (at approximately the same time), hence the observations in Figures 5.20 and 5.22 were probably due to variations in data processing. The possibility of precursor signals however cannot be ruled out at this stage and future tests should implement a higher acquisition rate for LVDT and friction.

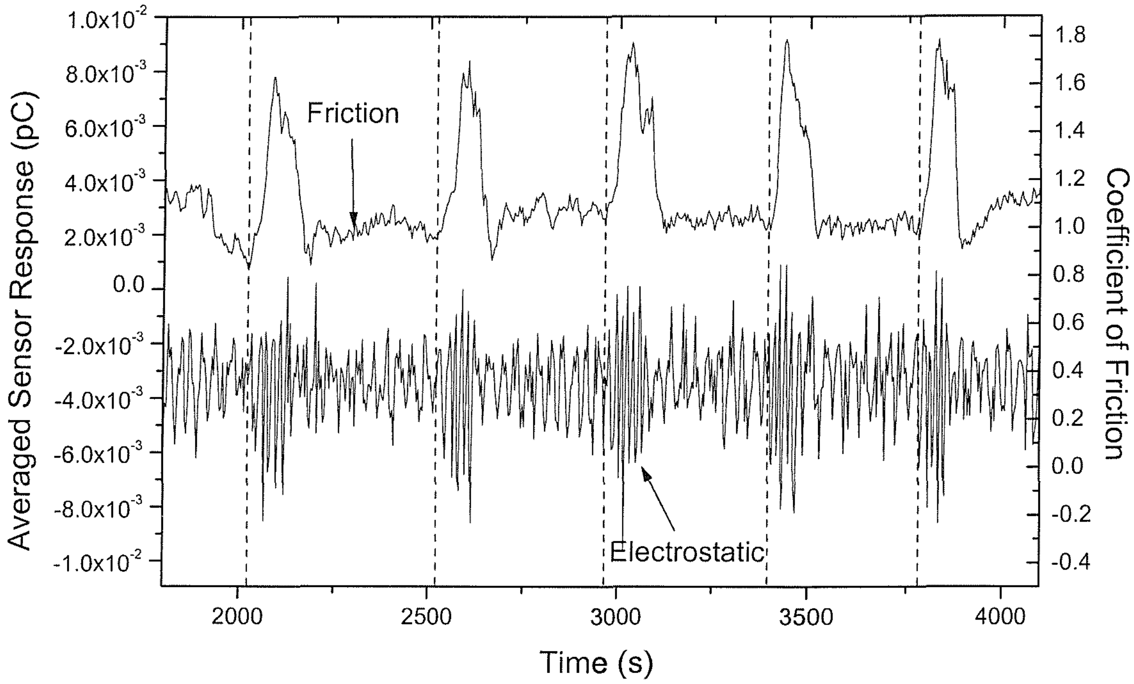

Figure 5.24 Plot of averaged electrostatic charge (4 seconds windowing) and coefficient of friction against time for Region 3.

Comparison between averaged electrostatic charge and specific wear rate

Figure 5.25 shows the averaged data from the electrostatic sensor and the specific wear rate. The moving average of the electrostatic sensor data was generated over a 50 second window. This duration was chosen as it is approximately a third of the period of peak activity and, through smoothing, the average will enhance the long duration features associated with wear events compared to the more variable background or random signals. Figure 5.26 shows that peak activities in the specific wear rate are accompanied by negative spikes on the averaged sensor response. This shows that any increase in wear results in a predominantly negative electrostatic charge. This corresponds with the contact potential difference theory. The sudden increase in wear is the result of delamination of oxide films, which reveals nascent metal surfaces. These nascent surfaces have a lower work function than the oxide or unworn metal surface, and hence they are charged positively and negatively respectively. Since the sensor view covers more unworn surface than wear track, thus an average negative charge is detected. The magnitude of the negative charge will vary corresponding to the oxidation-delamination-reoxidation process.

Charge due to solid-solid tribocharging (rubbing) is thought to exist as a constant background level and hence not detected by sensing system. Triboemissions were unlikely to be detected as the sensor was located away from the contacting surfaces and triboemission only occurs during the moment of actual physical damage. Charge from the wear debris formed in the contact will probably not be detected by the electrostatic sensor as it will be earthed instantly by contact with the earthed disc.

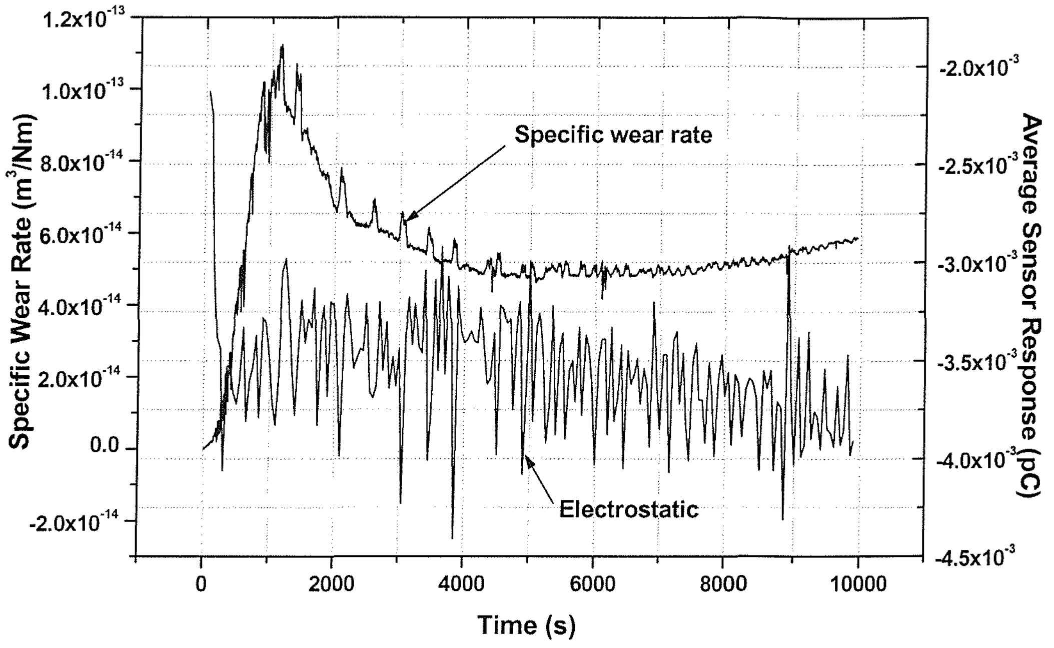

Figure 5.25 *Plot of averaged data (50 seconds windowing) from the electrostatic sensor and the specific wear rate against time for Test 2, 0.1 ms^{-1} sliding speed, RH = 22.3%, load = 10 N (~1 GPa).*

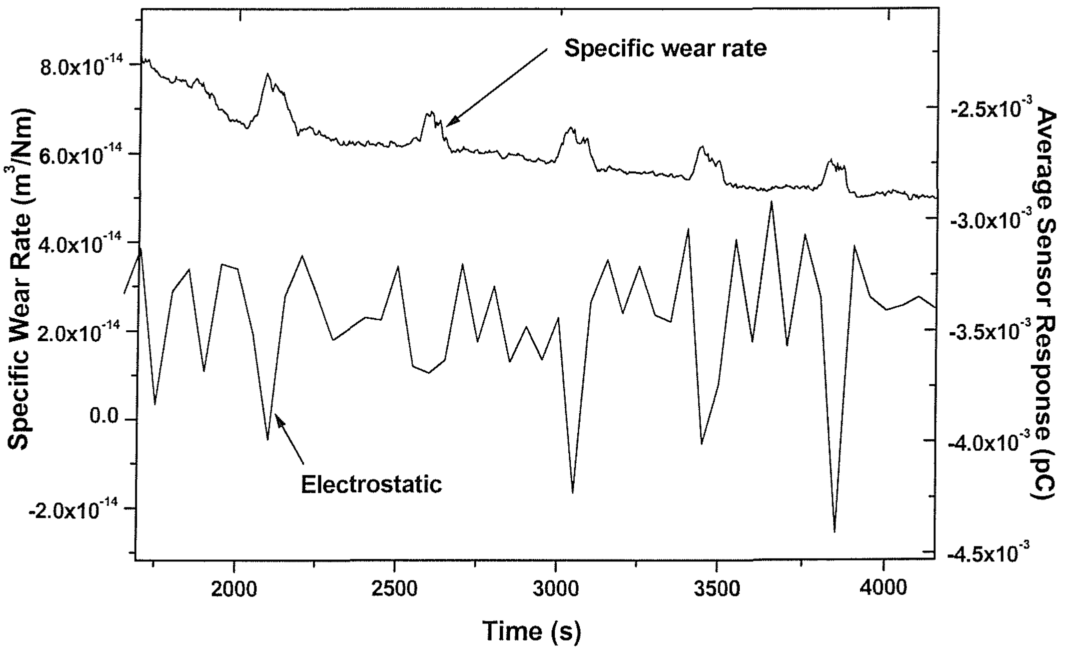

Figure 5.26 *Close-up of Region 3. 0.1 ms^{-1} sliding speed, RH = 22.3%, load = 10 N (~1 GPa).*

Micrographs of the pin, ring and debris

Figures 5.27 to 5.32 show, respectively, micrographs of the worn pin, ring and the debris. All the micrographs were taken of the pin and ring of Test 2. EDX analysis was also carried out on a selected area on the pin and ring to verify the presence of any oxidational products. Figures 5.33 to 5.35 show the EDX analysis for the worn and unworn surface of the test ring and pin as well as the wear debris.

From Figures 5.27 to 5.29 it can be seen that the wear track is dominated by grooves and abrasion marks with white patches. EDX analysis carried out on these white patches revealed that they are oxygen rich compared to the surrounding areas, indicating the presence of oxides (see Figure 5.33 (a) and (b)). This indicates that the test was stopped just after the removal of oxide films, i.e., at the beginning of a reoxidation process (which is evident from Figure 5.21). This explains the patchy oxide formation.

It can be seen from Figures 5.30 and 5.31 that there are smooth and jagged areas on the pin wear scar. EDX analysis on the jagged area showed this was oxygen rich relative to the parent material (and the smooth area) indicating the presence of oxides (see Figure 5.34 (a) and (b)).

Figure 5.32 shows a micrograph of the debris collected at the end of the test. The debris are very fine and 'powdery' with size generally around ≤ 3 μm. EDX analysis on the debris shown by Figure 5.35 shows that there is a very high presence of oxygen compared to the parent material of the ring and the pin. This is consistent with oxidative wear debris.

Figure 5.36 shows a micrograph of the wear surface when the test was stopped during the occurrence of a friction maxima. It can be seen that the surface is fairly smooth, typical of a ductile material subjected to a plastic strain. Figure 5.37 shows a micrograph of the wear surface when the test was stopped during the occurrence of friction minima. The surface is rougher compared to the surface in Figure 5.36. The EDX analysis of the whole area of both maxima and minima micrographs in Figure 5.38 shows that when the test was stopped during a friction minima, the presence of oxygen in terms of atomic weight is at least twice that when the test was stopped during a friction maxima. This further proves the oxidation-delamination-reoxidation process suggested earlier.

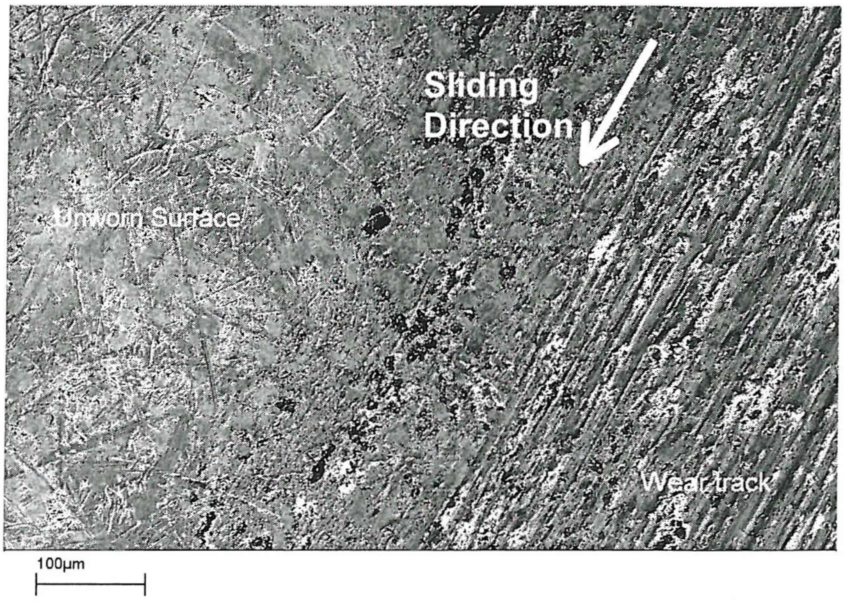

Figure 5.27 *Micrograph of the test ring showing part of worn and unworn surface, sliding speed = 0.1 ms^{-1}, load = 10 N (~1 GPa), RH = 22.3 %.*

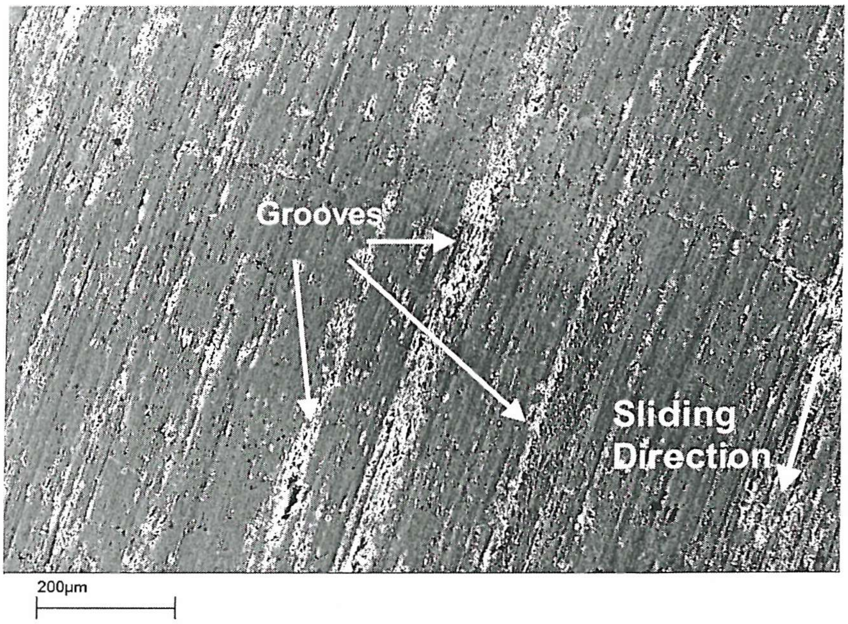

Figure 5.28 *Micrograph of the ring worn surface showing grooves and abrasion marks, sliding speed = 0.1 ms^{-1}. Load = 10 N (~1 GPa), RH = 22.3 %.*

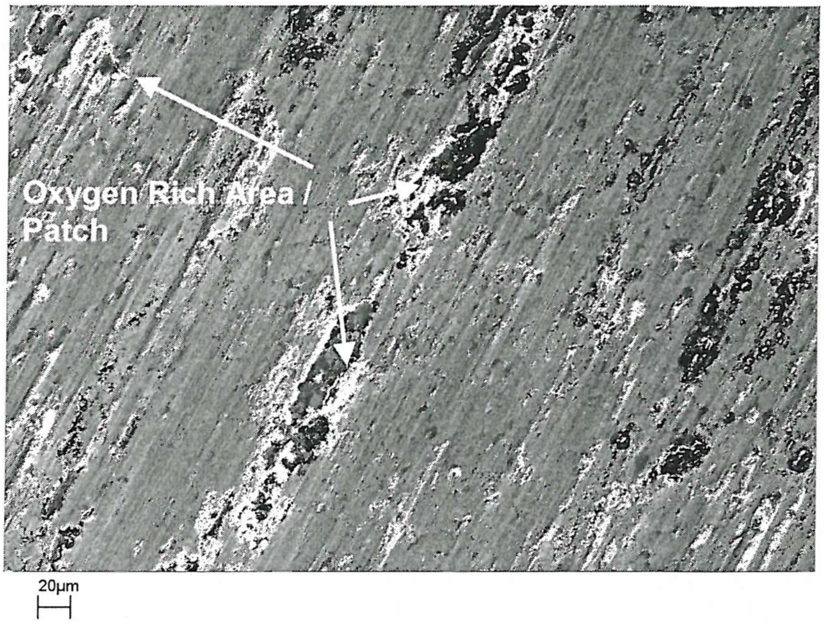

Figure 5.29 *Close-up of the grooves and white patches on the worn surface. EDX analysis showed that these areas are oxygen rich, indicating the presence of oxides (see Figure 5.33). Sliding speed = 0.1 ms^{-1}, load = 10 N (~1 GPa), RH = 22.3 %.*

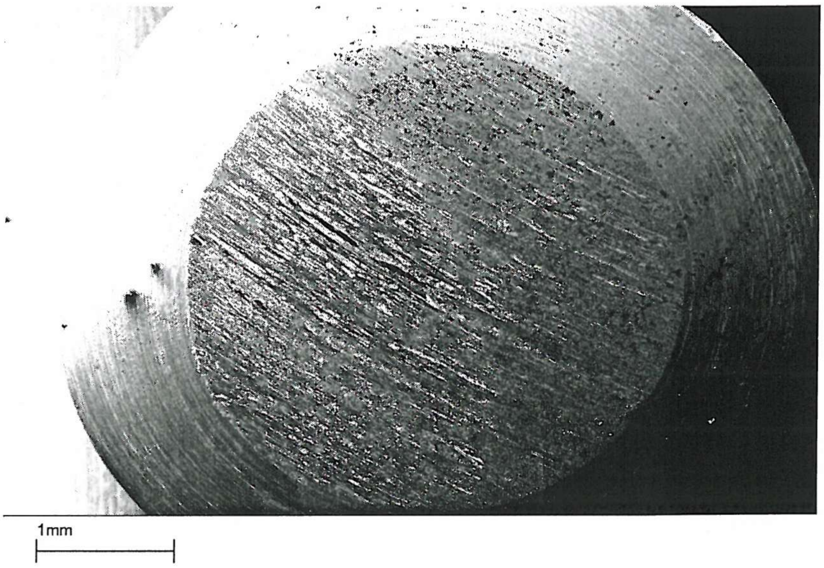

Figure 5.30 *Plan view of the wear scar on the test pin showing smooth and jagged areas. Sliding speed = 0.1 ms^{-1}, load = 10 N (~1 GPa), RH = 22.3 %.*

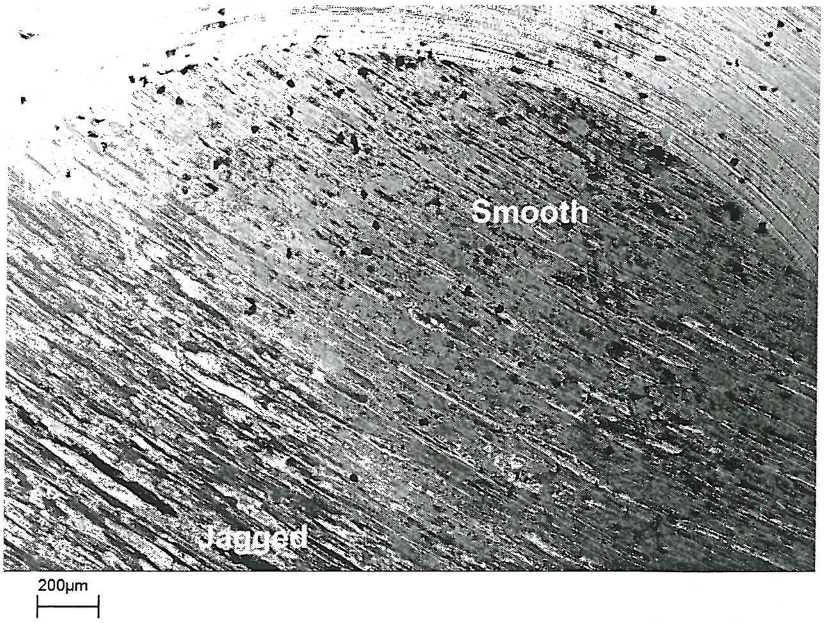

Figure 5.31 *Close-up of the smooth and jagged areas on the pin wear scar. Sliding speed = 0.1 ms^{-1}, load = 10 N (~1 GPa), RH = 22.3 %.*

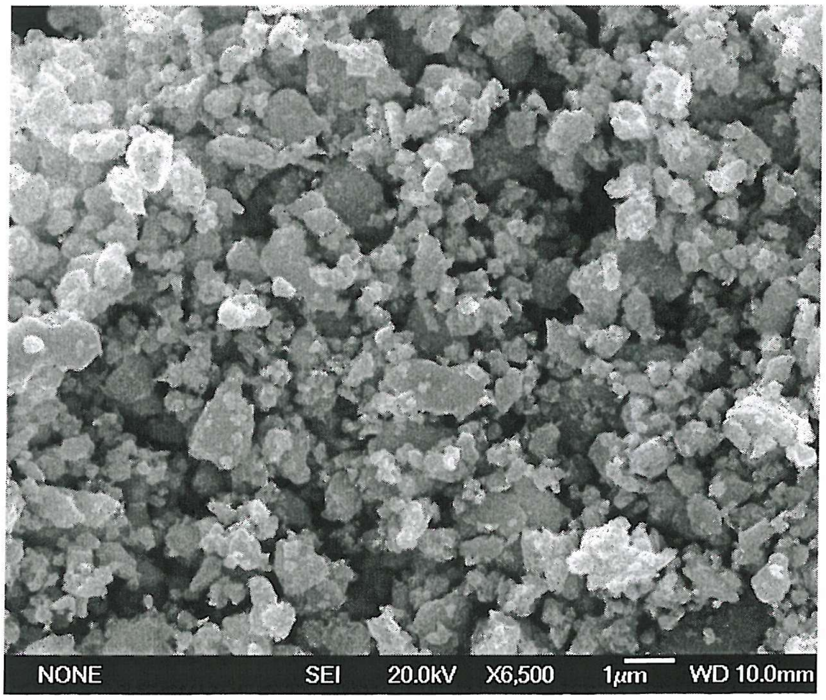

Figure 5.32 *Micrograph of wear debris collected at the end of the test. EDX analysis showed that the debris is oxygen rich (see Figure 5.35). Sliding speed = 0.1 ms^{-1}, load = 10 N (~1 GPa), RH = 22.3 %.*

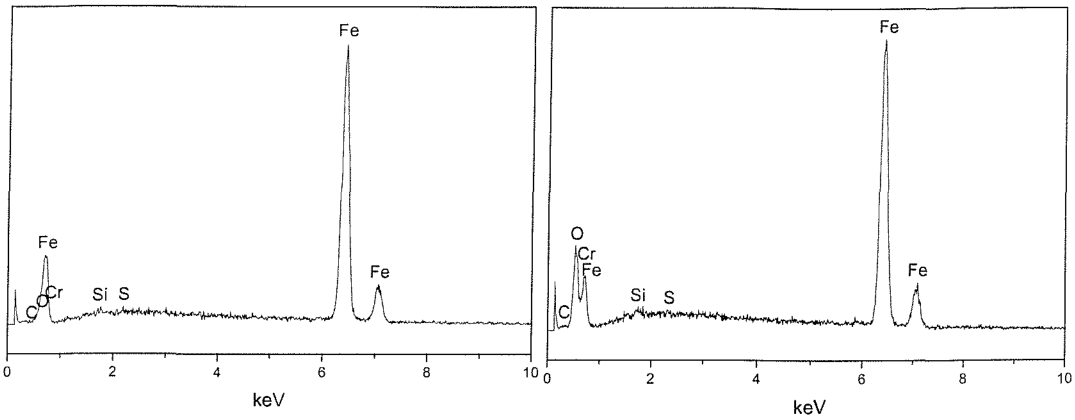

(a) (b)

Figure 5.33 EDX analysis of the test ring unworn surface (a) and the worn surface (b) showing the presence of high levels of oxides. Sliding speed = 0.1 ms^{-1}, load = 10 N (~1 GPa), RH = 22.3 %.

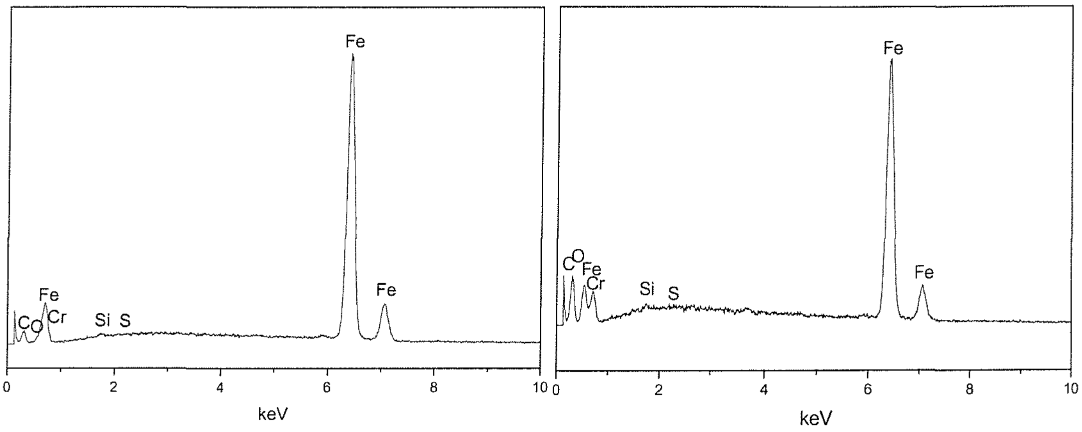

(a) (b)

Figure 5.34 EDX analysis of the test pin unworn surface (a) and the worn surface (b) showing the presence of high levels of oxides. Sliding speed = 0.1 ms^{-1}, load = 10 N (~1 GPa), RH = 22.3 %.

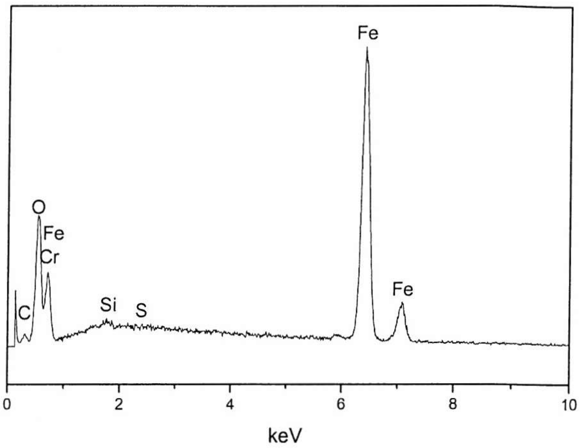

Figure 5.35 *EDX analysis of the wear debris showing the presence of high level of oxides. Sliding speed = 0.1 ms^{-1}, load = 10 N (~1 GPa), RH = 22.3 %.*

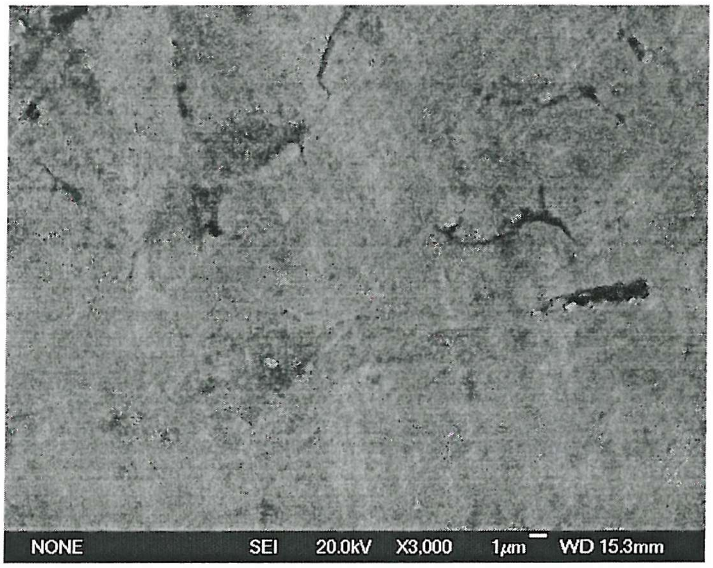

Figure 5.36 *Micrograph of the wear surface when the test was stopped during a friction maxima.*

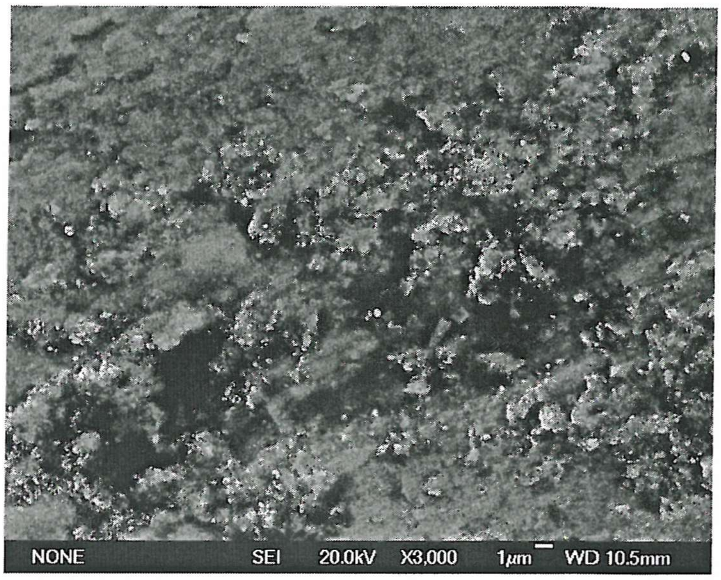

Figure 5.37 *Micrograph of the wear surface when the test was stopped during a friction minima.*

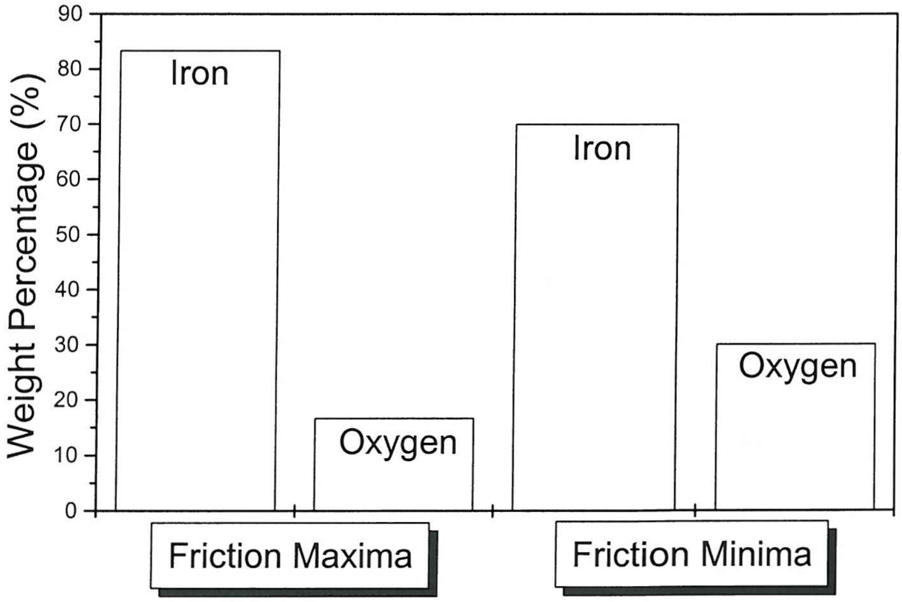

Figure 5.38 *Result of EDX analysis on wear surfaces for tests stopped during friction maxima and minima.*

5.4 CONCLUSIONS

The surface charging tests have demonstrated that the WSS is sensitive to charges generated when two different metals are present on the disc. The localised surface charge characteristic may be predicted from the work functions of the two metals, which indicates that the electrostatic sensor is detecting the CPD phenomenon. Of particular significance is the carbon steel insert test, which shows that WSS is sensitive to small changes in surface composition similar to those of phase-transformed regions seen in first transition scuffing. This proves that the electrostatic sensor is sensitive to precursor phenomenon related to this physical change. This would also explain the surface charge persistence observed during the occurrence of precursor signals to severe wear (see Test 1 in Chapter 4). During the tests with the Delrin^{TM} insert, the charge was dependent of pre-test handling and preparation and is prone to charge leakage, typical for insulators.

The wear mechanism generated in the unlubricated sliding wear tests was predominantly mild oxidational wear as predicted by the unlubricated steel sliding wear map [85]. Four regions of activity were identified. Region 1 is a 'running-in' period, which involved the removal of the initial oxide film on the untested samples. The wear rate and charge level in this region are very high. Region 2 is also a running-in period but it involves rough asperity-to-asperity contact, which produced a high wear rate and charge level. Region 3 is where the events of oxide stripping and growth dominate. The wear rate and charge level are lower than the running-in levels with fluctuations corresponding to an oxidation-delamination-reoxidation process. In Region 4 the frequency of the rise and recovery event increased. These distinct regions were shown by the volume loss, friction and also the electrostatic sensor plot, where high wear rates produced a high magnitude of response from the electrostatic sensor.

The moving average of the electrostatic sensor signal indicates that the charge from the oxidation-delamination-reoxidation processes is predominantly negative, which is consistent with expected changes in work function. Nascent metal surfaces have a lower work function than the unworn/oxidised metal surface and hence become positively and negatively charged, respectively. Average charge detected by the sensor was negative because the sensing face is larger than the wear track. The dominant charging mechanism is thought to be the contact potential difference variations between nascent and oxidised regions.

SEM micrographs and EDX analysis of the wear scar on the ring and pin as well as the debris collected confirmed that the predominant wear mechanism was mild oxidational wear.

Correlations between the signal from the electrostatic sensor and the delamination and formation of oxide films demonstrate that electrostatic charge monitoring is a useful tool to monitor the dynamic wear processes of sliding steel contacts.

6

REAL-TIME MONITORING OF CHARGED DEBRIS

6.1 INTRODUCTION

This chapter details experiments to investigate the charging behaviour of freshly generated wear debris monitored in real-time. An electrostatic monitoring system employing two sensors was used to study charging activities on the wear track as well as just outside. This was to investigate the influence of the generation, entrainment and transportation of wear debris (both normal and seeded) on the overall charge detected. One sensor was employed to monitor the wear track to detect charge associated with a combination of surface damage and wear debris while the other sensor monitored outside the wear track were to detect charge associated with wear debris only.

6.2 BACKGROUND

6.2.1 Abrasive Wear

According to the ASTM G 40-83 terminology standard, abrasive wear is defined as wear due to hard particles or hard protuberances forced against and moving along a solid surface [94]. Abrasive wear can be divided further into two general categories; namely, two-body (grooving) abrasion, and three-body (rolling) abrasion.

Two - body (grooving) abrasion

Figure 6.1 shows the schematics of two-body abrasion caused by hard protuberances or embedded hard particles. Figure 6.2 shows a typical micrograph of a wear scar resulting from two-body abrasion indicating the presence of a series of parallel grooves, a classical manifestation of two-body abrasion [95].

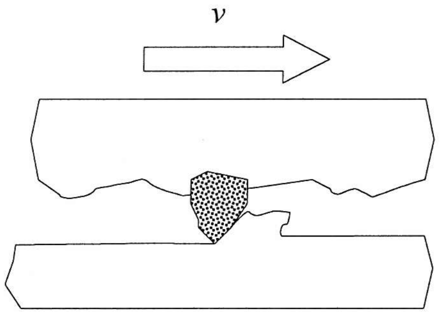

Figure 6.1 *Schematic representation of two-body abrasion mechanism.*

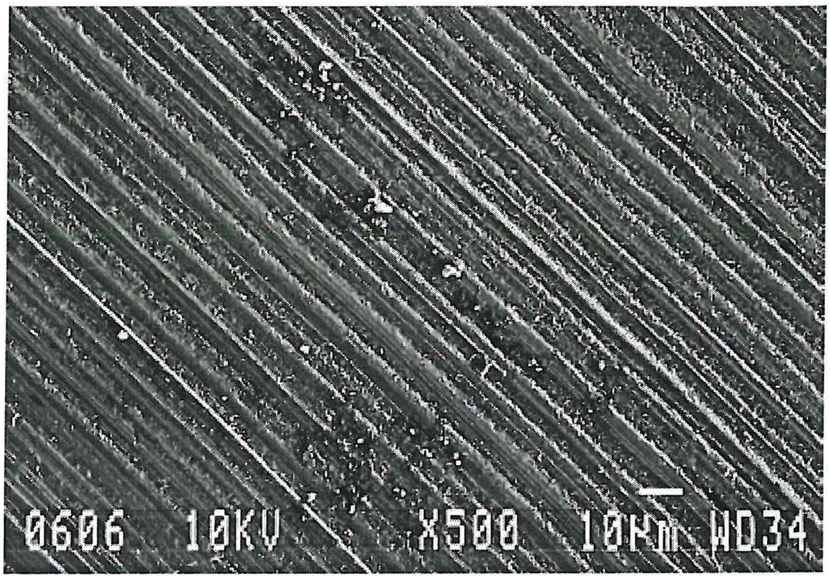

Figure 6.2 *Micrograph of a typical wear scar due to two-body abrasion [95].*

There are four types of interactions between abrasive particles and wearing surfaces; namely, microploughing, microcutting, microfatigue and microcracking [96], as shown by Figure 6.3. Generally, microploughing for a single pass does not result in any detachment of material from the wearing surface. A prow is formed ahead of the abrading particle and material is continuously displaced sideways to form ridges adjacent to the groove produced. Material detachment occurs due to repeated action of a single particle over the same area. Material that is displaced sideways repeatedly to form ridges can break off by low cycle fatigue; i.e., microfatigue. Microcutting results in a volume loss of the material equal to that of the volume of wear groove produced. Wear debris produced by microcutting generally exhibit a chip shape similar to debris produced during machining. When highly concentrated stresses are imposed by abrasive particles microcracking occurs, which is especially relevant to brittle materials. Microcracking produces large wear debris as a result of crack formation and propagation.

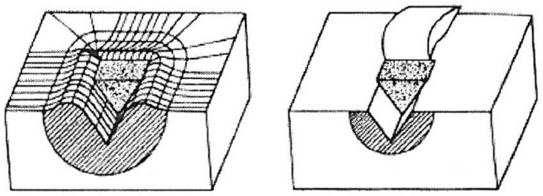

Microploughing **Microcutting**

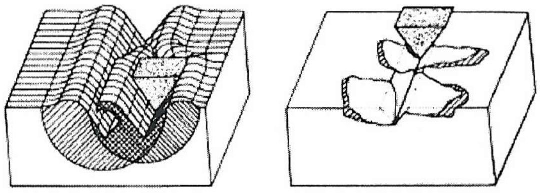

Microfatigue **Microcracking**

Figure 6.3 *Schematic representation of four different types of abrasive particle interactions with wearing surfaces [96].*

Three - body (rolling) abrasion

In three-body abrasion, the abrasive particles are free to roll between the contacting surfaces, as shown in Figure 6.4. Most wear damage is due to repeated indentation and microfracture [97]. Hence the wear scar from three-body abrasion is generally characterised by a heavily deformed, multiple indented appearance with little or no directionality, as shown in Figure 6.5 [95].

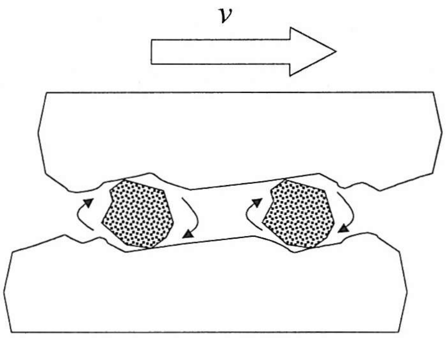

Figure 6.4 *Schematic representation of three-body abrasion mechanism.*

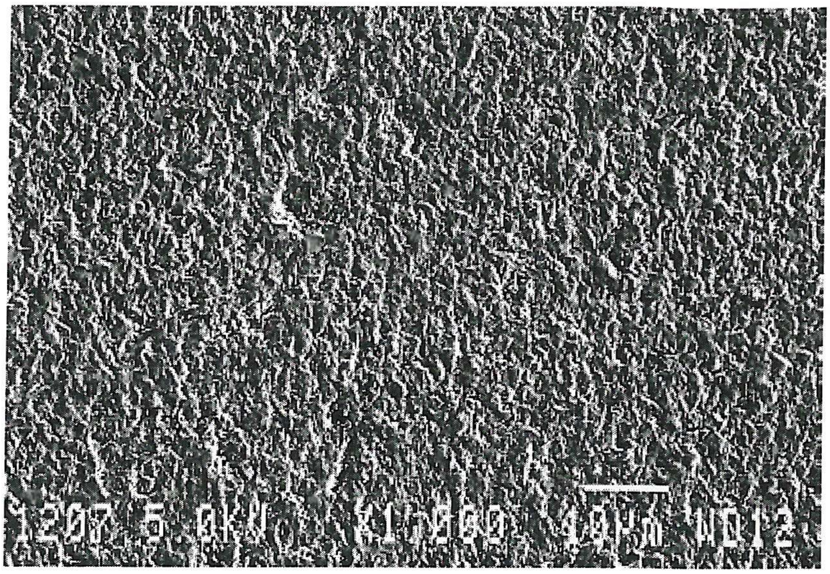

Figure 6.5 *Micrograph of a typical wear scar due to three-body abrasion [95].*

The rate of wear due to two-body abrasion is generally higher and can be one order of magnitude more compared to three-body abrasion [98-100]. This is due to the fact that rolling abrasive abrades the surface where they are located only 10% of the time, while they spend 90% of the time rolling.

6.3 EXPERIMENTAL PROCEDURE

Experiments were carried out using a modified pin-on-disc test rig fitted with two electrostatic sensors, as shown in Figure 6.6. Two electrostatic 'button type' wear site sensors (WSS) were employed; sensor 1 directly monitored the wear track, whilst sensor 2 monitored the disc surface 5 mm outside the wear track shown by Figure 6.7. The sensing face was positioned at approximately 0.5 mm above the disc surface. Contact sliding speed was kept constant at 5 ms^{-1} and Shell Vitrea ISO 460 mineral base oil was used as a lubricant, supplied continuously via a mist spray.

Three types of test were carried out:

- Test 1 (Normal wear debris) - Debris was generated naturally by means of gradually increasing the applied load to a sliding ball on disc to increase the wear. The initial load was 10 N and loading increments of 20 N were applied approximately every 10 minutes, in 4 stages. The test was stopped 18 minutes after the application of the final load (90 N).

- Test 2 (Steel debris seeding) – The pin was a bearing steel with radius of curvature of 63 mm and was loaded at 50 N against a bearing steel disc. Steel debris was seeded into the contact by application of oil droplets (containing seeded debris) to the inside of the track, see Figure 6.7. Steel debris was seeded five times to investigate repeatability at approximately 12 minutes intervals.

- Test 3 (Silicon nitride debris seeding) – This test had a similar methodology to Test 2, except the sliding ball had a radius of 3 mm, the load was constant at 10 N and silicon carbide debris was used instead of steel debris.

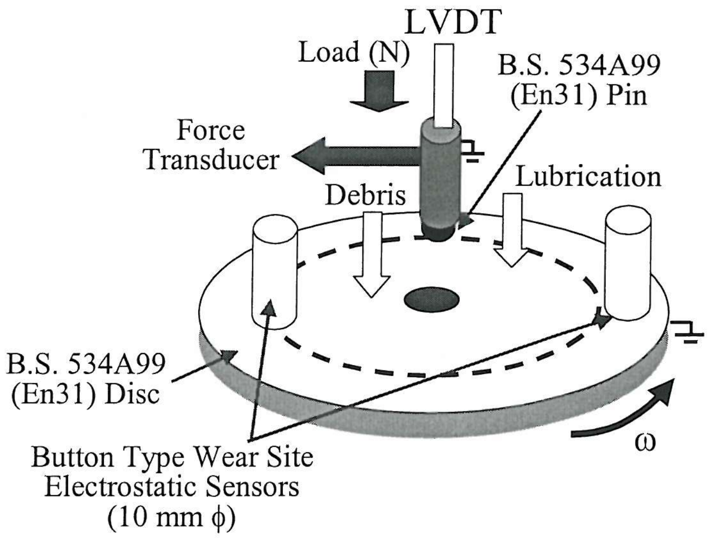

Figure 6.6 *Pin-on-disk wear test setup.*

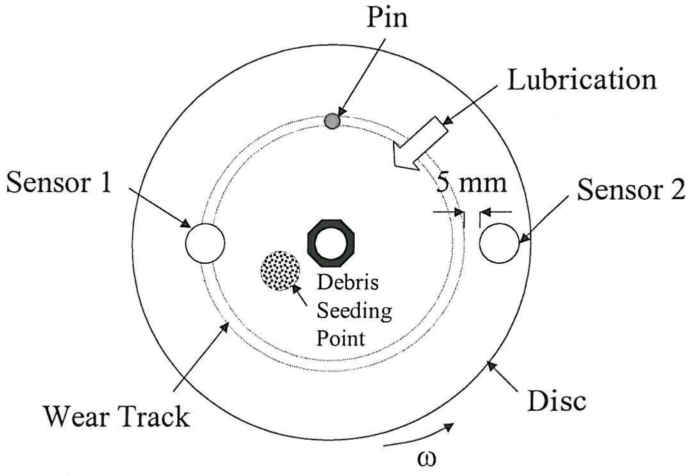

Figure 6.7 *Plan view of the pin-on-disk wear test setup.*

The steel and silicon carbide test debris were premixed with Shell Vitrea ISO 460 lubricant before being dropped onto the disc using a pipette. The sliding conditions were designed to produce minimum film thickness less than (but comparable to) the size of the seeded debris. Table 6.1 shows some physical properties of the seeded debris used while Table 6.2 summarises the test conditions.

Debris Material	**Tap Density (kg m^{-3})**	**Hardness (Hv)**	**Mass Conc. (g ml^{-1})**	**Nominal Size (μm)**	**Comp. (%)**	**Shape**
Silicon Carbide	1025	2500	0.0083	4-5	99 % SiC	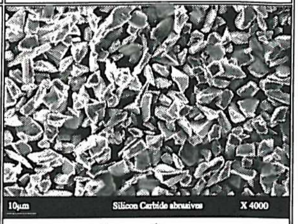 Angular
4140HC High Cr Steel	4500	250	0.025	< 3.7 (10%) < 8.8 (50%) < 16 (90%)	Cr = 0.99, Mn = 0.77, C = 0.52, Si = 0.33, Mo = 0.22,	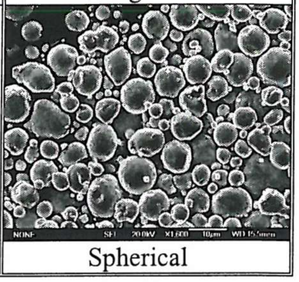 Spherical

Table 6.1 Some properties of the seeded debris used.

	Test 1	**Test 2**	**Test 3**
Pin material	Bearing steel B.S. 534A99 (EN31)		
Disc material	Bearing steel B.S. B.S. 534A99 (EN 31)		
Debris Material	-	High Cr Steel	Silicon Carbide
Track radius (mm)	30.6		
Sliding speed (ms^{-1})	5		
Contact radius (mm)	3	63	3
Load (N)	Variable (10 - 90)	50	10
Hertzian contact pressure (MPa)	Variable (1.5 – 3)	0.3	1.5
Min. film thickness (μm)	Variable [1.2 (@10N)]	4.45	1.2
Pin hardness (HV)	640	210	640
Disc hardness (HV)	220		
Pin roughness, R$_a$ (μm)	0.03	0.10	0.03
Disc roughness, R$_a$ (μm)	0.17		
Oil	Shell Vitrea ISO 460		
Conductivity (pS m^{-1})	11		
Oil relaxation constant, τ (s^{-1})	2.4		
Oil kinematic viscosity at 40° (cP)	455		
Initial λ value	7	22	7

Table 6.2 Summary of the test conditions.

6.3.1 Instrumentation

The instrumentation used was identical to the one used in the lubricated wear tests described in Chapter 3, except two electrostatic sensors were employed. A block diagram of the instrumentation used is shown by Figure 6.8.

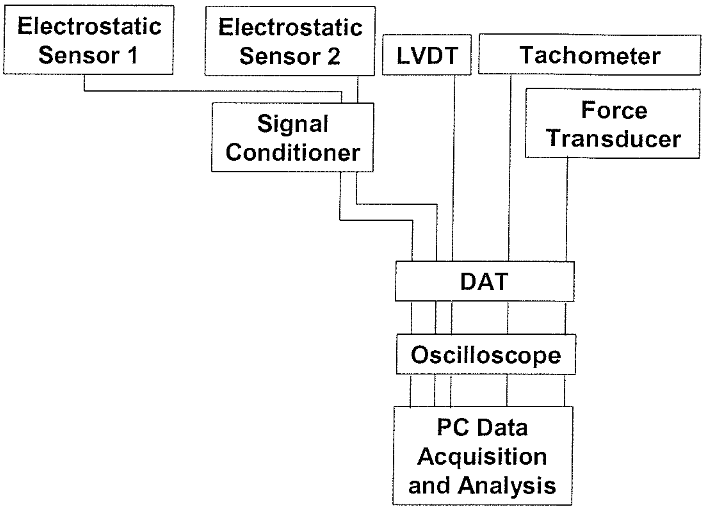

Figure 6.8 Block diagram of the instrumentation used

6.3.2 Signal Analysis Technique

The production of colour maps and calculation of the cumulative volume loss and specific wear rate have been shown in previous chapters (see Sections 4.2.2 and 5.3.3). During the calculation of the cumulative volume loss the wear of the disc; i.e., the increase in wear track depth is assumed to be negligible. As in the previous chapter, it is the trend of wear that is of interest and not the absolute value.

In this chapter, the colour maps are further manipulated by 'background subtraction'. This normalised plot is achieved by subtraction of background signal averages from which the mean signal is calculated and subtracted from the dataset used, to create the colour map. This method is very useful to show the trend of the charge magnitude change relative to the background level.

It is important to note that the magnitude of the wear site sensor response should not be compared critically as the magnitude of their responses is greatly influenced by the distance of the sensor face to the surface of the disc (i.e. charge source). Investigations carried out by Harvey [101] have established a relationship between the magnitude of the

WSS response and distance from the surface charge source, shown in Figure 6.9 below. For all tests employing WSS in this thesis, the sensing face to the disc surface was set 0.5 mm using a filler gauge. This technique is very crude and some variations inevitably exist between tests. Figure 6.9 shows that for distances smaller than 0.5 mm the change in the sensor response for small changes in sensor height is significant.

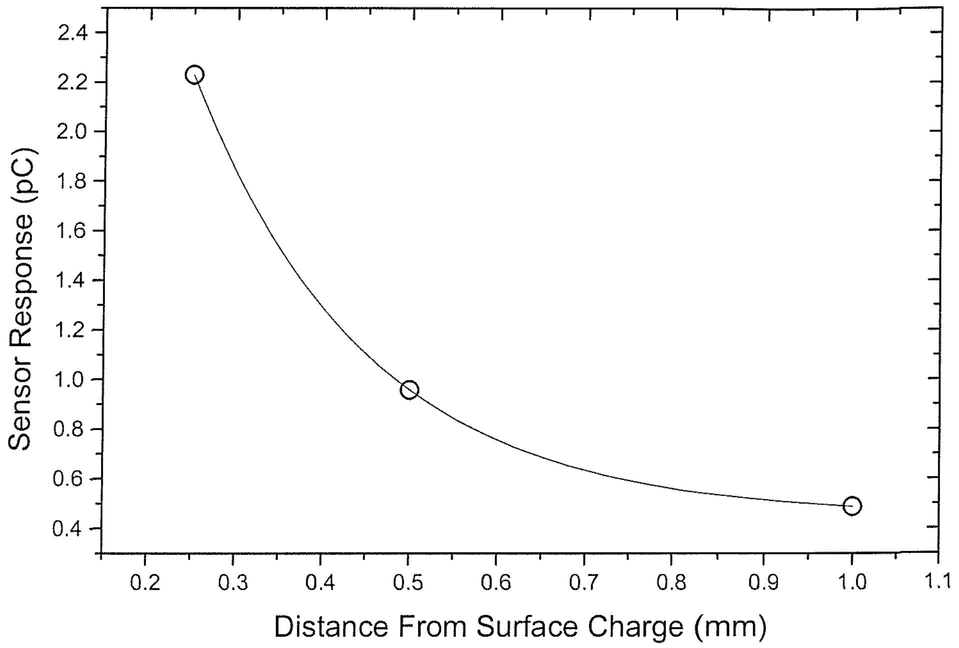

Figure 6.9 *The relationship between WSS response and sensor height above a surface charge source [101].*

6.4 RESULTS AND DISCUSSIONS

6.4.1 Test 1 - Normal Wear Debris

A background subtraction using the first 500 s after the initial load of 10 N was applied was used to calculate a normalised colour map. The background charge level was very low hence the difference between normalised and unnormalised colour map is minimal. From the sensor 1 normalised colour map, shown in Figure 6.10, it can be seen that there was little charging activity in the early stages of the test. After the total load reached 50 N however, there was a significant increase in charging activities, manifesting as bands of positive and negative features, which persisted to the end of the test. There are also positive (deep red in colour in the positive charge band and light blue in the negative charge band) dynamic features present. These features moved on the disc surface as the test progressed and were persistent right until the end of the test.

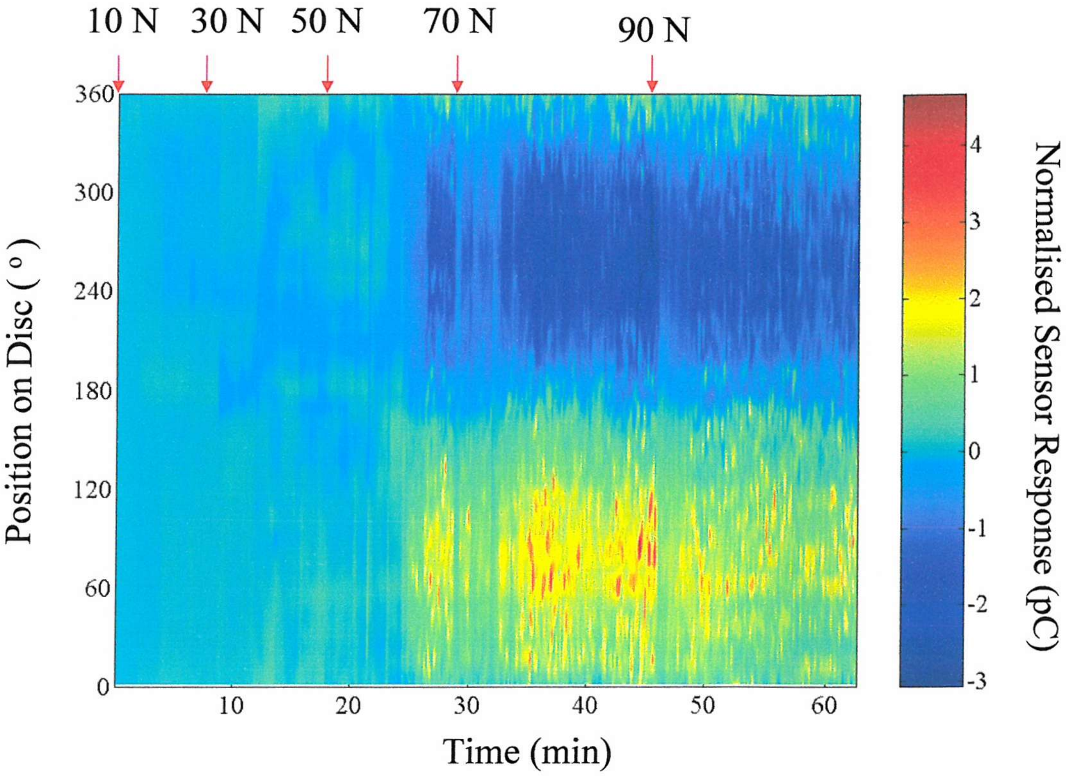

Figure 6.10 Normalised colour map of sensor 1 data showing an increase in charging activities and the presence of dynamic features after load reached 50 N. Shell Vitrea ISO 460, sliding speed = 5 ms^{-1}.

Figure 6.11 contains several normalised signal averages taken at the middle of each load stage which indicates an increase in charging activity with the increments of loads. It is interesting to note that the trend of charging is such that the bipolar background response (see inset) is enhanced as the load and hence wear severity is increased. It is also interesting to note that the magnitude of positive and negative charge levels are comparable. The reason for this is discussed further in Appendix A.

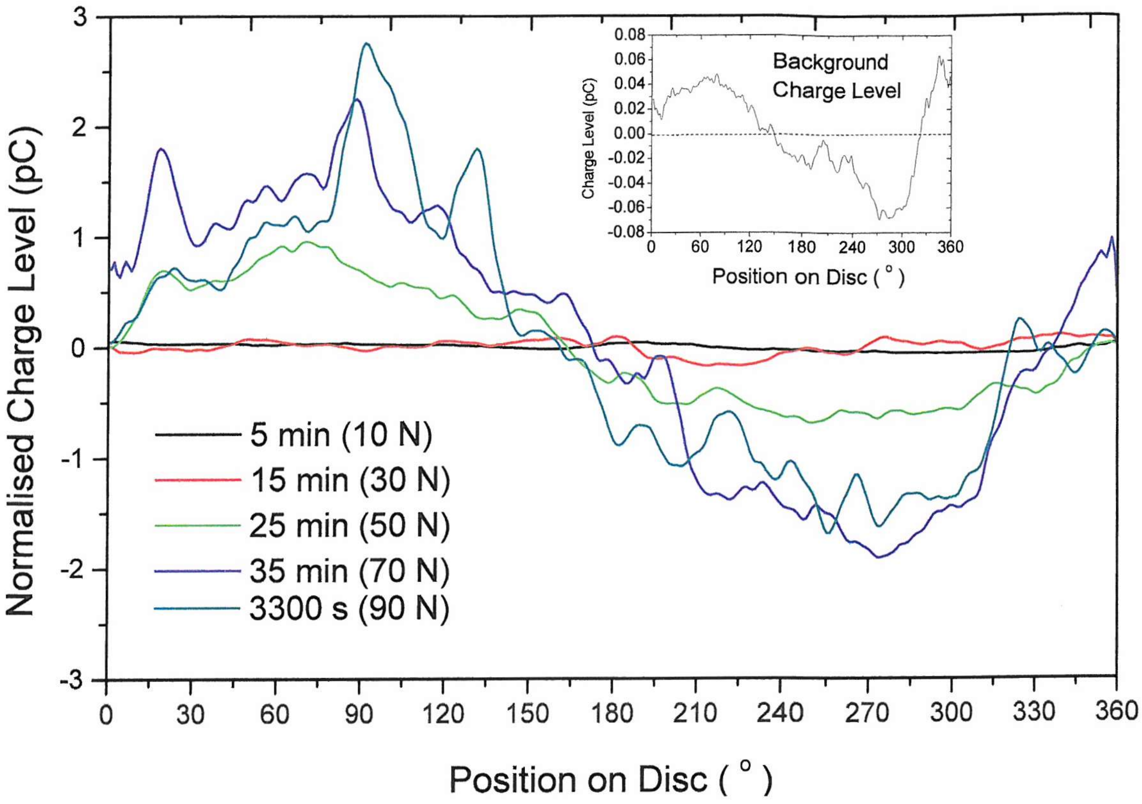

Figure 6.11 *Sensor 1 normalised signal average line plots for various load stages. Shell Vitrea ISO 460, sliding speed = 5 ms^{-1}.*

Figure 6.12 shows the background subtracted colour map of sensor 2 data indicating a significant increase in the charging activities just after 50 N load is applied, similar to the trend shown by Figure 6.10. During and after the 50 N load stage, positive dynamic charge features started to appear. The frequency of these features appears to increase with increasing load. Figure 6.13 shows the close-up of the area marked by the red circle on Figure 6.12, which clearly shows a positive charge feature moving from (approximately) 140° to 155° on the disc surface. This charge feature is thought to originate from single charge debris or a cluster of debris.

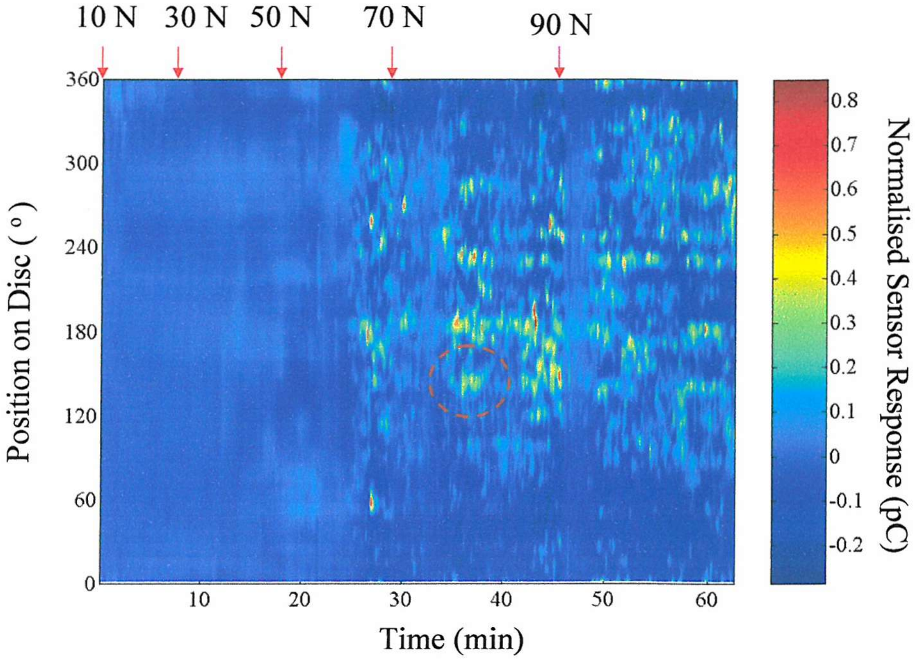

Figure 6.12 Normalised colour map of sensor 2 data showing an increase in charging activities and dynamic positive charge features during and after 50 N load stage. Shell Vitrea ISO 460, sliding speed = 5 ms^{-1}.

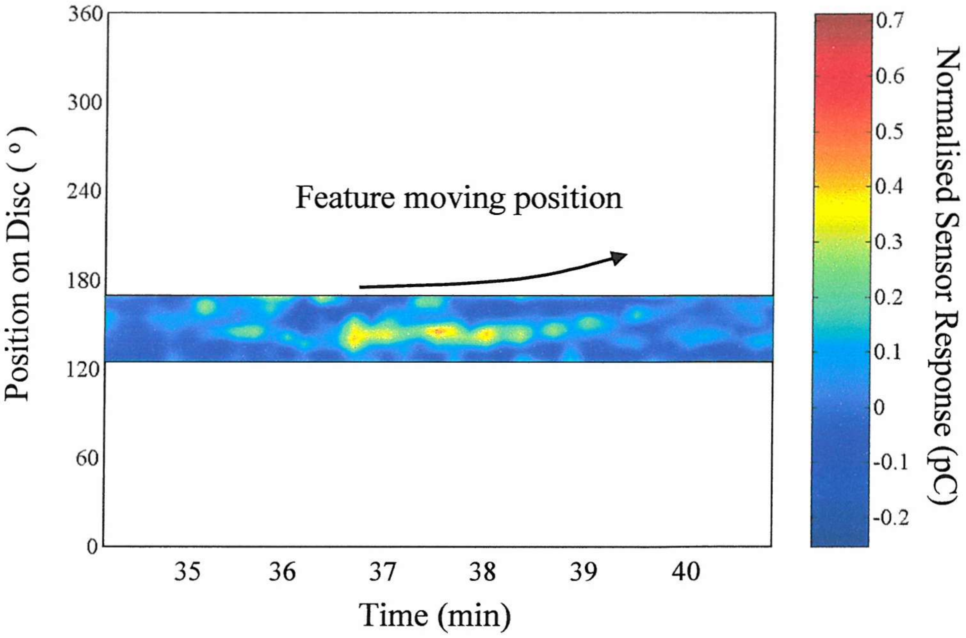

Figure 6.13 Close-up of the circled region in figure showing the presence of dynamic highly positive charge features. Shell Vitrea ISO 460, load = 70 N, sliding speed = 5 ms^{-1}.

Figure 6.14 shows normalised signal average plots from sensor 2 of typical dynamic, discrete positive charge events. It shows two averages taken 10 seconds apart, the positive feature (indicated by arrow in Figure 6.14) can be seen to move on the disc.

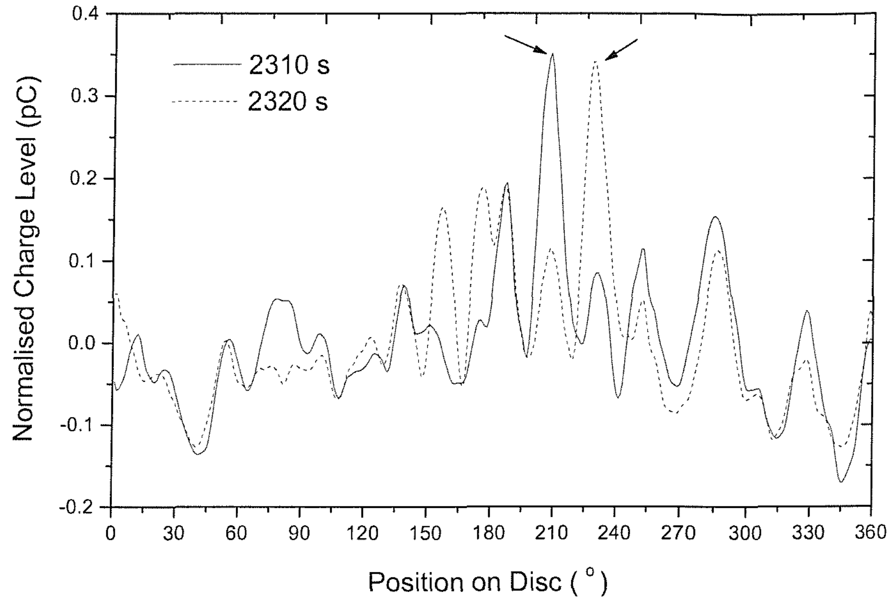

Figure 6.14 *Normalised signal average from sensor 2 at 2310 s and 2320 s into the test showing positive charge features moving on the disc surface. Shell Vitrea ISO 460, load = 70 N, sliding speed = 5 ms^{-1}.*

Charge features on the wear track due to active wear sites and due to the presence of charged wear debris can be easily distinguished. Charge features associated with a wear site hold position on the colour map while charge features associated with wear debris are dynamic in nature; i.e., their position on the colour map gradually changes with time. From the evidence presented, it is clear that wear site sensor 1 detects a combination of static charge features emanating from the wear site, as well as dynamic charge features from wear debris, while sensor 2 (remote sensor) detects only the latter.

From Figure 6.15 it can be seen that charge levels from sensor 1 and 2 show a direct correlation with the net volume loss, exhibiting increased charge levels and activity with increasing load stages. The largest increase in charge level occurs during the 50 N load which corresponded to the start of high frequency dynamic charge features observed on the real-time colour plot.

The volume loss in Figure 6.15 shows that immediately after the addition of load there is an increase in volume loss followed by a period of steady state. Quantifying the net volume loss by load stage shows increasing volume loss and therefore increasing amounts of debris with increasing load (apart from during 50 N load), as shown in Table 6.3.

The direct correlation between volume loss per loading stage and the charge from both sensor 1 and sensor 2 can be explained by relating the volume loss to the amount of debris formed due to the increase of the severity of the contact condition. As more load is applied, more wear debris will be produced as indicated by the increase in volume loss. This debris will be charged, resulting in higher overall charge present on the disc surface, explaining the increase in baseline level of the charge from both sensors. Charge features associated with wear debris are dynamic in nature due to the movement of wear debris as they are centrifuged out of the contact and eventually into the oil sump.

It is observed in Figure 6.15 that the specific wear rate (SWR, given in Equation 5.1) increases rapidly over the first two load stages and immediately after each additional load. It is also evident that the coefficient of friction varied throughout the test. The most significant variation was the decrease in the friction immediately after the load reached 30 N. Friction remained roughly constant during the 50 N and 70 N load stages before decreasing slightly after the total load reached 90 N.

The coefficient of friction was higher in the early stages because the contacting surfaces were relatively rougher than after the running-in period. It is interesting to note that at about the 37th minute into the test, the charge can be seen to increase suddenly without any load change. This increase was accompanied by a slight change in the friction coefficient (circled in Figure 6.15). This suggests that there was a slight increase in the severity of the wear and hence the amount of wear debris produced causing significant increase in the charging activities. This shows that electrostatic monitoring is sensitive to even small amounts of change in the wear rate (not detected by volume loss measurement) and friction. This is very encouraging as the objective of the development of this sensing technique is so it can be used to monitor the change in wear behaviour in real machinery components.

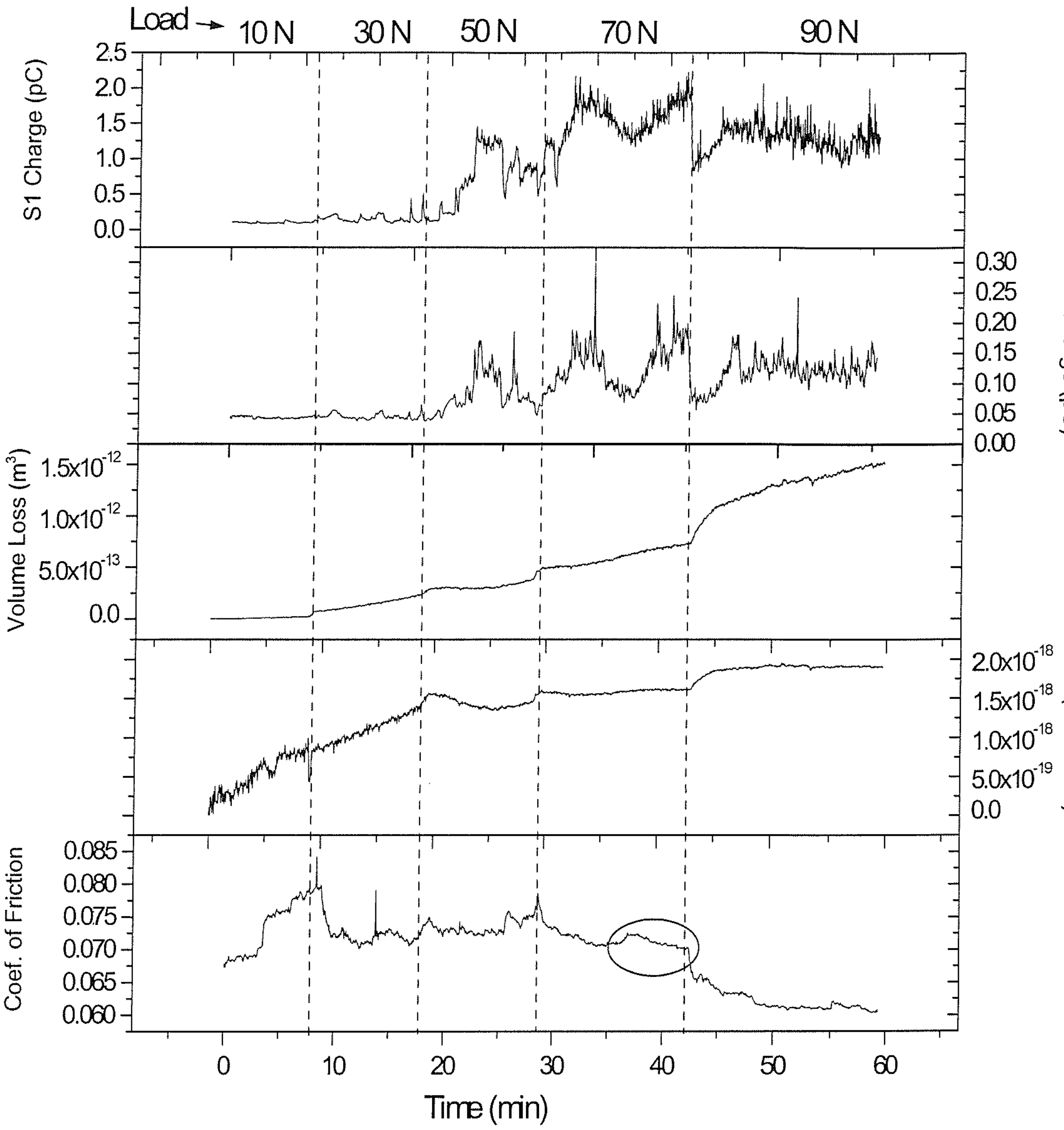

Figure 6.15 A plot of charge, volume loss, specific wear rate and coefficient of friction against time. Shell Vitrea ISO 460, sliding speed = 5 ms^{-1}, initial λ = 7.

Total Load (N)	10	30	50	70	90
Net Volume Loss (m^{-3})	0.24 x 10^{-13}	2.2 x 10^{-13}	1.7 x 10^{-13}	3.3 x 10^{-13}	8 x 10^{-13}
Contact stress (GPa)	1.5	2.1	2.5	2.8	3.0

Table 6.3 Net volume loss and maximum contact stress per load stage.

Surface profilometry

Surface profilometry indicates that the pin and disc wear scars from Test 1 are smooth with deep grooves at the centre. The wear track was approximately 0.75 mm wide and had a maximum depth of approximately 15 μm, as shown in Figure 6.16.

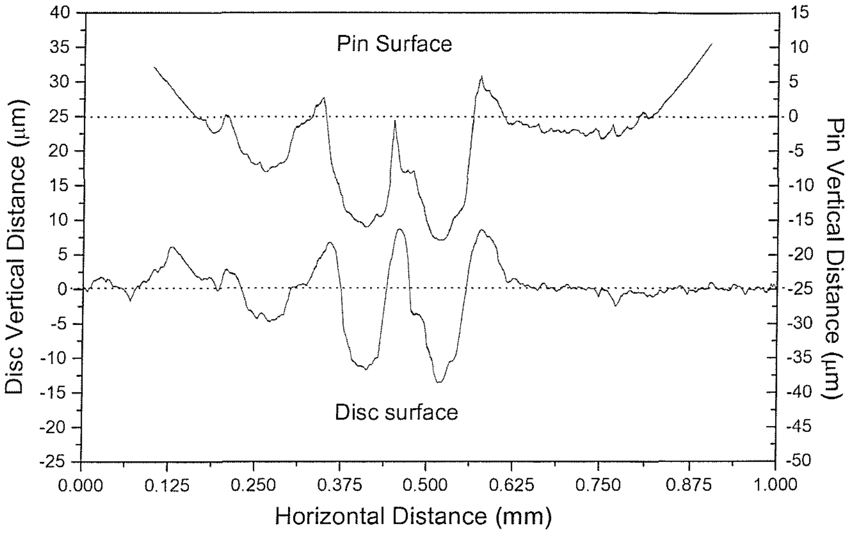

Figure 6.16 Surface profilometry of pin and disc from Test 1.

Scanning Electron Microscope (SEM) micrographs

Figure 6.17 shows that the worn surface of the pin from Test 1 is relatively smooth with some striations, typical of lubricated sliding wear [95]. A micrograph of the disc worn surface, shown in Figure 6.18 shows evidence of material delamination. Figure 6.19 shows wear debris from Test 1 indicating a typical length of 5 μm to 20 μm and their surfaces exhibit some striations. This correlates well with the size of delaminated material shown in Figure 6.18.

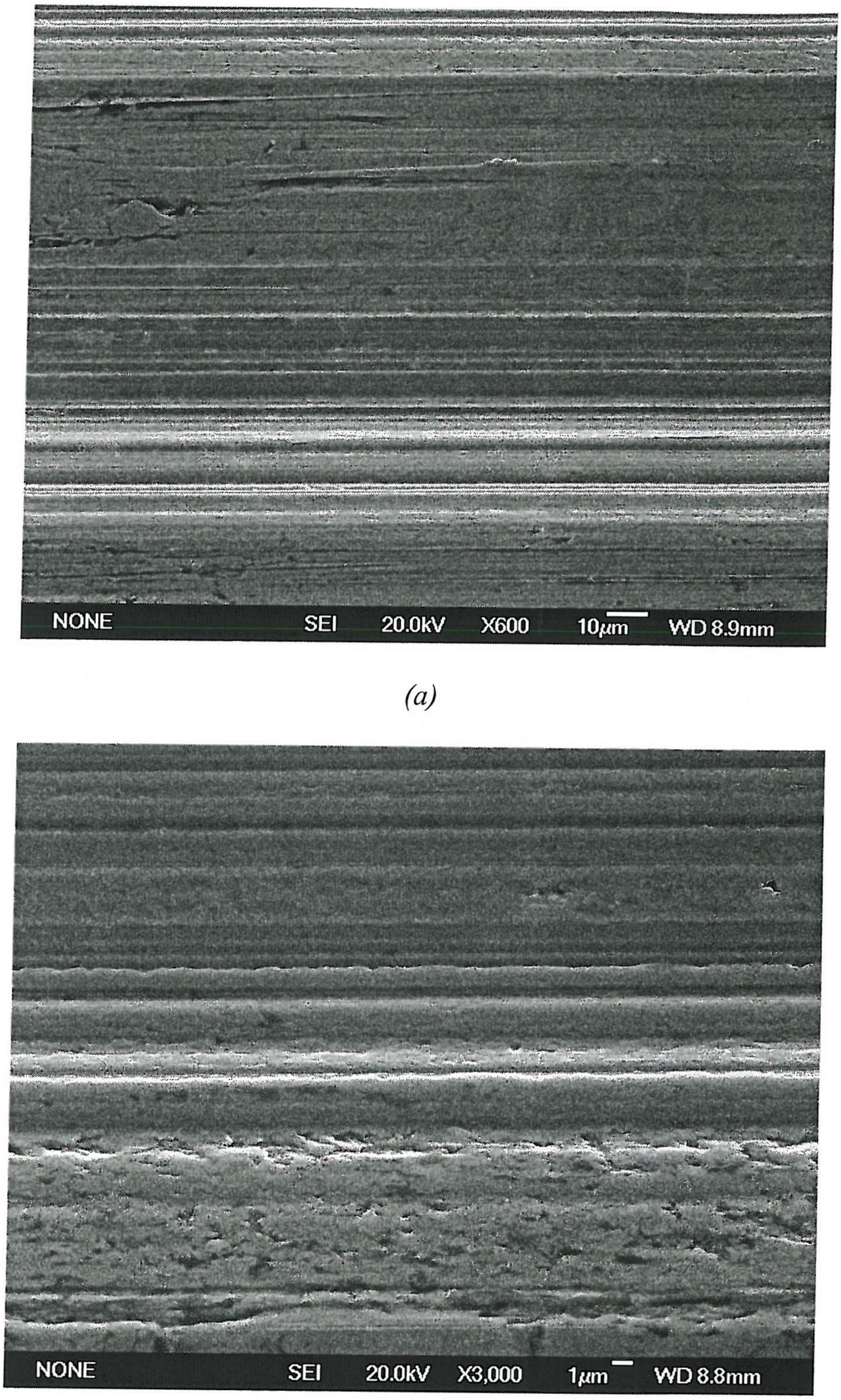

(a)

(b)

Figure 6.17 (a) Micrograph of the worn pin surface from Test 1 showing a smooth surface and striations. (b) Higher magnification micrograph of worn pin surface.

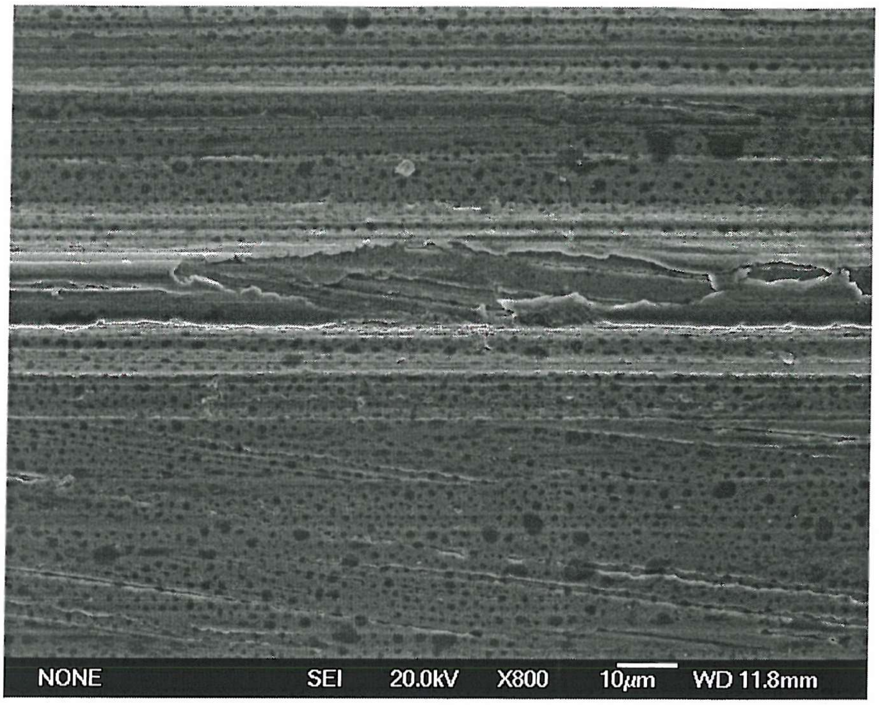

Figure 6.18 *Micrograph of the worn disc surface from Test 1 showing a smooth surface with some striations and delamination.*

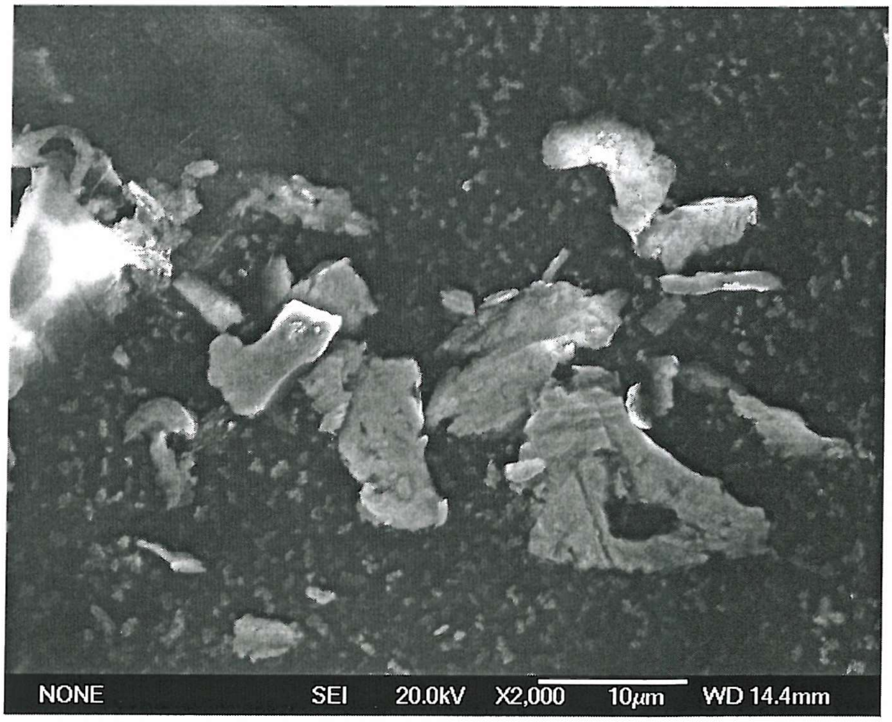

Figure 6.19 *Micrograph of wear debris from Test 1.*

6.4.2 Test 2 - Steel Debris Seeded

To preclude any charge features associated with the seeding procedure, a controlled test was performed using oil droplets only (no debris). From this test it was found that the seeding procedure does not produce any charge feature. It was then concluded that in the subsequent seeded test, the charge features are related to only the entrainment and presence of seeded debris.

A background subtraction using the first 600 s after the start of the test was used to calculate a normalised colour map. From the background subtracted colour map of sensor 1, seen Figure 6.20, it is evident that there are increases in the positive and negative charge features during and after debris seeding. These features exist as bands of charge features on the disc. The magnitude of the positive and negative charge feature can be seen to start to decay to a base level shortly after debris seeding.

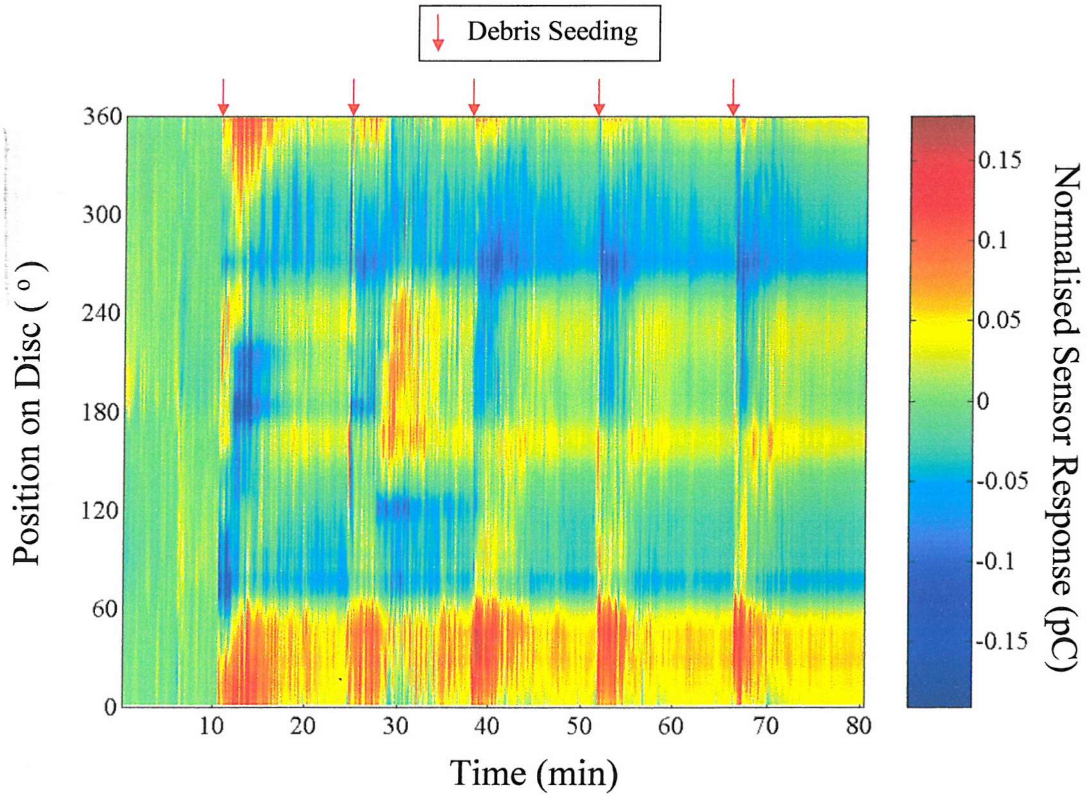

Figure 6.20 Normalised colour map of sensor 1 data showing an increase in charging activities steel debris was seeded into the contact. Steel seeded debris, Shell Vitrea ISO 460, load = 50 N, sliding speed = 5 ms^{-1}, initial λ = 22.

The normalised signal averages for sensor 1 in Figure 6.21 shows the charge during all the debris seeding events relative to the background level. Both positive and negative charge change was observed and their magnitude appears to be comparable.

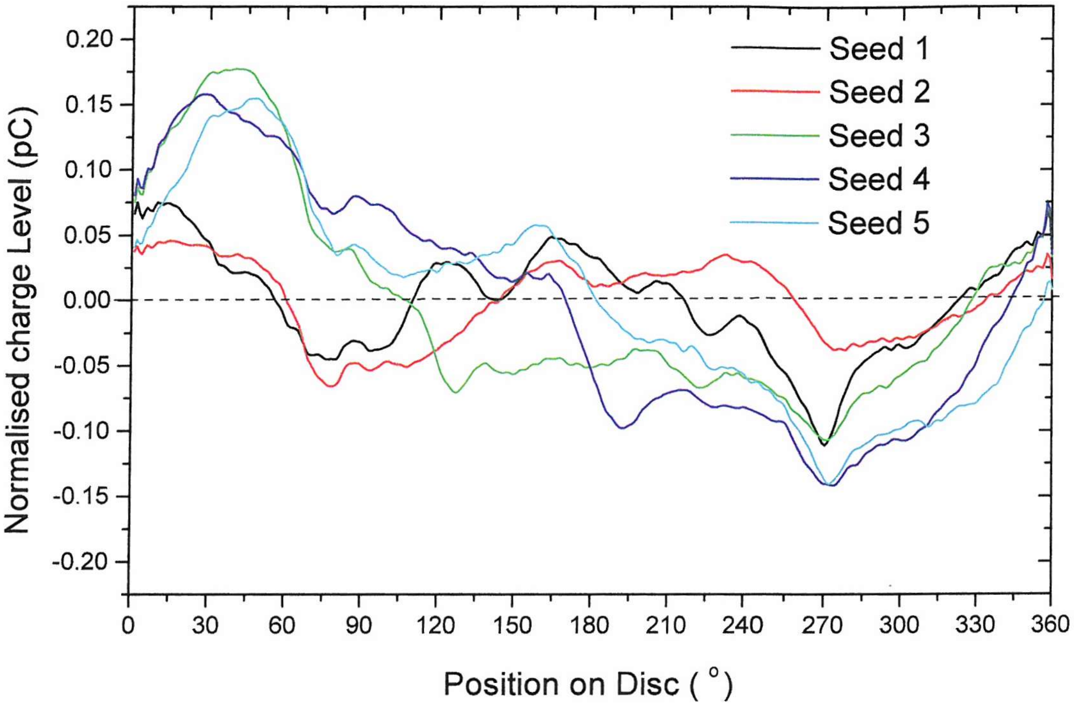

Figure 6.21 Sensor 1 background subtracted once per revolution charge line plots taken during all the debris seeding events. Steel seeded debris, Shell Vitrea ISO 460, load = 50 N, sliding speed = 5 ms^{-1}, initial λ = 22.

Figure 6.22 shows a series of sensor 1 normalised signal average taken prior to, during and after the first and the second debris seeding event. Prior to the first debris seeding, the charge level was relatively low. From both plots it is evident that during debris seeding negative charge features appeared between, respectively, 60°-120° and 250°-300°. There are also positive charge features at between 330°-50° and 150°-240°. Signal averages after the debris seeding show that the position of the charge features remained in the same position but their respective magnitudes decreased gradually. The charge level did not return to the level prior to debris seeding for the first debris seeding. A possible explanation of this is that the wear process has altered the surface topography. In contrast, the charge level returned to the level prior to seeding for the second event. At this point the surface topography of the wear track after debris seeding is thought to be similar to that prior to the second seeding process.

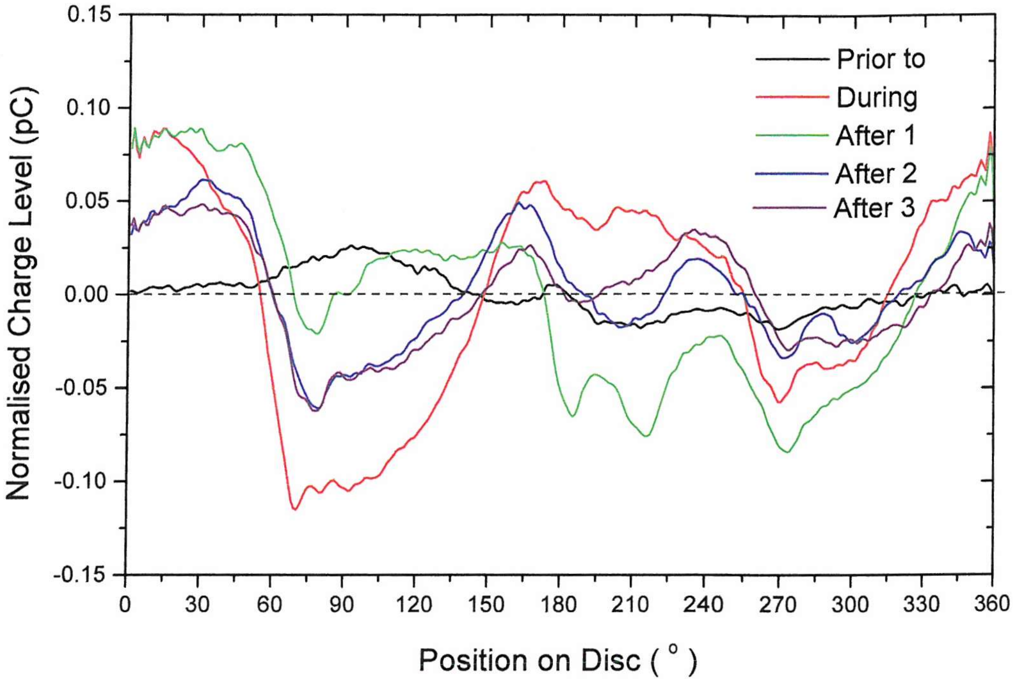

(a)

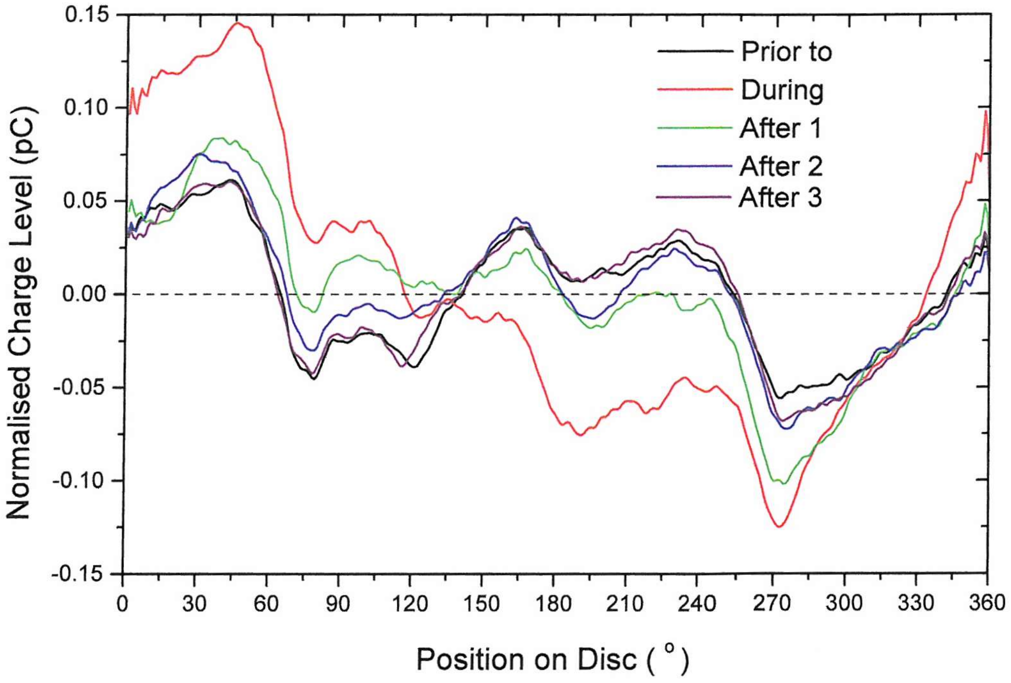

(b)

Figure 6.22 Signal average plots of sensor 1 background subtracted data prior to, during and after (a) the first and (b) the second debris seeding events. Steel seeded debris, Shell Vitrea ISO 460, load = 50 N, sliding speed = 5 ms^{-1}, initial λ = 22.

Figure 6.23 is a colour map of sensor 2 data showing that during debris seeding high magnitude charge features appear on the disc surface outside the wear track. Immediately after debris seeding, these charge features disappeared but negative dynamic charge features started to appear, which are present until the next debris seeding event. The frequency of the dynamic negative features increases after each successive debris seeding.

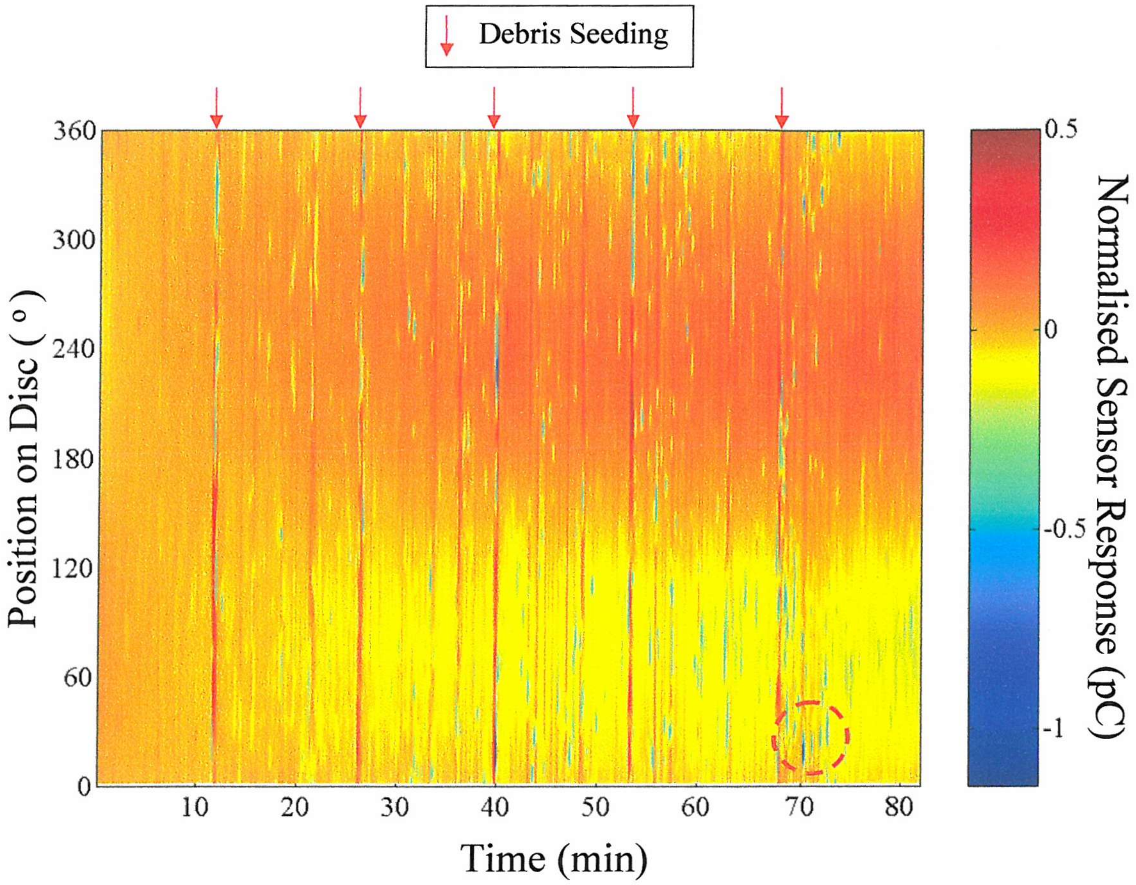

Figure 6.23 Normalised colour map of sensor 2 data showing an increase in charging activities and the appearance of dynamic negative charge features after steel debris was seeded into the contact. Steel seeded debris, Shell Vitrea ISO 460, load = 50 N, sliding speed = 5 ms^{-1}, initial $\lambda = 22$.

Figure 6.24 shows a close up of the region indicated by a red circle on Figure 6.23, which shows that a negative charge feature is moving its position from approximately 18° to 30° on the disc surface with the progression of time.

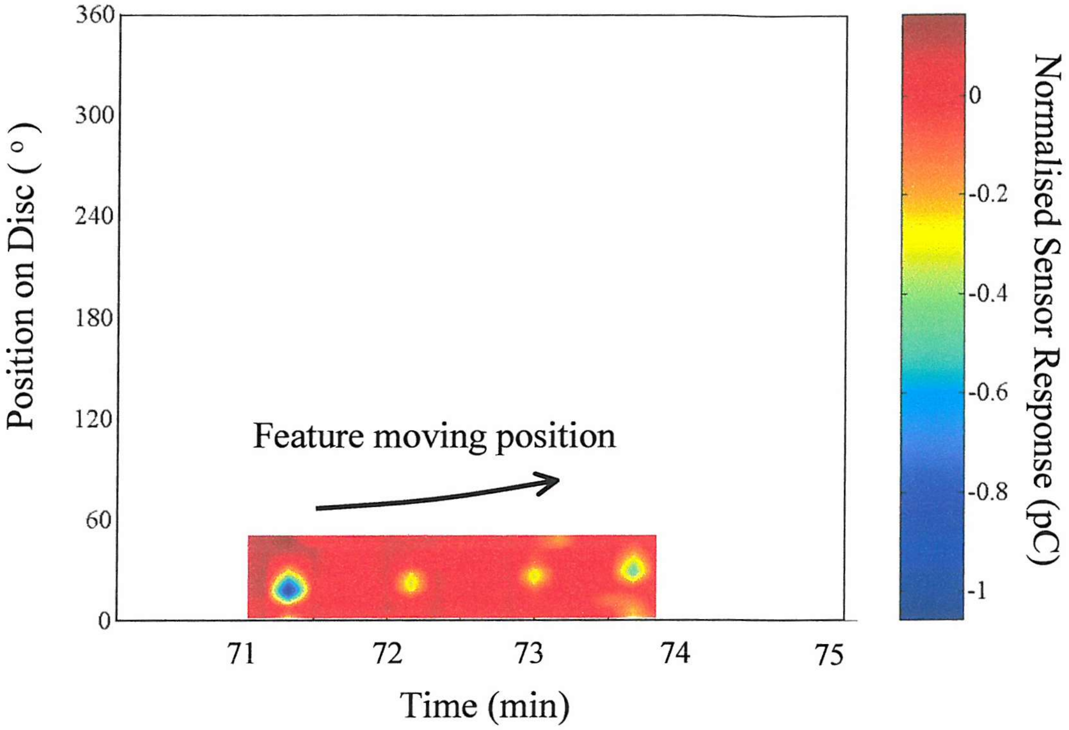

Figure 6.24 Close-up of the circled region in Figure 6.23 showing the presence of dynamic highly negative charge features. Steel seeded debris, Shell Vitrea ISO 460, load = 50 N, sliding speed = 5 ms^{-1}, initial λ = 22.

Figure 6.25 shows normalised signal average plots of the negative dynamic charge events shown in Figure 6.23 at 71 minutes and 140 seconds later. The negative charge feature is from a single charge source and appears to move 15° on the disc surface in the space of 140 seconds.

These dynamic features detected by sensor 2 were thought to be due to a combination of negatively charged entrained and normal wear debris due to the induced wear being centrifuged out of the contact area.

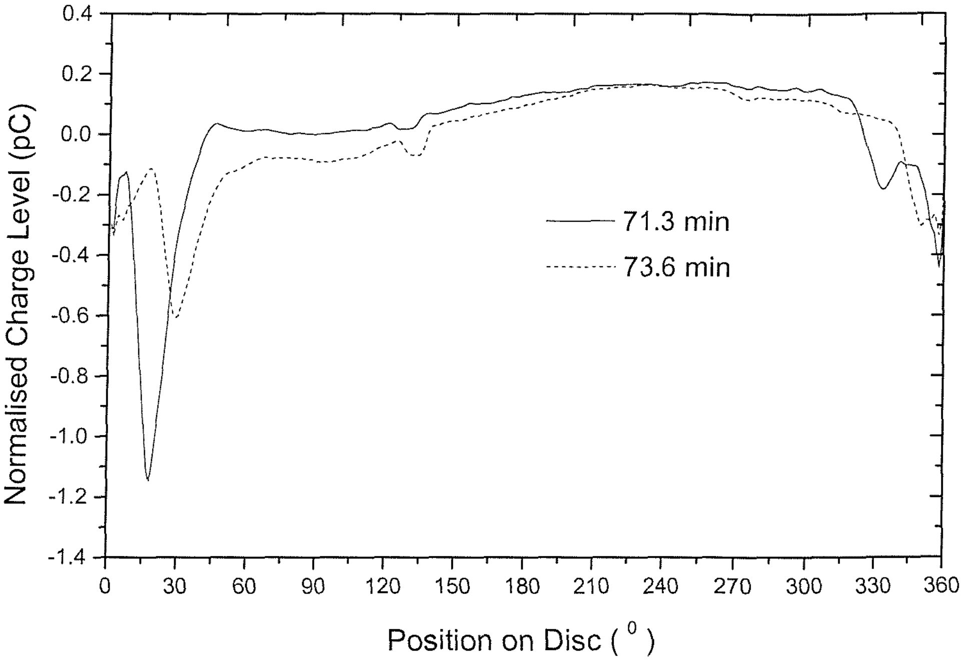

Figure 6.25 Normalised signal averages from sensor 2 at 4220 seconds and 4360 seconds showing a negative charge feature moving location on the disc surface. Steel seeded debris, Shell Vitrea ISO 460, load = 50 N, sliding speed = 5 ms^{-1}, initial $\lambda = 22$.

The graph of charge, volume loss, specific wear rate and coefficient of friction against time in Figure 6.26 shows that there were no significant charging activities present before debris seeding was carried out. During and just after the first debris seeding, the charge detected by sensor 1 increases abruptly before decreasing. After about a minute the charge increased slightly from this level and subsequently decays towards the baseline level. These trends were repeated for each subsequent debris seeding stages, indicating that charging is directly related to the severity of wear.

It is evident that during the seeding of steel debris (indicated by dotted line), there is a sudden increase in the level of charge detected by sensor 2, which reaches a peak before decreasing back to the original level. Several minutes after this however, fluctuations started to occur while retaining the same baseline level. The magnitude of the fluctuations peaks after several minutes and it is also evident that the magnitude of these fluctuations increases with each successive debris seeding. The charge increase during seeding was due to charged seeded and wear debris being centrifuged out together with the extra volume of oil. The increase in the charging activity several minutes after seeding can be explained by the time it takes for the wear debris induced by the seeding process to be centrifuged out of the wear track and detected by sensor 2.

The plot of volume loss shows that sudden increases in the rate of volume loss occur after debris seeding (indicted by the dotted line). This high rate of volume loss typically lasted for about 4 minutes before decreasing to a lower rate. Volume loss per seeding stage is approximately 1000 times higher than the unseeded Test 1.

The specific wear rate (obtained using Equation 5.1 on page 112) increases abruptly after each seeding followed by a gradual decrease. It is also interesting to note that the magnitude of the step increase in the specific wear rate decreases after successive seeding stages. This is due to the increase in the contact area resulting from further wear and hence the decrease in the contact pressure. As the severity of the contact condition is decreased, the induced wear, for the same amount of seeded debris is reduced.

The coefficient of friction before debris seeding is approximately 0.08. This changes to approximately 0.12 after the first debris seeding event due to the increase in the surface roughness due to induce wear and generally remains unchanged until the end of the test. There are fluctuations during debris seeding due to the abrasive interactions of the seeded debris with the contact surfaces.

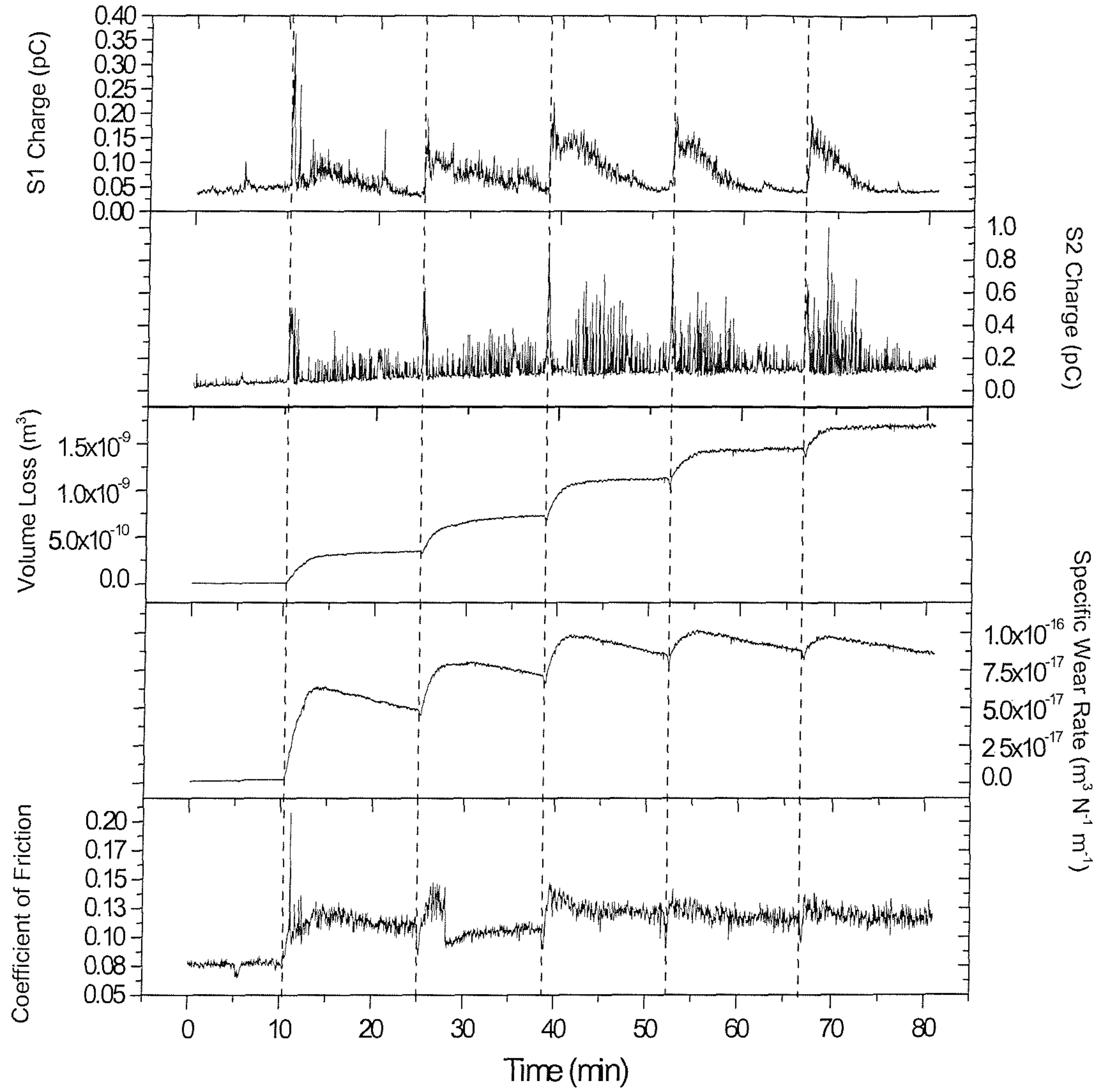

Figure 6.26 A plot of charge, volume loss, specific wear rate and coefficient of friction against time. Steel seeded debris, Shell Vitrea ISO 460, load = 50 N, sliding speed = 5 ms^{-1}, initial λ = 22.

A comparison of sensors 1 and 2 data in Figure 6.26, shows the difference in the baseline level due to debris seeding. The baseline in sensor 1 increases dramatically during and after debris seeding before decreasing gradually, whilst sensor 2 baseline charge drifted up gradually throughout the test. The magnitude of the charge features detected by sensor 1 is highest during seeding before gradually decreasing towards the original level prior to debris seeding. The charge baseline in sensor 2 on the other hand was not altered by debris seeding since it only picks up fluctuations due to the presence of negatively charged debris. The gradual increase in the sensor 2 baseline is caused by the increasing number of debris present on the disc surface outside the wear track.

In summary, it was observed that after debris seeding charge activity, volume loss and specific wear rate increased due to the increase in wear. Friction increased only after the first debris seeding events due to the increase in the surface roughness of the contacting surfaces.

Surface profilometry

The wear scars of the pin and disc wear scar from Test 2 are relatively large being just under 7 mm in width, as shown in Figure 6.27. The surfaces are also relatively rough, especially at the centre of the wear scar, with a maximum depth of the disc wear scar of about 7 μm.

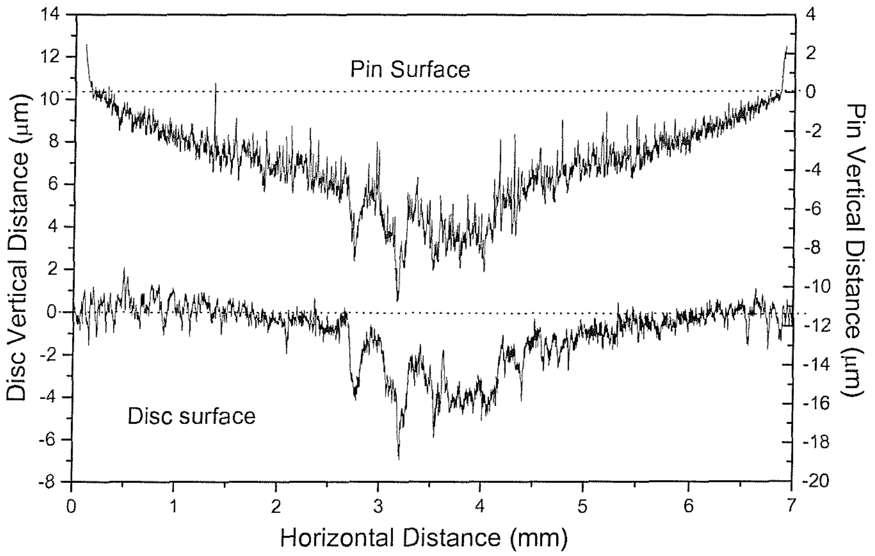

Figure 6.27 Surface profilometry of pin and disc from Test 2.

Scanning Electron Microscope (SEM) micrographs

The micrographs of the worn pin surface in Figure 6.28, clearly shows the presence of parallel grooves and surface indentations and microfractures. The grooves are manifestations of two-body (grooving) abrasion while the latter indicates three-body (rolling) abrasion. Upon further inspection of the wear scar, it was found that parallel grooves dominate the wear surface. This indicates that the predominant wear mechanism in Test 2 was two-body abrasion. From Figure 6.28 (b) it can be seen that parts of the ridge formed (due to two-body abrasion) are about to break off. During the test they will eventually break off after multiple passes to form wear debris. The width of the grooves corresponded well with the size of the seeded steel debris indicating that the grooving was not caused by asperities on the disc but from seeded steel debris embedded on the disc surface. Figure 6.29 shows evidence of seeded debris embedding on the pin surface. The higher magnification image (Figure 6.29 (b)) reveals a crater formed due to the dislodging of the embedded seeded debris during the cleaning process prior to SEM micrography. Figure 6.30 shows the micrographs of the worn disc track showing the evidence of the presence of both three-body and two-body abrasive wear. Further inspection of the worn disc surface reveals that three-body abrasion was predominant. The grooves seen in Figure 6.30 (b) correlates well with the seeded debris size. Figure 6.31 shows a seeded debris that has been embedded onto the wear surface of the disc and could have been responsible for two-body wear mechanism of the pin.

A micrograph of the steel debris before seeding, shown in Figure 6.32 (a), shows that they are spherical and typically 9 μm in diameter. Figure 6.32 (b) shows wear debris collected at the end of Test 2, which consist of two size groups. The larger debris generally has a size of >10 μm and the smaller debris <5 μm. The larger debris is thought to originate from deformed seeded steel debris as its size is well within the size range of the unseeded steel debris. The smaller debris is thought to originate from the spalled fragments of ridge formed by two-body abrasion and also surface microfracture due to three-body (rolling) abrasion. The presence of undeformed seeded steel debris can also be seen indicating some of them were not entrained into the contact.

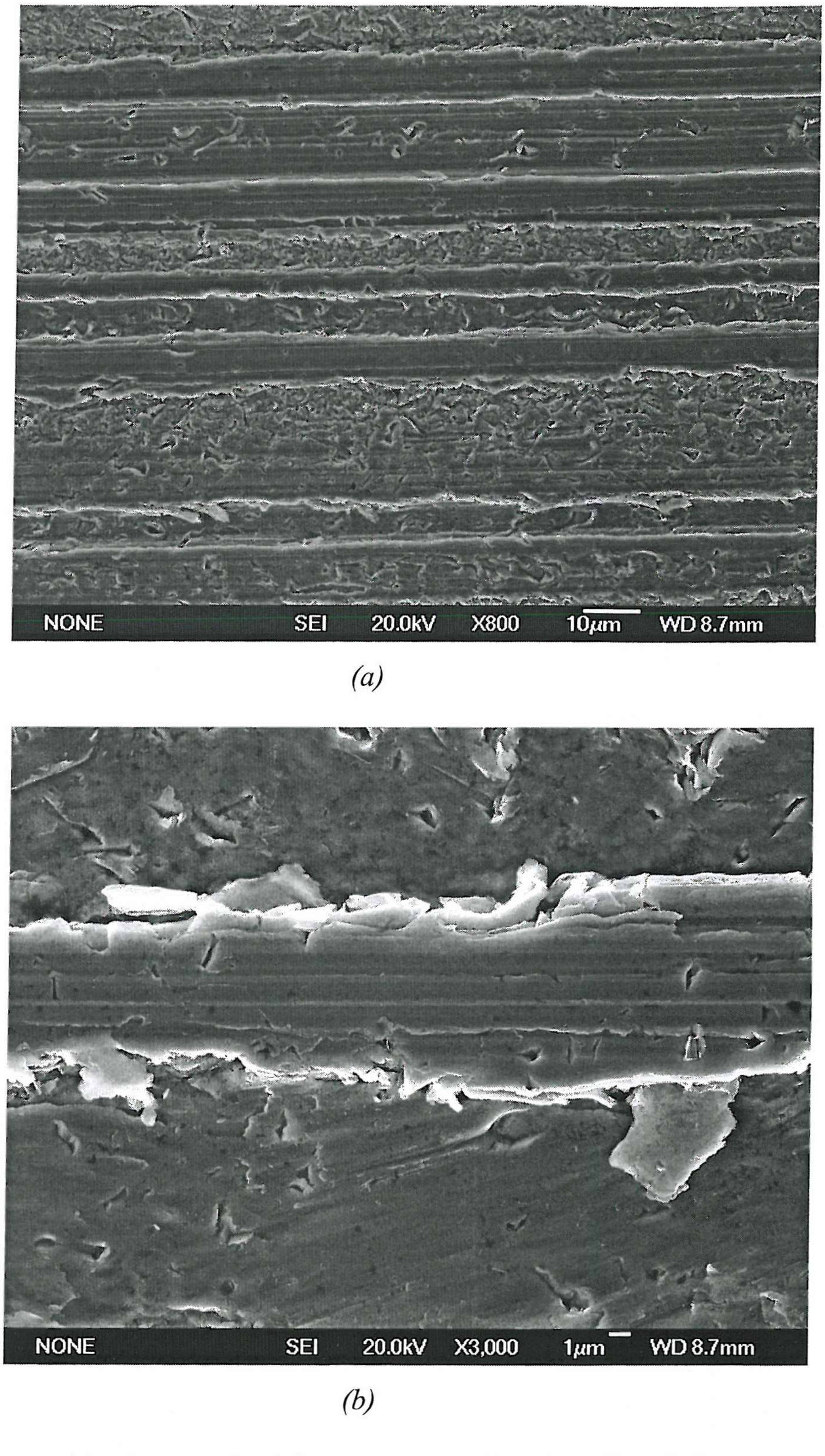

(a)

(b)

Figure 6.28 *(a) Micrograph of the pin worn surface from Test 2 showing parallel grooves and surface indentations and microfractures. This indicates the presence of both two-body and three-body abrasion. (b) Higher magnification micrograph of the pin worn surface from Test 2 showing a groove formed by two-body abrasion.*

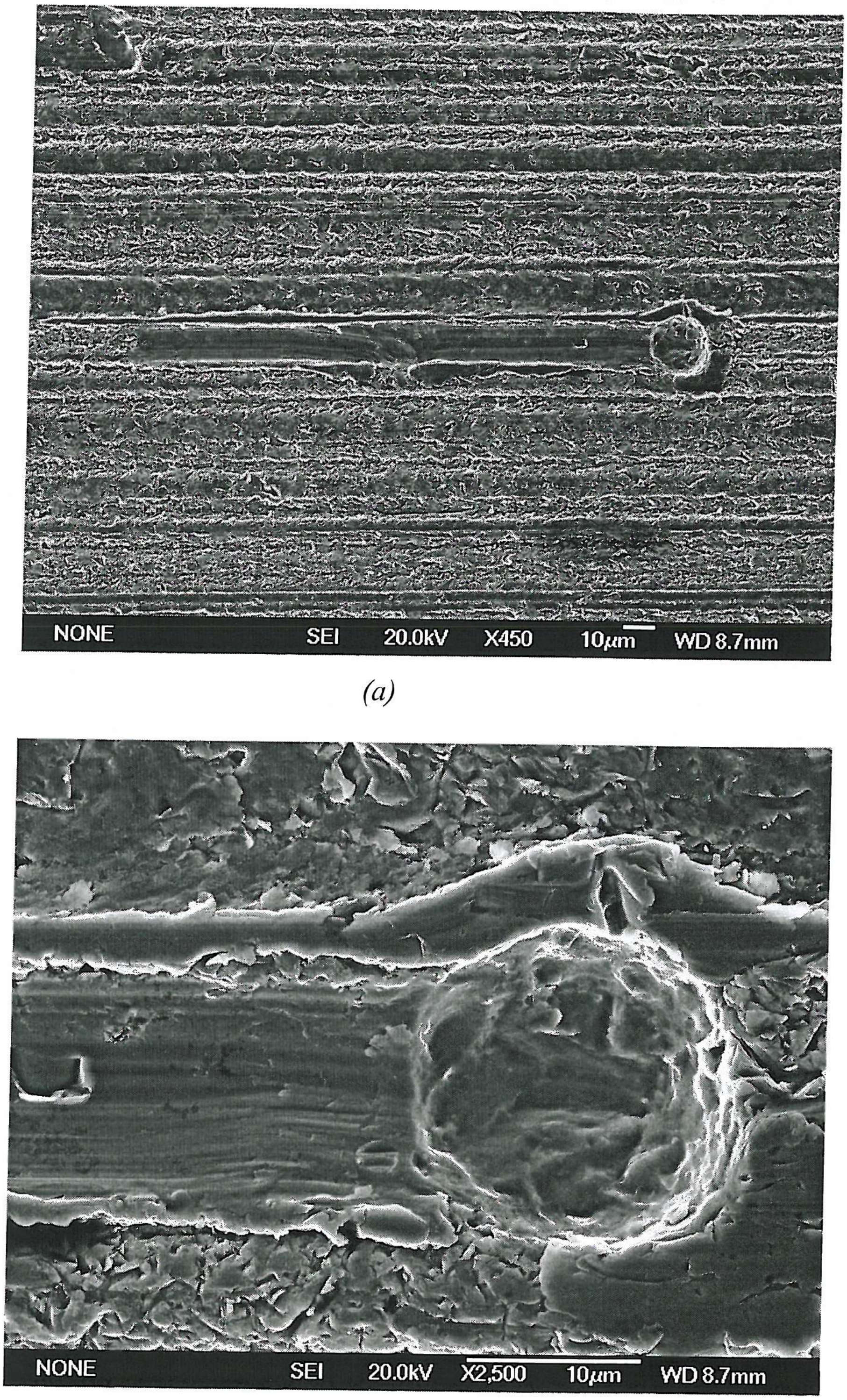

(a)

(b)

Figure 6.29 *(a) Micrograph of the pin worn surface from Test 2 showing a sign of seeded debris embedment onto the pin surface. (b) Higher magnification micrograph of (a) showing a crater formed as a result of the embedded seeded steel debris.*

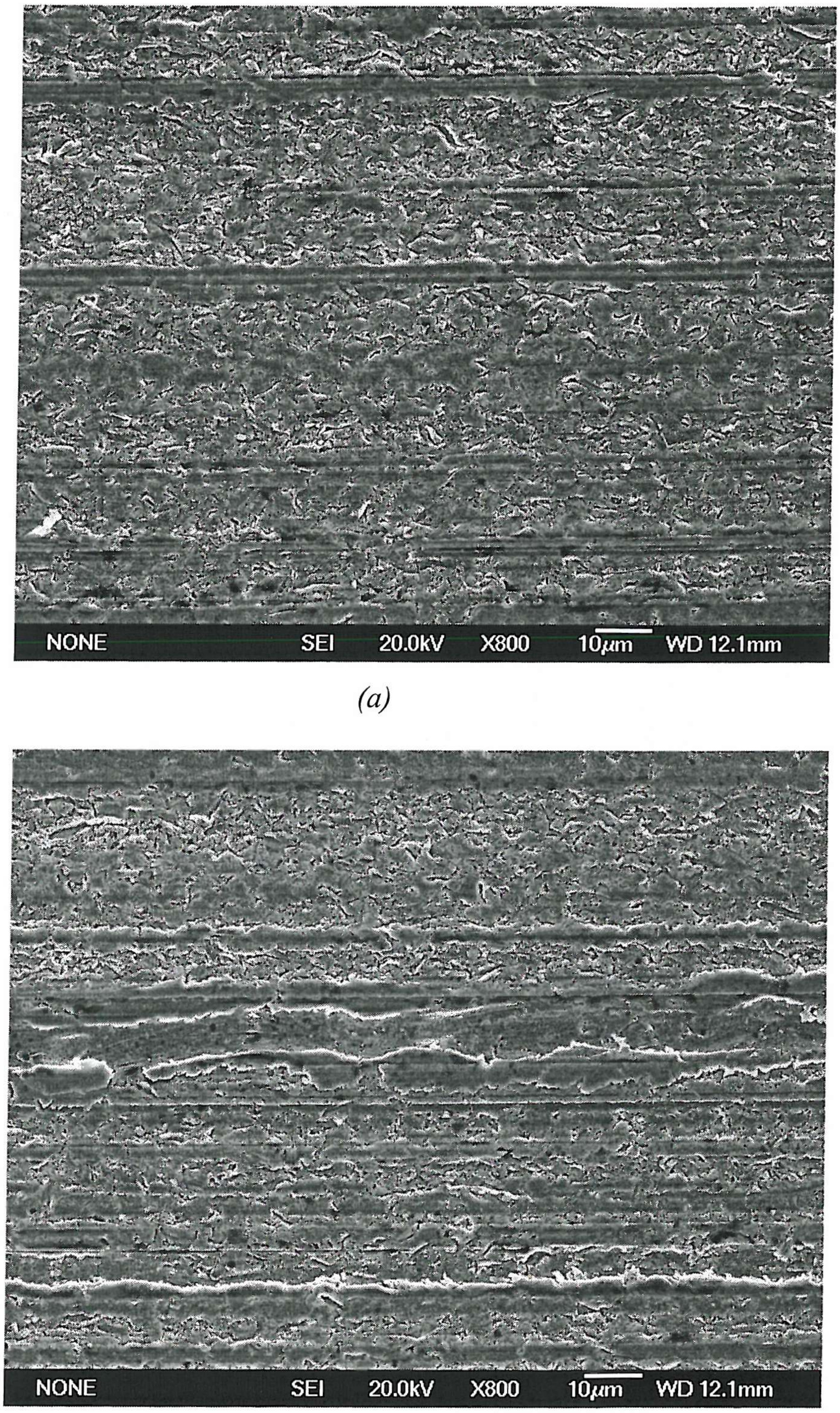

(a)

(b)

Figure 6.30 (a) Micrograph of the disc worn surface from Test 2 showing parallel grooves and surface indentations and microfractures. This indicates the presence of both two-body and three-body abrasion. The width of the groove is smaller than the average size of the seeded debris while (b) shows grooves that are comparable to the seeded debris size.

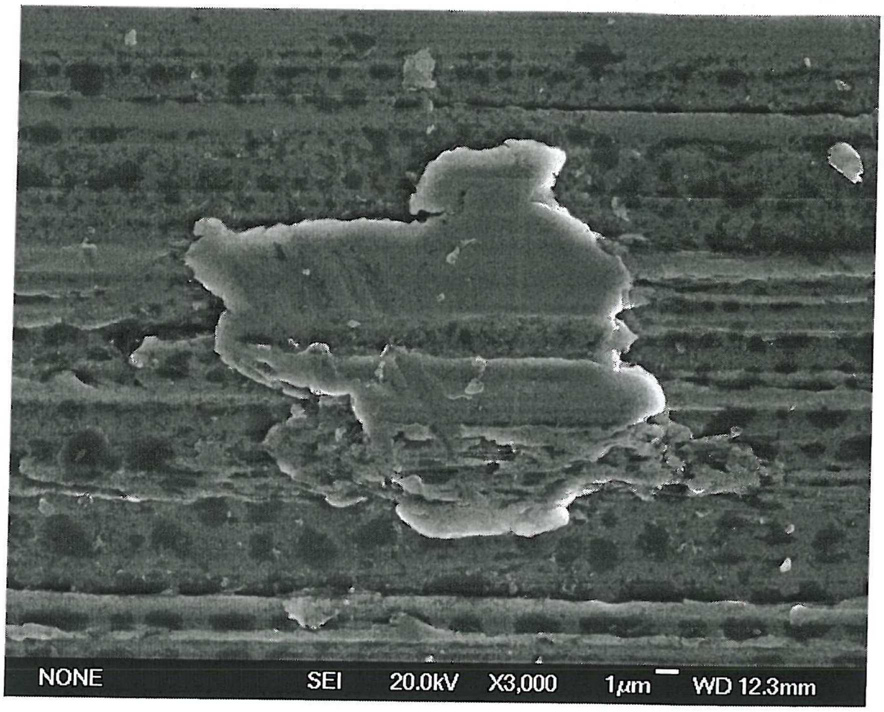

Figure 6.31 *Micrograph of the disc worn surface showing a flattened embedded seeded debris.*

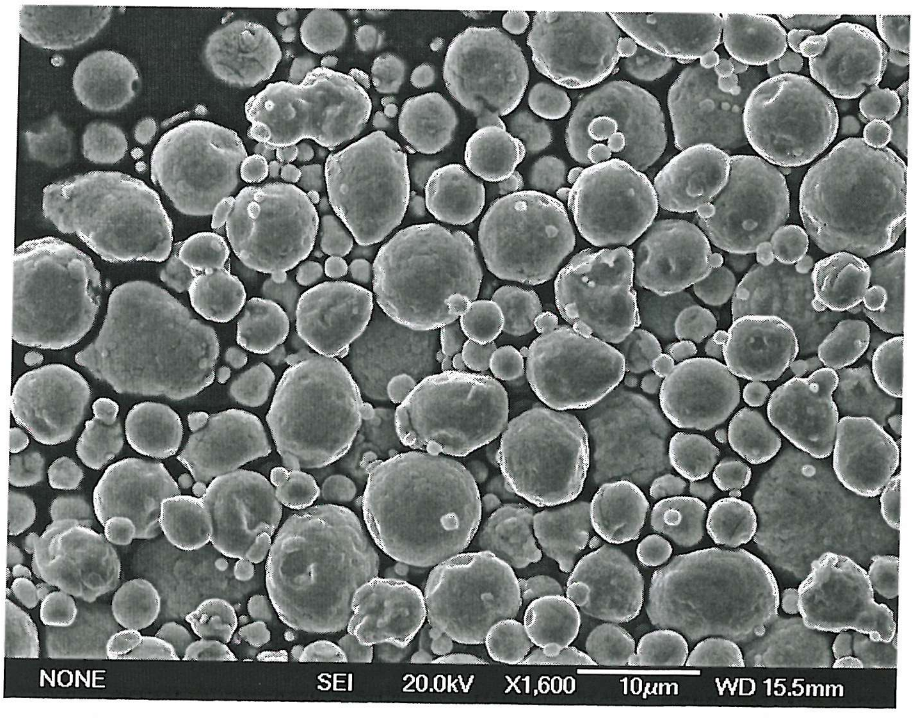

(a)

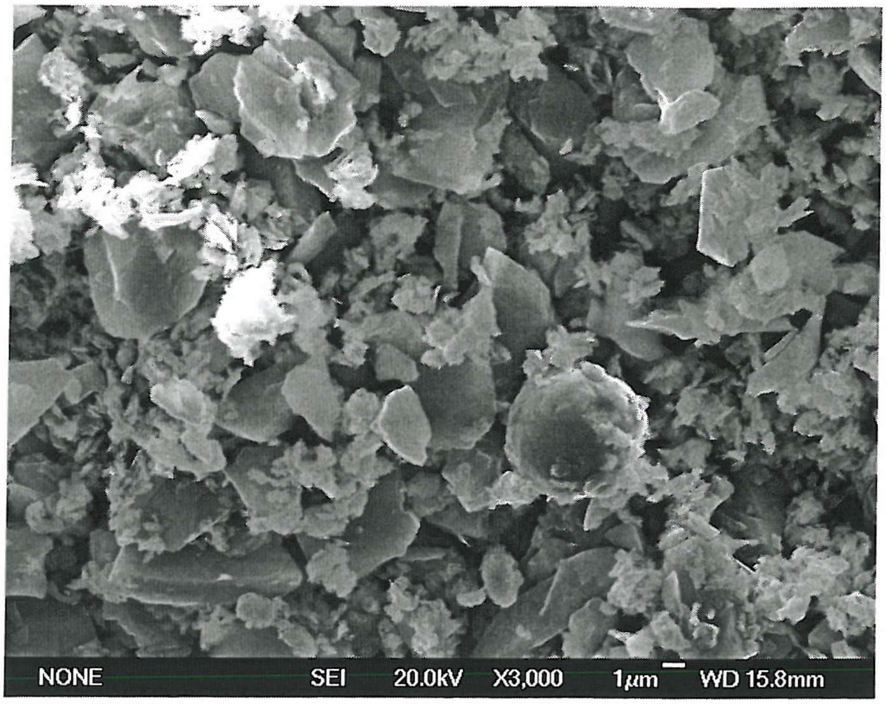

(b)

Figure 6.32 Micrograph showing steel debris (a) before and (b) after seeding.

6.4.3 Test 3 - Silicon Carbide Debris Seeded

A normalised colour map of sensor 1 data, see Figure 6.33, shows that after each debris seeding event, the charging activities increase abruptly before slowly decaying to a baseline level, similar to observations made during Test 2. Charge features consisted of positive and negative charge bands at positions of about 80° and 260°, respectively. Charge persistence was examined by lifting the contact after the last seeding event and it was found that all charge features disappear and a background level was attained. This is strong evidence that the detected charge did not persist and does not reside on the surface of the wear track but rather is due to the presence of seeded and wear debris and their interactions with the contact. The charge level from the effect of contact potential difference on the wear track due to the formation of active wear sites in this case is minimal compared to the overall charge detected. All significant charging was due to the entrainment of seeded particles and the formation of induced wear debris.

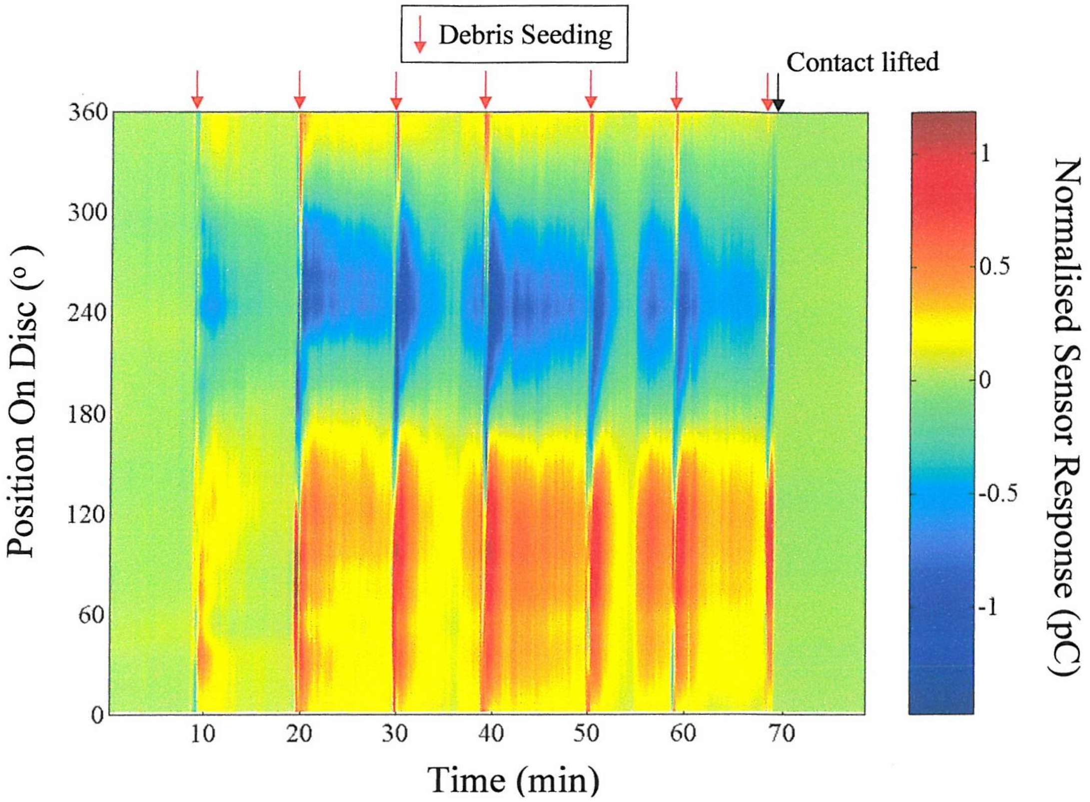

Figure 6.33 Normalised colour map of sensor 1 data showing an increase in charging activities during and after silicon carbide debris seeding. Silicon carbide seeded debris, Shell Vitrea ISO 460, load = 10 N, sliding speed = 5 ms^{-1}, initial λ = 7.

Figure 6.34 shows a plot of sensor 1 normalised signal averages taken prior to, during and after the first and second debris seeding event. Both plots show that, prior to seeding, a low level baseline charge exists. During seeding events the charge magnitude rose dramatically and is bipolar in nature. After seeding, the magnitude of these charge features starts to decrease towards the original background level. The explanation for this behaviour has been discussed in the discussion for Test 2 results earlier.

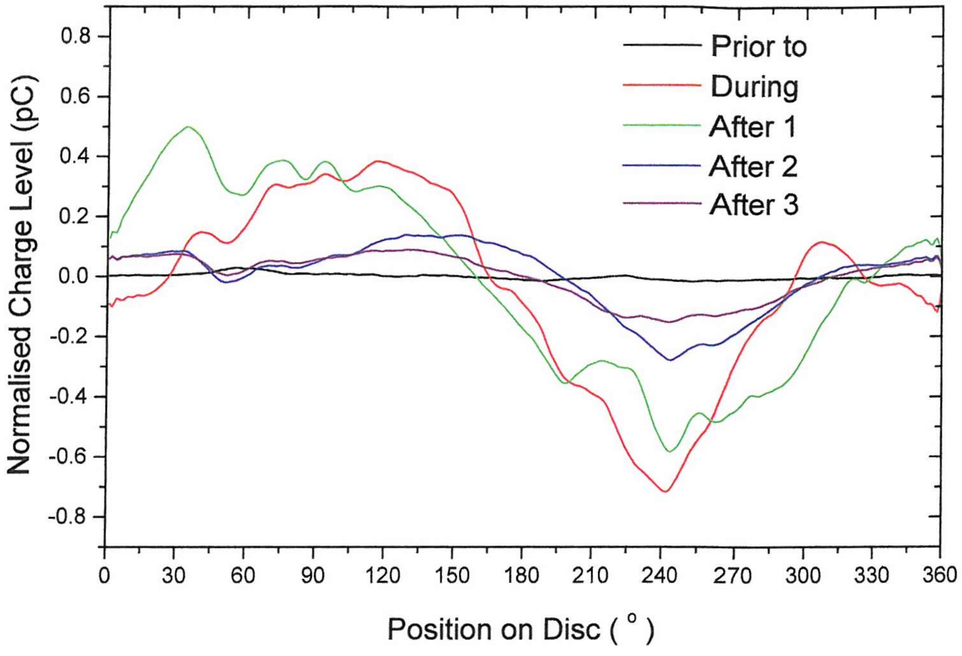

(a)

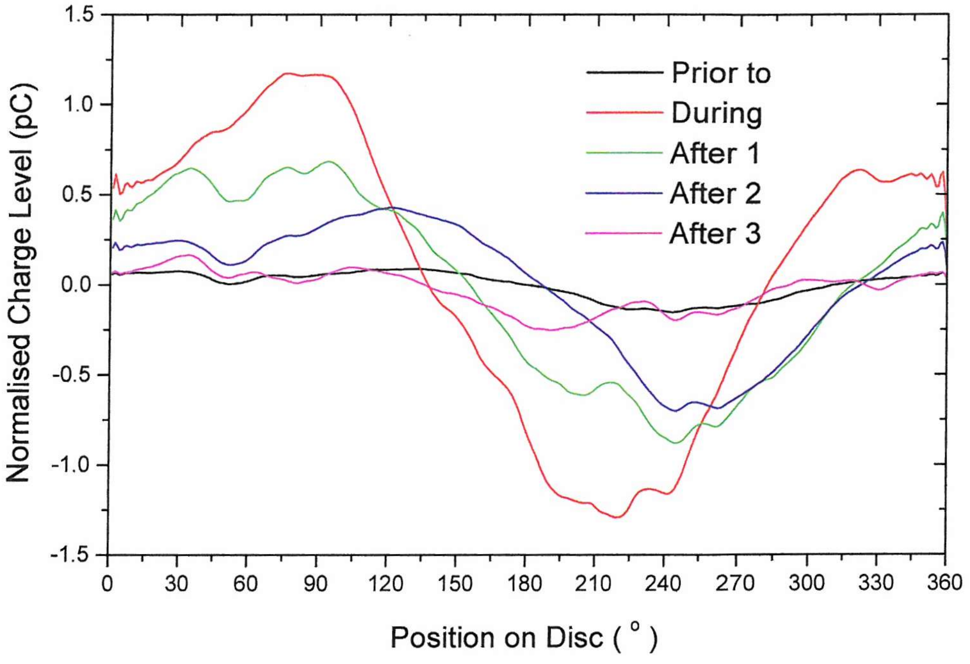

(b)

Figure 6.34 Normalised sensor 1 once per revolution signal average line plots taken prior to, during and after (a) the first debris and (b) the second debris seeding. Silicon carbide seeded debris, Shell Vitrea ISO 460, load = 10 N, sliding speed = 5 ms^{-1}*, initial* $\lambda = 7$*.*

A normalised colour map plot of sensor 2 data, see Figure 6.35, indicates that during debris seeding (indicated by dotted lines) charge increases dramatically and a magnified view showing typical charge feature is shown in Figure 6.36. These plots show that highly positive and negative charge features exist on the disc surface during debris seeding.

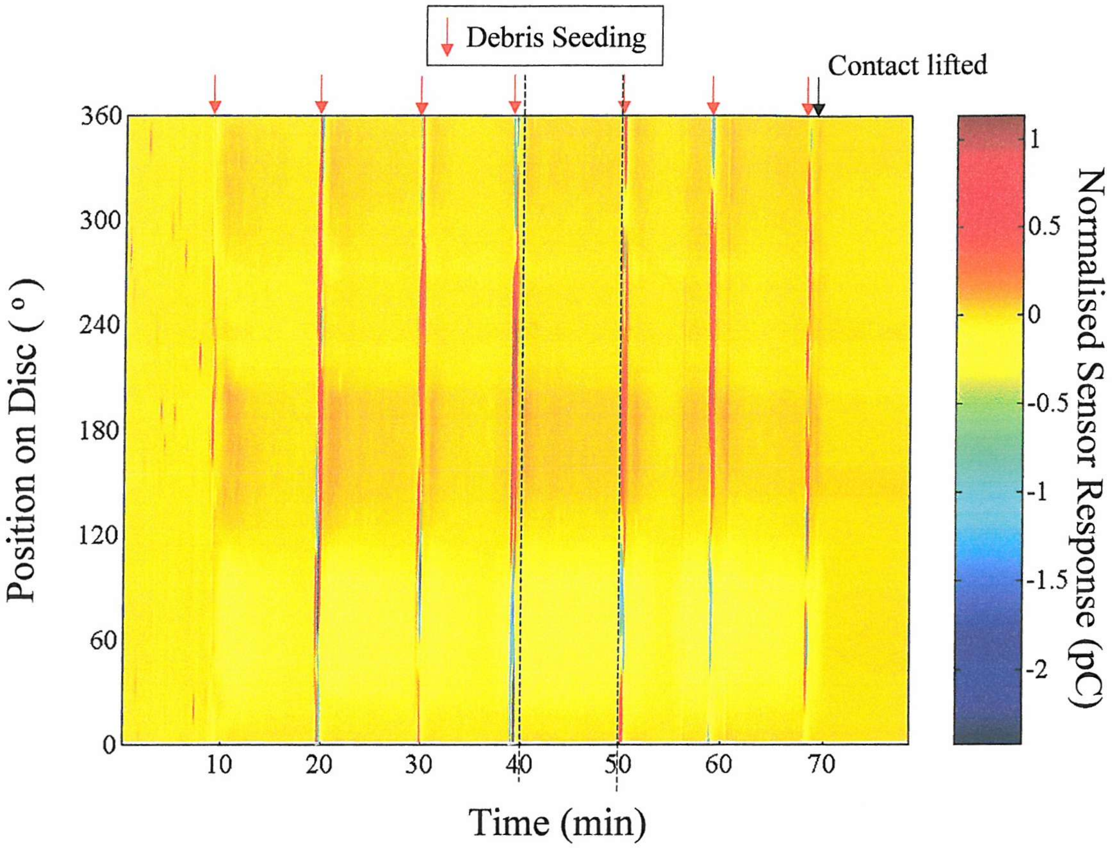

Figure 6.35 Normalised colour map of sensor 2 data showing an increase in charging activities silicon carbide debris was seeded into the contact. Silicon carbide seeded debris, Shell Vitrea ISO 460, load = 10 N, sliding speed = 5 ms^{-1}, initial $\lambda = 7$.

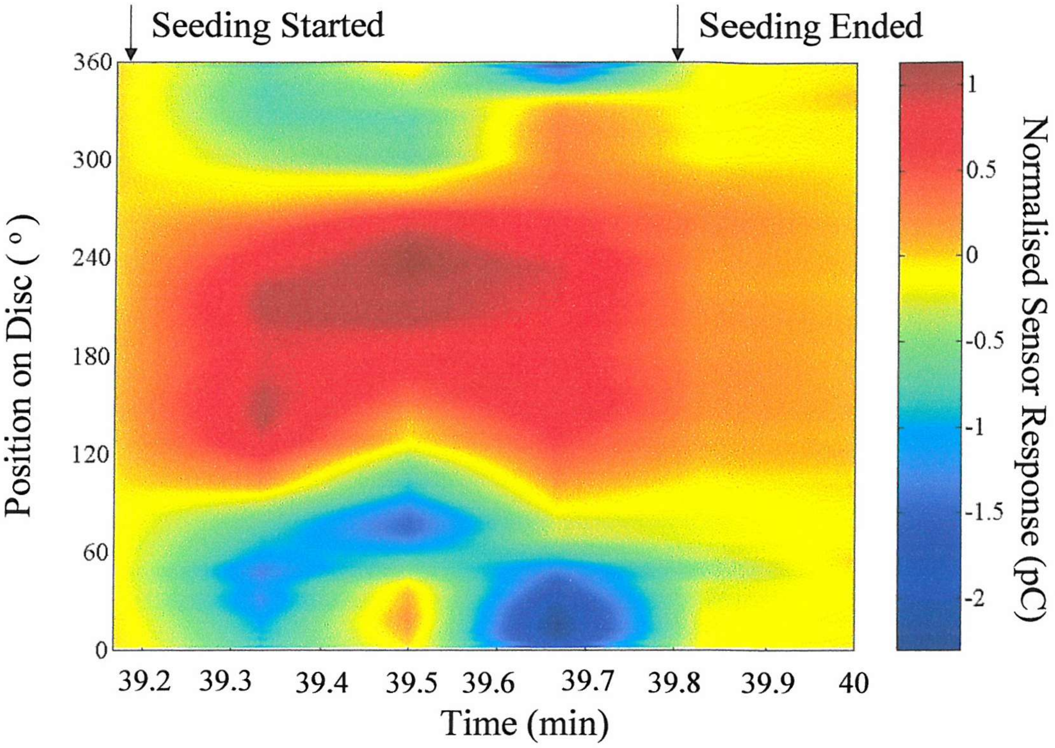

Figure 6.36 Normalised colour map for sensor 2 showing typical charge features during debris seeding. Silicon carbide seeded debris, Shell Vitrea ISO 460, load = 10 N, sliding speed = 5 ms^{-1}, initial λ = 7.

Figure 6.37 is a magnified view of the area indicated by the dotted line in Figure 6.35 showing dynamic negative charge features and some have been marked with dotted circles. It should be noted that these features are relatively small in magnitude compared to charge activity during debris seeding.

Figure 6.38 shows dynamic negative charge events signal averages at 4280, 4300 and 4310 seconds (circa 71 min) into the test. These dynamic features observed in Figures 6.37 and 6.38 is a 'tell tale' indication of the presence of negatively charged wear debris being centrifuged out of the wear track.

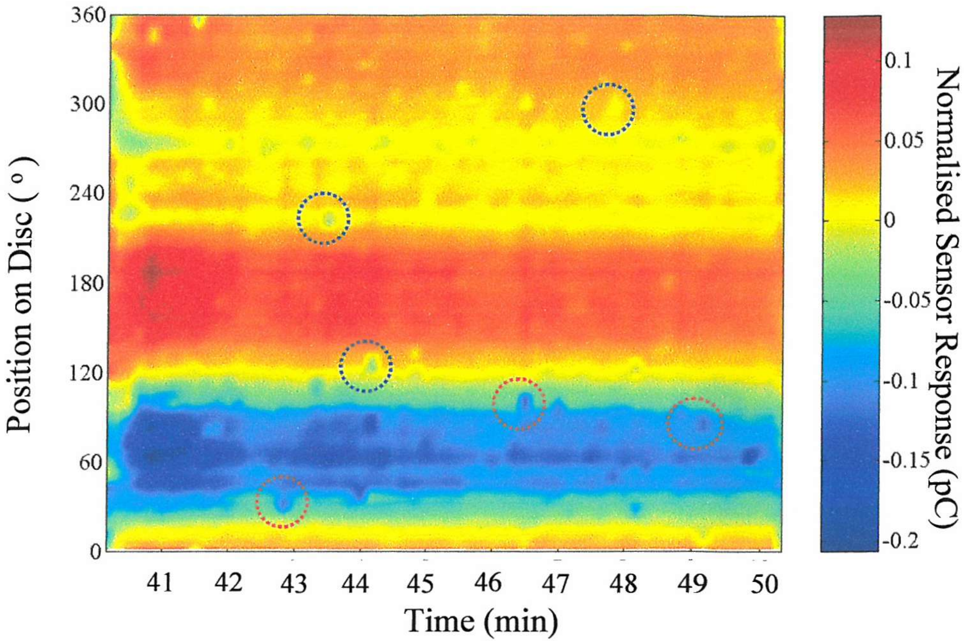

Figure 6.37 Close-up of the region marked by the dotted lines in Figure 6.36, excluding the debris seeding events, showing the presence of dynamic highly negative charge features. Silicon carbide seeded debris, Shell Vitrea ISO 460, load = 10 N, sliding speed = 5 ms^{-1}, initial λ = 7.

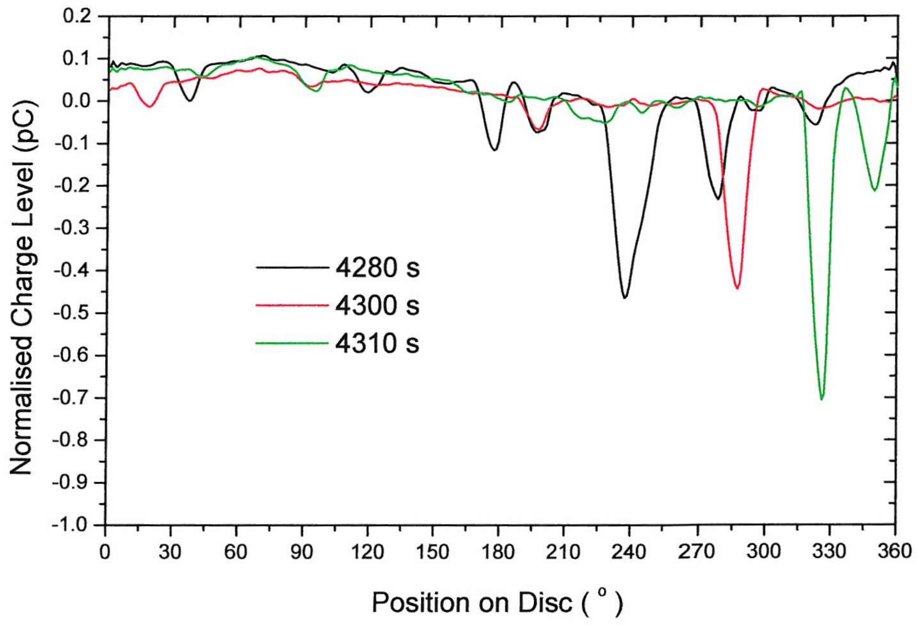

Figure 6.38 Normalised signal average from sensor 2 at 4280 seconds, 4300 seconds and 4310 seconds into the test showing high negative charge feature moving on the disc surface. Silicon carbide seeded debris, Shell Vitrea ISO 460, load = 10 N, sliding speed = 5 ms^{-1}, initial λ = 7.

A plot of, respectively, charge, volume loss specific wear and coefficient of friction in Figure 6.39 shows that during seeding, charge detected by both sensors increases dramatically before decaying towards a baseline level, similar to Test 2. It is interesting to note that the base line level has increased after the first debris seeding, which is thought to be the result of the presence of charged debris on the wear track. It is also evident that, except for the first debris seeding event, the maximum charge during debris seeding decreases with increasing number of seeding stages. Sensor 2 charge plot shows that the magnitude of charging due to the debris seeding is much higher relative to the background charge level compared to sensor 1. When the contact was lifted during the development of charge features, it can be seen that charge on the surface decreased to a level similar to the start of the test (before debris seeding). The charge fluctuations seen before the first debris seeding event was caused by the formation of large oil droplets on the disc surface from the oil mist spray. This was corrected just before the first seeding event and the fluctuations disappeared.

The volume loss plot shows a large increase just after debris seeding, before gradually returning to a steady state level. The overall step increase in volume loss per debris seeding event decreased with subsequent debris seeding, similar to the trend of the maximum charge fluctuation during seeding. The same explanations used to explain similar observations during Test 2 apply here. Since there is a direct correlation between volume loss and charging, this can also explain the reduction in the magnitude of maximum charge during subsequent debris seeding, mentioned above.

The specific wear rate and coefficient of friction trend are similar to the trends observed in Test 2. The coefficient of friction plot shows that friction was approximately 0.09 before the first debris seeding event; however, during the first debris seeding stage, the value increased to 0.14 and remained steady throughout the test, albeit increasing slightly possibly due to the increased roughness of the contact surface as a result of further abrasive wear. During subsequent debris seeding stages, the values of the coefficient of friction increased temporarily before returning to a steady-state value as soon as the debris seeding was stopped. This is due to the abrasive wear interaction between the seeded debris and the contact surfaces.

In summary, debris seeding increases the wear rate which is reflected in the volume loss and specific wear rate plots, causing charging activities to increase and fluctuation in the coefficient of friction, similar to Test 2.

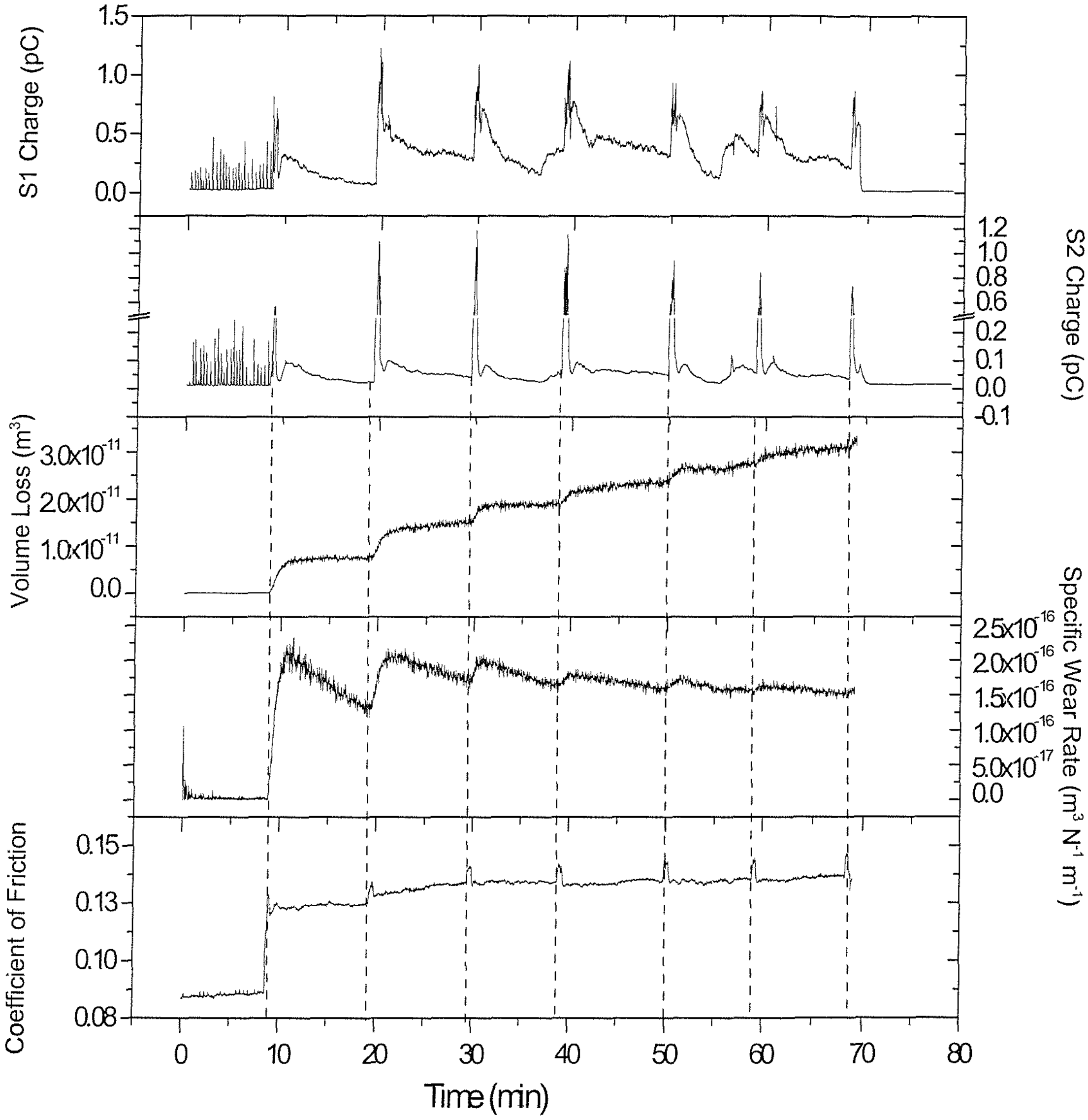

Figure 6.39 The plot of charge, volume loss specific wear rate and coefficient of friction for sensor 2. Silicon carbide seeded debris, Shell Vitrea ISO 460, load = 10 N, sliding speed = 5 ms^{-1}, initial λ = 7.

Surface profilometry

Comparing the scale of the surface profile from Test 3, the surfaces of the pin and disc are relatively smooth with wear mostly occurring at the centre of the track, with maximum disc wear depth of about 2.5 μm, as shown in Figure 6.40.

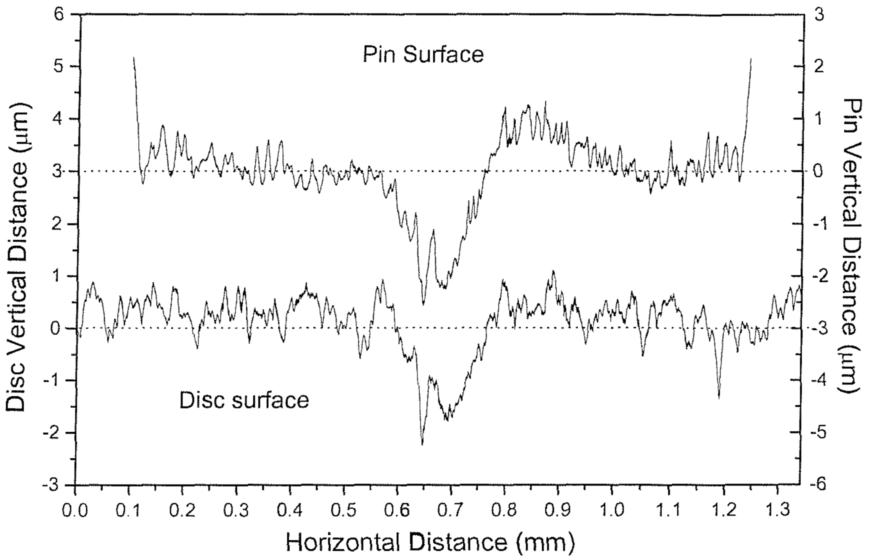

Figure 6.40 *Surface profilometry of pin and disc from test 3.*

Scanning Electron Microscope (SEM) micrographs

A micrograph of the pin wear scar, shown in Figure 6.41, shows that the surface is smooth with parallel and some non-parallel scratches. Microfracture is also evident on the disc surface as shown in Figure 6.41 (c), indicating three-body abrasion as the dominant wear mechanism.

Figure 6.42 shows silicon carbide debris before seeding which are 4-5 μm in size and angular. Figure 6.43 shows micrographs of the steel wear debris from Test 3 separated using a ferrographic technique (see Chapter 2) and generally exist in chunks larger than 50 μm. Despite the ferrographic process, some small silicon carbide particles were not separated, this was confirmed by EDX analysis (silicon carbide debris is circled in Figure 6.43 (c)). Comparing Figure 6.42 to Figure 6.43, it can be seen that the silicon carbide debris (circled in Figure 6.43 (c)) has been fractured due to entrainment. They were less angular than unseeded debris.

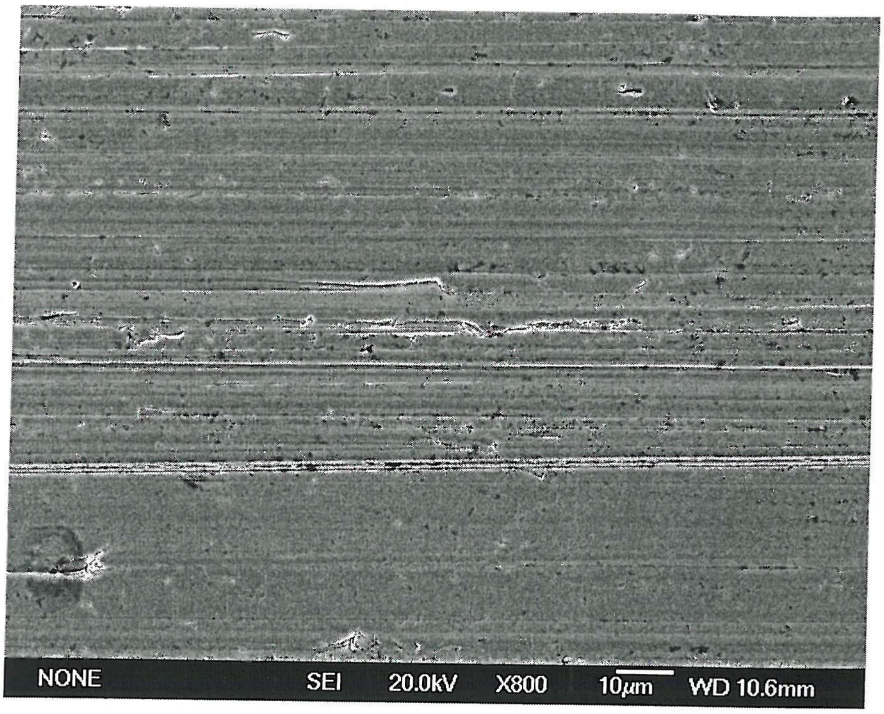
NONE
SEI
20.0kV
X800
10μm
WD 10.6mm

(a)

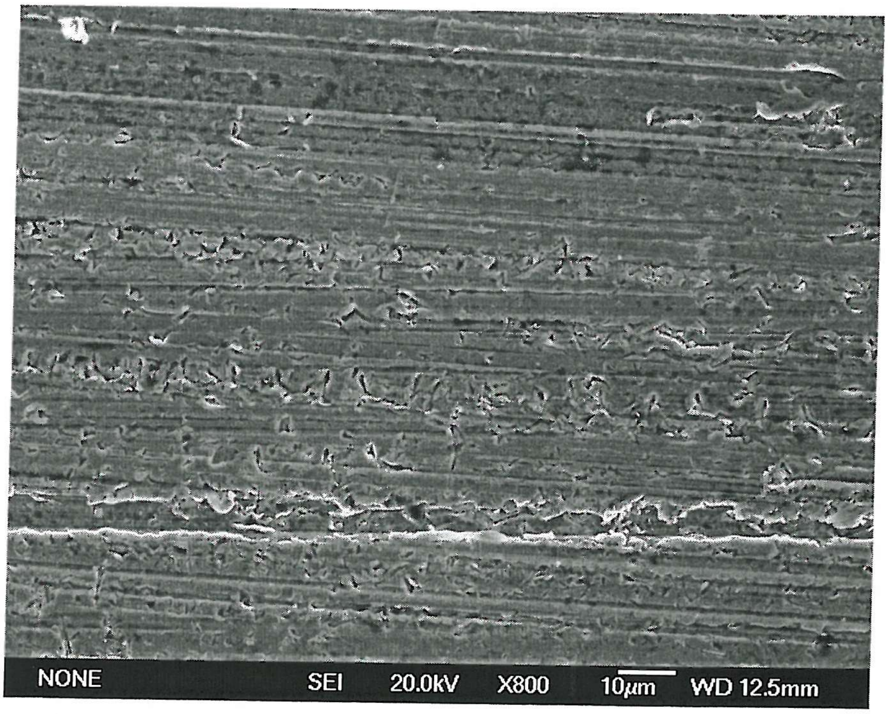
NONE
SEI
20.0kV
X800
10μm
WD 12.5mm

(b)

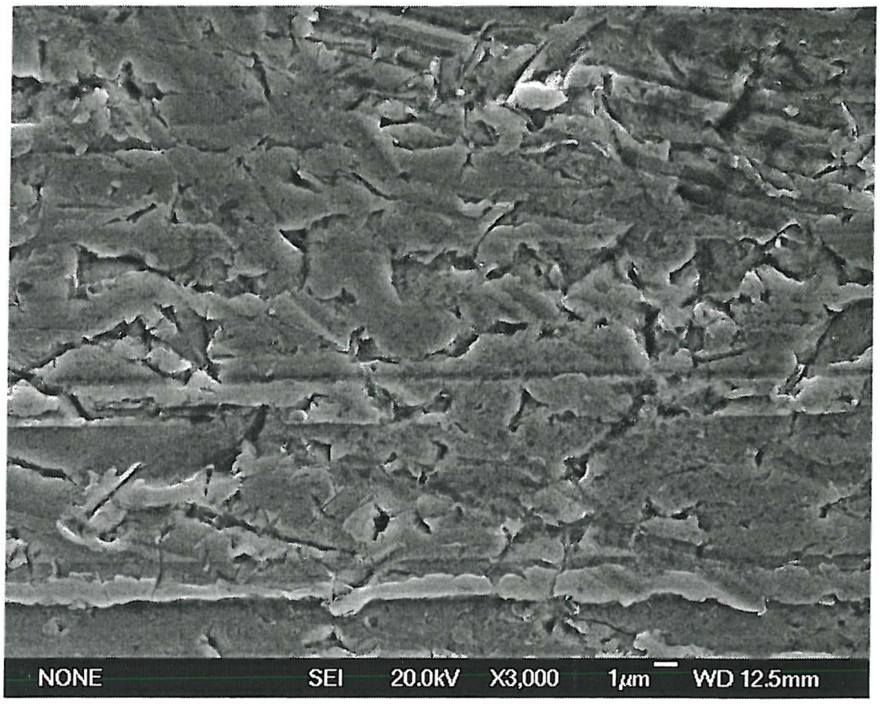

(c)

Figure 6.41 (a) & (b) Micrograph of the pin worn surface of Test 3 showing the presence of parallel and non-parallel grooves as well as some microfracture, indications the occurrence of two-body and three-body abrasion. (c) Close-up of the disc worn surface of Test 3 showing the presence of mostly microfracture and some grooves.

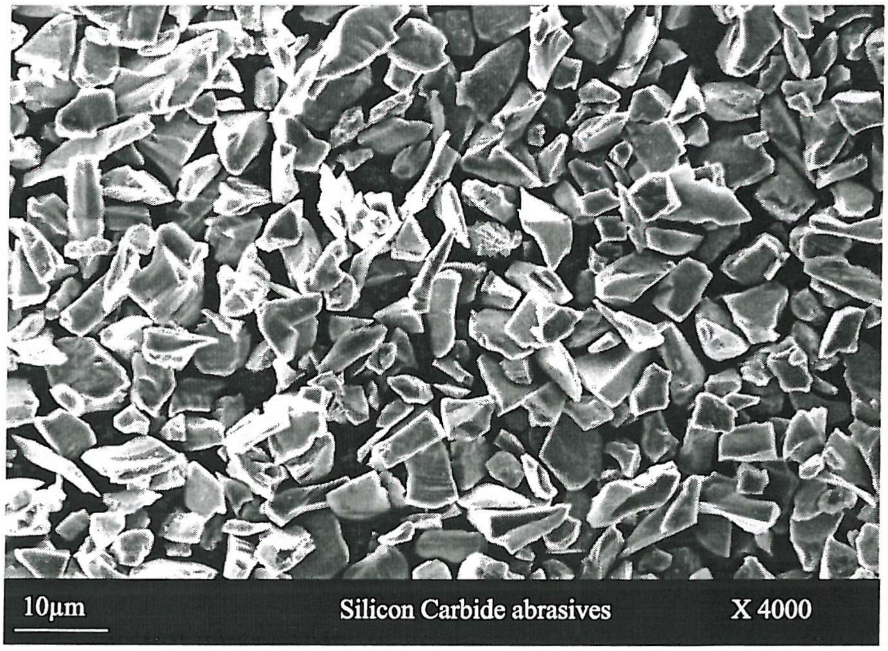

Figure 6.42 Micrograph of silicon carbide debris before seeding. They are generally 4-5 µm in size and are very angular.

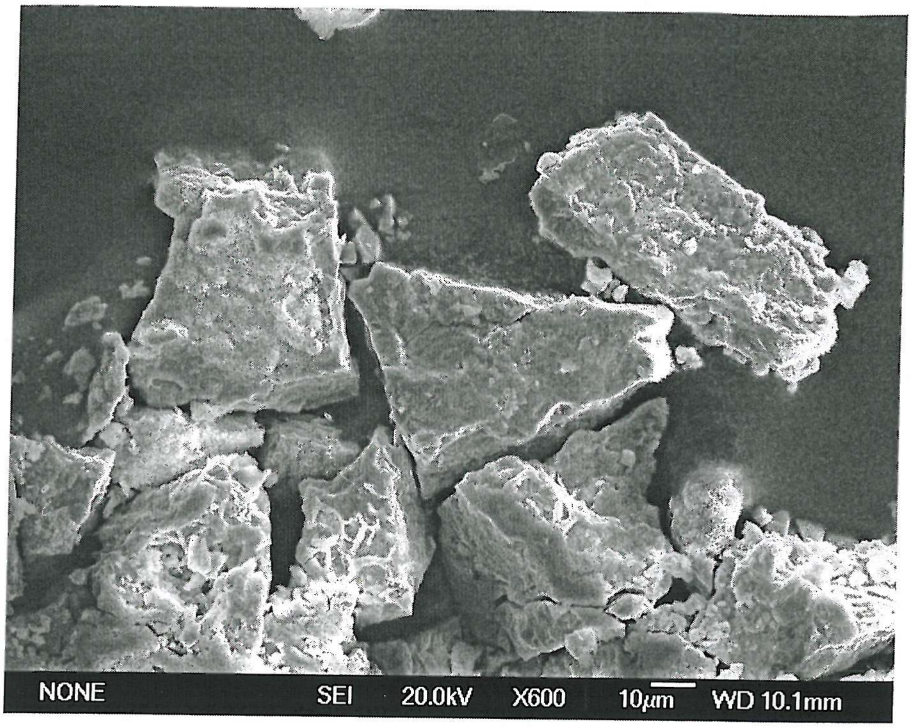
NONE
SEI
20.0kV
X600
10μm
WD 10.1mm

(a)

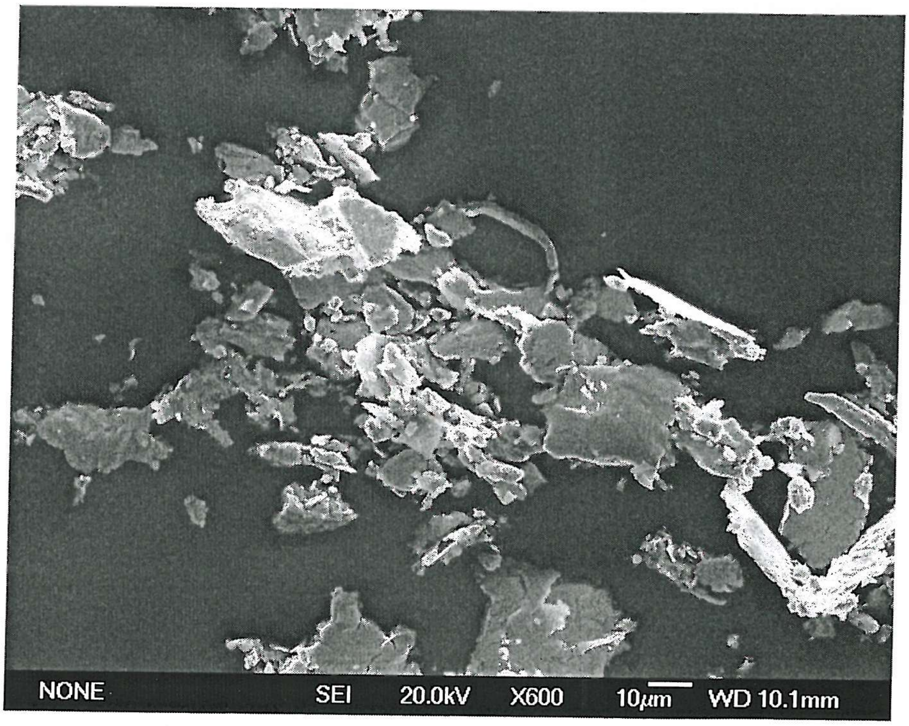
NONE
SEI
20.0kV
X600
10μm
WD 10.1mm

(b)

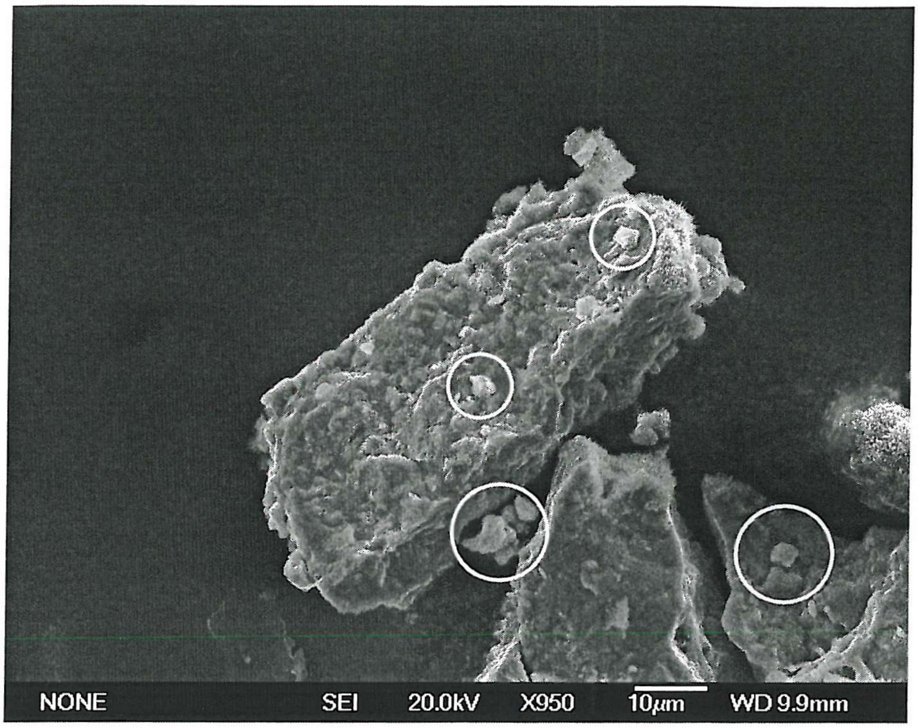

(c)

Figure 6.43 (a) & (b) Micrograph of steel wear debris from Test 3 separated using a ferrography technique indicating size of about 50 μm. (c) Close-up of a single steel wear debris. The circled particles are the seeded silicon carbide debris that has been entrained into the contact.

From all three tests discussed, the charging detected due to the increase in the severity of wear and also debris seeding seemed to enhance the background charge level. The mechanism of this is not known at the moment. In the case of the debris seeding, it is possible that the debris entrained within the region that already has, say a positive charge, will get positively charged. This will add to the positive charge that's already present in that region and hence cause the enhancement of the positive feature seen on the colour map and line plots. It is interesting to note that the magnitude change relative to the background level was much higher during the seeding of silicon nitride debris compared to during the seeding of steel debris. There are two possible explanations for this. Firstly, the silicon carbide is an insulator and can become highly charged when subjected to 'rubbing' with a dissimilar material, through its entrainment within the contact.

The second explanation is the difference in the actual number of debris seeded per seeding event, 28×10^6 for silicon carbide debris compared to only 1.8×10^6 for steel debris per seeding stage (detailed calculation is shown in Appendix B). Assuming that the majority of entrained seeded debris acquire charge, the higher the number of charged debris, the higher the overall magnitude of the charge produced.

The movement of dynamic features seen can be explained by the inertial forces on wear debris creating a spiral path. If we consider a charge feature, due to (a cluster of) wear debris, at time t_1 and position a^o, the feature's relative position on the disc surface will follow a spiral path shown in Figure 6.44.

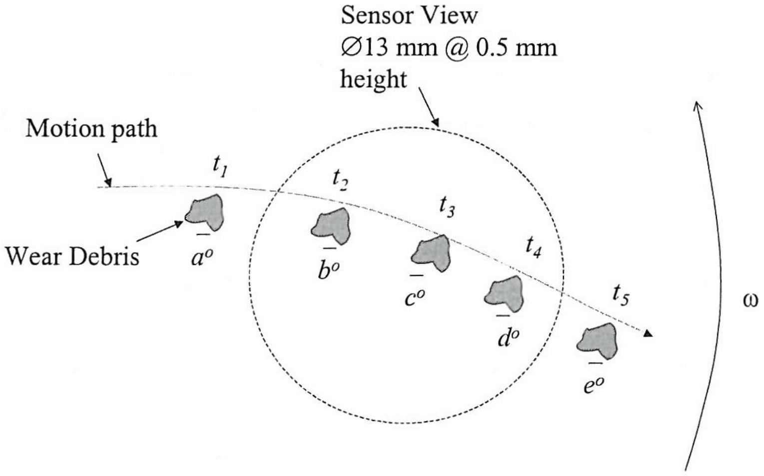

Figure 6.44 *Illustration of angular position of wear debris being centrifuged indicating a slight spiral path.*

At this point it is clear that charged debris was detected by sensor 2 downstream of the contact region in all three experiments. In Test 1, debris was also detected by sensor 1, which was not in both debris seeded tests. The reason for this is that sensor 1 monitors the wear track directly and hence any charged debris formed will be observed almost instantly. Inspections of the disc surface from Tests 2 & 3 revealed that debris was dispersed evenly (without distinct spoking), as shown in Figure 6.45. For sensor 1, the majority of the debris retains their charge and their uniform dispersion means no discrete charge will be seen. Sensor 2 monitors downstream allowing time for debris to discharge, creating areas (pockets) of charged and uncharged debris resulting in detection of discrete and dynamic charge features by the sensor. By comparing this to the distribution of wear debris on the disc surface in Test 1, shown in Figure 6.46, it is clear why discrete and dynamic charge features were seen by both sensors 1 and 2. Distinct spoking can be seen to emanate directly from the wear track with enough separation between spokes to be resolved as discrete charge features by the sensors.

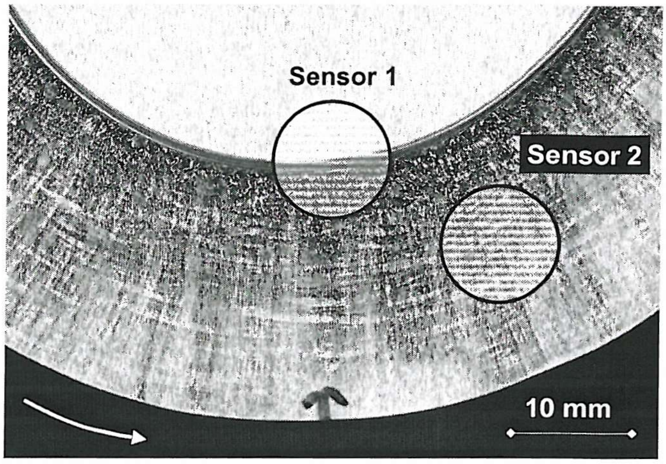

Figure 6.45 *Even dispersion of debris over the disc surface from Test 2 & 3.*

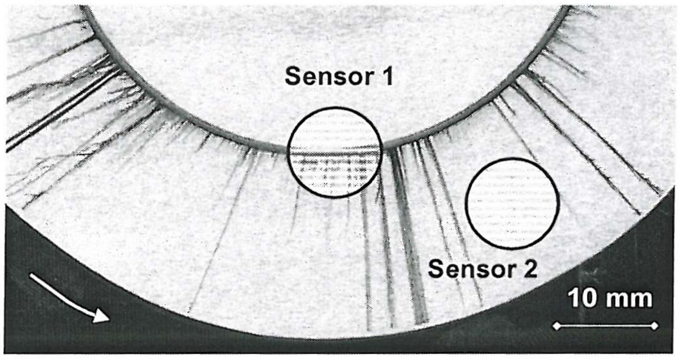

Figure 6.46 *Distinct spoking emanating directly from the wear track from Test 1.*

The exact debris charging mechanism is not clear at this point although it is believed that the charge on the debris is imparted during the formation and also once formed, by their interaction with the lubricant and solid surfaces (tribocharging) in its vicinity.

The dynamic charge features detected by sensor 2 in Tests 2 and 3 are caused by both charged entrained seeded debris and induced wear debris. The reason for the difference in polarity of the charge on the debris is not clear at this stage, although it is thought that the difference in the wear mechanisms, i.e. adhesive wear and transitions to abrasive wear adhesive wear (see Table 6.4), could be responsible.

Test	Debris	Charge Polarity	Wear Mechanism
1	Wear	Positive	Adhesive
2	Wear & Seeded	Negative	Two–body + Three-body Abrasive
3	Wear & Seeded	Negative	Two–body + Three-body Abrasive

Table 6.4 Summary of debris charge and wear mechanism involved for all tests.

Table 6.5 shows the approximated values of volume loss per seeding stages and the approximate number of seeded and induced wear debris for Tests 2 and 3 (see Appendix B for details of calculations and assumptions). The volume loss plot was calculated from LVDT data, assuming that the wear of the disc is negligible. However, since the LVDT records the reduction of the pin height due to the wear of the pin itself as well as the increase in the depth of the disc wear track, the actual volume loss is potentially higher than the listed values.

Test	Approx. volume loss per seeding stage	Approx. No. of debris seeded per seeding stage	Approx. No. wear debris produced per seeding stage
2	4.0×10^{-10} m^3	2×10^6	9×10^4
3	7.0×10^{-12} m^3	2.8×10^7	5×10^2

Table 6.5 The values of approximated volume loss per seeding stages and the number of seeded and induced wear debris for Tests 2 and 3.

For steel debris seeding (Test 2), the analysis shows that the number of particles seeded in each stage is comparable with the number of debris particle produced. This suggests that it is probable that the charge contribution of both types of debris are comparable. In the case of the silicon carbide debris seeding tests (Test 3), the quantity of debris particle formed due to induced wear is negligible compared to the number of particle seeded and hence the charge contribution from induced wear debris will be small. Charge detected in this case will be due to mostly entrained seeded silicon carbide debris.

Table 6.6 summarises the approximate values of total volume loss, specific wear and coefficient of friction for all tests. The specific wear rates of Tests 2 and 3 are an order of two magnitudes higher that Test 1. This is due to the different wear mechanism (adhesive and abrasive wear). Generally, the coefficient of friction values for all the tests are consistent with the partial EHL lubrication regime, as illustrated in Figure 3.22 on page 66.

Test	Volume Loss (m^3)	Specific Wear Rate ($m^3 N^{-1} m^{-1}$)	Coefficient of Friction
1	1.5×10^{-12}	2×10^{-18}	0.07
2	1.7×10^{-9}	1×10^{-16}	0.12
3	3.3×10^{-11}	2×10^{-16}	0.14

Table 6.6 Summary of the approximate maximum values of volume loss, specific wear rate and the coefficient of friction for all tests.

Figure 6.47 below shows a series of schematics identifying the proposed debris entrainment process and the charging. As the minimum film thickness, h_{min}, is smaller than the size of the seeded debris, the debris entrained into the contact will be physically deformed and/or fractured. This physical interaction between the debris and the surface of the pin and disc will impart charge on the debris, which mechanism will be discussed further in Chapter 7.

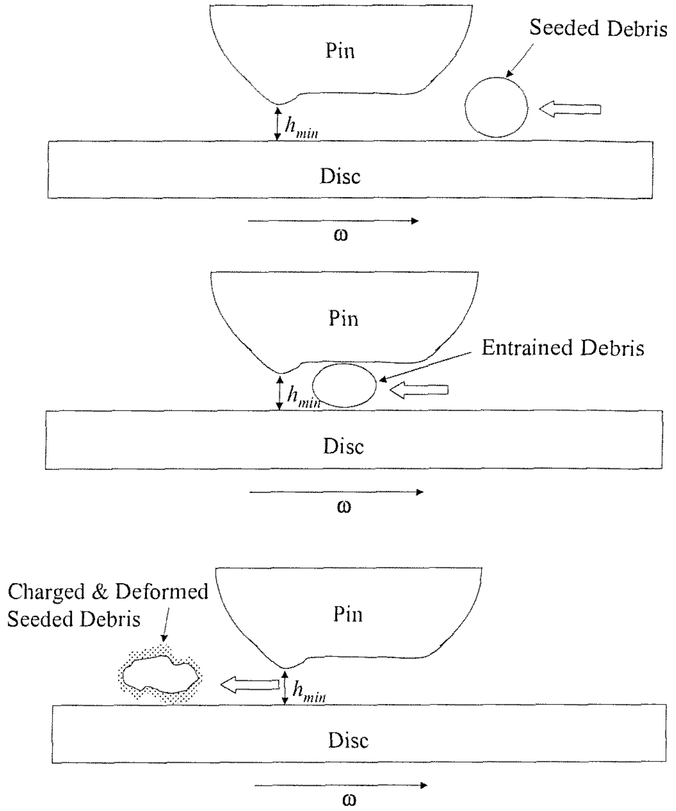

Figure 6.47 *Series of schematics showing the process of debris entrainment and the subsequent charging.*

Due to the entrainment of the debris, there are also possibilities of charging due to the interactions of the double layers on the debris and the disc surfaces. The interaction can also occur while the debris is in the process of being centrifuged out on the wear track. These effects will be discussed further in Chapter 7.

6.5 CONCLUSIONS

Charge due to freshly generated wear debris and entrained seeded debris has been monitored using electrostatic sensors. Dynamic charge features detected by the electrostatic sensors have been related to entrained seeded debris and wear debris.

In Test 1, adhesive wear is predominant while in Tests 2 and 3 there was a mixture of two-body and three-body rolling abrasion. Debris produced by adhesive wear was found to be positively charged while seeded debris and induced abrasive wear debris was found to be negatively charged.

In Test 1 the charge detected by the electrostatic sensors was dominated by the charge due to the production and presence of freshly generated wear debris. In the steel debris seeded test, the charging was dominated by a mixture of contributions from charged wear debris from induced wear as well as entrained seeded debris. In the silicon carbide debris test, the charge detected was dominated by charged entrained seeded debris.

Charge due to contact potential difference (CPD) effects was found to be negligible due to the lack of charge persistence on the worn surface. Charge features on the wear track are related directly to the severity of wear. Increased severity of wear results in an increased magnitude of charge features.

The magnitude of charging in Test 1 was directly related to the total volume loss, the higher the total volume loss, the higher the charging activity. In Tests 2 and 3 it was related directly to the amount of debris seeded into the contact.

Dynamic charge features due to the presence of charged debris were detected by both sensors in Test 1 but only by sensor 2 in Tests 2 and 3. This is possibly due to the decay of charges on the debris after the time it took to reach the area monitored by sensor 2.

Test 1 showed that the electrostatic sensing is sensitive to very small changes in wear not detected by volume loss measurement.

7

SIMULATED DEBRIS CHARGING AND OIL LINE SENSOR CALIBRATION

7.1 INTRODUCTION

The solid-solid tribocharging mechanism for debris charging was thought to be a possible debris charging mechanism in the preceding chapter. This chapter will discuss the work carried out to investigate and verify this possibility. The effects of lubricant conductivity on the charge retained on debris are also studied. The main objective of the simulated debris charging work is to investigate the effect of the material and size of the test debris on the magnitude of the surface charge acquired. Test debris were charged by means of solid-solid tribocharging in oil as well as using the corona charging technique in atmospheric conditions. Alongside these tests, the opimisation of oil line sensors (OLS) (cylindrical type electrostatic sensor) was also investigated. This optimisation is intended to establish the methodology to select the best sensor geometry to be used for real-time debris sensing in an oil line of oil lubricated systems.

7.2 SOLID – SOLID TRIBOCHARGING OF PARTICLES

7.2.1 Experimental setup

Figure 7.1 shows the experimental setup used to study the solid-solid particle tribocharging in oil. It comprises a funnel clamped directly above an OLS (cylindrical type electrostatic sensor) and an oil container. The inner diameter of the funnel outlet is approximately 4 mm. The test lubricant is poured into the funnel and allowed to flow out through the funnel outlet past the cylindrical sensor into the oil container. Test debris is then entrained in the flowing liquid, along the upper edge of the sloping wall of the funnel. The test debris slides down the funnel wall into the vertical lubricant flow passing through the cylindrical sensor and into the lubricant container. This procedure was carried out twenty times in order o provide a check on repeatability.

Either a glass or copper funnel was used. The OLS employed had an efficiency of 100 %, which means that the response is equivalent to the total amount of charge present on the test debris. The sliding duration of the test debris varies with the viscosity of the test lubricant and funnel as well as debris material. The charge on the test debris is recorded and analysed. A control test with the same setup but without the presence of a lubricant was conducted.

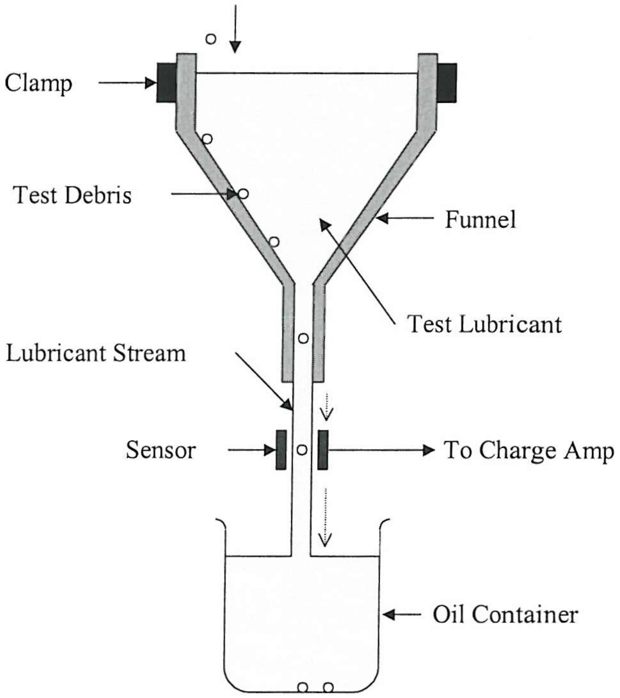

Figure 7.1 Schematic diagram of the test rig setup.

Test debris

Figure 7.2 shows the geometry of the test debris used and Table 7.1 shows the types of test debris materials used, with their work function values (obtained by photoelectric methods) arranged according to their position on the triboelectric series (see Section 3.6.2 on page 60). Test debris was made by cutting 2 mm lengths of respectively, 2 mm diameter copper, steel and lead rod (Figure 7.2), and 3 mm spheres of silicon nitride were used.

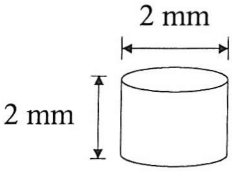

Figure 7.2 Test debris dimension.

Material	Work Function (Photoelectric) (eV)
Glass (SiO_2)	0.9
Lead	4.0
Aluminium	4.28
Steel (Fe)	4.4
Copper	4.65
Silicon Nitride (Silicon)	4.9

Table 7.1 Debris test materials and their work function value.

Table 7.2 lists the test lubricants and some of their properties. Different lubricating oils were studied to investigate the effects of lubricant conductivity on the debris charge magnitude. The lubricant conductivity was measured using a low conductivity fluid meter at room temperature.

Lubricant	Oil Type	Conductivity (pS^{-1})	Kinematic Viscosity @ 40 °C (cSt)
Shell Vitrea ISO32	Base Mineral	7.8	31.8
Shell Vitrea ISO100	Base Mineral	2	99.7
Timken TRB115-032	Base Mineral	55.5	32
Timken TRB115-250	Base Mineral	24.0	68
Exxon Turbo 2380	Fully Synthetic	1710.0	24

Table 7.2 Test lubricants and some of their properties.

Instrumentation

The block diagram in Figure 7.3 illustrates the instrumentation used. A cylindrical 'ring type' oil line sensor (OLS) was employed and was connected to a charge amplifier that was operated at a gain of 500 $mVpC^{-1}$ and a nominal frequency response from 10 Hz to 10 kHz. During the test, signal output was displayed in real-time on an oscilloscope and data was recorded by a DAT recorder, as well as captured by a PC acquisition system at a rate of 2000 Hz.

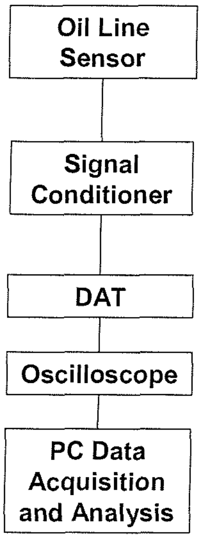

Figure 7.3 *Block diagram of the instrumentation used.*

Data analysis

A data acquisition program was used to record sensor data in text file format at a sampling rate of 2000 Hz. This data is then plotted using a graph plotting software to obtain the magnitude of the sensor response.

7.2.2 Results and Discussion

Influence of materials

Figure 7.4 shows a comparison of the charge measured on test debris against material type for a flowing lubricant (Shell Vitrea ISO 100) stream and the control test for a copper funnel, arranged according to their respective position on the triboelectric series (taking silicon nitride as silicon). Lead, aluminium, steel and copper became positively charged while silicon nitride became negatively charged. If copper is used as a reference point (same as the funnel), it can be seen that the magnitude of the average charge becomes increasingly positive toward the left hand side and negative towards the right hand side. It is also evident that the absence of lubricants caused a decrease in the charge magnitude, but not the relative charge order.

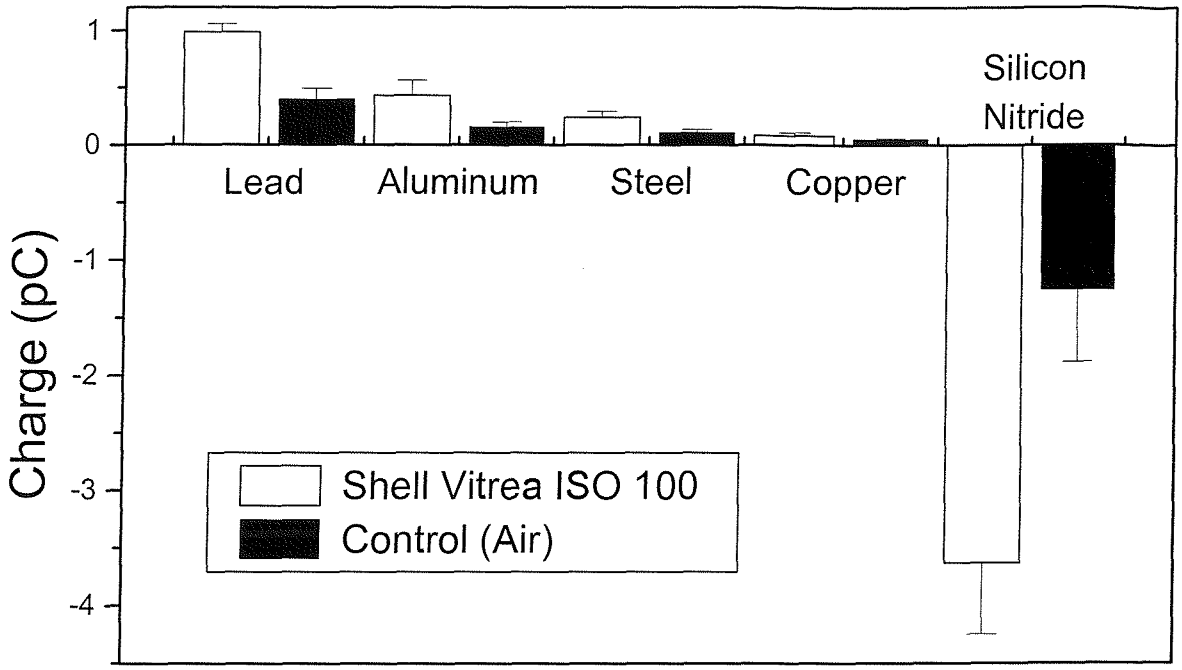

Figure 7.4 Plot of charge against test debris materials for Shell Vitrea ISO100 and control (air) test with copper funnel.

From the comparison of the charge against test debris material for a Shell Vitrea ISO 100 lubricant and the control test for the glass funnel shown in Figure 7.5, it can be seen that all debris became negatively charged. For lubricant tests, the magnitude of the charge becomes smaller (less negative) moving from lead to silicon nitride with the exception of copper. These variations of the magnitude contradict the triboelectric series, noting that glass lies on top of all the test materials in the series. The trend seen for the control test, where charging becomes more negative moving from lead to silicon nitride, is as expected and fits better with solid-solid tribocharging theory, which can be inconsistent especially for insulator-insulator and insulator-metal contact [102]. In the case of insulator-metal contacts, one of the proposed explanations for charging involves material transfer and localised heating. This is a very variable process especially with the presence of lubricants and could relate to the charging behaviour observed in Figure 7.5. Although the magnitude of variation did not conform to the general rule, the polarity did, given the position of glass with respect to the test debris materials on the triboelectric series.

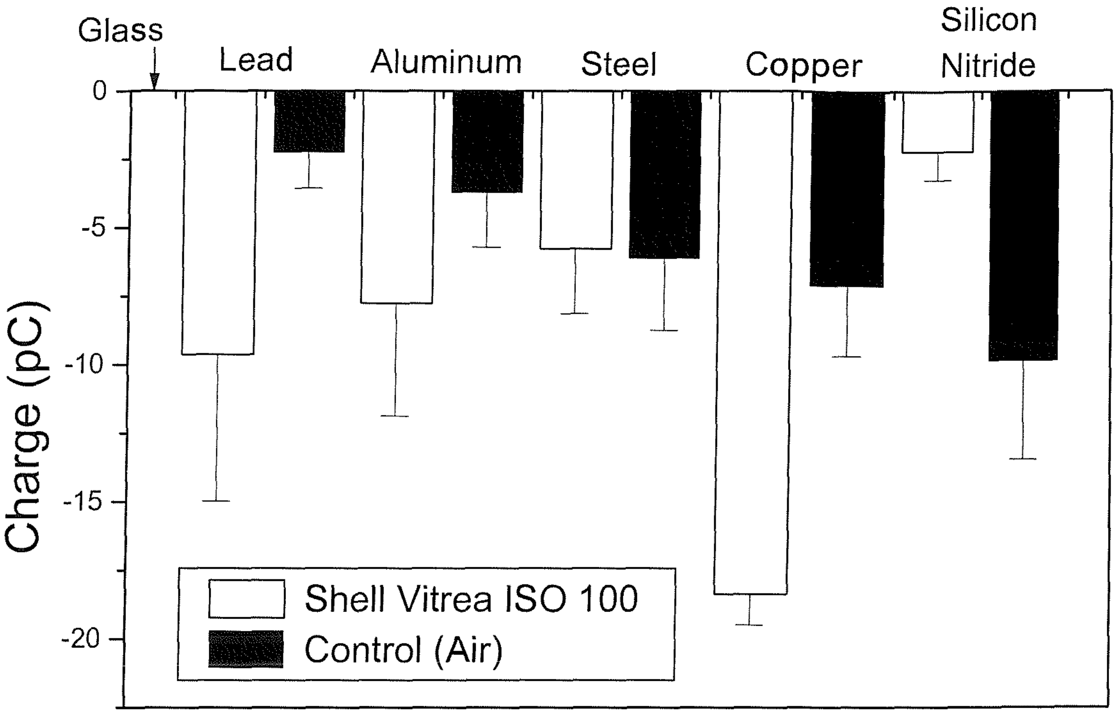

Figure 7.5 Comparison plot of average charge against test debris materials for Shell Vitrea ISO100 and control (air) test with glass funnel.

The reasons for the differences between the control tests and the lubricated tests are unclear. The presence of lubricants could influence solid-solid tribocharging and the difference in the charge magnitude between the control and lubricated tests could be due to a charging contribution from solid-liquid tribocharging. The test debris could acquire extra charge due to the interaction of the double layer regions of the debris and the funnel wall. Hence, the absence of oil will slightly reduce the overall magnitude of charge acquired by the test debris.

Theory based on the triboelectric series indicates charging should be directly proportional to the work function difference of a material pair, analogous to the contact potential difference effects as suggested by Equation 3.18 ($q = C_o V_c$). Figure 7.6 shows a plot of work function difference between the funnel and test debris against charge imparted on the test debris for the control tests. For a given funnel material, and assuming that the capacitance variation is negligible between different test debris, Equation 3.18 suggests that the plot should produce a straight line. Figure 7.6 shows plots for glass and copper funnels indicating a linear relationship (straight line) and hence show a close agreement with the theory. The value of the slopes approximates the effective contact capacitance in both cases, 2.045 pF and 7.245 pF for the copper and glass funnel tests respectively.

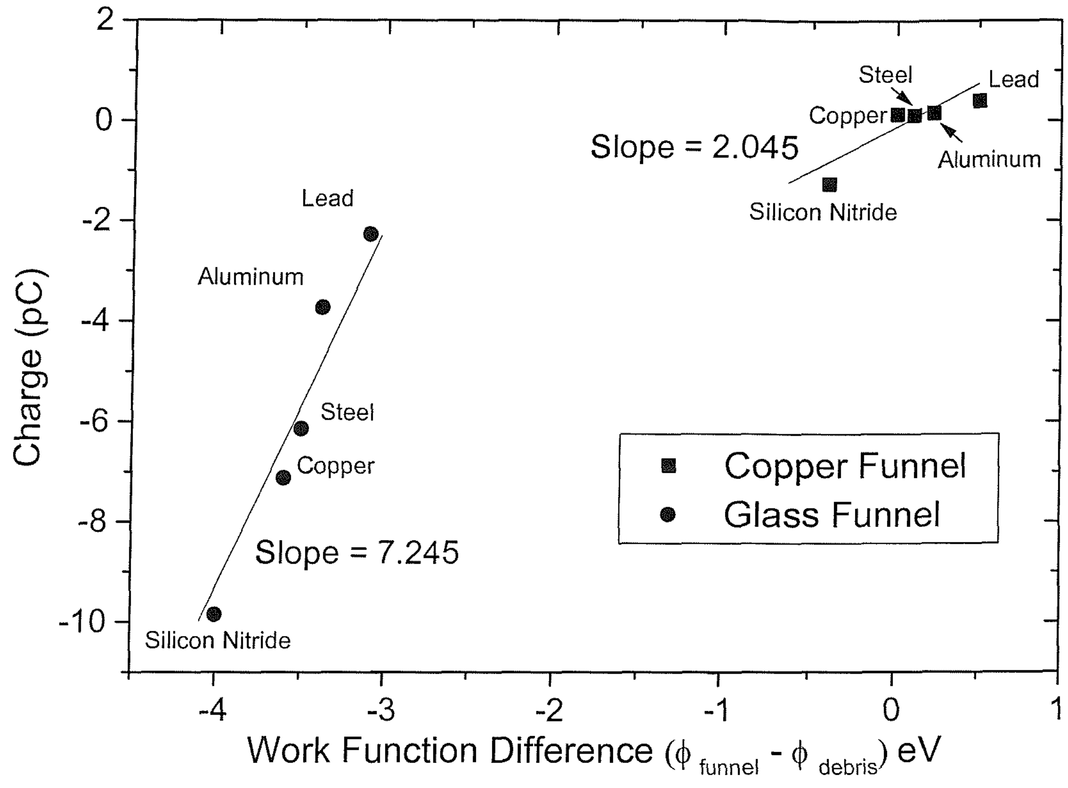

Figure 7.6 *Work function difference of the funnels and test debris against charge imparted on test debris for the control test.*

Affect of oil conductivity

The copper funnel and silicon nitride test debris were used to investigate the influence of oil conductivity on tribocharging. Figure 7.7 shows that charge was found to increase with the decreasing oil conductivity and all lubricants produced a negative charge. Exxon Turbo 2380 (1710 pS^{-1}) gave a charge of 0.15 pC compared to 6.05 pC with Shell Vitrea ISO 100 (2 pS^{-1}). This variation in chargability can be explained by charge decay as studied by Klinkenberg [103]. Charge decay was found to follow the equations below;

$$Q = Q_o e^{-(\frac{t}{\tau})}$$ *Equation 7.1*

$$\tau = \frac{\varepsilon\varepsilon_o}{\kappa} \qquad \textit{Equation 7.2}$$

Where, Q_o = initial charge, Q = charge remaining after time t, τ = relaxation constant, κ = conductivity, ε = dielectric constant of oil = 3 and ε_o = permitivitty of free space = 8.85×10^{-12} C^2 N^{-1} m^{-2}.

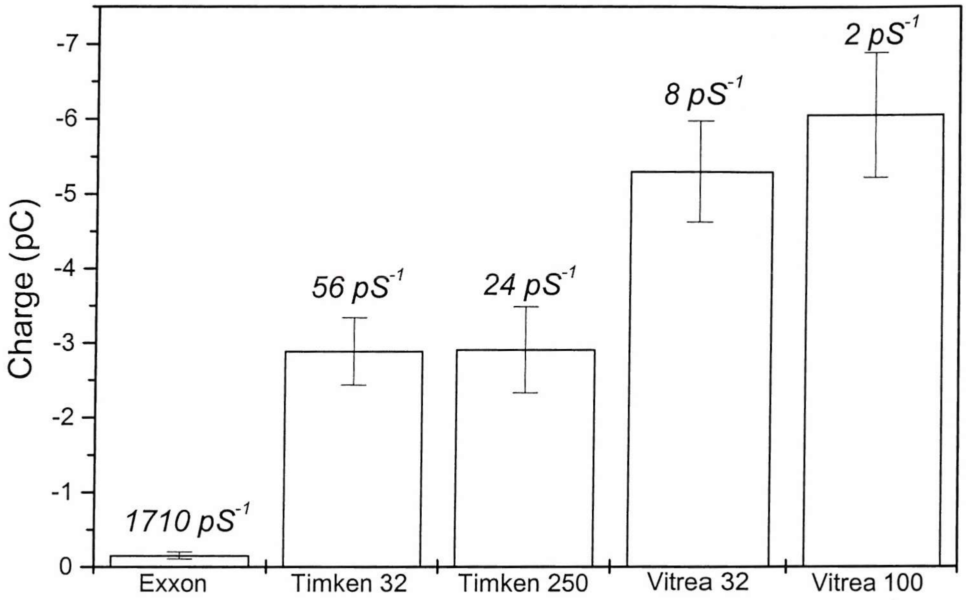

Figure 7.7 *Plot of charge against oil type. Copper funnel, silicon nitride debris.*

The relaxation constant, τ, is essentially the duration for a given charge on a debris to decay exponentially from its original magnitude to near zero. The charge on the surface of the test particle, induced due to solid-solid tribocharging with the funnel, will start to decay from the last point of contact as illustrated in Figure 7.8.

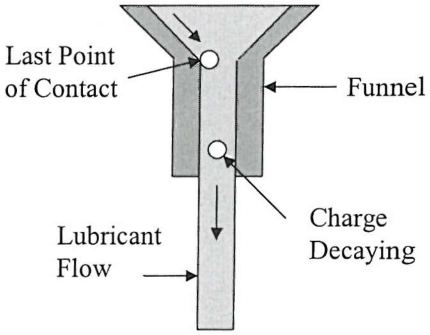

Figure 7.8 *Last point of contact for debris and funnel wall.*

Table 7.3 shows the relaxation constant, τ, calculated for the tests lubricants used. Thus, as the test debris is at the sensor face, the amount of the original charge at the last point of contact will have decayed into the bulk of the lubricant at an increasing rate with increasing conductivity.

Lubricant	**Conductivity (pS^{-1})**	**Relaxation constant, $\tau(s^{-1})$**
Shell Vitrea ISO100	2	13.275
Shell Vitrea ISO32	7.8	3.404
Timken 250	24.0	1.106
Timken 32	55.5	0.478
Exxon Turbo 2380	1710.0	0.016

Table 7.3 Values of the relaxation constant τ and conductivity for test lubricant used.

A general function has been derived to describe the contributions of the different charging mechanisms to the overall charge detected in an oil-lubricated contact [104-107]. A detailed proposed debris charging model can be found in Appendix D. Note that some of these models were constructed through speculations based on background fundamental physics and not from work conducted for this thesis.

Combining all the models of possible charging mechanisms, the relationship of charge can be summed up into:

Overall charge detected = f (Tribocharging, Surface charge, Triboemission, Debris)

Or

$$Q_{total} = f\,[Q_{tribo}, Q_{surface}, Q_{emiss}, Q_{debris}] \qquad 7.3$$

Where

$$Q_{tribo} = f\left[\frac{K_{\pm}}{K'_{\pm}}, D_{\pm}, (\varepsilon\varepsilon_o \rho n_{\pm}), \kappa, \nu, A\right]^{*} \qquad 7.4$$

$$Q_{surface} = f\left[Q_{CPD}, Q_{prefabs}\right] = f\left[\varepsilon\varepsilon_o \Delta\phi, \frac{N_{ads}\mu}{\varepsilon\varepsilon_o}\right] \qquad 7.5$$

---

[*] Impurities present in lubricants can exist in ionic form, which can have either positive or negative charge.

$$Q_{emiss} = f\left[\sum\left(E_{bond} N_{bond}\right), \alpha_{abs}\right] \qquad 7.6$$

In order to expand the debris charge term further, all possible debris charging mechanisms have to be taken into account. From Chapters 6 and this chapter, they are identified as solid-solid and solid-liquid tribocharging. The effects of the oil conductivity and surface area also need to be incorporated. The majority of the wear debris is thought to become charged due to their formation. Considering only metallic debris, from Equation 3.18 (page 59), solid-solid tribocharging relationship is given by:

$$Q_{solidtribo} = C_{eff} \Delta\phi \qquad 7.7$$

For solid-liquid tribocharging, Equation 7.4 above can be used. The charge imparted during debris formation can be represented by the function below:

$$Q_{debris} = f\left[\sum\left(E_{debris} N_{debris}\right)\right] \qquad 7.8$$

From Equation 7.2, the effects of the oil conductivity in terms of the charge relaxation constant, τ, is given by;

$$\tau = \frac{\varepsilon\varepsilon_o}{\kappa} \qquad 7.9$$

Combining all these terms produces a general but complex function for debris charging:

$$Q_{debris} = f\left[\ C_{eff}\Delta\phi,\ \frac{K_{\pm}}{K'_{\pm}},\ D_{\pm},\ \left(\varepsilon\varepsilon_o \rho n_{\pm}\right),\ \kappa,\ \nu,\ \tau,\ A, \sum\left(E_{debris} N_{debris}\right)\ \right] \qquad 7.10$$

Symbol	Definition	Units
A	Debris surface area	m^2
α_{abs}	Fraction of emitted species that are not absorbed by lubricant	Dimensionless
C_{eff}	Debris effective capacitance	F
$D_{\pm}$	Ionic diffusivities	$m^2 s^{-1}$
$\Delta\phi$	Work function difference	eV
E_{bond}	Energy of bonds broken during exoemission	J
E_{debris}	Energy of bonds broken during debris formation	J
ε	Permitivitty of lubricant	Dimensionless
ε_0	Permitivitty of free space	$F m^{-1}$
$K_{\pm}$	Adsorption rates	$mol s^{-1}$
$K'_{\pm}$	Desorption rates	$mol s^{-1}$
κ	Oil conductivity	$pS m^{-1}$
μ	Induced dipole moment	$C m^{-1}$
N_{ads}	Number of adsorbate molecules per unit area	m^{-2}
N_{bond}	Number of bonds broken during exoemission	Dimensionless
N_{debris}	Number of bonds broken during debris formation	Dimensionless
$n_{\pm}$	Localised ionic concentrations	$mol dm^{-3}$
ρ	Recombination rate	Dimensionless
$Q_{prefabs}$	Surface charge due to preferred absorption	C
τ_{debris}	Relaxation of charge	s^{-1}
ν	Entrained oil velocity	$m s^{-1}$

7.3 OIL LINE SENSOR CALIBRATION

7.3.1 Background

Debris charging in air was carried out using a corona charging technique. Before discussing the results, the fundamentals of corona particle charging will be reviewed.

Corona particle charging

Corona discharge

A corona discharge is a self–sustaining, partial breakdown of a gas subjected to a highly divergent electric field; a typical arrangement is a point to plane electrode arrangement as shown in Equation 7.11. In this arrangement the electric field on the tip of the pin, E_p, is significantly higher than those in the surrounding area of the gap. The value of E_p can be approximated using the following equation;

$$E_p = \frac{V}{r_{tip}} \qquad 7.11$$

Where V is the potential difference between the point and the plane and r_{tip} is the radius of the point.

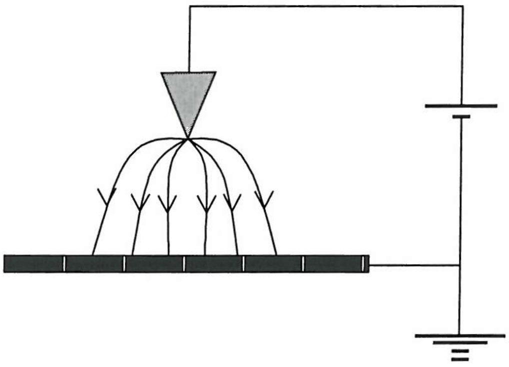

Figure 7.9 *Non-uniform field in a point-plane geometry showing a field that is arising near a point to a plane electrode [31].*

As V increases the electric field in the vicinity of the point becomes high enough to trigger an electron avalanche. During an electron avalanche the number of electrons will increase exponentially as a result of ionising collisions with the neutral gas molecules, this effect is called the Townsend α-process [31]. A fraction of these secondary electrons will attach to neutral gas molecules to form negative ions. The rapid increase in the number of free electrons will quickly cause breakdown. Ionisation is confined to a region near the tip (highest flux density), as shown in Figure 7.10. This ionisation zone manifests itself as a faint glow.

The existence of a drift zone in the gap prevents a complete electrical failure. It acts as the stabilising resistance in series with the ionisation zone.

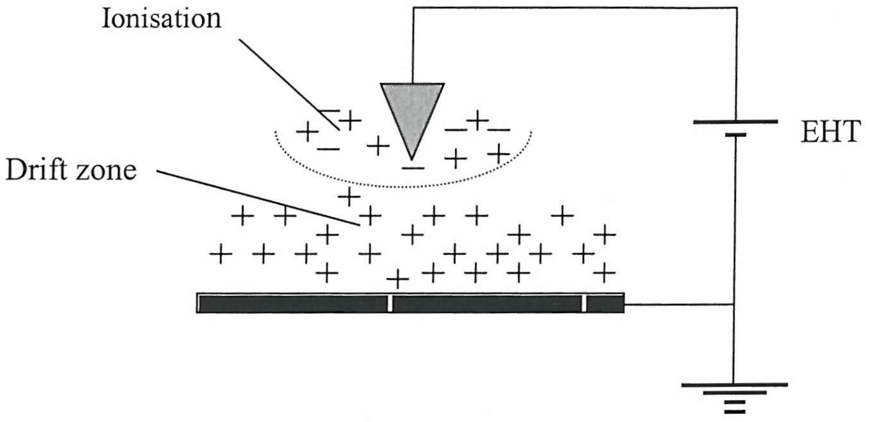

Figure 7.10 The two main zones in a corona discharge.

When a positive voltage is applied to the point, negative ions and electrons are accelerated towards the point while positive ions drift out of the ionisation zone and flow through the drift zone towards the planar electrode as shown in Figure 7.10. When a negative voltage is applied, negative ions drift out of the ionisation zone toward the planar electrode.

Corona charging utilises the unipolar ion flow in the drift zone, any object placed in this region will intercept the ion flow and become charged. The polarity of the charge collected on the particle is set by the polarity of the voltage applied.

Corona threshold voltage

For a corona to be started in air a threshold field must be exceeded, given by;

$$E_{critical} = \frac{0.18}{r_{tip}^{\ 0.5}} \qquad 7.12$$

Substituting this value into Equation 7.11 will give the critical voltage, $V_{critical}$, in volts as;

$$V_{critical} = 1.8 \times 10^5 (r_{tip}^{\ 0.5}) \qquad 7.13$$

Factors affecting the onset of corona (critical voltage)

The level of surrounding humidity influences the critical onset voltage (inception voltage). Fouad *et al* [108] reported that when increasing the relative surrounding air humidity from 60% to 80% the value of the critical voltage fell to up to 40% of the original value for a given electrode and plane separation. However, between a relative humidity range of 20% to 60% the values of the critical voltage change slightly. Figure 7.11 shows the relationship of humidity with the corona inception voltage.

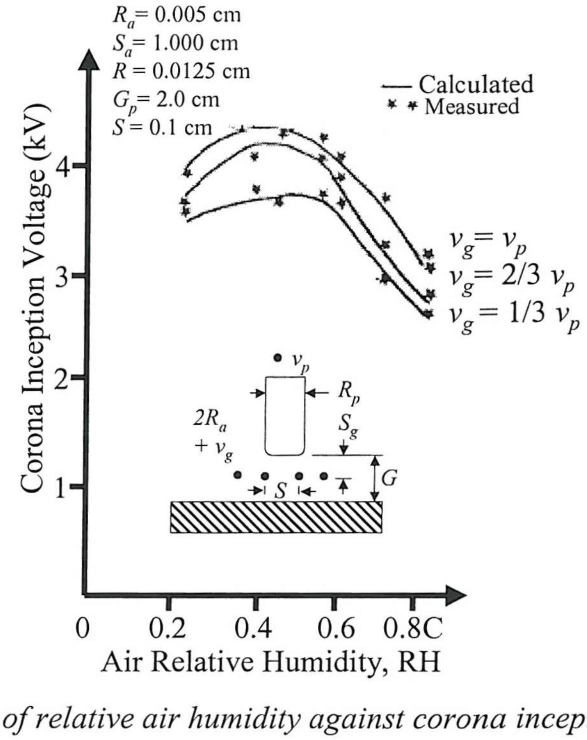

Figure 7.11 *Graph of relative air humidity against corona inception voltage [108].*

Corona charging of airborne particles

Any air borne particle that enters the drift zone will intercept the unipolar ion stream and as a result will become charged. When a spherical particle is placed in the drift zone, the field will be distorted from its original uniform condition; the flux line will bend toward the spherical particle as shown in Figure 7.12.

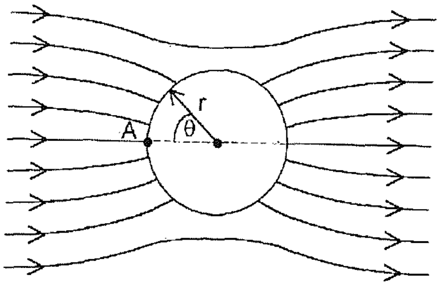

Figure 7.12 *Polarisation of a spherical particle causes a distortion in the previously uniform field [31].*

This symmetrical field pattern is the result of polarisation within the particle and is distorted when ions are intercepted and trapped on the particle surface. For a conductive particle the charge initially builds up on the surface that is facing the ion stream directly, the charge is then rapidly distributed evenly on the whole surface. For insulating particles this is not possible. However, due to the electrical torque acting on the non-uniform surface charge the particle will start to rotate randomly, thus ensuring all surfaces are exposed to the stream of ions resulting in uniform surface charge. In both cases, charging will continue until the electric field produced by the accumulated charges on the particle is sufficient to prevent any more ions reaching the particle as represented in Figure 7.13.

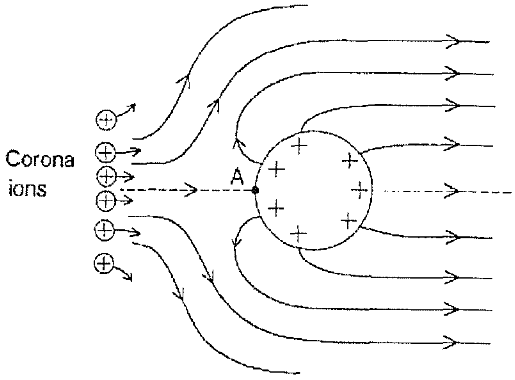

Figure 7.13 *Field pattern around a fully charge particle. The field at A is zero so that the ion flow is deflected around the particle [31].*

The time to reach this saturation depends on various factors such as ionic charge rate and density of the corona ion. The exact magnitude of the saturation can be determined by numerical analysis, as shown in the following section.

Maximum charge on spherical particle

The maximum charge, $q_{M,}$ that can be held on a spherical particle can be calculated using equation 7.14. This is called the Pauthenier limit.

$$q_M = 4\pi\varepsilon_o a^2 \left(\frac{3\varepsilon}{\varepsilon + 2}\right) E_a \qquad 7.14$$

Where ε_o is the relative permitivitty of free space, ε is the permitivitty of particle, E_a is the applied electric field and a is the particle radius.

7.3.2 Experimental Setup

Figure 7.14 shows the set up of the test rig used. Spherical test material (bearing steel and silicon nitride balls) with diameters ranging between 1 mm and 7 mm were used to simulate wear debris, as shown in Table 7.4. The balls are fed manually through an alignment plate with a hole slightly larger than the diameter of the balls clamped over the sensor. The balls becomes charged as they fall through a corona discharge region, consisting of an array of 3 × 3 corona electrodes clamped directly facing an earthed aluminium plate 3 cm away. A high voltage potential of 7 kV was applied to the electrode array.

An OLS is positioned directly below the corona charging area and is connected to a signal conditioner and fed to a PC data acquisition. Directly underneath the sensor is a Faraday cup, which is placed in an earthed cage to shield it from electrical noise produced by the corona charger and also noise from other external electrical sources. The Faraday cup picks up the exact charge present on the balls. The Faraday cup is connected to a Keithley 610C electrometer via a UHF connecter that amplifies the charge output to a PC data acquisition system. The outputs from the signal conditioner were also connected to an oscilloscope for real-time viewing.

Before each test the balls were cleaned using a solvent to remove any oil film or other contaminants. Rubber gloves were worn during the feeding process to prevent any contamination.

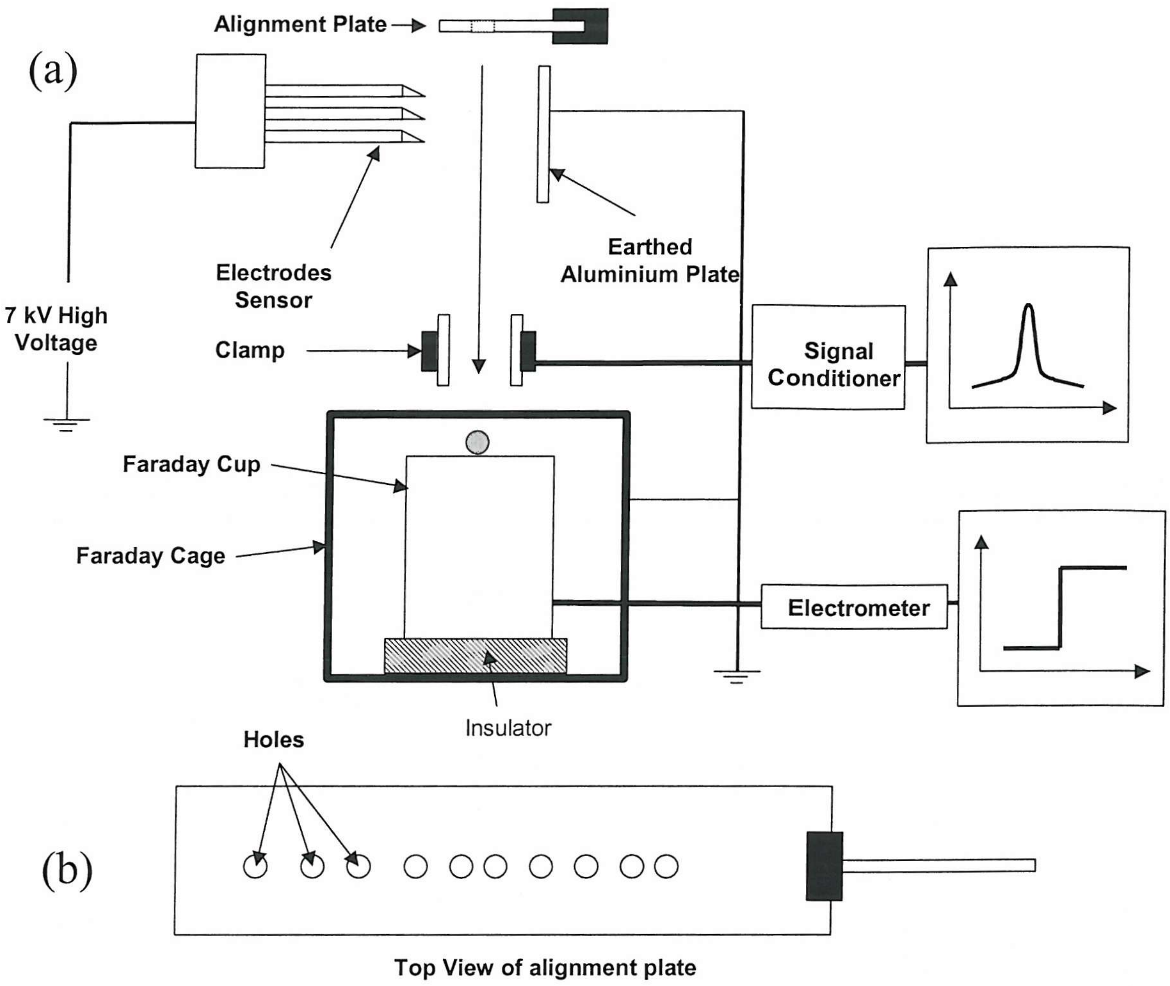

Figure 7.14 *(a) Schematic diagram of the test rig setup, (b) alignment plate.*

Figure 7.15 shows a schematic diagram of a corona charging region. A voltage of +7 kV was applied to the electrode array, which was high enough to produce a corona discharge region to form between the needles and plate, inducing a positive charge on the balls.

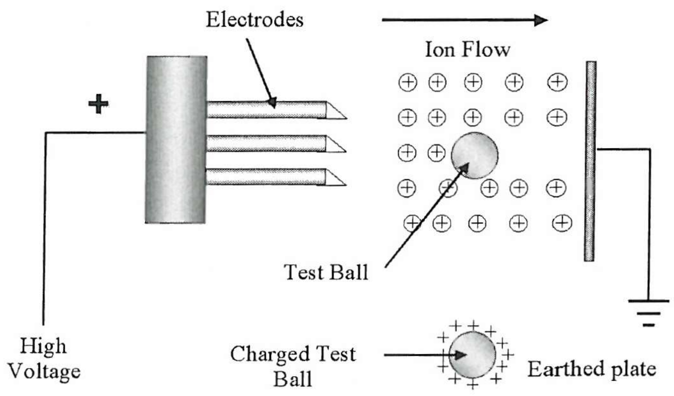

Figure 7.15 *Close up of corona charging area.*

Test materials

Table 7.4 shows the test balls, indicating material, dimension and supplier. The materials were chosen to represent common materials used in oil lubricated contacts and spherical geometry to study the effect of surface area on the amount of charge collected by the balls.

Diameter (mm)	**Surface Area (m^2)**
AISI Bearing Steel (Blue Diamond Ltd. UK)	
7.0	1.54×10^{-4}
6.5	1.33×10^{-4}
6.0	1.13×10^{-4}
5.55	9.68×10^{-5}
5.0	7.85×10^{-5}
4.75	7.09×10^{-5}
4.0	5.03×10^{-5}
3.165	3.15×10^{-5}
3.0	2.83×10^{-5}
2.0	1.26×10^{-5}
1.0	3.14×10^{-5}
Silicon Nitride (SKF)	
6.0	1.13×10^{-4}
4.76	7.11×10^{-4}
4.0	5.03×10^{-5}
3.0	2.83×10^{-5}

Table 7.4 Test ball details, indicating material, dimensions and supplier.

Description of sensors

Table 7.5 shows the dimensions of the sensors used and Figure 7.16 shows a schematic of a cylindrical sensor. The sensing face is made from copper foil wound around the outside surface of a glass cylinder. The purpose of the earth screen is to prevent interference from external electrical noise.

Diameter (mm)	Length (mm)
50	10
	6
30	0.25
	1
	2
	3
	5
	6.5
	8
	10
	17
	40
	60
	100
20	10

Table 7.5 Sensors details.

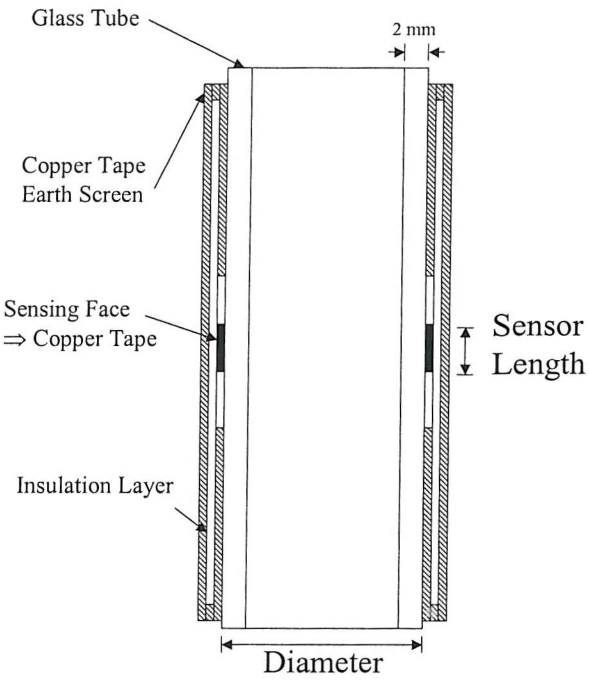

Figure 7.16 *Schematic diagram of a cylindrical sensor used in this test.*

Instrumentation

The instrumentation used was similar to that described in Section 7.2.1 but with the addition of an extra acquisition channel for the Faraday cup and the electrometer, as illustrated in the block diagram in Figure 7.17 below.

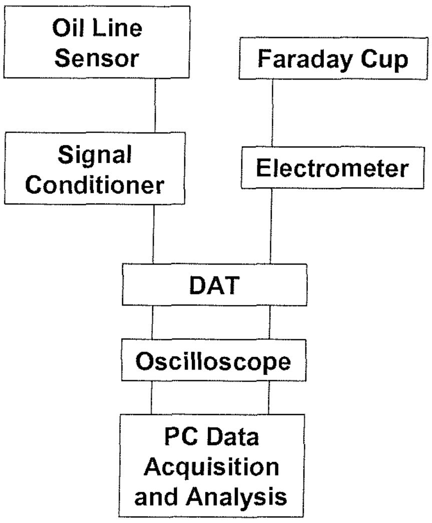

Figure 7.17 *Block diagram of the instrumentation used.*

Data analysis

The data analysis technique was similar to the one described in Section 7.2.1. Figure 7.18 shows a typical response of an array of three sensors which were individually connected, and the absolute charge system (ACS), i.e. the Faraday cup and the electrometer. The ACS measures the accumulating charge of any object that enters the Faraday cup, causing a 'step' type response. The sensor response to a charged object is a 'peak' and the difference between the peak height and baseline is a measure of the 'sensed charge'. From these two measurements of charge, the charge density (see Equation 7.15) and sensor efficiency (see Equation 7.16) are calculated.

$$\text{Charge density} = \frac{\text{ACS charge}}{\text{surface area}} \qquad 7.15$$

$$\text{Sensor Efficiency} = \frac{\text{sensed charge}}{\text{absolute charge}} \times 100 \qquad 7.16$$

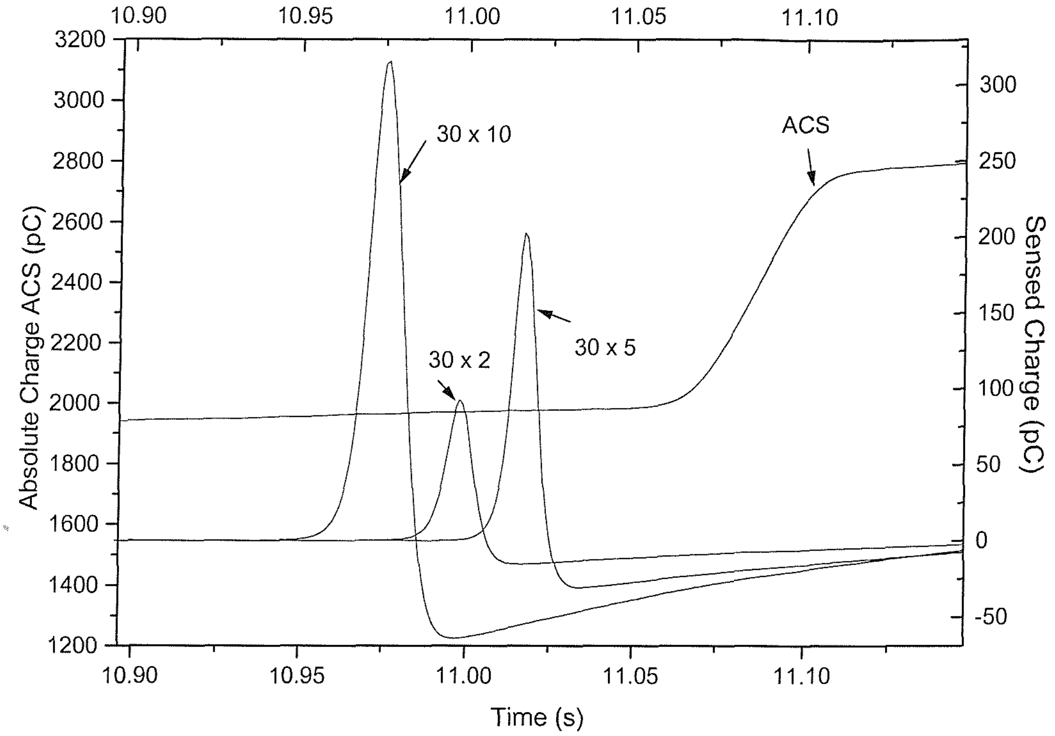

Figure 7.18 Plot of 30 mm diameter array sensor (30 x10, 5, 2) RH = 56.9% for test using a 7 mm diameter bearing steel test ball, charge amplifier high pass filter off.

7.3.3 Results and Discussions

Factors affecting magnitude of ball charge

Ball radius

Figure 7.19 indicates that charge density is approximately constant throughout the range of ball sizes. The rather large deviation with the smaller balls is thought to be due to handling difficulties. Rubber gloves were not worn when handling these balls as their size inhibits efficient handling. Inevitably, these balls would pick up oil contaminants from the skin and will probably affect the amount of charge acquired by the balls. Figure 7.20 shows the plot of charge against the ball radius squared for bearing steel, which clearly shows a linear relationship between surface area and acquired charge.

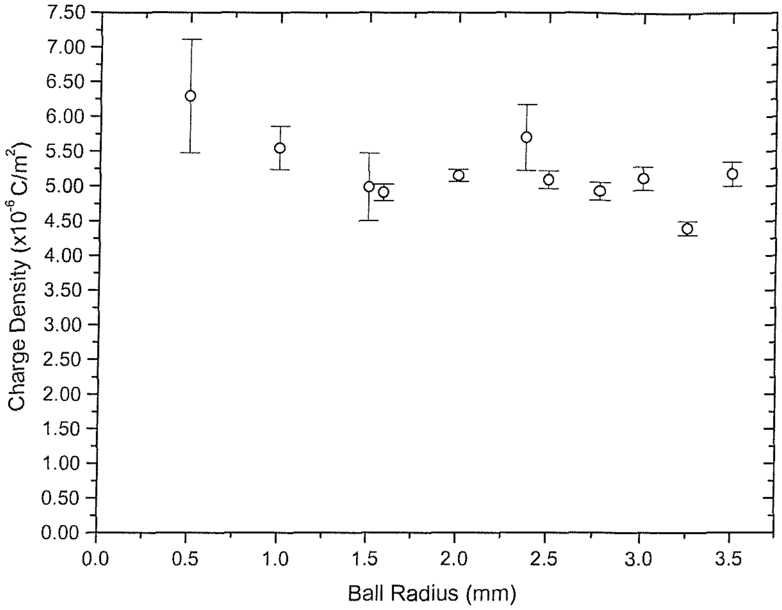

Figure 7.19 *Plot of charge density as measured by ACS against bearing steel balls radius, RH = 56.9%, 7 kV applied voltage.*

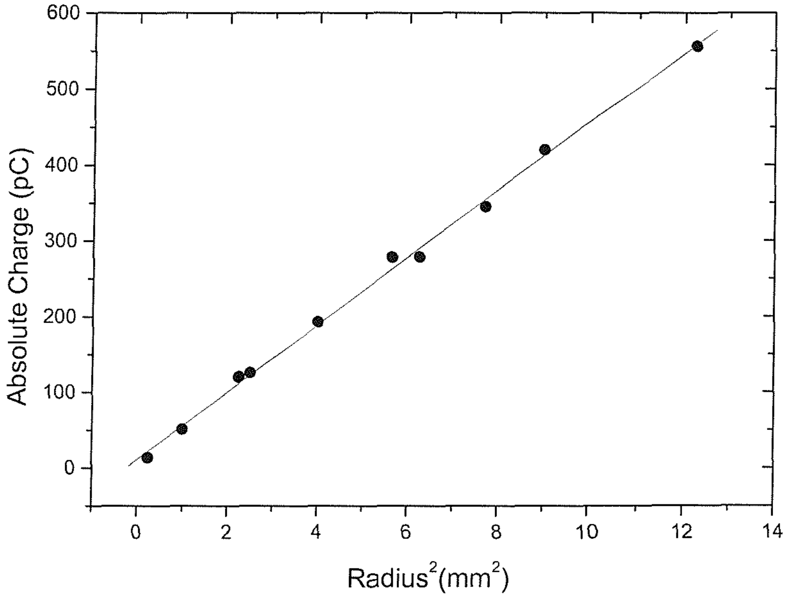

Figure 7.20 *Plot of absolute charge on bearing steel balls against the ball radius squared, RH = 56.9%, 7 kV applied voltage.*

Material

Figure 7.21 shows the plot of absolute charge against square of ball radius for both bearing steel (conductor) and silicon nitride (insulator) balls. The test was carried out at +7 kV applied voltage and 50% relative humidity (measured). Comparable charge for silicon nitride and steel balls is seen for the smaller radius. However, for the larger diameter balls (2.38 mm and 3.0 mm) the bearing steel gained a higher charge compared to silicon nitride.

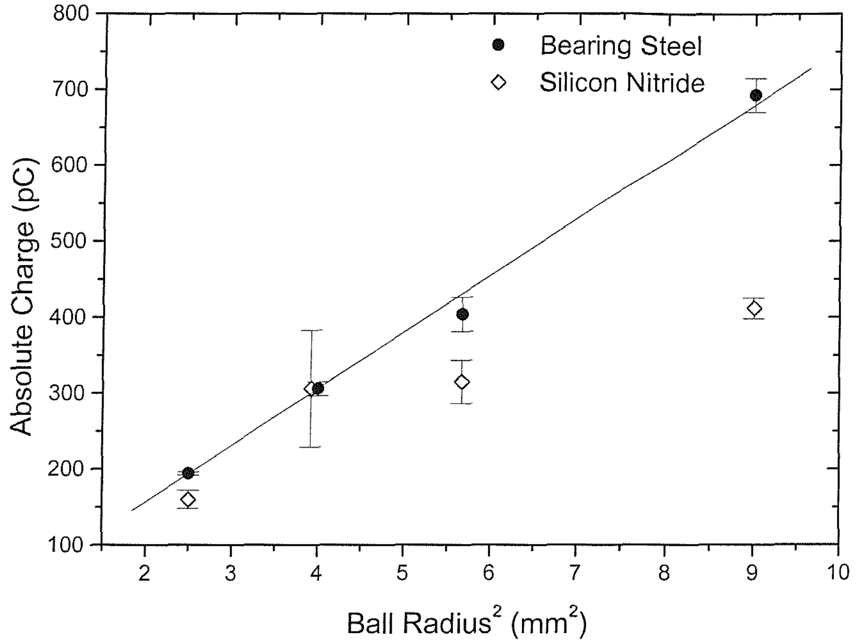

Figure 7.21 *Plot of absolute charge against the ball radius squared. 7 kV applied voltage, 50% relative humidity.*

The results presented above can be explained by the difference of charging behaviour of conductors and insulators in the corona charging region. Bearing steel balls are metallic and thus have a high conductivity, when they fall through the corona charging area, the unidirectional stream of positive charges will collect on one side of the ball. The surface charge will rapidly redistribute itself evenly throughout the whole surface.

Silicon nitride being an insulator has a very low conductivity. When a silicon nitride ball falls through the charging area, charge is acquired only on one side of the ball surface. The surface charge does not evenly distribute itself over the rest of surface. The incoming ion stream is repelled from the surface due to the saturated surface charge on that side of the ball. The discrepancy between charge levels on silicon nitride balls compared to those in the bearing steel balls is greater on the ball with larger diameter. Small balls (lighter) have low inertia and are easier to rotate by the electrical force and indeed variation in friction with air (due to surface variation) whilst in the charging area and hence could collect an even distribution of the surface charge. Larger balls (heavier) have higher inertia and thus are harder to rotate and thus do not collect maximum charge.

Sensor system characterisation and optimisation

Sensor length

Figure 7.22 shows a plot for the charge sensed against the sensor length using a 3mm radius ball and a sensor diameter of 30 mm. This figure shows that the charge sensed increases with increasing sensor length. A length of 60 mm was found to be a critical length where the value of charge sensed is equal to the value of the absolute charge on the ball (100% efficiency).

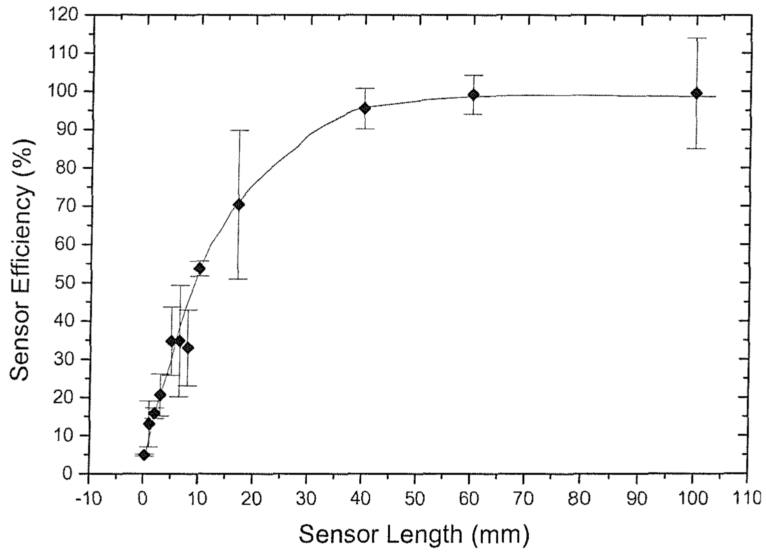

Figure 7.22 *Plot for the sensor efficiency against the sensor length for different 30 mm sensor. Test debris was 3 mm in radius.*

Sensor diameter

Figure 7.23 shows a plot of sensor efficiency variations with diameter, indicating that sensor efficiency increases as the diameter decreases.

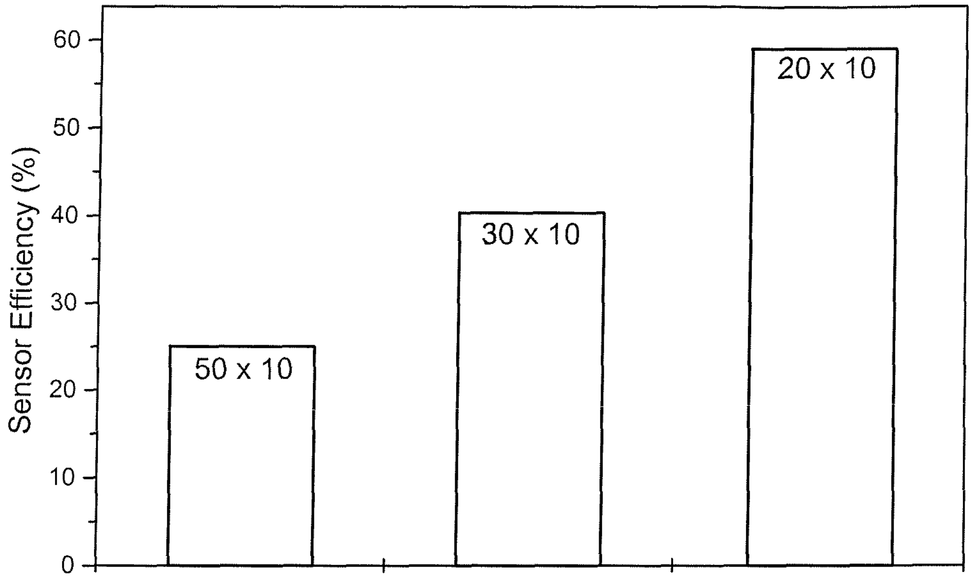

Figure 7.23 Sensor efficiency for 20, 30 and 50 mm sensor diameter at 7 kV applied voltage, 3.5 mm ball radius and 50 % relative humidity.

Sensor aspect ratio

Aspect ratio is defined as:

$$\text{Aspect ratio} = \frac{\text{sensor length}}{\text{sensor diameter}} \qquad 7.17$$

Figure 7.24 shows the plot for sensor efficiency versus aspect ratio showing that the compilation of experimental data follows one trend for all sensors tested. Two regions of the graph should be pointed out, the first is that nearly 100% sensor efficiency is achieved above a value of approximately 1.5 in the aspect ratio and secondly, there is a linear region below an aspect ratio of about 0.5.

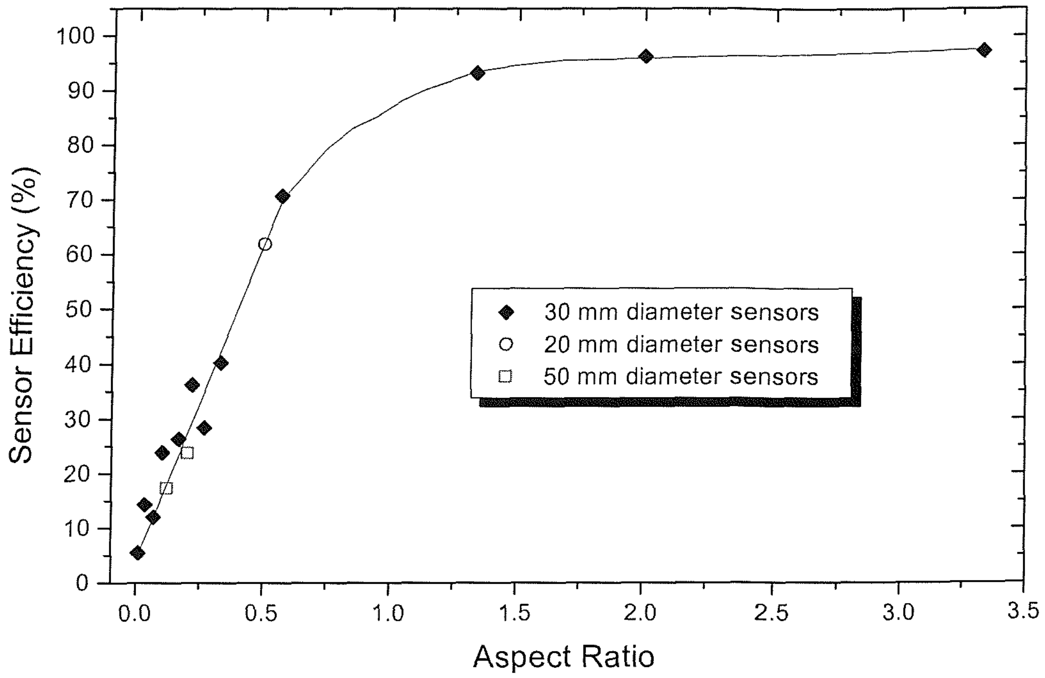

Figure 7.24 *Sensor efficiency against aspect ratio for 20, 30 and 50 mm diameter sensors for charging tests with bearing steel balls.*

The sensor efficiency is affected by the diameter and the length due to the difference in the amount of flux terminating on the sensing face. Increasing the sensor length will increase the amount of flux terminating on the sensing face and hence increase the magnitude of charge detected, see Figure 7.25. The magnitude of the charge sensed by the 20×10 sensor was more than that of the 30×10 sensor. In the case of the 20×10 sensor, the wall is closer to the charge source and hence the magnitude of the flux density (field displacement) on the sensing face is higher compared to 30×10 sensor (see Equation 3.6 on page 43). The 100% efficiency 30×60 and 30×100 sensors show that all the flux terminated onto the sensing face. The plot of percentage of response versus aspect ratio shows that there is a relationship between the aspect ratio and the percentage of response.

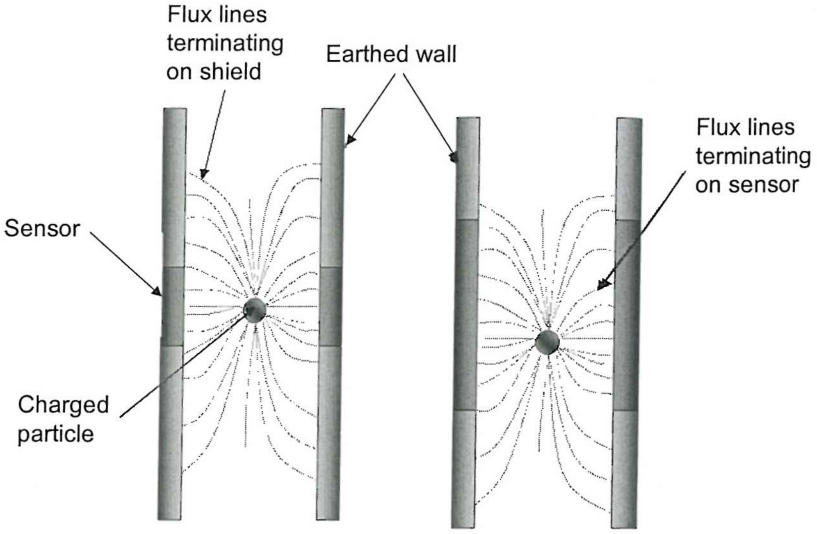

Figure 7.25 *Schematic representation of flux termination on sensors of different length.*

7.4 CONCLUSIONS

Relating the results from the simulated debris charging tests to the results in Chapter 6, it can be concluded that one of the possible mechanisms of debris charging is solid-solid tribocharging. The charging of copper debris sliding on a copper funnel is related to the charged steel seeded debris and indeed also the charging of wear debris. It is possible for similar materials to acquire charge due to frictional interactions with each other. The results presented here can also help explain why the charge magnitude change relative to the background level was much higher during the seeding of silicon nitride debris when compared to during the seeding of steel debris. As observed in Section 7.2.2, silicon nitride (analogous to silicon carbide debris) tends to charge highly negative compared to copper (analogous to steel debris). In a real lubricated system, this can be useful. For example, in a system that employs ceramic-steel hybrid bearings and copper lubrication piping, a negative signal can be attributed to ceramic debris while a positive signal can be attributed to steel debris.

Some charging contributions from solid – liquid tribocharging due to the interactions of the double layer of both the test debris and funnel wall surface was thought to account for the difference in the overall magnitudes of the control and oil medium tests. The exact amount of this contribution is not clear at this point and further investigative work is needed.

When the glass funnel was used, all test debris was negatively charged, consistent with the triboelectric series but the magnitudes for the tests with lubricant were inconsistent. This shows unpredictable behaviour of insulator-metal charging. The magnitude order from the control test results are consistent with the triboelectric series.

For debris charging in oil there is a direct relationship between the magnitudes of charge detected on the debris with the conductivity of the lubricants. An increase in the conductivity of the oil caused a decrease in the magnitude of the charge detected on the test debris.

A general function for debris charging has been proposed, combining the contribution of all possible debris charging mechanisms. This takes the form:

$$Q_{debris} = f\left[\ C_{eff}\Delta\phi\ ,\ \frac{K_{\pm}}{K'_{\pm}},\ D_{\pm},\ (\varepsilon\varepsilon_{o}\rho n_{\pm}),\ \kappa,\ \nu\ ,\ \tau,\ A, \sum\left(E_{debris}N_{debris}\right)\ \right]$$

Thus, debris charging depends on surface work functions, oil chemistry, impurity concentration and conductivity, wear rate and sliding velocity. From debris charging in air it can be concluded that the magnitude of the absolute charge acquired by the test ball is proportional to its surface area. Charge imparted by the corona charging technique depends on the type of test material. Silicon nitride balls (insulating) were found to charge differently from bearing steel balls (conducting), resulting in high charges for larger steel balls than silicon nitride.

The sensor response was found to be influenced by sensor geometry (length and diameter) and the dimensionless factor of aspect ratio. For steel balls of 1 mm – 7 mm diameter, sensor aspect ratio of ≥ 1.5 produced 100% sensor efficiency. For aspect ratio < 0.5 the relationship between sensor response and aspect ratio is linear. This will help optimize sensor designs for debris detection.

8

OIL LINE SENSOR OPTIMISATION

8.1 INTRODUCTION

The long term aim of the development of the oil line sensor is to produce sensors that detect not only charge on particles but also determine the size of these particles. Consider two scenarios for a given sensor geometry in Table 8.1:

Scenario	Diameter (mm)	Sensing face length (mm)	Particle diameter range (mm)
1	15	2	0.01 – 1
2	15	0.25	0.01 – 1

Table 8.1 Two different scenarios for a given sensor geometry.

For scenario 1, realistically, the particle will always be smaller than the sensor length, while for scenario 2 there will be instances where the particle diameter is either much larger, comparable, or much smaller than the sensing face length. It is thought that the change in efficiency for micro (0.25 mm) and macro (2 mm) sensors will be different for the same change in particle diameter. This difference in efficiency change can be exploited to develop a pair of sensors that can be used to detect particle size. This is called micro-macro sensor concept. The change in the flux linking behaviour (see Figure 7.25 on page 209) causes a change in the efficiency with particle size variations. Work has been conducted to investigate this phenomenon using the Mk II sensor design (see Figure 8.3), and some preliminary results are shown in Table 8.2.

Particle diameter (mm)	0.25 mm Efficiency, eff_1 (%)	2 mm Efficiency, eff_2 (%)	$\mathrm{eff}_2 - \mathrm{eff}_1$ (%)
1	10.2 ±0.4	27.9 ±0.4	17.7
2	10.1 ±0.4	27.63 ±0.4	17.5

Table 8.2 Preliminary micro-macro test results.

The results suggest that there are some possible differences in the efficiency of both sensor with decreasing particle size. However, the tests were hindered by several problems namely:

- Handling – Difficulties in charging and dropping single solid spheres accurately due to their small size which causes variations in efficiency due to off-centre effect.
- Field of view – Automated small particle (real size wear debris) handling was considered but the large field of view of the current micro-macro sensor inhibited the detection of a single particle.

This chapter describes the work conducted to optimise the *'field of view'* of the cylindrical sensor for monitoring wear debris in an oil line system. The field of view determines the resolution of the sensor; i.e., the smaller the field of view, the higher the resolution. However, since the field of view also governs the efficiency of the sensor, a compromise has to be established between resolution and efficiency to produce a signal with high signal to noise ratio for measurable charge detection.

8.2 EXPERIMENTAL METHOD

The oil droplet rig designed by Harvey [109], shown in Figure 8.1, consists of an oil reservoir, from which a valve feeds an electrically insulated metallic needle holder. A high voltage power supply is connected to the reservoir and needle holder (which can be fitted with needles of various sizes to alter droplet size and droplet formation time) so that potentials of up to ±500 V can be applied to the droplet. When the valve is opened a droplet forms on the needle and the applied potential between the needle and an earthed ring (used to stabilise the electrical field) induces charge on the oil droplet. When the droplet detaches, it falls through the electrostatic sensor(s) positioned at a set distance below the needle. The sensor(s) is (are) connected to a three-channel signal conditioner via microdot connections. The amplifier outputs to an oscilloscope and then to a computerised data acquisition system. The average diameter of an oil droplet in this test was 2 mm. The oil droplet rig was used because the drop path through the sensor can be varied more accurately compared to solid particles.

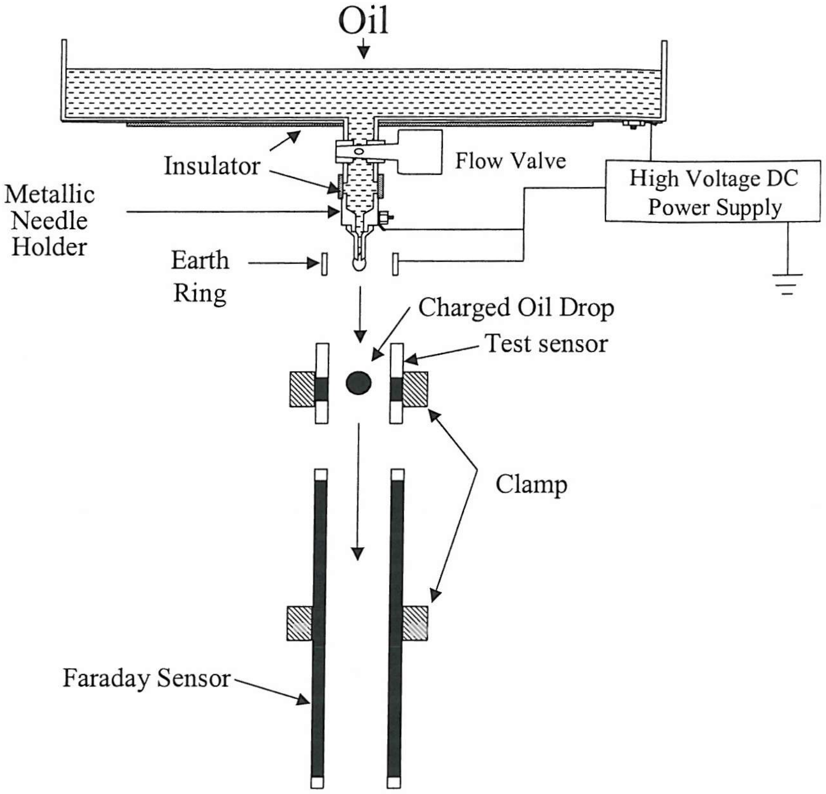

Figure 8.1 *Schematics of the experimental setup for the field of view test.*

8.2.1 Test Sensors

The sensing face of the Mk I sensor was made by winding a 0.25 mm diameter copper wire around a cylindrical glass surface. The shielding was wound on top of the sensing face using thin copper tape but separated by an insulation tape (see Figure 8.2). The Mk I design was used in the previous chapter (Chapter 7). The Mk II sensor consists of two sensing faces, 0.25 mm and 2 mm, wound on the same glass tube with an approximate separation of 70 mm. Only the 0.25 mm sensor is studied. The copper shielding of the Mk II sensor is spaced 12.5 mm away from the sensing face (see Figure 8.3). The Mk III sensor is very similar to Mk II sensor, except the copper shielding length is shorter and there is only one sensor (see Figure 8.4). The Mk IV sensor is similar to Mk III, except the sensing face is recessed 9 mm away from the glass wall, using a PCB disc to separate the glass and the copper wire (see Figure 8.5). All of the sensors were wired through microdot coaxial connections.

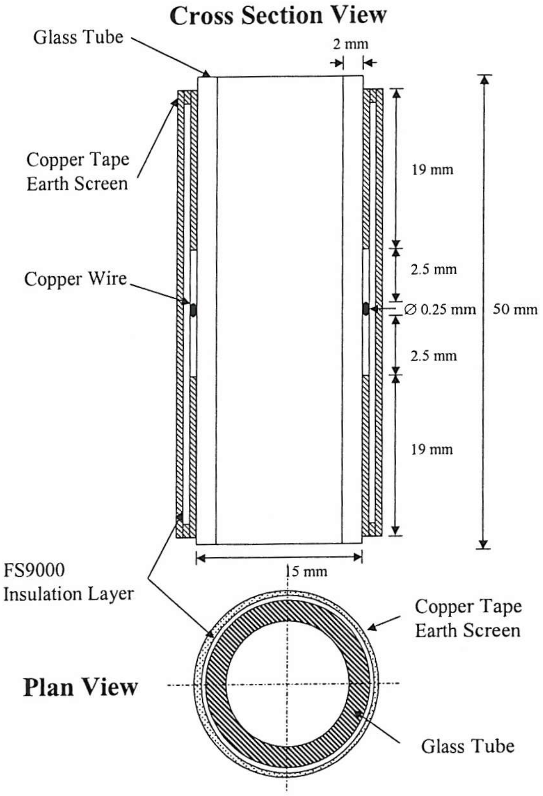

Figure 8.2 *Schematic of cross section and plan view of Mk I sensor.*

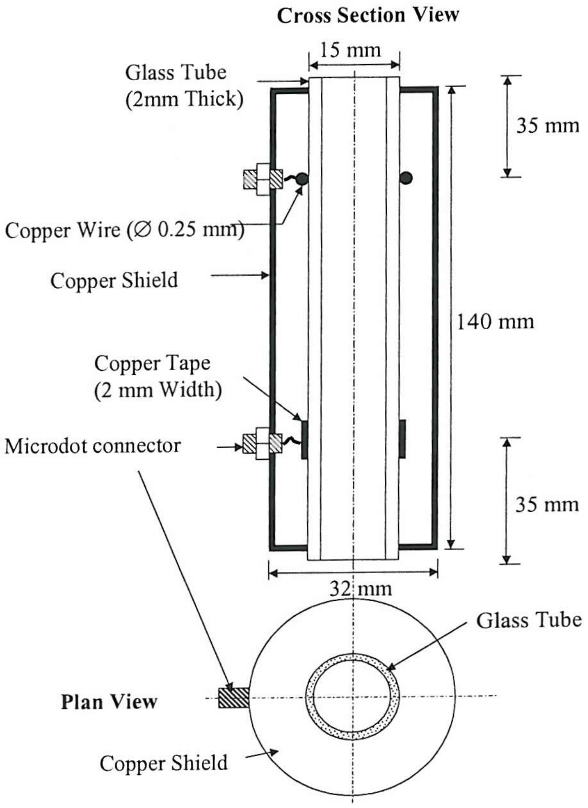

Figure 8.3 *Schematic of cross section and plan view of the Mk II sensor.*

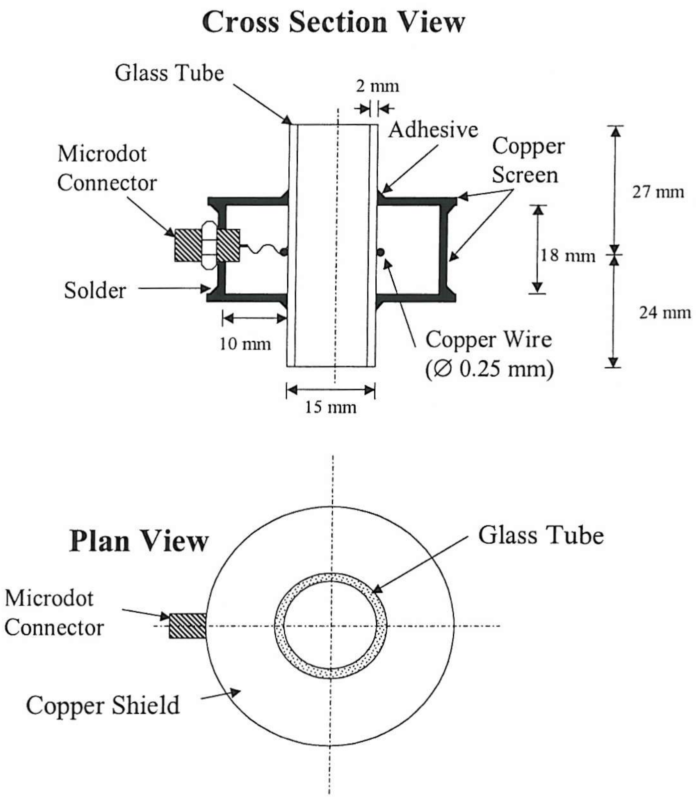

Cross Section View

Plan View

Figure 8.4 *Schematic of cross section and plan view of Mk III sensor.*

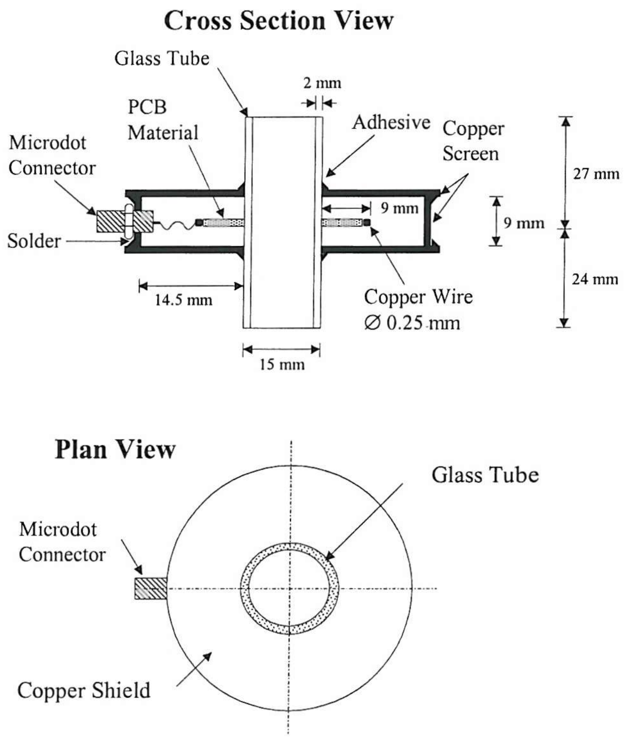

Cross Section View

Plan View

Figure 8.5 *Schematic of cross section and plan view of the Mk IV sensor.*

8.3 RESULTS AND DISCUSSION

8.3.1 Analysis of Results

The field of view was calculated in the following way:

- After a peak from a single charged debris is plotted, the full duration (width) in seconds of the peak is obtained. The baseline of the peak is determined, as shown by the dotted line in Figure 8.6. The start of a peak is taken at the first instance where the level rises above the baseline, denoted by *a* in Figure 8.6. The end of a peak is taken at the point where the level falls back to the baseline level, denoted by *b* in Figure 8.6. The duration from *a* to *b* is taken as the peak duration, t_{peak}

- The velocity, v_c, of the charged oil droplet at point *c* in Figure 8.7 is calculated using the equation below:

$$v_c = \sqrt{2gh_a} \qquad 8.1$$

Where gravity, $g = 9.81\ \text{ms}^{-2}$ and h_a = the distance of the release point to point *c*. The velocity is assumed as the terminal velocity.

- The average size of the droplets in this test was 2 mm and the time taken for it to move past a sensor of width w_{sensor}, $t_{droplet}$, is calculated using:

$$t_{droplet} = \frac{2 + w_{sensor}}{v_c} \qquad 8.2$$

- The total field of view, m_{fov}, is then calculated using;

$$m_{fov} = 2\left(v_c\left(t_{peak} - t_{droplet}\right)\right) \qquad 8.3$$

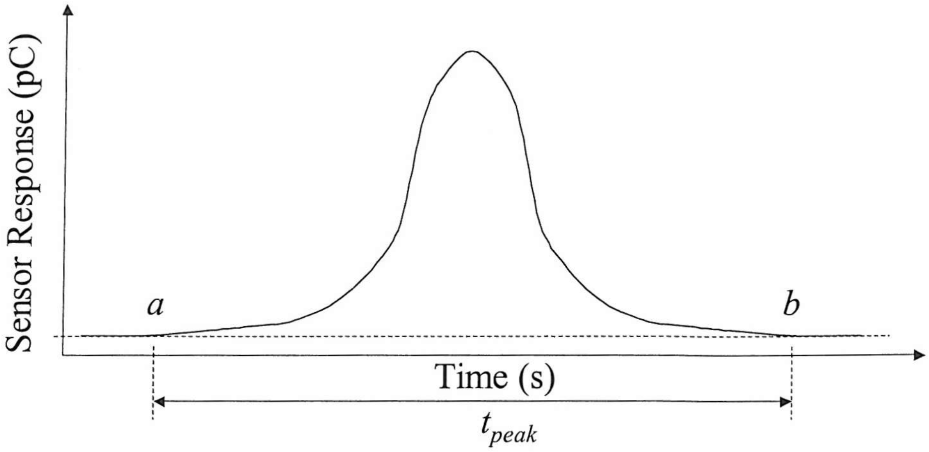

Figure 8.6 Peak response to a charged debris particle moving pass sensing face, the dotted line indicates the baseline and point a denotes the start of the peak while point b denotes the end of the peak.

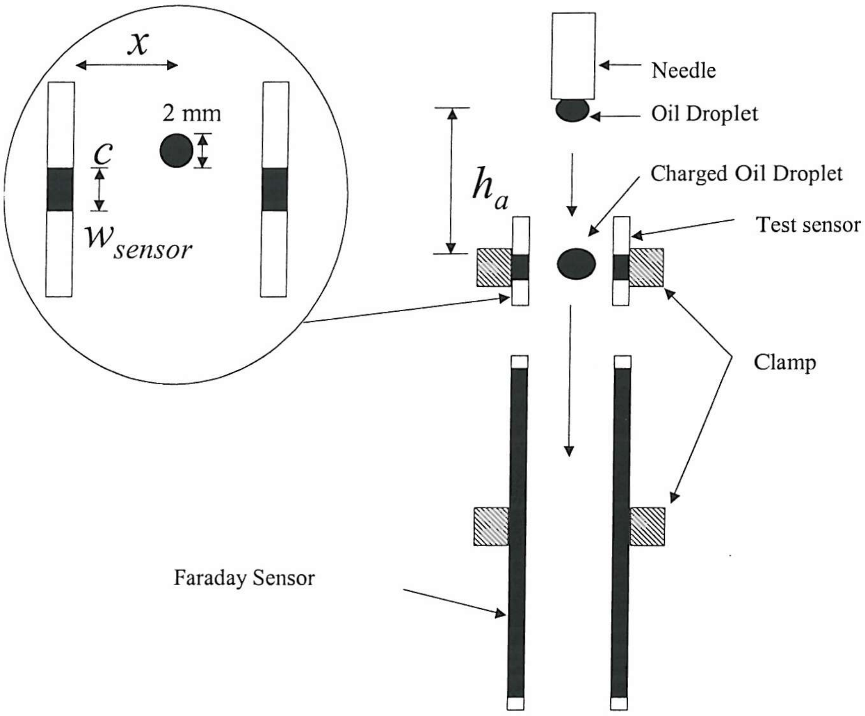

Figure 8.7 Schematic diagram indicating parameters used to calculate sensor field of view.

8.3.2 Field of View Test

The field of view for the Mk I, Mk II, Mk III and Mk IV sensors were found to be 21 mm, 93 mm, 50 mm and 160 mm, respectively, as shown by Figure 8.8. The results show the

Mk I sensor had the smallest field of view (21 mm), while Mk IV had the largest (160 mm) (see Figure 8.9) and Mk II had the highest efficiency (57 %) (see Equation 7.16 on page 203), while Mk I had the lowest (10 %) (see Figure 8.10).

The field of view for the Mk I and Mk II sensor decreases with increasing off-centre distance, see Figure 8.11 Mk I (Mk III and IV was not tested for off-centre effects), this is analogous to the change in the efficiency with increasing off-centre distance discussed in Section 3.5.2. The schematic of the field of view of Mk I cylindrical sensor is shown by Figure 8.12. Note that the point at 0 radial position was not measured but was extrapolated.

In micro-macro sensor design, the variations in efficiency due to off-centre effects are undesirable. Ideally, any charge particle to be monitored should be in the vicinity of 0.5 – 1 normalised radial position (see Figure 8.11), to minimise off-centre effects. In real applications, this can be done by restricting the flow within the vicinity using special piping.

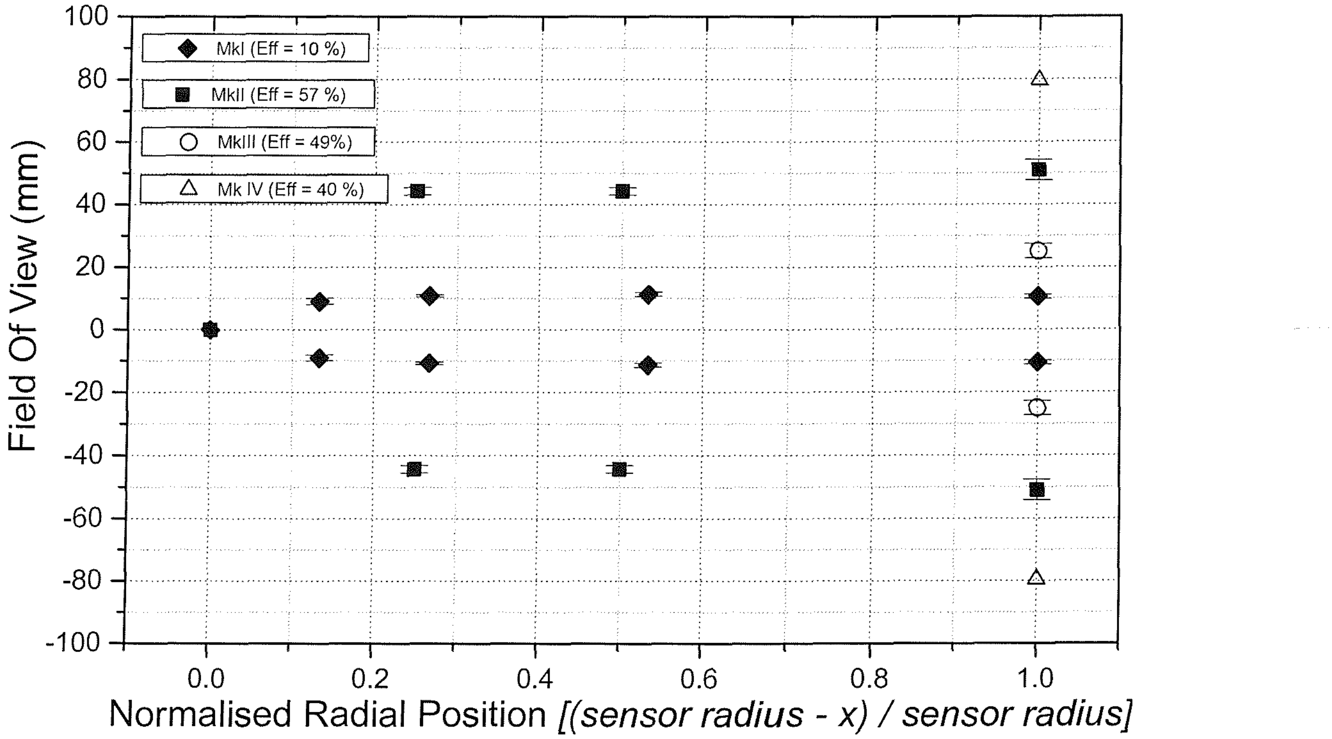

Figure 8.8 *Graph showing the comparison of the field of view for Mk I, Mk II Mk III and Mk IV sensors.*

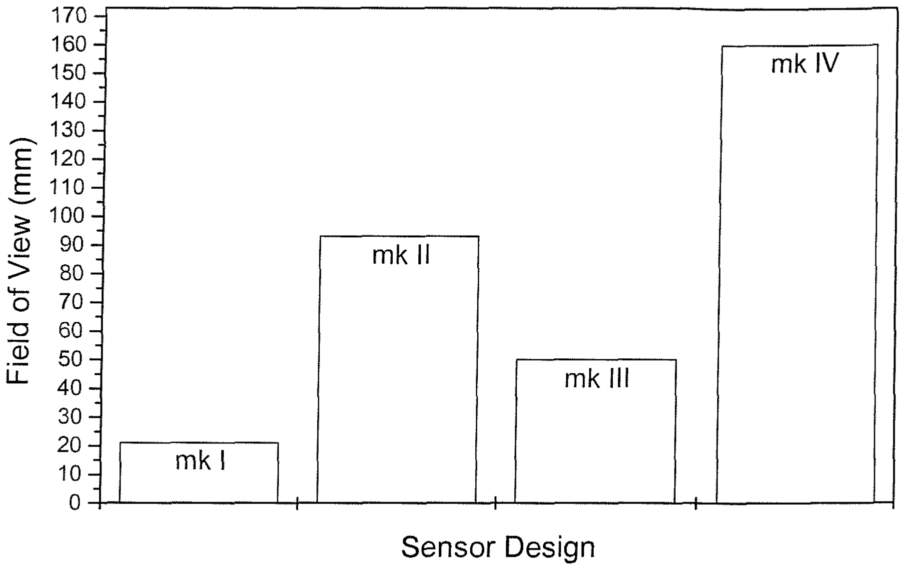

Figure 8.9 *Maximum field of view graph for sensors tested*

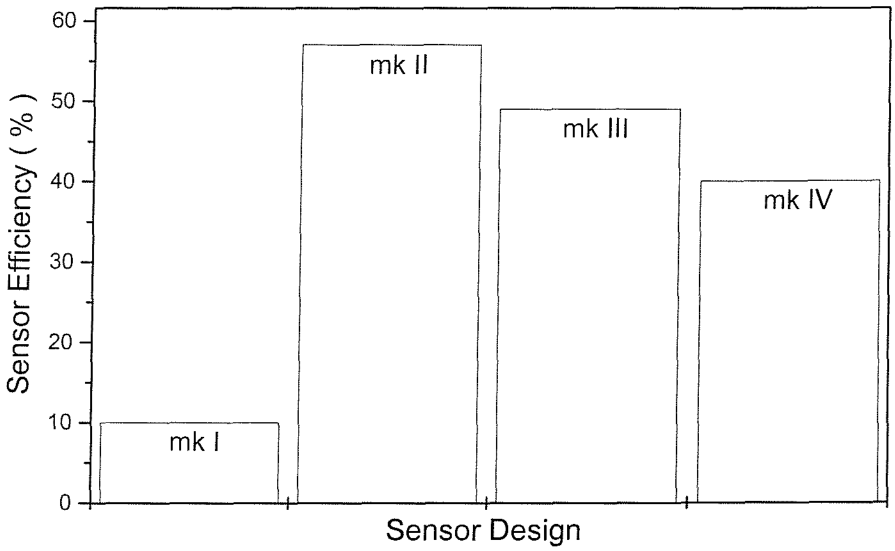

Figure 8.10 *Mean efficiency graph for sensors tested*

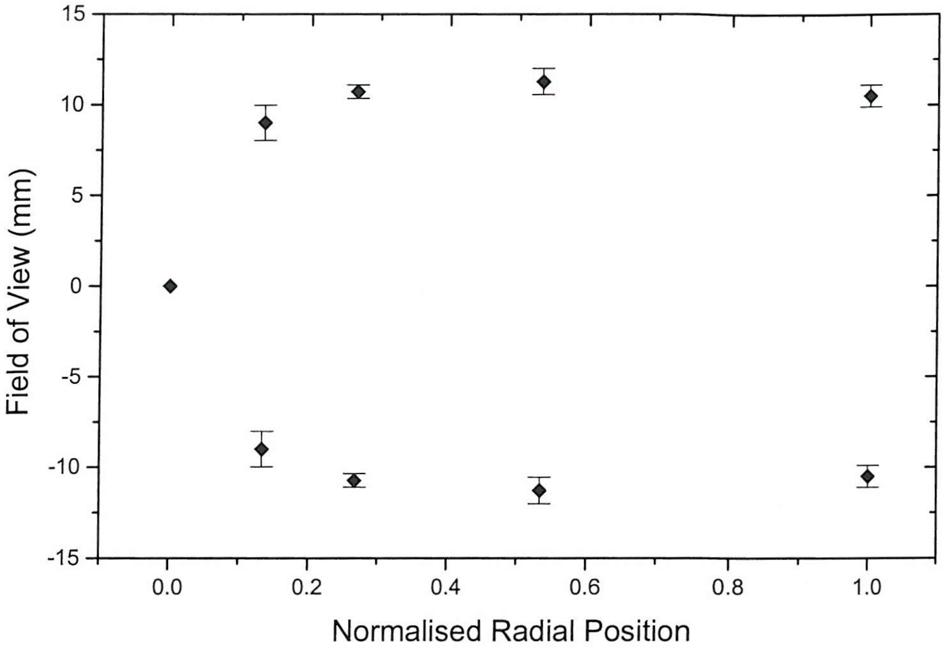

Figure 8.11 *Mk I field of view showing that there is a decrease in the field of view with increasing off-centre distance.*

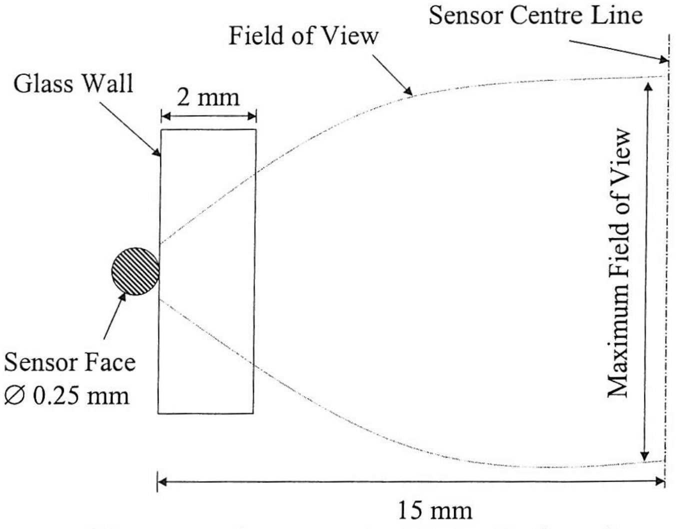

Figure 8.12 *Schematic diagram of a Mk I cylindrical sensor field of view.*

The series of tests indicate the importance of the proximity of the shielding on the field of view and sensor efficiency: For the Mk I sensor the shielding is very close to the sensor face thus, when a charged particle passes the sensor, the field lines will link onto both the shield and the sensor face. This 'competition' for flux lines on the surface will affect sensor efficiency. For the Mk I design, the flux lines only link to the sensor face over a short distance in the sensor and even then the majority are still linked to earthed planes resulting in a small field of view (20 mm) and low efficiency (10%). Despite the desired small field of view, the low efficiency of the sensor is a major limitation as the signal to noise ratio is very low (approximately 5 dB), as shown in Figure 8.13. An example of a high signal to noise ratio (approximately 56 dB) is shown by Figure 8.14. The signal to noise ratio is important because it affects the accuracy of data analysis. The lower the signal to noise ratio is, the more a peak signal is affected by small perturbations of the background noise, causing errors.

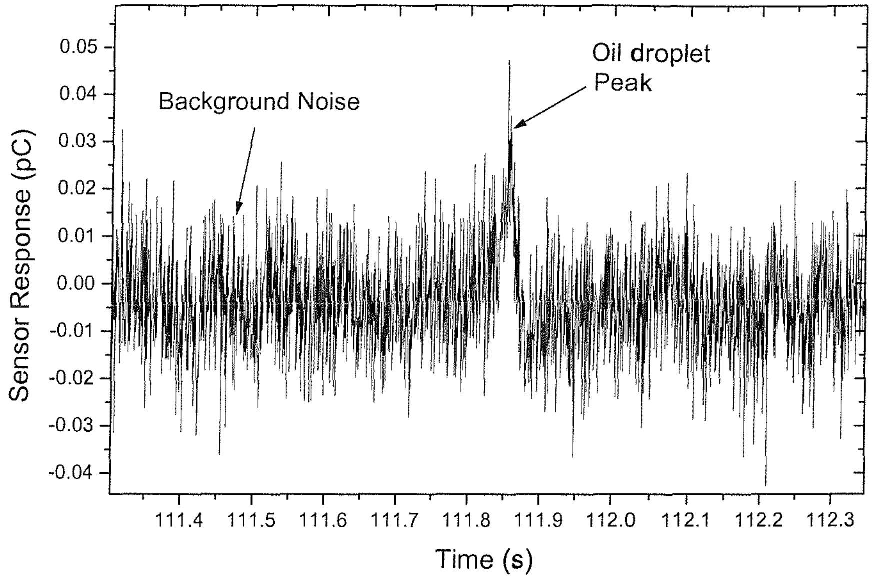

Figure 8.13 *Low signal to noise ratio (8 dB). Signal due to an oil droplet (with charge Q) from a sensor with very low efficiency.*

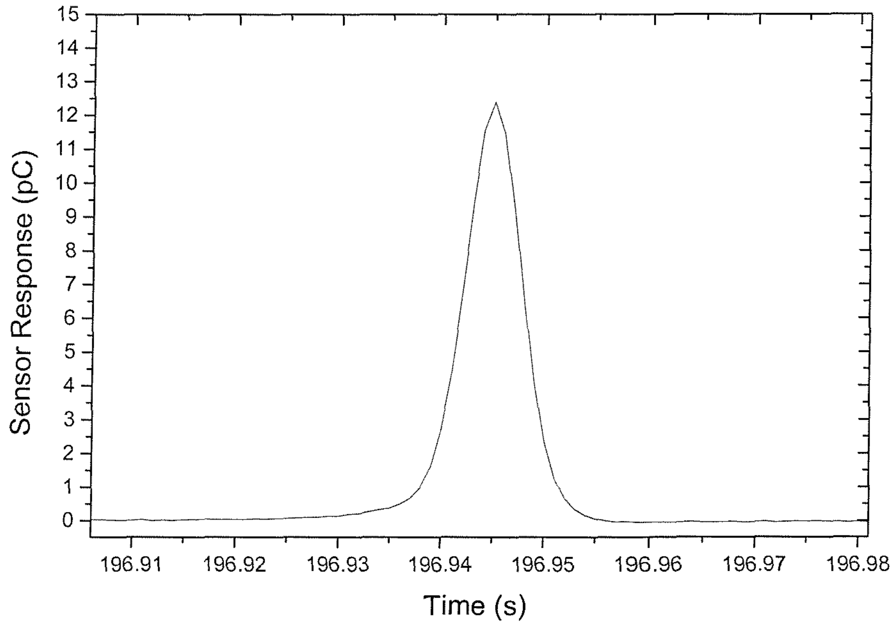

Figure 8.14 *An example of high signal to noise ratio (56 dB). Signal due to the same charged oil droplet as in Figure 8.13, from a high efficiency sensor.*

Moving the shielding further away as in the Mk II design increases the efficiency and the field of view. There is now less 'competition' for flux line termination on the shield and hence a greater flux density on the sensor face resulting in higher efficiency. The flux lines begin terminating much earlier (and leave much later) on the sensor face increasing the field of view. The efficiency (55%) of the Mk II reveals much improvement over the Mk I design (10%), but there is a corresponding increase in the field of view. A compromise between the first two designs led to the manufacture of the Mk III sensor, which has a reduced field of view (50 mm) compared to Mk II (90 mm) with a slight reduction in the sensor efficiency (50%).

The Mk IV sensor design was based on the Mk III, except the sensing face was recessed (and the shielding was moved accordingly) using a PCB spacer in an attempt to further reduce the field of view. This produced unexpected results; the efficiency decreased (40%) compared to Mk III but the field of view increased dramatically. It is obvious that a response from Mk IV, shown in Figure 8.15, is very asymmetric compared to the response from the Mk III sensor. Figure 8.15 shows normalised charge to enable a direct comparison. It is worth noting that the first half of both peaks are nearly identical and that the asymmetry of Mk IV comes from the second half of the peak, (i.e., when the charged test object moves away from the sensor face). It is as if the flux lines are 'reluctant' to 'let go' once they have terminated on the sensor face, thus resulting in the 'trailing off' effect. The only difference between the Mk IV and Mk III sensor designs is the presence of the PCB material between the sensing face and the charged object. The PCB material has a higher dielectric constant (typically 4-5) compared to air (1). Thus, after the flux lines have linked on to the sensing face, as the charged particle is moving away, they prefer to stay terminated on the sensing face (with presence of higher dielectric constant) rather than 'migrating' to the shield, as illustrated in Figure 8.16. Further design improvements are needed to eliminate this problem.

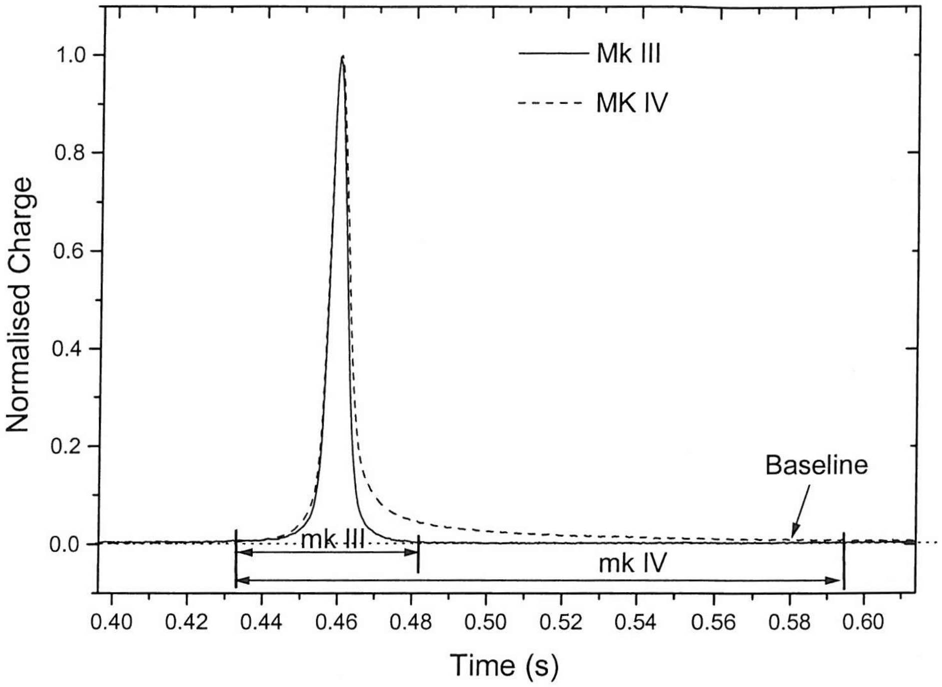

Figure 8.15 Comparison of normalised single peak response of Mk III and Mk IV sensor showing the asymmetric nature of Mk IV response and the increase in the field of view.

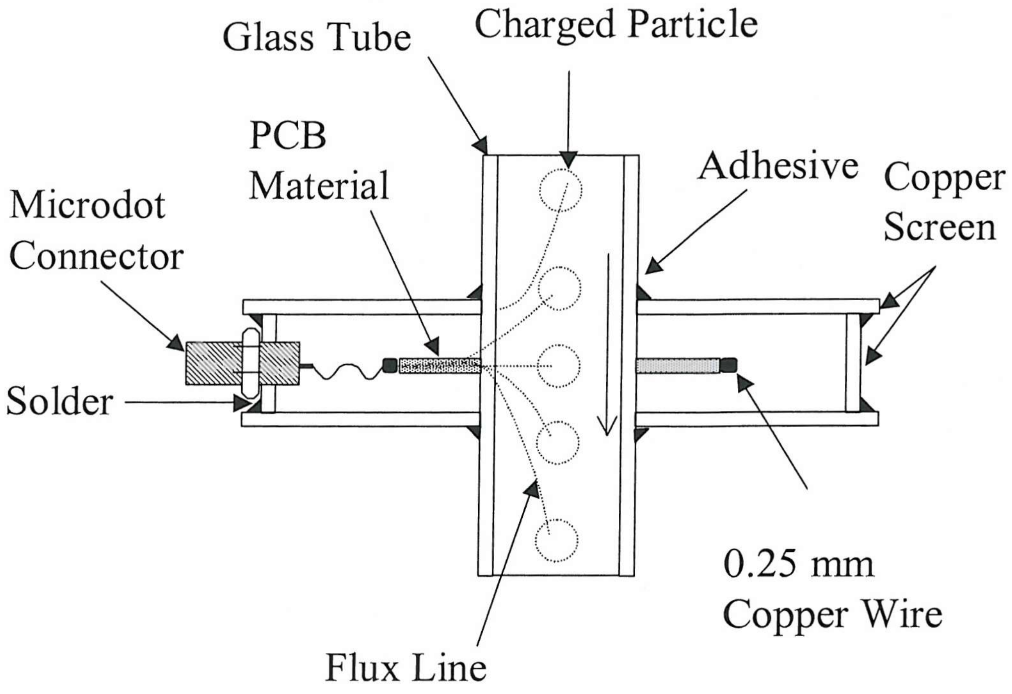

Figure 8.16 Illustrating the reluctance of the flux line to leave the sensing face as the charged particle is moving away from the sensing face.

Computer modelling work has been attempted using three-dimensional boundary element modelling software to design and optimise micro-macro sensors. A Commercially available software package, 'Coulomb Boundary Element Field Modelling Version 6.0' from Integrated Engineering Software (220-1821 Wellington Avenue, Winnipeg, Manitoba R3H 0G4) was used. Computer modelling has the potential to eliminate particle handling problems and facilitate optimising of new sensor designs by allowing each design to be tested virtually before being manufactured. Details on the background to Coulomb operations and some preliminary results can be found in Appendix C. The potential of Coulomb to be a useful tool for electrostatic sensor design and optimisation has been demonstrated. However, operational software bugs that were critical to the accuracy and reliability of more complex modelling have hindered further progress. Optimisation of the software itself needs to be carried out to solve the specific modelling required. Unfortunately, this work cannot be completed in time for discussion in this thesis.

8.4 CONCLUSIONS

The feasibility of establishing a micro-macro sensor design that can detect particle size has been investigated. However, particle handling and resolution issues have hindered further progress. Attempts have been made to address the resolution issue in this chapter.

It has been established that in order to achieve a high resolution OLS, compromise needs to be made between the field of view and sensor efficiency. The design of the earth shield played an important role in determining the efficiency and field of view of the sensors.

The smallest field of view of the cylindrical sensor was achieved using the Mk III sensor design. The Mk IV design produced unexpected results and further design and testing needs to be done to correct the problem.

For oil-line debris monitoring purposes, the Mk II sensor design is ideal if the charge level on the debris is generally low and if the field of view is not an issue, due to its high efficiency.

The Mk III sensor design is suitable for oil-line debris monitoring if it is desired to have high probability of resolving individual debris due to its compromise in the efficiency and resolution.

Computer modelling using Coulomb has the potential to address the problems associated with particle handling and sensor design and optimisation although optimisation of the software itself is essential to solve problems specific to this research.

9 CONCLUSIONS AND FURTHER WORK

9.1 CONCLUSIONS

Condition monitoring is a practice that is essential in current maintenance management of mechanical machinery in order to detect faults at an early stage and avoid catastrophic failure and complete seizure of operation. There are three key components for successful monitoring activities; dependable detection, effective diagnosis and reliable decision. The advantages of condition monitoring compared to other maintenance strategies include improved availability of equipment, reduced breakdown costs, improved reliability and safety and improved planning. The most common condition monitoring techniques used in industry are manual inspections, vibration, temperature, performance, expired life and oil and wear debris analysis.

Offline debris analysis has long been employed as a monitoring technique to monitor component health and aid in the planning of maintenance schedules. Debris monitoring can be divided into two main categories; namely, trend monitoring and debris morphology analysis. Trend analysis is the process by which a change in machine condition is determined from an examination of changes of specific sensors or output. Debris morphology analysis on the other hand is the close examination of wear debris collected from a system to determine the exact nature of the predominant wear mechanism. Properties such as shape, size, surface topography and colour and thickness are examined and experience as well as standard information are used to conclude findings. This technique is usually more accurate as it gives a good picture of the wear activities of the components. However, the main disadvantages of offline debris analysis are that it is time consuming and the need to employ an expert to carry out the analysis. In-line and on-line debris analysers does not give as much information as the off-line analysis technique as they only provide size distribution information. However, the speed of retrieving this information is a good compromise to the lack of information.

Electrostatic condition monitoring has the potential to address the shortcomings of the lack of information of current in-line and on-line condition monitoring techniques. This technique was first developed to monitor the detection of debris in the gas path of jet engines and turbines. Previous preliminary work has been carried out by other researchers at the University of Southampton to implement similar systems into oil-lubricated systems. Early investigative tests were carried out on a laboratory scale using test rigs such as a pin-on-disc rig, a Plint TE/77 reciprocating rig and FZG gear test rigs. Precursor signals relating to the onset of scuffing have been detected. The signals were thought to relate to one or more of the following: tribocharging phenomena, triboemission, surface charge variation and debris generation.

Electrostatic sensors based on charge induction principles can be designed in various shapes and sizes. The differences in response of each sensor geometry are influenced by the signal processing that is used to analyse the output from the sensor. The properties of the monitored charge source also influence the output from these sensors. For example, both the standoff distance and the speed of the charge source affect the charge sensed.

Previous studies by various researchers suggested that there are several charging mechanisms than can contribute to charge detected in a lubricated contact, namely tribocharging, contact potential difference and charged particle emission. Tribocharging can be divided further into 2 categories; solid-solid and solid-liquid tribocharging. Surface phase changes can cause variations in surface contact potential differences. This will produce a surface charging effect due to electron transfer. Charged particle emissions occur when bonds are physically broken due to the formation of cracks and fracture on the contacting surfaces and the charge emission depends on the properties of the materials.

The tests conducted for this thesis have been designed to obtain information on the level of charge associated with surface charge variations and wear debris to help evolve the sophistication of electrostatic wear monitoring techniques. Electrostatic theory has been used and simple models developed to help understand the fundamental charging mechanism and to predict charging events.

In this investigation, lubricated sliding wear tests were carried out to investigate the possibilities for monitoring and identifying precursor signals prior to significant wear in a controlled environment. Precursor charge signals were detected and found to originate from surface charging as a result of contact potential difference (CPD) effects due to the formation of white layers. Wear debris was also found to contribute to the observed charge features. The charge features due to CPD effects and wear debris can be distinguished on the colour map and rms charge amplitude as a function of location on the disc and test duration; CPD effects produce static features while wear debris produces dynamic (moving on the disc surface) features. A colour map was found to be the best way to monitor charge as it provides information on charge features magnitude and exact location. The predominant polarity of the precursor charge features were different for the different lubricating oils used. Precursor signals with mineral base oil were predominantly positive while with fully formulated synthetic oils both positive and negative precursor charges were present. This difference is thought to arise from the difference in oil chemistry but further study is required to identify the exact chemistry responsible. The electrostatic sensing system was sensitive to small changes (indicated by friction change) in wear but undetectable by volume loss measurement, which is an important indicator of the potential of the system to be used to monitor wear trends and the behaviour of critical oil lubricated machinery components.

Two main contributors to significant charge features and precursor signals have been identified as CPD effects and wear debris. Further experiments were specifically designed and conducted to investigate both factors in more detail in an attempt to assess their levels of contribution. The tests were also used as a calibration study for the 'button type' wear site sensors (WSS) and cylindrical 'ring type' oil line sensor (OLS).

In order to quantify and assess the sensitivity of the WSS to surface charge variation, simulated surface charging and dynamic CPD effect tests (dry sliding) were carried out using the pin-on-disc test rig. The electrostatic sensor and sensing system were found to be sensitive to surface charge variations created by inserting various metal inserts into a bearing steel disc. The response was consistent to that predicted by the work functions of the metal inserts. Significantly, the electrostatic sensing system is sensitive to very small (<< 0.05 eV) CPD, represented by a mild steel insert within a bearing steel disc. Sensitivity to such small CPD, associated with subtle changes in surface composition similar to those of white layers (phase-transformed regions), demonstrates the technique can monitor wear initiation on a surface. The ability of the electrostatic sensing system to monitor dynamic CPD effect was demonstrated by monitoring the oxidation-delamination-reoxidation process during unlubricated sliding tests of steel pairs. This also demonstrated the ability of the system to provide distinctions between mild and severe oxidational wear processes.

After establishing the sensitivity of the WSS to surface charging due to CPD effects, investigation into the sensitivity of the WSS to freshly generated wear debris was carried out using a pin-on-disc test rig. Tests were divided into two categories; normal wear and induced wear by debris seeding both using a mineral base oil lubricant. In all categories, the WSS were found to be sensitive to charge related to the formation, entrainment and transportation of wear and seeded debris. The response from the WSS directly monitoring the wear track indicated that the contribution of charge from the wear and seeded debris dominated over (10 times more) charging from CPD effects. The WSS sensor monitoring the disc surface outside the wear track (downstream) showed dynamic charge features due to centrifuged (debris transportation) charged debris. During normal wear the charge detected by the electrostatic sensors was dominated by the charge due to the production and presence of freshly generated wear debris. In the steel debris seeded test, charging was dominated by a mixture of contributions from charged wear debris from induced wear as well as entrained seeded debris. In the silicon carbide debris seeded test, the charge detected was dominated by charged entrained seeded debris. The WSS was also sensitive to small changes in the contact severity (indicated by fluctuations in friction) and hence changes in the rate of wear (not detectable from volume loss measurements) and the amount of wear debris produced. Debris charged positively for normal wear and negatively for induced wear by debris seeding. The explanation for the difference in the polarity was not clear, although it is thought that the difference in the wear mechanism (adhesive and abrasive wear) was the probable cause.

Research into simulated debris charging was designed to gain a better understanding of debris charging mechanisms in oil lubricated contacts. Cylindrical type oil line sensors (OLS) were used, as they are the most effective sensor geometry for electrostatic debris monitoring. It was established that one of the possible charging mechanisms for wear debris is solid-solid tribocharging. The polarity and magnitude of this charging was shown to be related to the triboelectric series. Copper test particles were found to charge slightly after sliding on a copper surface. This is analogous to normal wear debris and seeded steel debris charging observed during pin-on-disc testing. The change of the charge magnitude is 10 times higher than the background level during the seeding of silicon nitride debris compared to steel debris and this can be related to a high work function difference. Some contribution of solid-liquid tribocharging was also observed although it is thought to be minimal and more refined tests need to be designed in order to study it further. In a real system, the predominance of solid-solid tribocharging can very useful. For instance, when monitoring debris downstream in a system that employs hybrid ceramic-steel bearings and copper lubrication pipes, a negative signal can be attributed to ceramic debris while a positive signal can be attributed to steel debris. The conductivity of the lubricants used affects the charge on wear debris as it influences the rate of charge decay. The higher the conductivity, the higher the rate of decay.

A general but complex charging model has been proposed for debris charging, taking into account tribocharging, surface charge, triboemission and debris charging mechanisms. It takes the form of:

$$Q_{debris} = f\left[\ C_{eff}\Delta\phi\,,\ \frac{K_{\pm}}{K_{\pm}^{'}},\ D_{\pm},\ \left(\varepsilon\varepsilon_{o}\rho n_{\pm}\right),\ \kappa,\ \nu\,,\ \tau,\ A,\sum\left(E_{debris}N_{debris}\right)\ \right]$$

Thus, debris charging depends on surface work functions, oil chemistry, impurity concentration and conductivity, wear rate and sliding velocity. The (MkI) OLS response was found to be influenced by its geometry (length and diameter) and the dimensionless factor of aspect ratio due to changes in the flux termination characteristics. For a given (MkI) sensor diameter, an increase in the sensing face length resulted in increased efficiency. For a given sensing face length however, the increase in the diameter results in the decrease of efficiency. The optimum aspect ratio was found to be 1.5 at which point the efficiency of the sensor reaches 100 %.

The concept of a micro-macro sensor design that has the potential to detect debris size has been proposed. Feasibility studies have been carried out but particle handling and resolution issues hindered further progress. In order to achieve the design, preliminary work has been carried out to improve the resolution of the current sensor design. The resolution of OLS is related to the field of view and overall efficiency. The higher the resolution unfortunately, the lower the efficiency. High resolution on the OLS is desired, but a compromise between resolution and efficiency has to be made to produce responses with good signal to noise ratio. Various designs of sensor were tested and the Mk I design was found to have the smallest field of view (21 mm). The Mk II sensor possesses the highest efficiency (57 %) and is currently employed in the oil line of a bearing test rig for real-time debris monitoring in an on-going bearing test programme at the University of Southampton. The high efficiency of Mk II sensor is ideal for the test programme as charge levels on the debris are generally low and the field of view is not an issue since only the trend of debris presence is of interest and not the detection of individual debris. The Mk III design possesses a good compromise between the field of view and efficiency.

Figure 9.1 illustrates the complexity of possible events that can influence the amount of charge present on wear debris before, during and after the wear debris reaches the sensing area. At position 1, at the instant after wear debris formation, charge Q_1 is present on the majority of the debris, imparted by the formation process (details can be found in Appendix D). As the debris moves out of the contact area, addition and reduction in magnitude of the charge can occur due to its interaction with the surrounding oil and surfaces, for example, tribocharging, decay to earth and charge recombination. The net charge on the debris will now become Q_2 at position 2. At the sensing area, position 3, the magnitude of the detected charge, Q_3, can be influenced by the sensor geometry, the distance of the debris to the sensor and the relative position of the debris to the centre of the sensing face. The electronics of the signal conditioning can also influence the detected charge, altering it further to become Q_4. As the debris moves out of the sensing area, there is a possibility that it will remain on the wear surface, re-entrained into the contact and interact with freshly generated debris in the next cycle.

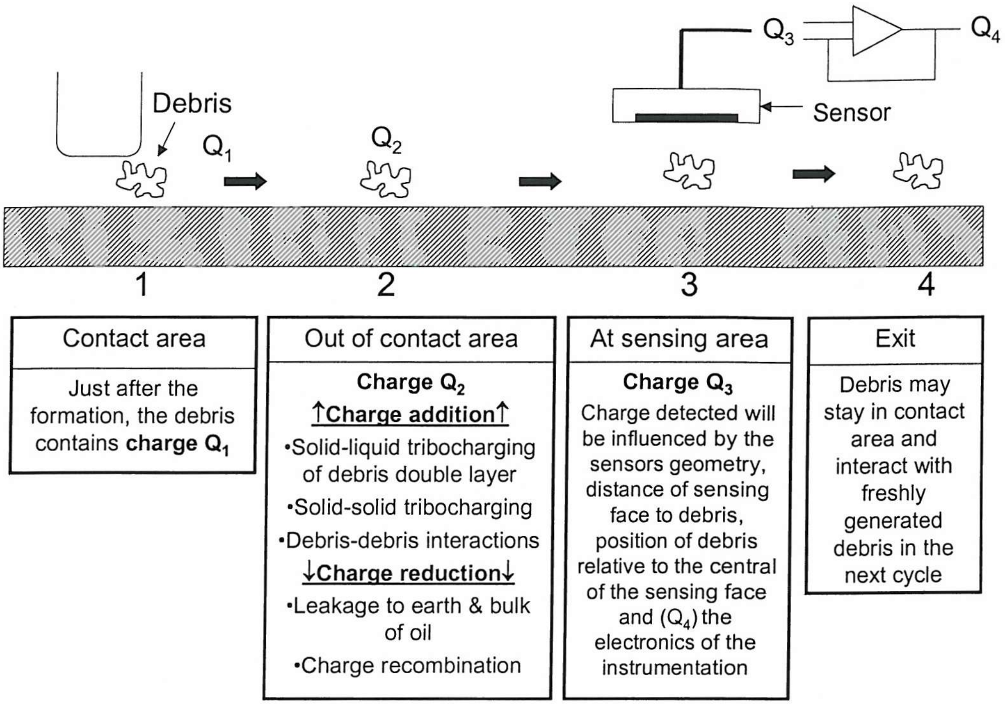

Figure 9.1 Schematic of possible events that can influence the amount of charge present on wear debris before, during and after the wear debris reaches the sensing area and produce a response.

The relationship between the tribological parameters, wear, debris characteristics and charge are shown in Figure 9.2. This figure illustrates the general dependence of the charge magnitude and polarity on the wear process, which has been demonstrated in this thesis. Chapters 4 and 6 demonstrated that increased wear rates occur as a result of the deterioration in the contact condition, which then leads to increased amounts and size of wear debris produced. This in turn increases the magnitude of the charge detected from the wear site as well as outside it. Chapter 6 also demonstrated a probability that the wear mechanisms influence the polarity of charge imparted on wear debris. Work detailed in Chapter 7 established the influence of the debris material on the charge polarity as well as the magnitude of charge imparted. This is potentially very useful in real systems, as it will enable the source of the debris to be identified given a prior knowledge of the type of materials present. It has also been established that in air, the surface area and hence the size of test debris are directly proportional to the magnitude of charge imparted. Preliminary work to optimize the OLS for debris monitoring has been carried out and is discussed in Chapters 7 and 8. The objective to establish a sensor design and geometry that, coupled with suitable electronics and data analysis, can be used to discern debris size and morphology was partially met within the timeframe of this thesis but future work to achieve this aim is outlined. This potentially creates a very powerful tool for debris monitoring as it will provide information for the identification of wear severity, rate, type and source.

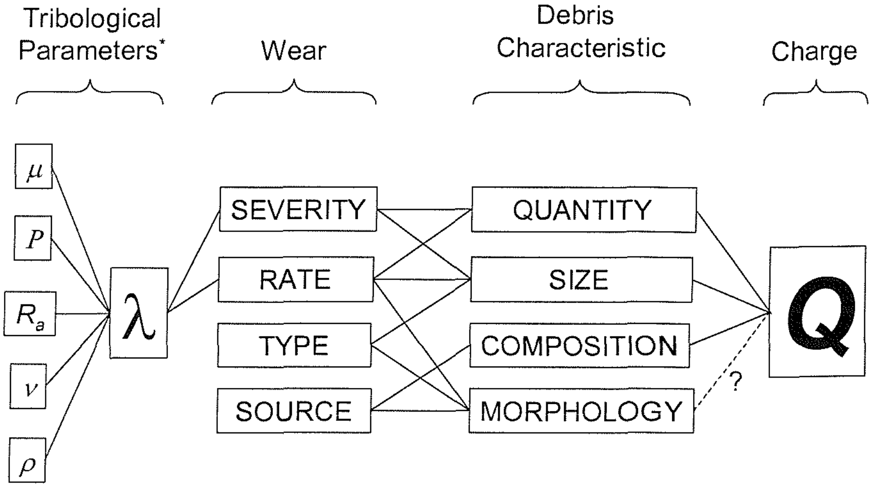

$^{*}\mu$ = coefficient of friction, ρ = oil viscosity P = contact pressure, v = sliding velocity, R_a = surface roughness, λ = ratio of minimum film thickness to surface roughness, Q = charge.

Figure 9.2 Relationship between tribological parameters, wear, debris characteristic and charge.

9.2 FURTHER WORK

Debris Charging Mechanism

Tests to investigate possible charging mechanisms presented in this thesis used idealised test debris. Although the materials used are similar to that found in real lubricated systems, neither the size nor the morphology of the test debris closely represent real situations. Better debris handling techniques need to be devised to enable the testing of test real life size wear debris. Furthermore, the real-time debris monitoring work (Chapter 6) is not a well controlled debris charging test and charge on debris was probably imparted by a combination of mechanisms.

Work conducted in this thesis (Chapter 7) has found a possible contribution of solid-liquid tribocharging on debris charging. The test, however, was not designed specifically to investigate this effect and hence, a refined test programme should be designed to establish the real extent of the contribution from debris charging.

Oil properties are known to affect the double layer characteristics and the rate of solid-liquid tribocharging and hence, tests need to be conducted with various types of lubricating oil and debris material.

A more refined test needs to be carried out to investigate debris charge characteristic due to different wear mechanisms, for example, adhesive wear and abrasive wear mechanisms. Although the investigation of charge characteristics on debris due to adhesive wear in this thesis has been carried out using the best methodology, the abrasive wear debris testing methodology could be improved further. Instead of inducing abrasive wear by debris seeding, a pure two-body abrasion with the use of abrasive disc-soft pin or abrasive pin-soft disc pairings will give a more controlled mechanism. This will reduce the possibility of having three-body rolling abrasion wear mechanisms occurring simultaneously.

Oil Chemistry Effects

Oil chemistry is thought to influence the polarity of precursor signals detected during lubricated sliding wear tests in Chapter 4. It is thought that the characteristic of surface charging can depend on the type of lubricating oil used. This is related to the presence of additives and other chemicals and impurities that can react with active wear surfaces producing surface charging. These effects need to be studied further and refined tests should be carried out in order to establish their level of influence.

Computer Modelling

Computer modelling work using Coulomb has a massive potential in facilitating the design of more sophisticated sensors particularly in supplementing the work presented in Chapter 8. Design and optimisation of the electrostatic sensor for the purpose of debris monitoring using Coulomb will allow possible sensor designs to be virtually built and tested without the need of manufacture. Once the optimised designs have been identified, sensors can then be built and tested in the lab. Current experience with Coulomb has highlighted the need to optimise the software itself to be used to solve problems that are specific to this research.

Coulomb can also be used to model the charge on debris to establish any electric field characteristics that can be exploited to be used to design sensor and sensing system that are able to discern debris of different morphologies. It can also be used to model the behaviour of surface charge on active wear sites in relation to its surrounding and wear site sensor position.

Total Charge Generation Equation

The overall charge detected function discussed earlier was postulated based on knowledge of related fundamentals and is by no means precise. Further work with a refined test methodology to investigate debris charging mechanisms should be able to provide more detailed information into the significance of each parameter, which can then be used to develop more precise relationship.

APPENDICES

APPENDIX A

Origin of Background Charge

The background charge level variation is typically sinusoidal in nature. Although the disc is earthed, it does not have a common earth to the sensor and the sensing system. The electrostatic sensor and sensing system used is sensitive to capacitive change caused by changes in the disc surface – sensor face distance. To confirm this hypothesis, a simple test was conducted involving a non-contact test employing a rotating bearing steel disc monitored by and electrostatic sensor at the same radial position of sensor 2 in Chapter 6 and the charge response was recorded. The electrostatic sensor was then replaced by a laser vertical displacement probe to measure the variation in the altitude of the disc surface. Figure A1 and Figure A2 show the colour map of the output of the electrostatic and laser probe respectively indicating that the characteristic response is very similar. High altitude produced high (positive for electrostatic sensor) response while low altitude produced low (negative for electrostatic sensor) response. Line plots, shown in Figure A3 further indicate that the electrostatic sensor is indeed sensitive to the altitude variations of the disc surface. The resolution of the laser probe is much higher than the electrostatic sensor and this is reflected in detail shown in the plots.

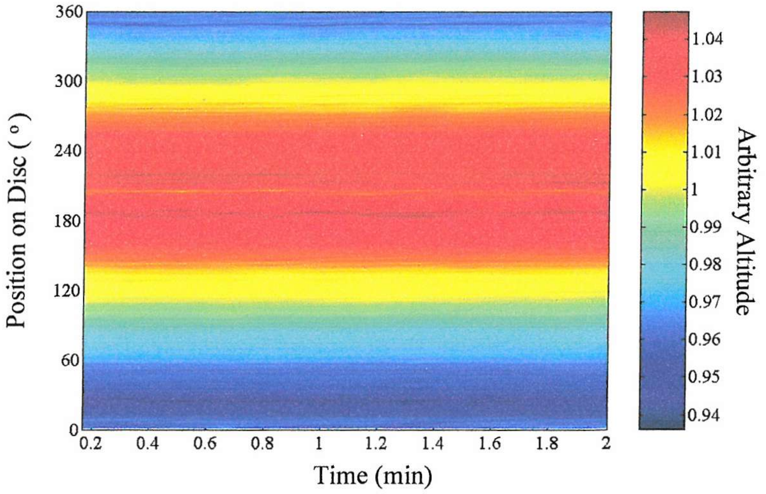

Figure A1 Unnormalised colour map plot from the laser vertical displacement probe output. Non-contact, 1 ms^{-1} sliding speed, bearing steel disc.

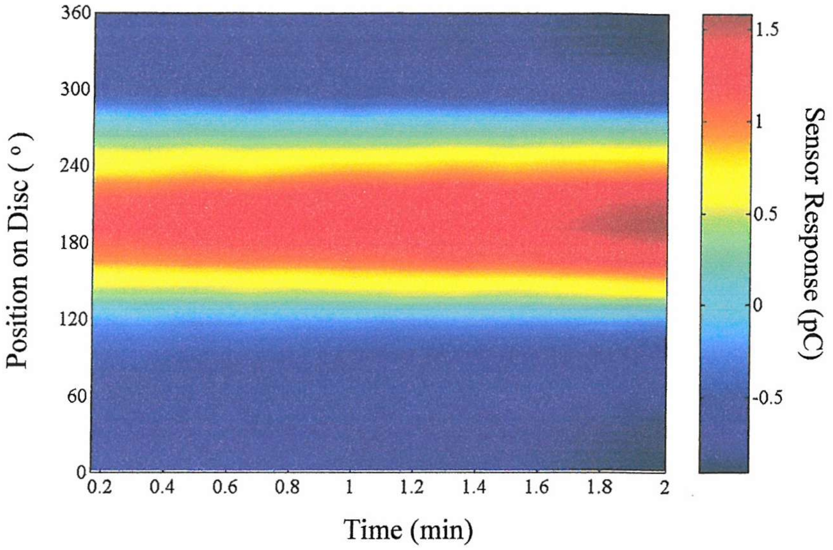

Figure A2 *Unnormalised colour map from the electrostatic sensor output. Non-contact, 1 ms^{-1} sliding speed, bearing steel disc.*

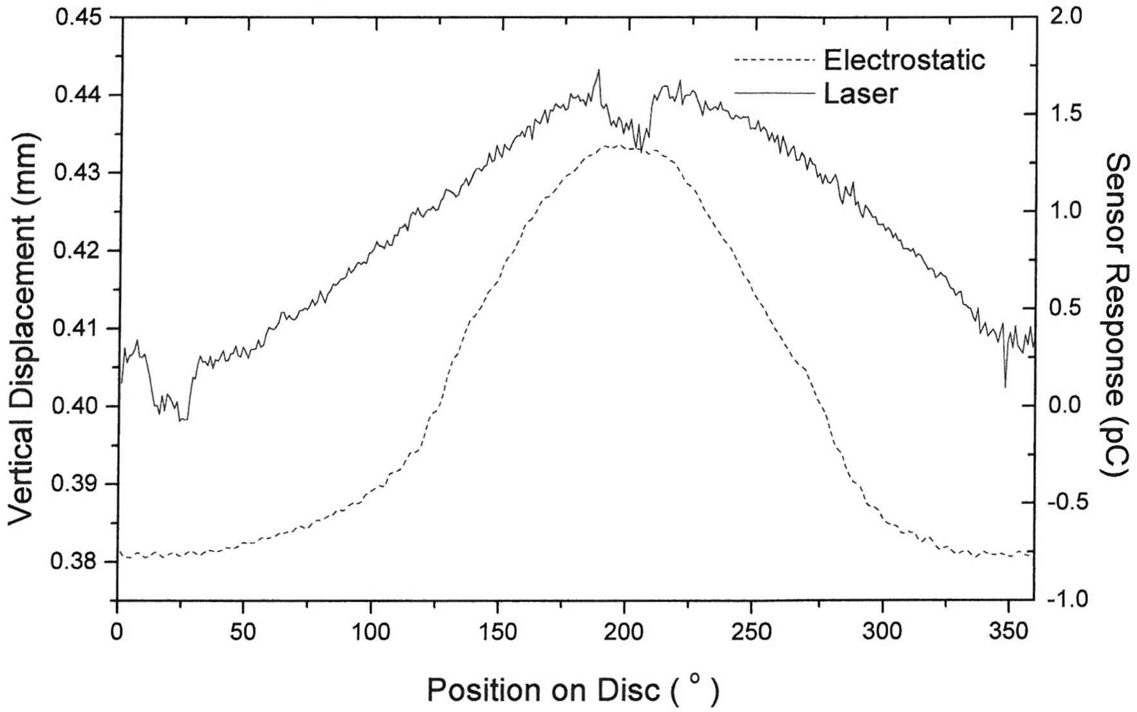

Figure A3 *Line plots comparing the output from the laser vertical displacement probe and the electrostatic sensor confirming that the electrostatic sensor is sensitive to variation in the disc attitude. Non-contact, 1 ms^{-1} sliding speed, bearing steel disc.*

Assuming that there is no influence from nearby charge or electric field, the sum of all charge on the disc surface should be zero, to be electrically neutral. This would explain the sinusoidal behaviour of the background charge level detected by the sensor. Any positive charge regions on the disc surface will be balanced by a negative charge on other regions of the disc to maintain electrical neutrality. Summing up points in the electrostatic line plot in Figure A3 however will not produce zero. This is because the sensor is only monitoring a small area of the disc.

Wear Site Sensor Resolution

At a height of 0.5 mm above the surface of the disc, the 10 mm diameter WSSs are known to have a circular field of view approximately 13 mm in diameter [101]. Taking this into consideration, and given that the position of sensor 2 in Chapter 6 is about 35.6 mm from the centre of the disc, this translate to approximately 20° of rotation, shown in Figure A4.

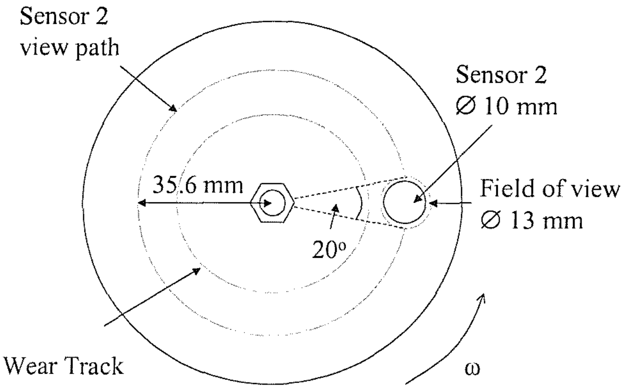

Figure A4 *Field of view of an electrostatic sensor. For the given position of sensor 2 the field of view has a radius of 13 mm.*

A simple test was carried out to find out the resolution of the electrostatic sensor. Small rectangular (1 mm × 5 mm) strips of carbon adhesive tape were position on the view path of the sensor, as shown in Figure A5. The carbon having a higher work function than steel producing negative surface charge (see Chapter 3). Four pairs of carbon adhesive tape were position on the disc, with separation of 3°, 6°, 21°, and 27° respectively. The charged detected by the sensor is shown in the colour map plot in Figure A6. It is evident that the WSS is able to resolve down to 3° of surface charge separation on the disc surface, equivalent to approximately 1.9 mm of separation distance. Figure A7 shows the signal average of the sensor response. It shows that for 3° and 6° separation, the pairs of surface charge produced twin peaks while larger separation produced two distinct separate peaks.

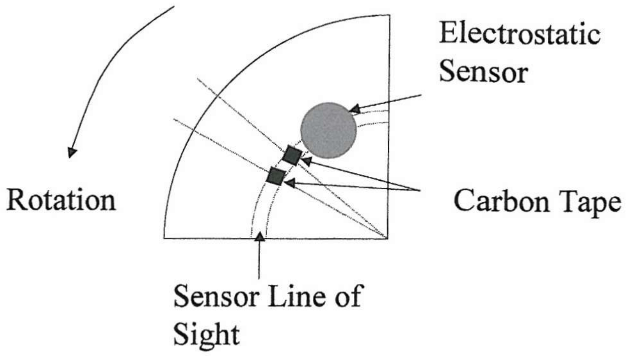

Figure A5 *Schematics illustrating the position on the carbon adhesive tape strips.*

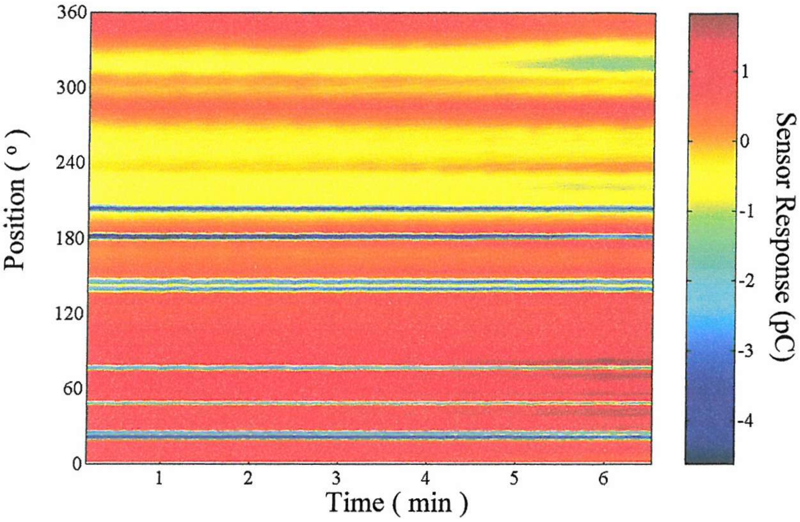

Figure A6 *Colour map showing the charge features detected due to simulated surface charge.*

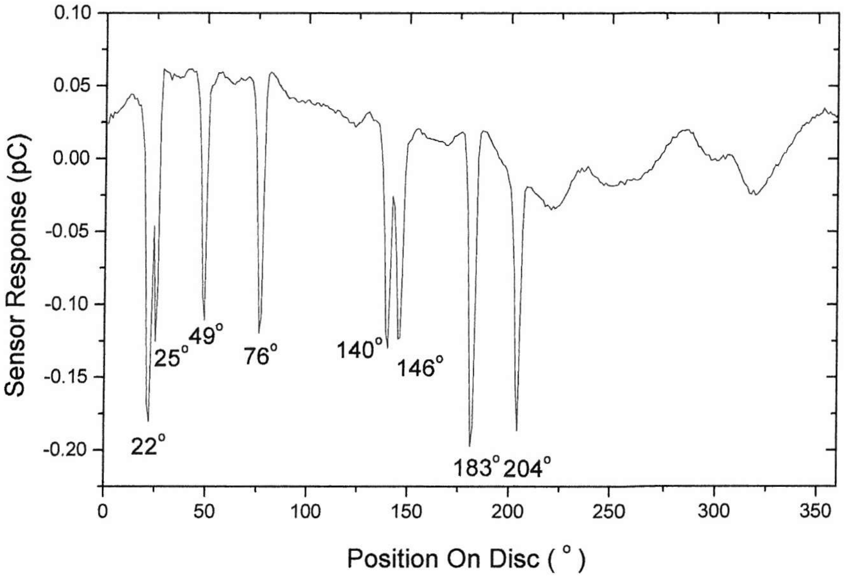

Figure A7 *Signal average plot derived from Figure A6 showing the electrostatic sensor can resolve down to 3° of charge separation.*

APPENDIX B

This section contains detailed assumptions and calculations for the estimation of seeded and induced debris quantity in Chapter 6.

Debris Quantity Calculation

Measurements made:

- Seeded debris was pre-mixed in a vial containing 13 ml of oil.
- During each seeding event, the volume of total seeded debris and oil mixture used were measured to be approximately 1 ml.
- 0.3 g of steel seeded debris was used per vial.
- 0.1 g of silicon carbide seeded debris was used per vial.

Assumptions made:

- Debris is distributed evenly within the oil before seeding.
- Steel seeded debris is spherical with diameter of 8.8 μm (Test 2).
- Induced wear debris is spherical with diameter of 5 μm (guesstimate) (Test 2).
- Seeded debris diameter is spherical with of diameter 4 μm (guesstimate) (Test 3).
- Induced wear debris is spherical with diameter of 15 μm (guesstimate) (Test 3).

Test 2

Seeded Debris Calculation

$$\textit{Total debris volume used} = \frac{\textit{total mass}\ (kg)}{\textit{tap density}\ (kg/m^3)}$$

$$= \frac{0.0003}{4500} = \mathbf{6.67 \times 10^{-8}\ m^3\ in\ 13\ ml}$$

$$Volume\ per\ ml = \frac{6.67 \times 10^{-8}}{13} = \mathbf{5.13 \times 10^{-9}\ m^3/ml}$$

$$No. of\ debris\ per\ seeded\ event = \frac{volume\ per\ ml}{volume\ of\ debris}$$

$$= \frac{5.13 \times 10^{-9}}{\frac{4}{3} \times \pi \left(8.8 \times 10^{-6}\right)^3} = \mathbf{1.8 \times 10^6\ debris}$$

Induced wear Debris

$$No.\ of\ debris\ produced\ per\ seeding\ event = \frac{volume\ loss\ per\ seeding\ event}{volume\ of\ debris}$$

$$= \frac{4.0 \times 10^{-10}}{\frac{4}{3} \times \pi \times \left(5 \times 10^{-6}\right)^3} = \mathbf{8.5 \times 10^4\ debris}$$

Test 3

Seeded Debris Calculation

$$Total\ debris\ volume\ used = \frac{total\ mass}{tap\ density}$$

$$= \frac{0.0001}{1025} = \mathbf{9.75 \times 10^{-8}\ m^3}$$

$$Volume\ per\ ml = \frac{9.75 \times 10^{-8}}{13} = \mathbf{7.5 \times 10^{-9}\ m^3}$$

$$No.\,of\ individual\ debris\ per\ seeded\ event = \frac{volume\ per\ ml}{volume\ of\ debris}$$

$$= \frac{7.5\times 10^{-9}}{\frac{4}{3}\times\pi\left(4.0\times 10^{-6}\right)^{3}} = \mathbf{2.8\times 10^{7}\ debris}$$

Induced wear Debris

$$No.\ of\ debris\ produced\ per\ seeding\ event = \frac{volume\ loss\ per\ seeding\ event}{volume\ of\ debris}$$

$$= \frac{7.0\times 10^{-12}}{\frac{4}{3}\times\pi\times\left(15\times 10^{-6}\right)^{3}} = \mathbf{495\ debris}$$

APPENDIX C

Coulomb Boundary Element Field Modeller

Coulomb Boundary Element Field modeller uses boundary element method (BEM) to solve field calculations. BEM has several key advantages over other methods such as finite element method (FEM) and finite difference method (FDM) [110]. They include:

- Only discrimination of the dielectrics and conductors surfaces is needed when using BEM, illustrated in the two-dimension case of a parallel plate capacitor shown by Figure C1. To analyse the same case using FEM or FDM, the problem space needs to be truncated at some arbitrary distance from the model of the device. Meshing will then needed to be done on the entire problem space up to the truncation, illustrated by Figure C2. User input and storage requirements for the final solution are greatly reduced due to the discretisation of the dielectric and conductor surfaces in the BEM.

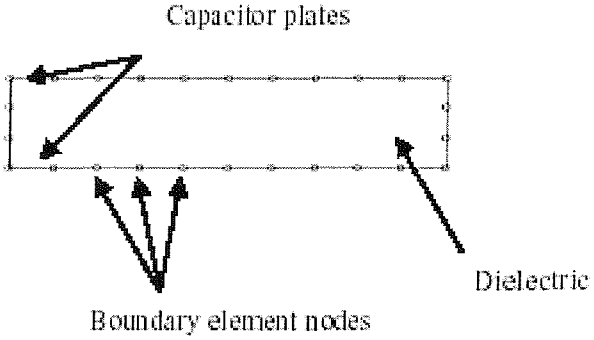

Figure C1 *Boundary element discretisation of a parallel plate capacitor model [110].*

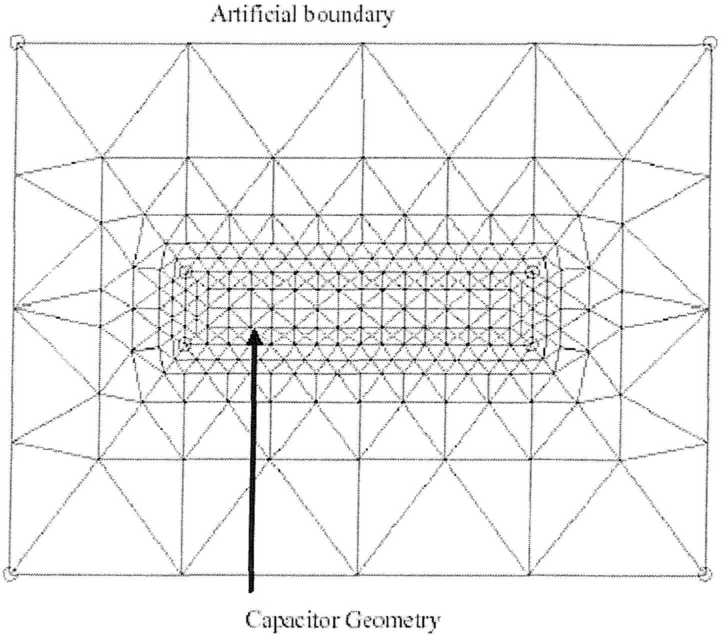

Figure C2 *Finite element mesh of a parallel plate capacitor model [110].*

- BEM allows the fields and potentials to be calculated at any point including the interior of devices and the exterior space to infinity. FEM and FDM require an artificial boundary condition to be placed at the truncation of the problem space introducing further approximations.
- Calculating the fields using BEM as opposed to FEM introduces smoothing. BEM is much less sensitive to numerical errors in the potential calculation.

Coulomb Validation

To validate the accuracy of coulomb model solution, a simple experimental was carried out to obtain results for comparison with Coulomb solutions. Figure C3 shows the test setup, which is very similar to the test setup in Chapter 8. A button sensor was tested and the geometry is shown in Figure C4. The efficiency of the button sensor is tested for different x (see Figure C3) of 10, 20, 30 and 40 mm.

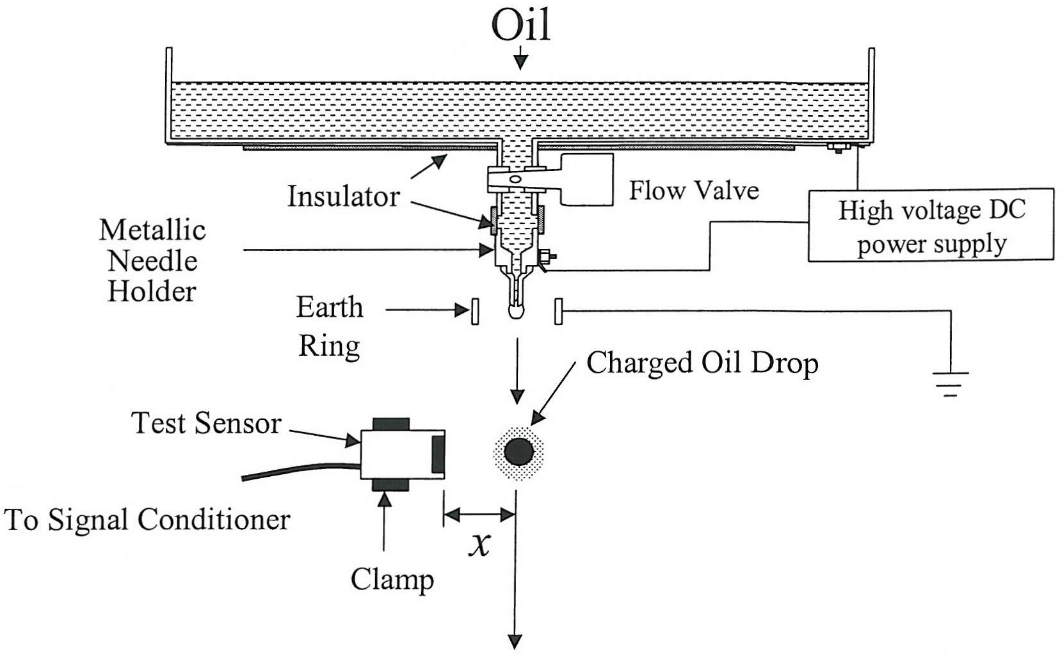

Figure C3 Validation test set up.

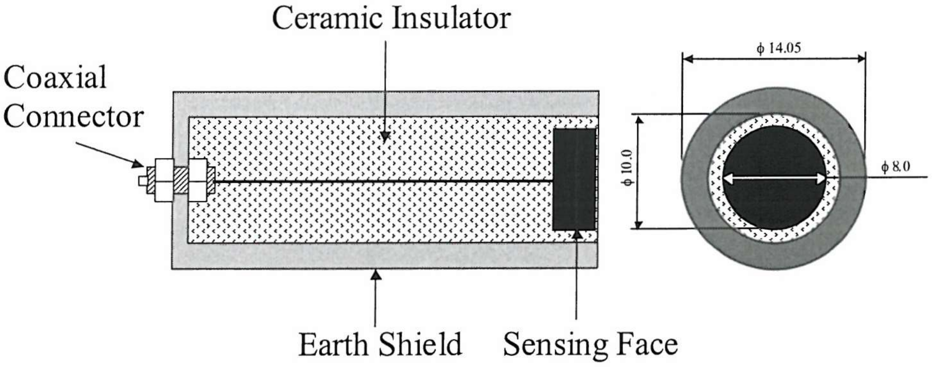

Figure C4 Button sensor geometry.

In Coulomb, the button sensor and the charged oil droplet are represented as 60° sections since they are symmetrical (see Figure C5), to minimise calculation time. The different colour denotes different materials assigned. Models were solved for 10, 20, 30, and 40 mm distance of the centre of the charged droplet to the sensing face and the comparison between the experimental results is shown in Figure C6.

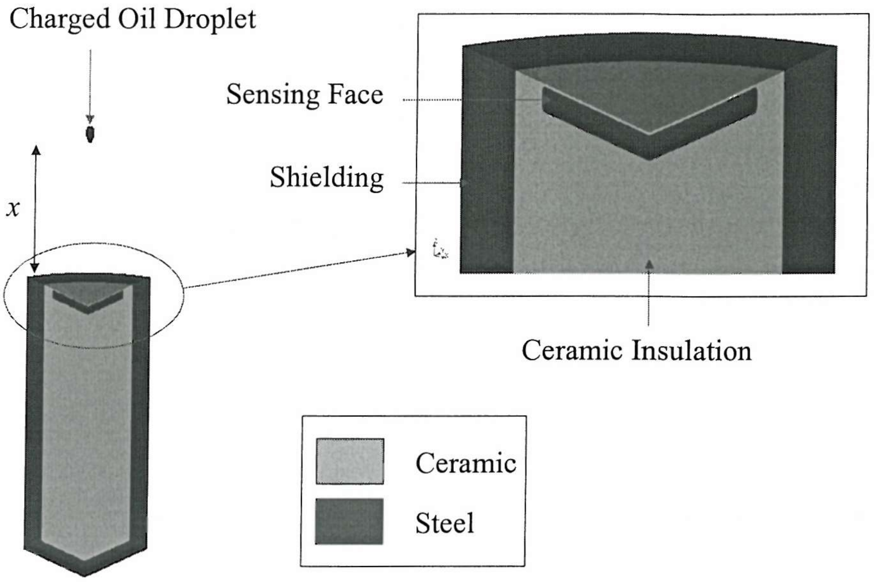

Figure C5 *60^o section representation of the button sensor Coulomb.*

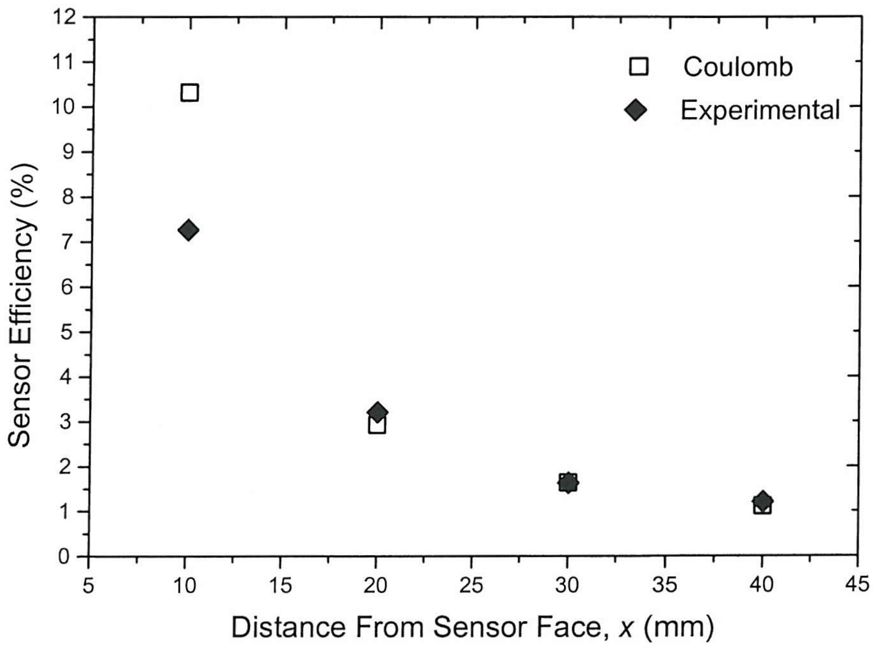

Figure C6 *Comparisons between the efficiency obtained from experimental results and Coulomb solutions.*

Figure C6 shows very close agreement between experimental results and Coulomb solutions. The Coulomb predicted efficiency for the droplet distance of 10 mm is slightly higher than that found experimentally. This is thought to be due to experimental errors. The results have demonstrated the potential of Coulomb to be used as a tool for sensor design and optimisation.

APPENDIX D

Proposed Debris Charging Mechanisms

This section will propose possible debris charging mechanisms in a lubricated system. It should be noted that some of the proposed mechanisms have not been investigated experimentally, and were proposed by speculation based on related fundamentals. Debris charging models can be divided into 2 broad categories; debris formation and tribocharging. These categories can be expanded further to describe specific charging mechanisms.

Charge Acquired During Formation

Wear debris is formed by physically removing materials from a surface. In the context of a lubricated tribocontact this can involve the removal of bulk material, stripping off part of oxide layers, regions of material that have reacted with oil additives and removal of material that has been transferred to the surface from the counter surface. All the described surfaces will have different work functions in comparison with the bulk material. Before being physically removed they would have caused localised surface charging with polarity based on their work function differences described in Section 3.6.3 on page 60. Upon removal and hence the formation of debris, they will retain this charge, as illustrated by Figure D1. This charge will be retained at a duration determined by the conductivity of the lubricant that the debris is suspended in (as discussed in Section 7.2.2).

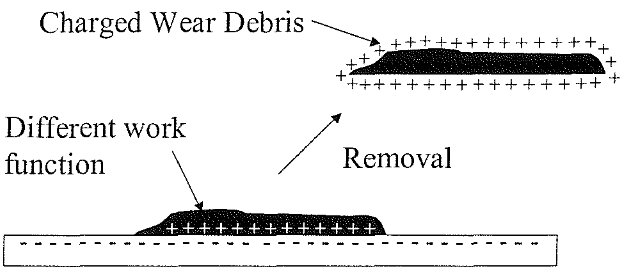

Figure D1 *The removal of an area of a different work function leads to the formation of charged debris.*

Very high and localised 'flash' temperatures have been known to occur during unlubricated and lubricated wear [50]. This rise in local temperature is likely to render some electrons mobile in which case they will tend to accumulate in the less hot part of the material by a process analogous to the Thompson effect (sometimes Kelvin effect) in metal. The Thompson effect is a phenomenon whereby if a metal (rod) is heated on one side, electrons will migrate to the less hot area (end) creating a potential difference as illustrated in Figure D2 [111].

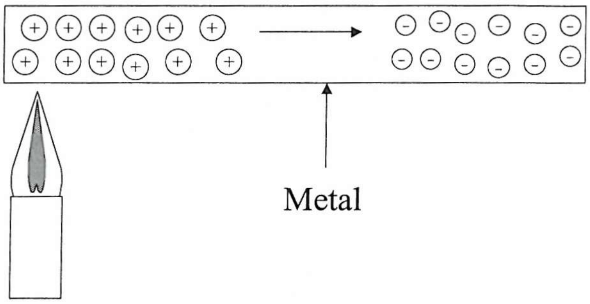

Figure D2 The Thompson effect. Movement of electrons due to temperature gradient in a metal.

Localised 'hot spots' will have a deficiency of electrons and hence become positively charged as illustrated in Figure D3. The presence of hot spots can cause localised welding with another surface and cause 'plucking' (micro-scuffing) to form positively charged wear debris.

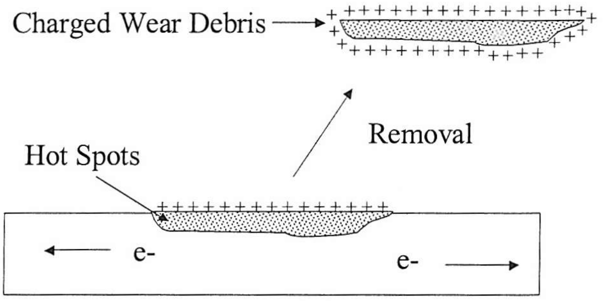

Figure D3 Migration of electrons away from hot spot creates a localised positive charge, which creates positively charged debris upon removal.

The formation of wear debris generally involves surface damage of one type or another and hence will certainly be accompanied by triboemissions. It is possible that the emissions produced a field emission charging effect similar to corona charging described in Chapter 7. Streams of ions and charged particle could impart charge on wear debris upon formation or indeed any debris that happens to be in the vicinity at the time of emission. The polarity and magnitude of the charge imparted will depend on the type of emission, their intensity and the surrounding medium. The 'electric fissure model' mentioned in Section 3.6.4, can also cause charge injection. This emission of electrons can ionise the medium surrounding it causing streams of charged particle to be injected, which can impart charge on wear debris within the vicinity, illustrated by Figure D4.

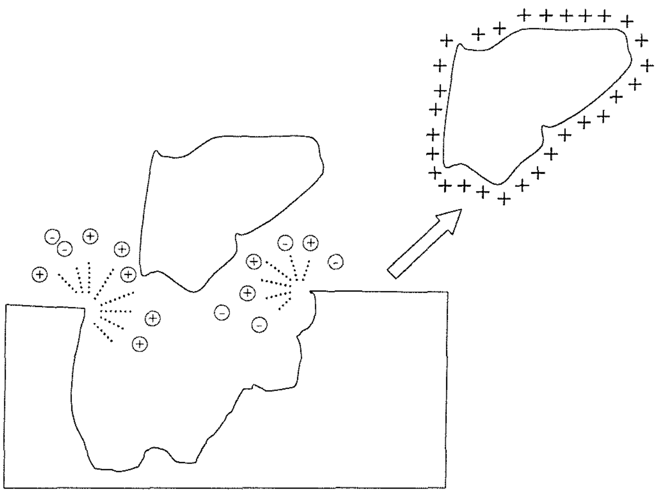

Figure D4 *Charge injection causes the debris in the vicinity to become charged.*

Tribocharging

Debris charging due to tribocharging consists of two main mechanisms, solid-solid interaction and solid-liquid interactions.

Solid-solid interactions

Solid-solid tribocharging of wear debris can occur when wear debris comes into contact with solid surfaces within a lubricated system. Figure D5 shows the schematic of this charging process. This interaction can occur at any location in the lubricated systems. It can occur just after debris formation with surfaces of other components of the tribocontact, filter surfaces, valve components as well as surfaces such as lubrication pipe walls. In the latter, flow regimes will influence the level of the contribution of charging in this way. In turbulent flow, wear debris is more likely to come into contact with the tube inner wall as compared to a laminar flow.

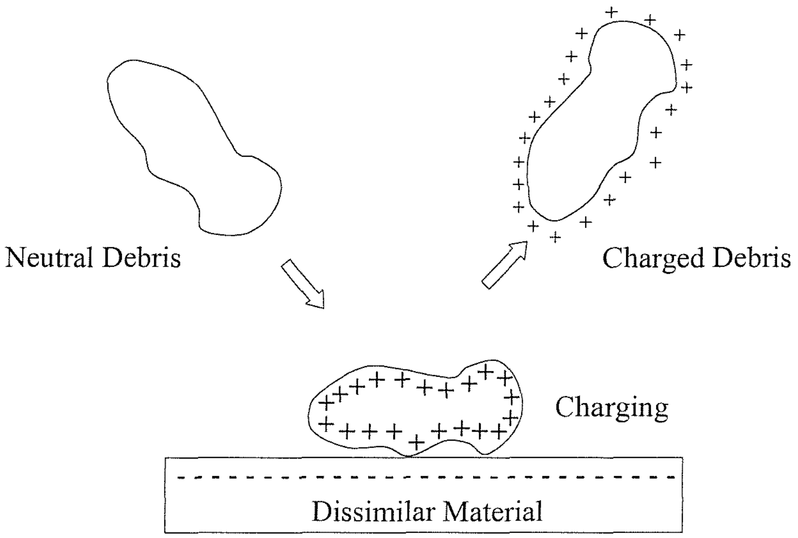

Figure D5 *The schematic diagram of solid-solid tribocharging process of wear debris.*

Solid-solid interaction can also occur amongst wear debris as shown in Figure D6. It has been found through experimental tests (Chapter 7) that it is possible for solids of similar material to get charged when contacting although the magnitude tends to be smaller than interactions of two dissimilar materials [31]. The reason for this is thought to related to local variation [50] which can lead to localised work function differences. This is indeed very conceivable as debris can become oxidise after formation [27]. This could be due to high and localised temperatures that occurred during its formation and chemical reactions with the lubricant. Chemical interaction of the nascent surface of debris with additives in the lubricant can also cause change in the local work function [33]. For a system that contains debris of two different materials such as a hybrid bearing system, this debris charging mechanism is highly plausible.

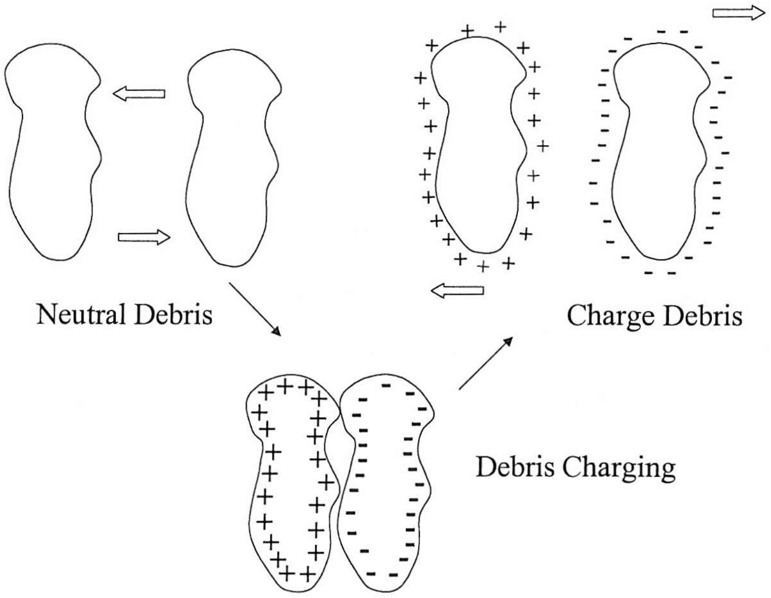

Figure D6 *The schematic diagram of debris solid-solid tribocharging process.*

Solid liquid interactions

Debris can also become charged by the solid-liquid tribocharging process, i.e. double layer theory. For debris suspended in a liquid it will have its own double layer. The shearing of this double layer due to movements of the liquid can cause a net charge to remain on the debris, illustrated by Figure D7.

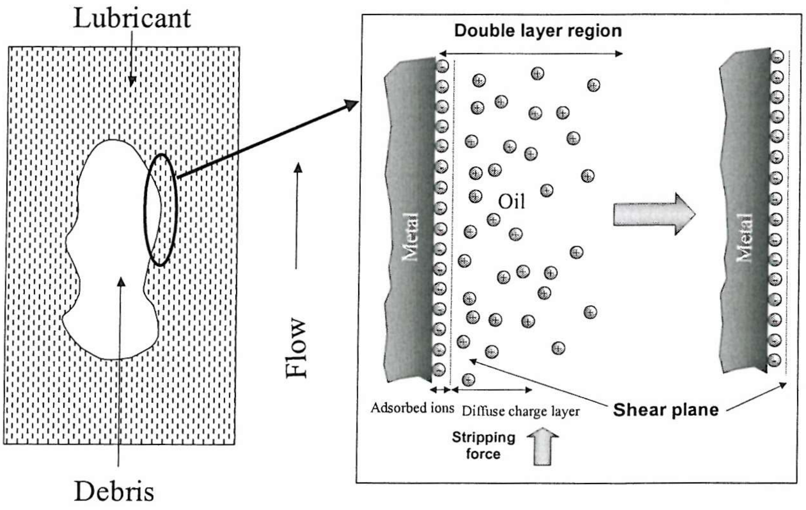

Figure D7 *Charging of wear debris due to the shearing of its double layer*

Wear debris can also become charged indirectly due to the interaction of neutral wear debris with a fully established double layer of solid surface e.g. the inner surface of a lubrication tube (see Figure D8), or another wear debris (see Figure D9). Neutral debris could collect charge if it enters the inner layer of the established double layer.

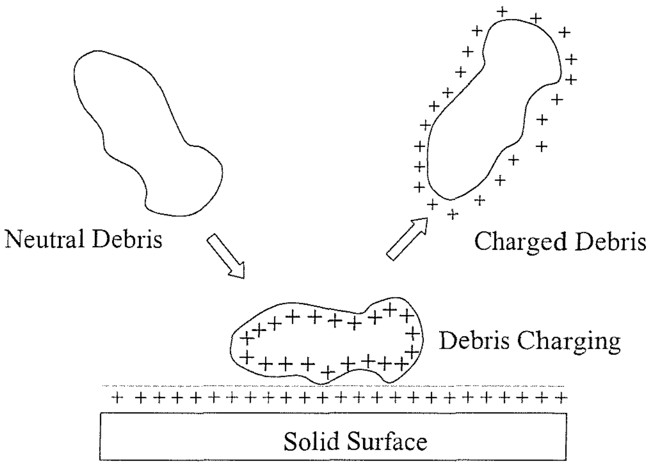

Figure D8 *Wear debris charging due to interaction with the inner layer of an established double layer of a solid surface*

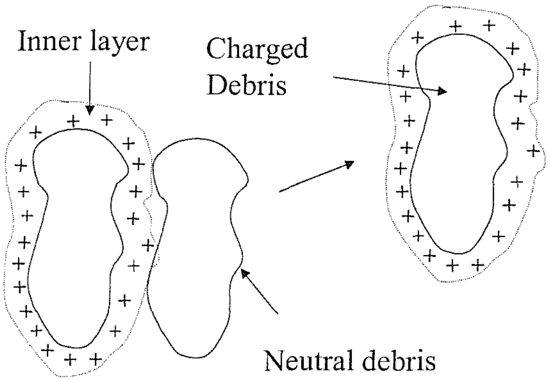

Figure D9 *Interaction of neutral debris with the inner layer of double layer of debris can cause debris to become charged.*

The change in viscosity of the lubricant will affect the magnitude of the charging due to solid-liquid tribocharging. It has been found that with an increase in viscosity, the rate of charging decreases [39]. This can be explained by Equation 3.15 in Section 3.6.2. With increasing viscosity Debye length increases, thus reducing the charging tendency. Furthermore, the increase in the thickness of the stagnant layer decreases the shear rate of the double layer, decreasing the charging ability further.

REFERENCES

[1] O.D. Tasbaz, R.J.K. Wood, M. Browne, H.E.G. Powrie, G. Denuault, Electrostatic monitoring of oil lubricated sliding point contacts for early detection of scuffing, Wear 230 (1999) 86-97.

[2] O.D. Tasbaz, R.J.K. Wood, H.E.G. Powrie, Electrostatic monitoring of oil lubricated contacts for early detection of wear, Proceedings of the International Conference on Condition Monitoring, Swansea, 1999, Coxmore Publishing, Oxford, ISBN 901892115.

[3] H.E.G. Powrie, O.D. Tasbaz, R.J.K Wood, C.E. Fisher, Performance of an electrostatic oil monitoring systems during an FZG gear scuffing test, Proceedings of the International Conference on Condition Monitoring, Swansea, 1999, Coxmore Publishing, Oxford, ISBN 901892115, 155-174.

[4] S. Courtney, Condition monitoring – Why it sometimes goes wrong, Proceedings of the International Conference on Condition Monitoring, Oxford, 2001, Coxmore Publishing, Oxford, ISBN 190189214, 344-349.

[5] B.J. Roylance, Machine failure and its avoidance – What is tribology's contribution to effective maintenance of critical machinery?, The Donald Julius Groen Lecture , Mission of Tribology Research 2002, IMechE, London.

[6] R. Barron, Engineering condition monitoring. Practice, methods and applications. Longman, 1996, ISBN 0582246563.

[7] M. J. Neale, The principles behind condition monitoring techniques, Condition monitoring: the practice, edited by E.D. Yardley, Professional Engineering Publishing, 2002, ISBN 186058361, 21 – 34.

[8] J. Nurse, C. Petch, C.E. Fisher, Engine gas path integrity monitoring, Aerotech 94, Paper C470/6/52.

[9] H.E.G. Powrie, K. McNicholas, Gas path condition monitoring during accelerated mission testing of a demonstrator engine, American Institute of Aeronautics and Astronautics (1997) Paper 97-2904.

[10] H.E.G. Powrie, C.E. Fisher, Monitoring of foreign objects ingested into intake of a gas turbine aeroengine, Proceedings of the International Conference on Condition Monitoring, Swansea, 1999, Coxmore Publishing, Oxford, ISBN 901892115, 175-190.

---

[11] B.J. Roylance, J.A. Williams, R. Dwyer-Joyce, Wear debris and associated wear phenomena, Proc IMechE 214 Part J (2000), 79-105.

[12] B.J. Roylance, S. Raadnui, The morphological attributes of wear particles – their role in identifying wear mechanisms, Wear 175 (1994) 115-121.

[13] B.J. Roylance, T.M. Hunt, Wear Debris Analysis, Coxmoor Publishing Company First Edition (1999), ISBN 1901892026.

[14] P. Podsiadlo, G.W. Stachowiak, Characterization of surface topography of wear particles by SEM stereoscopy, Wear 206(1-2) (1997) 39-52.

[15] T.G. Barraclough, T.P. Sperring, B.J. Roylance, T. Nowell, D. Hodges, Generic-based wear debris identification – the first step towards morphological classification. Proceedings of the International Conference on Condition Monitoring, Swansea, 1999, Coxmore Publishing, Oxford, ISBN 901892115, 525-538.

[16] N.K. Myshkin, H. Kong, A.Y. Grigoriev, Yoon ES, The use of color in wear debris analysis, Wear 250(2) (2001) 1218-1226.

[17] B.J. Roylance, Wear studies through particle size distribution application of the Weibull distribution to ferrography, Wear 90(1) (1983) 113-136.

[18] S. Raadnui, B.J. Roylance, The classification of wear shape. STLE J. Lubrication Engineering 51(5) (1995) 432-437.

[19] T.B. Kirk, G.W. Stachowiak, A.W. Batchelor, Fractal parameters and computer image-analysis applied to wear particles isolated by ferrography, Wear 145(2) (1991) 347-365.

[20] S.R. Ge, G.A. Chen, X.Y. Zhang, Fractal characterization of wear particle accumulation in the wear process, Wear 250(2) (2001) 1227-1233.

[21] Z. Peng, T.B. Kirk, Computer image analysis of wear particles in three-dimensions for machine condition monitoring, Wear 223(1-2) (1998) 157-166.

[22] G.W. Stachowiak, P. Podsiadlo, Characterization and classification of wear particles and surfaces, Wear 249(3-4) (2001) 194-200.

[23] P. Podsiadlo, G.W. Stachowiak, Scale-invariant analysis of wear particle surface morphology II. Fractal dimension, Wear 242(1-2) (2000) 180-188.

[24] S. Raadnui, B. J. Roylance, The classification of wear shape. STLE Journal of Lubrication. Engineering 51(5) (1995) 432-437.

[25] Z. Peng, T.B. Kirk, Two-dimensional fast Fourier transform and power spectrum for wear particle analysis, Tribology International 30(8) (1997) 583-590

---

[26] T.P. Sperring, B.J. Roylance, T. Nowell, D. Hodges, A. Curran, From research to application – The development of the wear debris classification system – SYCLOPS, Proceedings of the International Conference on Condition Monitoring, Oxford, 2001, Coxmore Publishing, Oxford, ISBN 190189214, 365-373.

[27] F.T. Barwell, Wear of machine elements, Proc. Int. Conf. On Fundamentals of Tribology (1978), MIT Press, 401-440.

[28] T.M. Hunt, Handbook of Wear Debris Analysis and Particle Detection in Fluids, 1993, Elsevier, Amsterdam, ISBN 1851669620.

[29] T.M. Hunt, Monitoring particles in liquids, Filtration & Separation 32(3) (1995) 205-211.

[30] R.W. Chapman, D.J. Hodges, T.J. Nowell, Micro to macro – wear debris analysis as a condition monitoring tool, Insight 44(8) (2002) 498 – 502.

[31] D.M. Taylor, P.E. Secker, Industrial electrostatics fundamentals and measurement, Research Studies Press (1994), ISBN 0863801587.

[32] H.E.G. Powrie, R.J.K. Wood, T.J. Harvey, L.Wang and S. Morris, Electrostatic Charge Generation Associated with Machinery Component Deterioration, IEEE Aerospace Conference Proceedings (2002), ISBN 0780372328.

[33] S. Morris, R.J.K. Wood, T.J. Harvey, H.E.G. Powrie, Use of electrostatic Charge Monitoring in Early Detection of Adhesive Wear in Oil Lubricated Contacts, Journal of Tribology 124 (2002) 288 – 295.

[34] J.B. Gajewski, Continuous non-contact measurements of charges of solid particles in pipe of pneumatic transport. Part I: Physical and mathematical models of a method, Proc. IEEE/IAS San Diego (1989).

[35] J.B. Gajewski, B. Glod, R.A. Grobelny, W. Kala, Continuos non-contact measurements of charges of solid particles in pipe of pneumatic transport. Part II: Measuring systems and its application, Proc. IEEE/IAS San Diego (1989).

[36] J.B. Gajewski, Mathematical model of non contact measurement of charges while moving, Journal of Electrostatics 15(1) (1984) 81-92.

[37] J.B. Gajewski, A. Szanok, Charge measurement of dust particle in motion, Journal of Electrostatics 10 (1981) 229-234.

[38] P.H.W. Vercoulen, Electrostatic Processing of particles. A tool in particle technology, Delft Technical University PhD Thesis, (1995) 39-65.

[39] T.J. Harvey, G. Denuault, H.E. Powrie, R.J.K. Wood, Electrostatic sensor calibration, oil charging ability and sensor sensitivity to contact potential difference, ONR Grant No. N00014-97-1-0100, Annual Technical Progress Report 98-99, Mechanical Engineering Department, School of Engineering Science, University of Southampton.

[40] H.L.F. Helmholtz, Studies of electric boundary layers, Ann. Phys. Chem. 7 (1879) 337-382.

[41] G. Gouy, Constitution of the electric charge at surface of an electrode, J. Phys. 9(4) (1910) 457-467.

[42] D.L. Chapman, A contribution to the theory of electrocapillarity, Philos. Mag. 25 (1913) 475-481.

[43] O.Z. Stern, The theory of the electrolytic double-layer, Elektrochem. 30 (1924) 508-516.

[44] D.C. Grahame, The electrical double layer and the theory of electrocapillarity, Chem. Rev. 41 (2-3) (1947) 441-501.

[45] W.F. Schmidt, Electrons in non-polar dielectric liquids, IEEE transactions on Electrical Insulation 26(4) (1991) 560-566.

[46] M. Popi, Determination of polyclyclic aromatic hydrocarbons in white petroleum products, Analytical Chemistry 47(12) (1975) 1947-1950.

[47] I.M. Williams, The origin of conduction in hydrocarbons. Proceedings of the International Conference on Conduction and Breakdown in Dielectric Liquids, Froutieres, Dreux, (1978) 49-55.

[48] S. Italashi, State of water in hydrocarbon liquids and its effects on conductivity, IEEE Transactions on Dielectrics and Electrical Insulation 2(6) (1995) 1117-1121.

[49] J.K. Nelson, Electrokinetic effects in pumped dielectric fluids, Whitehead memorial Lecture 1992, Annual Report IEEE CEIDP, # 93CH3269-8, 1993, 25-61.

[50] W.R. Harper, Contact and frictional electrification, Oxford University Press, 1967, ISBN 188554006.

[51] J. Lowell, Contact electrification of metals, J. Phys. D: Applied Physics 8 (1975) 53-63.

[52] B.A. Unger, Electrostatic discharge failures of semiconducting devices, IEEE/Proc IRPS (1981) 193-199.

[53] D.J. Montgomwry, Static electrification in solids, Solid State Physics 9 (1959) 139-197.

[54] Y Yang, T Kurfess, S Liang, S. Danyluk, Application of a specialized capacitance probe in bearing diagnosis, Wear 229(2) (1999), 1215-1221.

[55] Y. Yang, S. Danyluk, W. Hoeprich, A study on rolling element skew measurement in a tapered roller bearing with a specialized capacitance probe Journal Of Tribology 122 (3) (2000), 534-538.

[56] E.S. Zanoria, K. Hamall, S. Danyluk, A.L. Zharin, The nonvibrating Kelvin probe and its application for monitoring surface wear, Journal Of Testing And Evaluation 25 (2) (1997), 233-238.

[57] T. Kasai, X.Y. Fu, D.A. Rigney, A.L. Zharin, Application of a non-contacting Kelvin probe during sliding, Wear 229(2) (1999), 1186-1204.

[58] A.M. James, M.P. Lord, Chemical and physical data, MacMillan Press Ltd., London, 1992, ISBN 0333511670, 174.

[59] C. Kajdas, M.J. Furey, A. Ritter, G.J. Molina, Triboemission as a basic part of the boundary friction regime, Proceedings of the 12th International Colloquium Tribology 2000-Plus, Technische Akademie Esslingen, Ostfildern, Germany, (2000).

[60] K. Nakayama, H. Hashimoto, Triboemission from various materials in atmosphere, Wear 147 (1991) 335-343.

[61] K. Nakayama, H. Hashimoto, Triboemission of charged particles and photons from ceramic surfaces in various gases, Wear 185 (1995) 183-188.

[62] K. Nakayama, Triboemission of charged particles and photons from solid surfaces during frictional damage, J Phy D: Applied Physics 25 (1992), 303-308.

[63] K. Nakayama, H. Hashimoto, Triboemission of charged particles and photons in hydrocarbon atmospheres, Proc 6th international congress on Tribology, Eurotrib '93 Budapest Hungary (1993).

[64] K. Nakayama, Triboemission of charged particles from various solids under boundary lubrication conditions, Wear 178(1-2) (1994) 61-67.

[65] K. Nakayama, H. Hashimoto, Effect of surrounding gas pressure on triboemission of charged particles and photons from wearing ceramic surfaces, Tribology Transactions 38(1) (1995) 35-42.

---

[66] K. Nakayama, Triboemission of charged particles and resistivity of solids, Tribology letters 6 (1999) 37-40.

[67] K. Nakayama, Tribocharging and friction in insulators in ambient air, Wear 194(1-2) (1996) 185-189.

[68] K. Nakayama. H. Hashimoto, Triboemission of charged particles and photons from wearing ceramic surfaces in various hydrocarbon gases, Wear 185(1-2) (1995) 183-188.

[69] B. Sujak, A. Gieroszbski, K. Gieroszinska, Energy distribution of exoelectrons emitted into vacuum from plastically deformed, oxide covered aluminum at low temperatures, Acta Polonica, A46 (1974) 1-17.

[70] J.T. Dickinson, D.B. Snyder, E.E. Donaldson, Acoustic emission and electron emission during deformation of anodised aluminium, Journal of Vacuum Science & Technology 17 (1980) 429-432.

[71] M.J. Neale, M. Gee, Guide to wear problems and testing for industry, Professional Engineering Publishing Ltd. London, 2000, ISBN 1-860582877.

[72] M. Aksoy, O. Yilmaz, M.H. Korkut, The effect of strong carbide-forming elements on the adhesive wear resistance of ferritic stainless steel, Wear 249 (2001) 639–646.

[73] J.A. Williams, Engineering Tribology, Oxford University Press, Oxford, 1994, ISBN 0198565038, 341.

[74] D. Dowson, G. R. Higginson, Elasto-Hydrodynamic Lubrication, Int. Series in Material Sci. & Tech, Pergamon Int. Library, 23, 158.

[75] J. W. Stead, Journal of West Scotland Iron Steel Inst., 19 (1911-12), 169.

[76] E. M. Trent, Journal of Iron Steel Inst., 143 (1941), 401

[77] M.D. Rogers, Metallographic characterisation of transformation phases on scuffed cast iron diesel engine components, Tribology 2 (1969) 123-127.

[78] B.J. Griffiths, Mechanisms of White Layer Generation With Reference to Machining and Deformation Processes, ASME/ASLE Joint Lubrication Conference, Pittsburgh, PA, (1986), paper 86-Trib. 30.

[79] T.S. Eyre, A. Baxter, The formation of white layers at rubbing surfaces, Tribology (1972) 256-261.

[80] D. Scott, A.I. Smith, J. Tait, G.R. Tremain, Materials and metallurgical aspects of piston ring scuffing in a literature survey, Wear 33 (1975) 293-315.

[81] J.F. Archard, The temperature of rubbing surfaces, Wear 2 (1959) 438-455.

[82] Y.Y. Jang, H.S. Fang, W.G. Huang, A study on wear resistance of the white layer, Tribology International 29(5) (1996) 435-428.

[83] S.B. Newcombe, W.M. Stobbs, Transmission electron microscopy study of the white etching layer on a rail head, Material. Science. Engineering 66 (1984) 195-204.

[84] A.M. James, M.P. Lord, Chemical and physical data, MacMillan Press Ltd., London, (1992), ISBN 0333511670, 174.

[85] M.F. Ashby, S.C. Lim, Wear mechanism maps, Scripta Metallurgica et Materialia 24 (1990), 805-810.

[86] F.P. Bowden, D. Tabor, Friction and lubrication, Methuen's Monographs on Physical Subjects, London, 1956, 33-43.

[87] J.E. Wilson, F.H. Stott, G.C. Wood, The development of wear protective oxides and their influence on sliding friction, Proc. R. Soc. London, Ser A, 369 (1980) 557-574.

[88] F.H. Stott, G.C. Wood, The influence of oxides on the friction and wear of alloys, Tribology International 11 (1978) 211-218.

[89] T.F.J. Quinn, Oxidational wear, Wear, 15 (1971) 413.

[90] D.G. Powell, S.W.E. Earles, A.S.L.E. Trans. 11 (1968) 101.

[91] M.J. Khadim, S.W.E. Earles, Unlubricated sliding at high speeds between copper and steel surfaces, Proceedings of the IMechE 181(30) (1966) 25-30.

[92] K. Williams, E. Giffen, Proc. IMechE 178 (1963/64) 24.

[93] I.M. Hutchings, Tribology – Friction and wear of engineering materials, Arnold, 1992, ISBN 03405614.

[94] N.K. Myshkin, C.K. Kim, M.I. Petrokovets, Introduction to Tribology, Cheong Moon Gak, 1997, ISBN 8970884653, 102.

[95] R.I. Trezona, D.N. Allsopp, I.M. Hutchings, Transitions between two-body and three-body abrasive wear: influence of test condition in the microscale abrasive wear test. Wear 225–229 (1999) 205–214.

[96] K.H. Zum Gahr, Wear by hard particles, Tribology International 31 (1999) 587–596.

[97] G.B. Stachowiak, G.W. Stachowiak, The effects of particle characteristics on three-body abrasive wear, Wear 249 (2001) 201–207.

[98] E. Rabinowicz, L. A. Dunn, P. G. Russell, A study of abrasive wear under three-body conditions. Wear 4 (1961) 345–355.

[99] L. Fang, X. L. Kong, J.Y. Su, Q. D. Zhou, Movement patterns of abrasive particles in three-body abrasion. Wear 162–164 (1993) 782–789.

[100] Y. Xie, B. Bushan, Effects of particle size, polishing pad and contact pressure in free abrasive polishing. Wear 200 (1996) 281–295.

[101] T.J. Harvey, R.J.K. Wood and H.E.G. Powrie, Dual probe measurements of contact potential difference created by bimetallic discs at University of Southampton, SES Number: ME0302, June 2003.

[102] J. Lowell, A.R. Akande, Contact electrification - Why is it variable, Journal of Physics D-Applied Physics 21(1) (1988) 125-137.

[103] A. Klinkenberg, J. L. Van der Minne, Electrostatics in the Petroleum Industry, Elsevier Publishing Company, Amsterdam (1958).

[104] T.J. Harvey, S. Morris, H.E.G. Powrie and R.J.K. Wood, "Electrostatic monitoring of boundary and mixed lubrication", 2nd World Tribology Congress, Vienna, Sept 2001, paper A-83-11-856.

[105] H.L. Walmsley, The generation of electric currents by turbulent flow of dielectric liquids: II. Pipe of finite length, Journal of Physics. D: Applied Physics 16 (4) (1983) 553-572.

[106] J.C. Gibbings and E.T. Hignett, Dimensional analysis of electrostatic streaming current, Electrochimica Acta 11 (1966) 815-826.

[107] E.M. McCash, Surface Chemistry, Oxford University Press, Oxford, 2001, ISBN 0198503288, 62-63.

[108] L. Fouad, S. Elhazek, Effect of humidity on positive corona discharge in a three electrode system, Journal of Electrostatics 35 (1995) 21-30.

[109] T.J. Harvey, R.J.K. Wood, G. Denuault, H.E.G. Powrie, Investigation of electrostatic charging mechanisms in oil lubricated tribo-contacts, Tribology International 35 (2002) 605–614.

[110] J. Lopez-Roldan, P. Ozers, T. Judge, C Rebizant, R. Bosch, J. Munoz, Experience using the boundary element method in electrostatic computations as a fundamental tool in high voltage switchgear design, IEEE International Symposium on Electrical Insulation, Washington DC, WA, USA, June 1998.

[111] F.W. Sears, Principal of Physics II – Electricity and Magnetism, Addison-Wesley Press INC 1946.